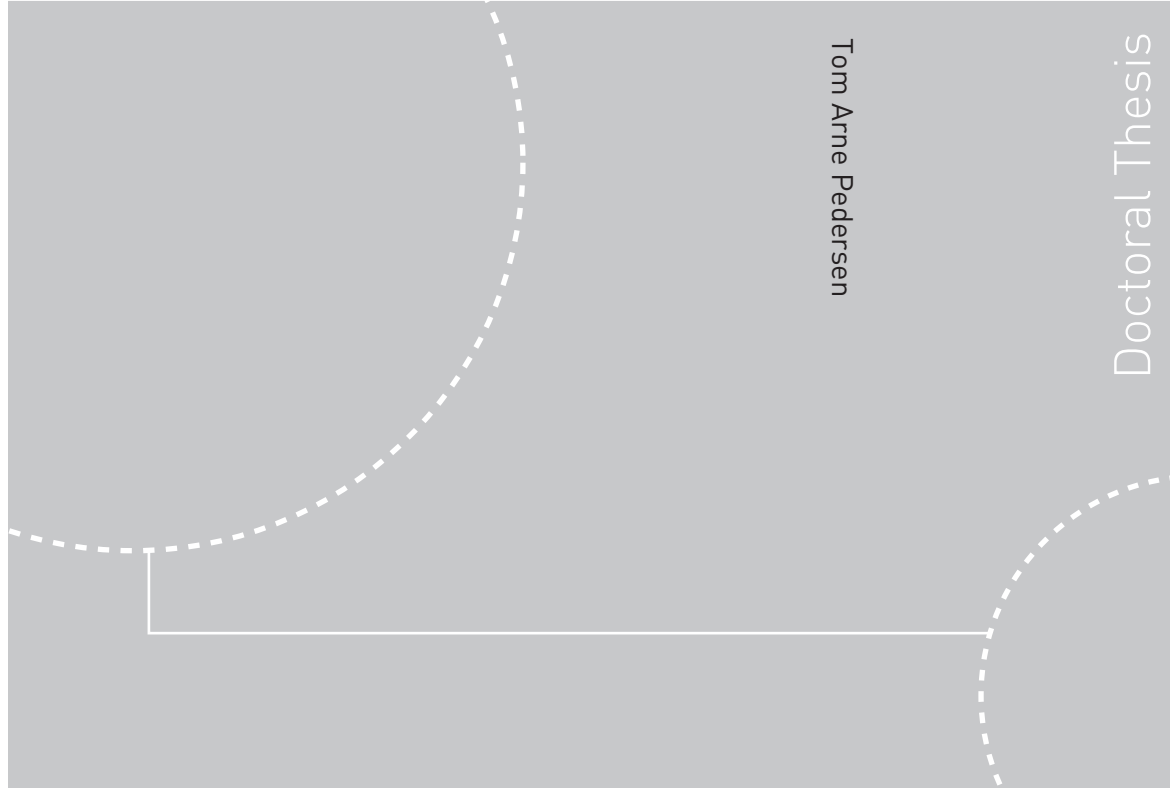


ISBN 978-82-471-1486-5 (printed ver.)  
ISBN 978-82-471-1487-2 (electronic ver.)  
ISSN 1503-8181



Doctoral theses at NTNU, 2009:56

Tom Arne Pedersen  
**Bond Graph Modeling of Marine  
Power Systems**

Doctoral theses at NTNU, 2009:56

NTNU  
Norwegian University of  
Science and Technology  
Thesis for the degree of  
philosophiae doctor  
Faculty of Engineering Science and Technology  
Department of Marine Technology

 **NTNU**  
Norwegian University of  
Science and Technology

 NTNU

 **NTNU**  
Norwegian University of  
Science and Technology

Tom Arne Pedersen

# Bond Graph Modeling of Marine Power Systems

Thesis for the degree of philosophiae doctor

Trondheim, March 2009

Norwegian University of  
Science and Technology  
Faculty of Engineering Science and Technology  
Department of Marine Technology



**NTNU**

Norwegian University of  
Science and Technology

NTNU  
Norwegian University of Science and Technology

Thesis for the degree of philosophiae doctor

Faculty of Engineering Science and Technology  
Department of Marine Technology

©Tom Arne Pedersen

ISBN 978-82-471-1486-5 (printed ver.)  
ISBN 978-82-471-1487-2 (electronic ver.)  
ISSN 1503-8181

Doctoral Theses at NTNU, 2009:56

Printed by Tapir Uttrykk

# Bond Graph Modeling of Marine Power Systems

by

Tom Arne Pedersen

Faculty of Engineering Science and Technology  
Department of Marine Technology  
Norwegian University of Science and Technology

Trondheim, March 2009



## Abstract

Mathematical models for an All Electric Ship component library is developed in this thesis.

The main motivation for writing this thesis is to develop a model library that gives the opportunity to simulate both existing and new machinery systems without having to remodel the entire system each time. The model library should support the process of modeling and reuse, and also emphasize openness to brace the modeler during the development and refinement phase.

The bond graph approach is good when it comes to physical modeling of systems, it is a good tool for combining different energy domains and it may help understanding the system. In addition, bond graph is a powerful method to find dependencies between different components. By using causal analysis any problems in the model, e.g. algebraic constraints or dependent system variables will be detected, and necessary remodeling may be performed to handle such problems. The bond graph approach is therefore used when developing the component library.

The component library consists of selected power producers like diesel and gas engines, fuel cell and synchronous generator, and power consumers like asynchronous motor with voltage source converter and generic load used for hotel and auxiliary loads. The library also consist of a ship model, propeller and environmental loads. Most of the components have been verified using test measurements from manufacturer and full scale measurements from a supply vessel operating in the North Sea.

The main contributions of the thesis are:

- Development of a flexible component library used for modeling and simulation of existing and new marine power plants.
- Component models are verified using test measurements performed by manufacturer and full-scale measurements from a supply-vessel.
- Simulation of selected cases of combined power plants during extreme dynamic loads are conducted.
- Development of a hybrid causality generator model for increased flexibility when simulating combined power plants.

The library components are developed using 20Sim. 20Sim is also used for time

domain simulation of the power plant test cases.

## Acknowledgements

This thesis is submitted in partial fulfillment of the requirements for the degree of philosophiae doctor (PhD) at the Norwegian University of Science and Technology (NTNU) and is based on research done in the period January 2004 through September 2008. The research has been funded by NTNU and is a part of the project *Energy Efficient All-Electric Ship* (EEAES).

This work has been carried out under supervision of Associate Prof. Eilif Pedersen at Department of Marine Technology, Faculty of Engineering Science and Technology, Norwegian University of Science and Technology. First I would thank him for convincing me to do a PhD and making it possible to do part of the PhD from Lillestrøm. I would also express my gratitude to him for answering all my questions and encouraging me during the research period.

I would like to thank PhD student Kristine Bruun, whom I shared office with, for many fruitful and interesting discussions.

I would also like to thank Olve Mo at Marine Cybernetics for taking the discussions about converter modeling, and to Professor Asgeir Sørensen for giving me the last push to finish this thesis.

A special thank goes to Sven Wertebach for being a good motivator and friend.

At last I would like to thank my wife, Tonje Evanger, and daughter, Tyri Evanger, for their love, patience and support when it was most needed. I don't think this would have been possible without you.

Trondheim, October 15<sup>th</sup> 2008

Tom Arne Pedersen



# Contents

<b>Abstract</b>	<b>iii</b>
<b>Acknowledgements</b>	<b>v</b>
<b>Nomenclature</b>	<b>xi</b>
<b>1 Introduction</b>	<b>1</b>
1.1 Background	1
1.2 Diesel electric power system	3
1.2.1 System description	3
1.2.2 Use of electric propulsion	4
1.2.3 New concepts	5
1.3 Design of an all electric ship	6
1.3.1 System design	6
1.3.2 Numerical simulation tools	8
1.3.3 Is bond graph modeling a way to go?	10
1.4 Motivations	11
1.5 Previous work	12
1.6 Main contribution	13
1.7 Bond graph modeling	14
1.8 Organization of the thesis	14
<b>2 AES library</b>	<b>17</b>
2.1 Modeling environments	17
2.2 Model structure	19
2.2.1 Technical component layer	19
2.2.2 Physical concept layer	20
2.2.3 Mathematical layer	20
2.3 Model documentation	21
<b>3 System modeling</b>	<b>27</b>
3.1 Diesel and gas engine	27
3.1.1 Mathematical description	27
3.1.2 Bond graph representation of the engine model	29
3.2 Synchronous generator	29
3.2.1 Mathematical description	30
3.2.2 Bond graph representation of the generator model	33

3.3	Magnetic saturation in the generator model . . . . .	35
3.3.1	Method I . . . . .	35
3.3.2	Method II . . . . .	38
3.3.3	Procedure for calculating saturation using method II. . . . .	40
3.4	Power invariant transformation . . . . .	41
3.4.1	Mathematical description . . . . .	41
3.4.2	Bond graph representation of power invariant transformation. . . . .	42
3.5	Circuit breaker . . . . .	43
3.5.1	Theory of switched power junction . . . . .	44
3.5.2	Bond graph representation of the circuit breaker . . . . .	46
3.6	Fuel cell . . . . .	47
3.6.1	Mathematical description . . . . .	47
3.6.2	Bond graph representation of a fuel cell power plant. . . . .	52
3.7	Asynchronous motor . . . . .	54
3.7.1	Mathematical description . . . . .	54
3.7.2	Bond graph representation of the induction motor. . . . .	57
3.8	Power converters . . . . .	59
3.8.1	A basic rectifier. . . . .	60
3.8.2	DC-link with brake. . . . .	63
3.8.3	The inverter. . . . .	64
3.8.4	VSI-PWM converter. . . . .	74
3.9	Propeller. . . . .	74
3.9.1	Mathematical description . . . . .	74
3.9.2	Bond graph representation of the propeller . . . . .	77
3.10	Hotel and auxiliary loads . . . . .	78
3.10.1	Mathematical description . . . . .	78
3.10.2	Bond graph representation of hotel and auxiliary loads . . . . .	78
3.11	Ship . . . . .	78
3.11.1	Mathematical description . . . . .	78
3.11.2	Bond graph representation of a ship. . . . .	80
3.12	Environmental loads. . . . .	80
3.12.1	Mathematical description . . . . .	80
3.12.2	Bond graph representation of waves and current loads . . . . .	83
<b>4</b>	<b>Model verification</b> . . . . .	<b>85</b>
4.1	Generator . . . . .	85
4.1.1	Verifying excitation data . . . . .	85
4.1.2	Magnetic saturation . . . . .	88
4.1.3	Synchronization of three phase generator to bus . . . . .	90
4.2	Fuel cell . . . . .	93
4.2.1	Stand alone fuel cell . . . . .	93
4.2.2	Fuel cell and grid . . . . .	96
4.3	Asynchronous motor . . . . .	100
4.3.1	Verifying asynchronous motor data . . . . .	100
4.4	PWM converter . . . . .	105
4.4.1	Direct torque control. . . . .	105

4.4.2	Field oriented control . . . . .	107
4.4.3	Field oriented control using average converter model . . . . .	109
4.4.4	Comparison of advanced and average inverter model . . . . .	110
4.4.5	Model characteristics of the average PWM converter . . . . .	112
4.5	Bow propeller . . . . .	116
<b>5</b>	<b>Case simulation</b>	<b>119</b>
5.1	Case I: Extreme load variations . . . . .	119
5.1.1	System setup . . . . .	119
5.1.2	Simulation . . . . .	121
5.2	Case II: Dynamic positioning and errors on generators . . . . .	125
5.2.1	System setup . . . . .	125
5.2.2	Simulation . . . . .	125
5.3	Case III: Generator and fuel cell in a combined power plant . . . . .	131
5.3.1	System setup . . . . .	131
5.3.2	Simulation . . . . .	131
5.4	Summary . . . . .	135
<b>6</b>	<b>Modified generator model</b>	<b>137</b>
6.1	Mathematical description . . . . .	137
6.2	Basic setup with 2 generator models . . . . .	141
6.2.1	System setup . . . . .	141
6.2.2	Simulations . . . . .	141
6.3	Use of modified generator model in a power plant . . . . .	149
<b>7</b>	<b>Conclusions and recommendations</b>	<b>151</b>
7.1	Conclusions . . . . .	151
7.2	Recommendations for future work . . . . .	152
	<b>Bibliography</b>	<b>155</b>
<b>A</b>	<b>Introduction to Bond Graph Modeling</b>	<b>a-1</b>
A.1	Basics . . . . .	a-1
A.2	Generalized variables . . . . .	a-1
A.3	Bond graph elements . . . . .	a-2
A.4	Causality and state equations . . . . .	a-3
A.5	Mechanical and electric system example . . . . .	a-5
<b>B</b>	<b>Contents of the AES library</b>	<b>a-7</b>
B.1	Power generation . . . . .	a-8
B.2	Power consumption . . . . .	a-9
B.3	Vessel . . . . .	a-10
B.4	Environment . . . . .	a-10
B.5	System models . . . . .	a-10

<b>C Generator</b>	<b>a-11</b>
C.1 Calculation of per unit scaling matrices . . . . .	a-11
C.2 Calculation of model parameters . . . . .	a-15
<b>D Induction motor</b>	<b>a-21</b>
D.1 Calculation of model parameters . . . . .	a-21
<b>E Full Scale Measurements</b>	<b>a-27</b>
E.1 Synchronization of three phase generator to bus . . . . .	a-27
E.1.1 Generator set 1 . . . . .	a-27
E.1.2 Generator set 2 . . . . .	a-30
E.2 Bow propeller . . . . .	a-32

# Nomenclature

## Abbreviations

AC	Alternating current
AES	All electric ship
AUV	Autonomous underwater vehicles
BDF	Backward Differentiation Formula
CSI	Current source inverters
DC	Direct current
DOF	Degrees of freedom
DOL	Direct on line
DP	Dynamic positioning
DTC	Direct torque control
EMS	Energy management system
EP	Electric propulsion
FFT	Fast Fourier transform
FOC	Field oriented control
FMEA	Failure mode and effects analysis
FMECA	Failure mode and effects criticality analysis
GUI	Graphical user interface
HV	High voltage
IMO	International Maritime Organization
KCL	Kirchoff's Current Law
LC	Inductance and capacitance (trap)
NED	North-East-Down (frame)
LNG	Liquefied natural gas
LV	Low voltage
MCFC	Molten carbonate fuel cell
MEA	Membrane-electrolyte assembly
mna	Modified nodal analysis
NO <sub>x</sub>	Nitrogen oxide
NS	Not specified

---

OLMECO	Open Library for Models of Mechatronics Components
OOM	Object oriented modeling
PCU	Power conditioning unit
PI	Proportional integral
PIT	Power invariant transformation
PM	Pierson-Moskowitz (spectrum)
PMS	Power management system
PWM	Pulse width modulation
RK4	Runga Kutta 4
RLC	Resistance, inductance and capacitance (network)
ROV	Remotely operated vehicles
SOFC	Solid oxide fuel cell
SOx	Sulphur oxide
SPJ	Switched power junction
TPB	Triple phase boundary
VSI	Voltage source inverters
VTB	Virtual Test Bed

#### Lowercase

$a, b, c$	[-]	Axes of 3 phase armature windings
$b_e(P)$	[g/kWh]	Specific fuel consumption
$c$	[m]	Chord length
$c_R$	[Nm/rad/s]	Coefficient of rotational losses.
$d, q$	[-]	Axes of fictitious commutator windings
$e$	[·]	Bond graph effort
$f$	[·]	Bond graph flow
$g$	[m/s <sup>2</sup> ]	Acceleration of gravity
$h_n$	[J/kg]	Lower heat value of fuel
$i_a, i_b, i_c$	[A]	Three phase armature winding currents
$i_{as}, i_{bs}, i_{cs}$	[A]	Three phase stator currents given in $abc$ -frame.
$i_{\alpha s}, i_{\beta s}$	[A]	Currents given in two-phase stationary reference frame
$i_{cd}$	[A]	$d$ -winding converter current
$i_{cq}$	[A]	$q$ -winding converter current
$i_d$	[A]	$d$ -winding current
$i_{d_{pu}}$	[-]	$d$ -winding current
$i_{DC}$	[A]	DC current
$i_{dr}, i_{qr}$	[A]	Rotor currents for transformed induction motor model

$i_{ds}, i_{qs}$	[A]	Stator currents for transformed induction motor model
$i_D$	[A]	<i>D</i> -amortisseur winding current
$i_{D_{pu}}$	[pu]	<i>D</i> -amortisseur winding current
$i_f$	[A]	<i>Field</i> -winding current
$i_{fc}$	[A]	Current, fuel cell
$i_{f_{pu}}$	[pu]	<i>Field</i> -winding current
$i_{md_{pu}}$	[pu]	<i>d</i> -winding magnetic current
$i_q$	[A]	<i>q</i> -winding current
$i_{q_{pu}}$	[pu]	<i>q</i> -winding current
$i_Q$	[A]	<i>Q</i> -amortisseur winding current
$i_{Q_{pu}}$	[pu]	<i>Q</i> -amortisseur winding current
$\mathbf{i}_{pu}$	[pu]	Current vector
$k$	[-]	Saturation factor
$k'$	[-]	Ratio between generator voltage and field current of an unloaded generator
$l$	[m]	Thruster duct length
$m$	[·]	Bond graph transformer modulus
$m_c$	[-]	Amplitude modulation index
$\dot{m}_f$	[kg/s]	Fuel flow rate
$m_{inj}$	[kg/inj]	Injected fuel
$n$	[rps]	Propeller speed
$n_p$	[-]	Number of pole pairs
$p$	[NS]	Momentum
$p_{H_2}$	[Pa]	Partial pressure of hydrogen
$p_{H_2O}$	[Pa]	Partial pressure of water
$p_{O_2}$	[Pa]	Partial pressure of oxygen
$q$	[NS]	Displacement
$q_{H_2}$	[mol/s]	Molar flow of hydrogen
$q_{H_2O}$	[mol/s]	Molar flow of water
$q_{O_2}$	[mol/s]	Molar flow of oxygen
$r$	[·]	Bond graph gyrator modulus
$r$	[rad]	Rotation about z-axis
$r$	[Ω]	Ohmic loss coefficient
$r_a, r_b, r_c$	[Ω]	Three phase armature winding resistances
$r_{H_2O}$	[-]	Hydrogen-oxygen flow ratio
$r_r, r_s$	[Ω]	Rotor and stator resistances for transformed induction motor model

---

$s$	[-]	Slip
$t$	[s]	Time
$t$	[m]	Maximum chord thickness
$u, v$	[m/s]	Body fixed velocities
$u_0$	[V]	Voltage, zero system.
$u_a, u_b, u_c$	[V]	Three phase armature winding voltages
$u_{as}, u_{bs}, u_{cs}$	[V]	Three phase stator voltages given in <i>abc</i> -frame
$u_{\alpha s}, u_{\beta s}$	[V]	Induction motor voltages given in two-phase stationary reference frame
$u_{cd}$	[V]	<i>d</i> -winding converter voltage
$u_{cq}$	[V]	<i>q</i> -winding converter voltage
$u_d$	[V]	<i>d</i> -winding voltage
$u_{dr}, u_{qr}$	[V]	Rotor voltages for transformed induction motor model
$u_{ds}, u_{qs}$	[V]	Stator voltages for transformed induction motor model
$u_D, u_Q$	[V]	<i>D</i> - and <i>Q</i> -amortisseur winding voltage
$u_f$	[V]	<i>Field</i> -winding voltage
$u_{fc}$	[V]	Fuel cell voltage
$u_{Nn}$	[V]	Voltage of bottom terminal <i>N</i> on the DC side of rectifier with respect to AC source neutral
$u_{Pn}$	[V]	Voltage of top terminal <i>P</i> on the DC side of rectifier with respect to AC source neutral
$u_q$	[V]	<i>q</i> -winding voltage
$u_{q_{pu}}$	[pu]	<i>q</i> -winding voltage
$u_{td}$	[V]	<i>d</i> -winding transformer voltage
$u_{tq}$	[V]	<i>q</i> -winding transformer voltage
$u_{t_{pu}}$	[pu]	Generator rated voltage
$\mathbf{u}_c$	[V]	Voltage vector given in converter reference frame
$\mathbf{u}_{pu}$	[pu]	Voltage vector
$x$	[m]	Position along a <i>x</i> -axis
$x_{d_{pu}}$	[pu]	<i>d</i> -winding self inductance
$x_{dh_{pu}}$	[pu]	Mutual inductance
$x_{dhs_{pu}}$	[pu]	Saturated mutual inductance
$x_{ds_{pu}}$	[pu]	<i>d</i> -winding saturated self inductance
$x_{D_{pu}}$	[pu]	<i>D</i> -winding self inductance
$x_{Ds_{pu}}$	[pu]	<i>D</i> -winding saturated self inductance
$x_{D\sigma_{pu}}$	[pu]	<i>D</i> -winding leak inductance
$x_{f_{pu}}$	[pu]	<i>Field</i> -winding self inductance

$x_{fs_{pu}}$	[pu]	<i>Field</i> -winding saturated self inductance
$x_{f\sigma_{pu}}$	[pu]	<i>Field</i> -winding leak inductance
$x_{q_{pu}}$	[pu]	<i>q</i> -winding self inductance
$x_{qh_{pu}}$	[pu]	Mutual inductance
$x_{qhs_{pu}}$	[pu]	Saturated mutual inductance
$x_{qs_{pu}}$	[pu]	<i>q</i> -winding saturated self inductance
$x_{Q_{pu}}$	[pu]	<i>Q</i> -winding self inductance
$x_{Qs_{pu}}$	[pu]	<i>Q</i> -winding saturated self inductance
$x_{Q\sigma_{pu}}$	[pu]	<i>Q</i> -winding leak inductance
$x_{s\sigma_{pu}}$	[pu]	<i>d</i> - and <i>q</i> -winding leak inductance
$y$	[m]	Position along <i>y</i> -axis

## Uppercase

0	[ · ]	Bond graph zero junction
1	[ · ]	Bond graph one junction
$A$	[m <sup>2</sup> ]	Thruster duct area
$A_{DC}$	[V]	Average value of output voltage
$A_e/A_0$	[-]	Expanded blade-area ratio
C	[ · ]	Bond graph capacitive element
$C_{D_{max}}$	[-]	Drag coefficient
$C_{DC}$	[F]	DC capacitor
$C_{L_{max}}$	[-]	Lift coefficient
$C_Q$	[-]	4-quadrant propeller torque coefficient
$C_T$	[-]	4-quadrant propeller thrust coefficient
$D$	[m]	Propeller diameter
$D$	[N]	Blade drag
$\mathbf{D}$	[Ns/m]	Damping matrix
$E$	[Wh]	Energy
$F$	[N]	Time varying force
$F$	[Cb/mol]	Faraday's constant
$GY$	[ · ]	Bond graph gyrator element
$H_s$	[m]	Significant wave height
$I$	[ · ]	Bond graph inertia element
$I_{dn}$	[A/pu]	<i>d</i> -winding scaling factor
$I_{Dn}$	[A/pu]	<i>D</i> -winding scaling factor
$I_{DC}$	[A]	Average DC-link current
$I_{fn}$	[A/pu]	<i>f</i> -winding scaling factor

---

$I_n$	[A/pu]	Current base value
$I_{qn}$	[A/pu]	$q$ -winding scaling factor
$I_{Qn}$	[A/pu]	$Q$ -winding scaling factor
$\mathbf{I}$	[A]	Current vector for two axis model
$\mathbf{I}^{SR}$	[A]	Current vector for physical model
$J_a$	[-]	Advance number
$\mathbf{J}$	[-]	Rotational matrix
$K_Q$	[-]	Torque coefficient
$K_{Q0}$	[-]	Nominal torque coefficient
$K_T$	[-]	Thrust coefficient
$K_{T0}$	[-]	Nominal thrust coefficient
$L$	[H]	Transformer inductance
$L$	[N]	Blade lift
$L_d$	[H]	$d$ -winding self inductance
$L_{d_{pu}}$	[pu]	$d$ -winding self inductance
$L_{df}$	[H]	$d$ - and $field$ -winding mutual inductance
$L_{df_{pu}}$	[pu]	$d$ - and $field$ -winding mutual inductance
$L_{dD}$	[H]	$d$ - and $D$ -winding mutual inductance
$L_{dD_{pu}}$	[pu]	$d$ - and $D$ -winding mutual inductance
$L_D$	[H]	$D$ -winding self inductance
$L_{D_{pu}}$	[pu]	$D$ -winding self inductance
$L_{DC}$	[H]	DC-link inductance
$L_f$	[H]	$Field$ -winding self inductance
$L_{f_{pu}}$	[pu]	$Field$ -winding self inductance
$L_{fD}$	[H]	$Field$ - and $D$ -winding mutual inductance
$L_{fD_{pu}}$	[pu]	$Field$ - and $D$ -winding mutual inductance
$L_m$	[H]	Stator and rotor mutual inductance
$L_q$	[H]	$q$ -winding self inductance
$L_{q_{pu}}$	[pu]	$q$ -winding self inductance
$L_{qQ}$	[H]	$q$ - and $Q$ -winding mutual inductance
$L_{qQ_{pu}}$	[pu]	$q$ - and $Q$ -winding mutual inductance
$L_Q$	[H]	$Q$ -winding self inductance
$L_{Q_{pu}}$	[pu]	$Q$ -winding self inductance
$L_r$	[H]	Rotor self inductance
$L_s$	[H]	Stator self inductance
$L_s$	[H]	AC side inductance
$\mathbf{L}$	[H]	Inductance matrix for two axis model

$L^{SR}$	[H]	Inductance matrix for physical model
$L_{pu}$	[pu]	Inductance matrix
$MTF$	[ · ]	Bond graph modulated tranformer
$M_f$	[-]	Final slope of saturation function
$M_i$	[-]	Initial slope of saturation function
$M$	[kg]	Mass and added mass matrix for vessel
$N_0$	[-]	Number of cells in series in the stack
$P$	[W]	Power
$P$	[W]	Active power
$P_{a,b,c}$	[W]	Three phase power
$P_{brake}$	[W]	Brake power of thruster
$P_{d,q,0}$	[W]	$d,q,0$ -phase power
$P_c$	[W]	Power, converter
$P_{fc}$	[W]	Power, fuel cell
PF	[-]	Power factor
$P_{inv}$	[W]	Power, inverter
$P_{rectifier}$	[W]	Active power rectifier
$P/D$	[-]	Pitch ratio
$Q$	[VA]	Reactive power
$Q_a$	[Nm]	Propeller torque
$Q_{rectifier}$	[VA]	Reactive power rectifier
$R$	[ · ]	Bond graph power dissipation element
$R_0$	[J/kg K]	Universal gas constant
$R$	[m]	Propeller radius
$R_d$	[Ω]	$d$ -winding resistance
$R_D$	[Ω]	$D$ -winding resistance
$R_{DC}$	[Ω]	DC resistance
$R_f$	[Ω]	<i>Field</i> -winding resistance
$R_n$	[-]	Reynolds number
$R_q$	[Ω]	$q$ -winding resistance
$R_Q$	[Ω]	$Q$ -winding resistance
$R_t$	[Ω]	Transformer resistance
$R$	[Ω]	Resistance matrix for two axis model
$R^{SR}$	[Ω]	Resistance matrix for physical model
$S_e$	[ · ]	Bond graph effort source
$S_f$	[ · ]	Bond graph flow source
$S_i$	[pu/A]	Current scaling matrix

$S_T$	[-]	Torque control parameter
$\mathbf{S}_u$	[pu/V]	Voltage scaling matrix
$\mathbf{S}_\psi$	[pu/Wb-t]	Flux linkage scaling matrix
$\mathbf{S}_\psi$	[-]	Flux linkage control parameter
$S_\theta$	[-]	Stator position control parameter
$T$	[Nm]	Torque
$T$	[K]	Temperature
$T_a$	[N]	Propeller thrust
$T_e$	[Nm]	Electromechanical torque
$T_f$	[s]	Transfer function response time
$T_R$	[Nm]	Rotational losses
$TF$	[·]	Bond graph transformer element
$U$	[V]	Time varying voltage
$U_0$	[V]	Reversible open circuit voltage
$U_{dn}$	[V/pu]	$d$ -winding scaling factor
$U_{Dn}$	[V/pu]	$D$ -winding scaling factor
$U_f$	[-]	Fuel utilization
$U_{fn}$	[V/pu]	$f$ -winding scaling factor
$U_n$	[V/pu]	Voltage base value
$U_{LL}$	[V]	Line to line rms voltage
$U_{qn}$	[V/pu]	$q$ -winding scaling factor
$U_{Qn}$	[V/pu]	$Q$ -winding scaling factor
$U_{rev}$	[V]	Reversible voltage potential
$\mathbf{U}$	[V]	Voltage vector
$\mathbf{U}^{SR}$	[V]	Voltage matrix
$V_a$	[m/s]	Inflow water velocity
$V_{an}$	[m <sup>3</sup> ]	Volume of anode
$V_c$	[m/s]	Current magnitude
$V_p$	[m/s]	Axial fluid velocity at propeller
$Z$	[-]	Number of blades

## Greek

$\alpha\beta$ -frame	[-]	Two phase stationary reference frame
$\beta$	[rad]	Propeller blade angle of attack at radius $0.7R$
$\Delta\beta$	[-]	Flux coefficient
$\gamma$	[-]	Added mass coefficient
$\delta$	[rad]	Thruster angle

$\delta_c$	[rad]	Commanded phase angle
$\eta$	[-]	Efficiency
$\eta$	[-]	Thermal efficiency
$\theta$	[rad]	Rotor position angle
$\theta_c$	[rad]	angular position of converter reference frame
$\theta_{ce}$	[rad]	Angular displacement of the converter reference frame from the synchronous reference frame
$\lambda_i$	[m]	Wave length
$\rho_w$	[kg/m <sup>3</sup> ]	Water density
$\zeta_a$	[m]	Wave amplitude
$\tau$	[N,Nm]	Propulsion forces and torques
$\tau_E$	[N,Nm]	Environmental forces and moments
$\tau_T$	[-]	Tighness of transition from initial slope to final slope with respect to $\psi_{md_{pu}}$
$\phi$	[rad]	Phase angle
$\phi_C$	[NS]	General function relating the two variables $q$ and $e$
$\phi_I$	[NS]	General function relating the two variables $p$ and $f$
$\phi_R$	[NS]	Static function relating $e$ and $f$ .
$\psi$	[rad]	Ship heading
$\psi_{\alpha_s}, \psi_{\beta_s}$	[Wb-t]	$\alpha$ -axis and $\beta$ -axis stator flux linkages
$\psi_c$	[rad]	Current direction
$\psi_d$	[Wb-t]	$d$ -winding flux linkage
$\psi_{d_{pu}}$	[pu]	$d$ -winding flux linkage
$\psi_{dr}, \psi_{qr}$	[Wb-t]	Rotor flux linkages for transformed induction motor model
$\psi_{ds}, \psi_{qs}$	[Wb-t]	Stator flux linkages for transformed induction motor model
$\psi_D$	[Wb-t]	$D$ -winding flux linkage
$\psi_{D_{pu}}$	[pu]	$D$ -winding flux linkage
$\psi_f$	[Wb-t]	<i>Field</i> -winding flux linkage
$\psi_{f_{pu}}$	[pu]	<i>Field</i> -winding flux linkage
$\psi_{m_{pu}}$	[pu]	Magnetic flux
$\psi_{md_{pu}}$	[pu]	$d$ -winding magnetic flux
$\psi_{mq}$	[pu]	$q$ -winding magnetic flux
$\psi_q$	[Wb-t]	$q$ -winding flux linkage
$\psi_{q_{pu}}$	[pu]	$q$ -winding flux linkage
$\psi_Q$	[Wb-t]	$Q$ -winding flux linkage

---

$\psi_{Q_{pu}}$	[pu]	$Q$ -winding flux linkage
$\psi_T$	[pu]	Point of transition
$\psi$	[Wb-t]	Flux linkage vector for two axis model
$\psi_{pu}$	[pu]	Flux linkage vector
$\psi^{SR}$	[Wb-t]	Flux linkage vector for physical model
$\Psi_{dn}$	[Wb-t/pu]	$d$ -winding scaling factor
$\Psi_{Dn}$	[Wb-t/pu]	$D$ -winding scaling factor
$\Psi_{fn}$	[Wb-t/pu]	$f$ -winding scaling factor
$\Psi_n$	[Wb-t/pu]	Flux linkage base value
$\Psi_{qn}$	[Wb-t/pu]	$q$ -winding scaling factor
$\Psi_{Qn}$	[Wb-t/pu]	$Q$ -winding scaling factor
$\omega$	[rad/s]	Bus frequency
$\omega_p$	[rad/s]	Peak wave frequency
$\omega_r$	[rad/s]	Rotating speed of shaft
$\omega_s$	[rad/s]	Synchronous speed

# Chapter 1

## Introduction

### 1.1 Background

Marine power systems on board supply vessels, drill ships, ice-breakers, cruise liners and other offshore installations include generation, distribution, control and consumption of power. The basic idea of an all electric ship is to replace the direct driven diesel engine propulsion system with a propulsion system driven by electric motors. The power production is split into several generator sets driven by e.g. diesel engines, gas engines, gas turbines, steam turbines or a combination of these. In the future, even fuel cells may be used.

The main advantages and disadvantages using electric propulsion (EP) can be summarized as [Ådnanes 2003] and [Hansen 2000]:

Advantages:

- Reduced fuel consumption for ships and other offshore installations with large variations in operational conditions. The operational profile for a typical dynamic positioned (DP) vessel is approximately equally divided between transit and DP operations. In transit, the vessel often has a high power demand, while in DP the average power demand is much less. By reducing the number of generator sets running at low power demand, the prime movers are operated at optimized fuel consumption, thus reducing the fuel consumption per produced kWh.
- The vessel is less vulnerable to single failure since use of more than one switchboard give the possibility to isolate the error and still have sufficient power available. That way, the vessel availability is improved.
- The need for maintenance decreases considerably when the engines are operated optimal. In addition, using several generator sets give the possibility to perform maintenance to one generator set and still be in normal operation.
- When using EP, it is possible to equip the vessel with azimuthing thrusters or podded propulsion which increase the maneuverability of the vessel.
- When using conventional diesel propulsion, the engine room has to be located near the propeller since the engine is fixed to the propeller. Electric propulsion motors are much smaller and may be placed right above or inside

the thrusters, while the generator sets may be placed in any suited place. More flexible and less space consuming engine room arrangement increases the payload of the vessel and may also be used to improve stability.

- EP will result in less propulsion noise and vibration. The rotating shaft lines will be shorter, the prime mover runs on constant speed and the use of pulling type propellers give less cavitation due to more uniform water flow.
- Environment consideration is another reason for the change towards electric propulsion. The “International Maritime Organization” (IMO) has issued world wide exhaust emission regulations for ships, setting limits on sulphur oxide (SO<sub>x</sub>) and nitrogen oxide (NO<sub>x</sub>) emissions. In addition are several areas designated as “SO<sub>x</sub> Emission Control areas” with a maximum of 1.5% by mass (m/m) (15000 ppm) sulphur content in marine fuel oil, whereas the m/m sulphur content in marine fuel oil is set to 4.5% worldwide [MARPOL 1973/1978]. NO<sub>x</sub> emissions cause or add to regional problems as acid rain and health problems in local areas such as harbours, and SO<sub>x</sub> emissions creates environment problems on certain routes, including English Channel, South China Sea and Strait of Malacca [IMO 1997]. Today, there exists even stricter requirements when it comes to SO<sub>x</sub> and NO<sub>x</sub> emissions which will be invoked in near future, and it is a political desire to further reduce SO<sub>x</sub> and NO<sub>x</sub> emissions. Conventional propulsion systems using diesel engines may not be able to meet these demands, so the emission requirements may force a development towards combined power plants for energy production to be used in the offshore industry.
- Improved ability for fast and accurate propulsion control based on combination of speed, torque and power including anti-spin thruster control and allocation, see [Smogeli 2006] and [Ruth 2008].

Disadvantages:

- EP systems require more components than conventional propulsion systems. This, together with use of new technology, give increased investment costs. The investment cost will probably decrease somewhat when number of installed units are increased.
- The power plants become much more complex and will consist of new components which require change in operation, manning and maintenance strategies.
- There have been some initial problems with electric power systems resulting from use of relatively new technology. With a more mature technology and increased knowledge about EP systems, these initial problems will probably be negligible.
- The extra components replacing the shaft between the prime mover and the propeller will result in additional losses in full-load operation in the order of approximately 10% [Ådnes 2003]. Thus, the fuel saving potential is not because of the electric components. Instead the fuel saving potential appears when looking at the efficiency of the prime movers in an EP system at constant speed and high load compared to a conventional system with

strongly varying load. The differences may be significant, especially on low thrust operations as dynamic positioning and maneuvering [Ådnanes 2003]

## 1.2 Diesel electric power system

### 1.2.1 System description

Diesel electric power systems are most frequently found in passenger vessels like cruise ships and ferries and in the oil industry on board supply vessels, drill ships and production vessels. EP is found on board ice going vessels like icebreakers, and also on board other offshore installations and u-boats.

Figure 1.1 shows a single line diagram for a typical diesel electric propulsion system. The prime movers are usually combustion engines fueled by diesel or heavy fuel oil, but also gas engines, gas turbines, steam turbines or hybrid engines are used. The prime movers are generally connected to synchronous generators supplying the switchboard with active and reactive power. The main switchboard is usually split in two, three or four sections to incorporate adequate redundancy according to existing rules and regulations for electric propulsion. The different switchboard sections are usually connected together during transit to give the best flexibility for optimal use of the power plant. During DP operations, the buses are usually split to be tolerant to failure of one switchboard.

The normal load currents and the short circuit currents will increase when installed power increases. There are limitations on handling thermal and mechanical stresses in bus bars and on switching capacity of switch gears, thus the power distribution system is often split into at least two parts with different voltage levels. The high voltage (HV) system with reduced current level, is used for large thrusters, pumps, compressors and so on, while the low voltage (LV) system is used for auxiliaries and hotel loads. Transformers are used between high and low voltage distribution systems.

The main power consumers on board ships and offshore installations are often motor drives for propulsion and thrusters and process equipment. In addition also pumps and winches may be large consumers. An asynchronous motor is the preferred electric motor in ship applications, but synchronous motors may also be used, especially for large propulsion drives. Direct on line (DOL) motors are normally asynchronous motors which often are installed together with soft starter devices due to high starting currents for asynchronous motors. The rotational speed of the DOL motor is directly given by the net frequency, thus for propulsion, pumps and winches it is preferable to use additional motor drives to control the speed of the motor. The frequently found motor drives are voltage source inverters (VSI), current source inverters (CSI) and cycloconverters. VSIs are used for both synchronous and asynchronous motors, while CSIs and cycloconverters are normally used for

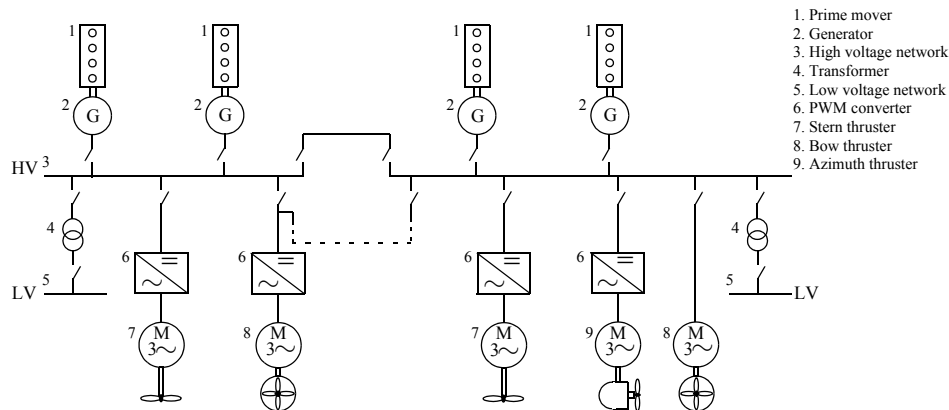


Figure 1.1: Single line diagram for a typical diesel electric propulsion system.

synchronous motors.

The overall control of the power system is performed by the power management system (PMS) which purpose is to ensure sufficient available power for the actual operating condition. The status of power generation and power consumption are monitored at all times. If the margin of available power is too small compared to the power consumption, an extra generator set will be started, synchronized and connected to the bus bar. The PMS may have extended functionality as monitoring and control of energy flow to maintain optimum fuel efficiency for the installed equipment. The extended PMS system is then called an energy management system (EMS). The main functions of the PMS and EMS are; power generation management with frequency and voltage control, active and reactive load sharing, load dependent start and stop of generator sets, load management with load monitoring and power load limitation functions, and distribution management configuring the power distribution system to fit requirements of the operational mode of the vessel [Ådnanes 2003].

## 1.2.2 Use of electric propulsion

Utilization of electric propulsion is continuously increasing.

The requirement for on board comfort when it comes to noise and vibration is very high for passenger vessels, cruise ships and ferries. The reliability and availability is critical for the safety of the passengers and the vessel, thus electric propulsion was early introduced for this kind of vessels. The desire for reducing emission, spill of oil and damages on coral reefs by anchoring the cruise ships in open locations, further increased the need for diesel electric power system with podded propulsion in the cruise market. For ferries with frequent crossing schedules and quay docking, the fuel saving potential may be huge because of improved maneuverability when using podded propulsion.

In the oil and gas industry, new resources are often found in more inaccessible areas than a few years ago. Deep-water drilling and floating production using dynamic positioning or thruster assisted position mooring is probably the only way of utilizing the new fields to get acceptable economy and profit. Often, the drilling units, production vessels and tankers have a common power plant for thruster loads, production, drilling, utilities and hotel loads, thus the operation may be very energy effective and the availability for the vessels are good. Today, many shuttle tankers used for transport of oil from offshore facilities to processing or storage terminals onshore, are using DP systems with electric tunnel or azimuth thrusters together with conventional shaft lines. Podded propulsion may be more cost efficient, and this may influence the design of new diesel electric shuttle tankers.

Electric propulsion was early introduced for vessels such as diving support vessels, crane ships and pipe layers, with DP as the main operating mode. If the vessel has a highly varying operational profile, both fuel consumption and environmental emissions may be reduced up to 30 to 40% [Ådnanes 2003].

### 1.2.3 New concepts

Utilization of gas as fuel is in principle not new, since liquefied natural gas (LNG) carriers have been using boil of gas as fuel since the first ship was put in operation in 1964 [Einang and Haavik 2000]. But what is relatively new, is the use of natural gas as bunker fuel. Today only a few ships are fueling on natural gas, most of them stores the gas as compressed natural gas and the engines are dual fuel engines. Recently, a few vessels equipped with gas engines, using LNG as bunker fuel have been built [Einang and Haavik 2000].

Today, several research groups are contributing in finding and evaluating alternatives to the synchronous generator. The car industry has come far when it comes to using fuel cells for producing power in cars, but also in the ship industry they are looking into the possibility of using fuel cells.

The fuel cell is an electrochemical device combining hydrogen and oxygen to produce electricity, heat and water. The fuel cell is almost pollution free and operates at much higher efficiencies than internal combustions engines. There are no moving parts in the fuel cell, thus it is a quiet and reliable power source. The fuel cell generates DC voltage, thus it could either be connected to DC distribution system with DC loads, or there could be a DC-AC conversion of the power before distributing the power on the existing busbus.

The FellowSHIP (Fuel Cells for Low Emissions Ships) is a research group working on installing molten carbonate fuel cell (MCFC) on ships, and if everything goes as planned, they will demonstrate the use of a 330 kW MCFC on board an offshore supply vessel in 2008 [Tronstad 2007].

Marine power plants often consist of either gas turbines, steam turbines, diesel engines or dual fuel engines with an electricity generation efficiency of about 40 %.

This efficiency may be increased by combining either gas and steam turbines, i.e. combined cycle power plant, which has a total efficiency of about 50 – 55 %, or by combining gas turbines and high temperature solid oxide fuel cell, SOFC, where efficiencies up to 65 % have been reported [Tanaka et al. 2000], [Palsson et al. 2000]. New emission requirements may also force a change towards combined power plant systems consisting of any combination of diesel engines, gas engines, gas turbines and fuel cells.

A combined torque/power controller and a combined speed, torque and power controller were designed by [Smogeli 2006]. He also proposed an anti-spin thruster controller enabling use of torque and power control in extreme operating conditions, where large and rapid variations in propeller loading may occur. Fast and accurate anti-spin thruster control would not be possible without the use of electric motor drives. An anti-spin thrust allocation procedure is proposed by [Ruth 2008] where online performance estimation is used to distribute control forces to the most efficient thrusters.

## 1.3 Design of an all electric ship

### 1.3.1 System design

The task of designing a new ship may be very comprehensive, and both creative and analytical skills have to be used when deciding ship dimension, engine arrangement, auxiliary equipment and so on. A more thorough discussion about system design may be found in [Ådnanes 2003].

Generally, the design phase may be divided into the following stages; market study, purpose, requirements, concept design, detailed design, specifications, system engineering and detailed engineering.

The first three stages are accomplished at the beginning of the design phase and serves as the basis for the design process.

The next two stages deal with conceptual and detailed designing. The vessel capability is specified and analyzed and necessary thrust for the intended operational profile is estimated. Next, type of propulsion and number, size and location of propulsion units are determined, in addition to optimal configuration and splitting of power generation and distribution system. The outcome of the conceptual and detailed designing is a set of technical specifications for the vessel.

The last two stages of the design phase are system engineering and detailed engineering. To achieve safe and reliable operation, standard network analysis or electric power system studies has to be performed, including load flow calculation, short circuit calculation, ground fault calculation, relay coordination study, harmonic analysis and voltage drop calculation at inrush of transformers and starting of motors. In some cases, also an extended analysis may be required, consisting of transient analysis of network behavior after disturbance and reliability

or failure mode analysis.

The load flow and short circuit calculations are done to find if thermal and mechanical stresses on the on board equipment is within predefined limits. Ground fault calculations determines the amount of ground fault current that is flowing if one phase is short-circuited to ground. The magnitude is dependent on how the system is grounded.

A relay coordination study is done to determine the level of fault currents accepted and the time before disconnecting of the in and out feeder in relation with the switchboards. If the current in the relay is higher than a predefined limit, a time counter is started, and the relay is disconnected after a certain time. A higher limit normally has a shorter time period before disconnection.

The level of harmonic distortion is often significant in electric propulsion systems. Harmonic distortion is caused by nonlinear loads that are connected to the network. The distortion may lead to accelerated aging of insulation material, overloading of electronic equipment and malfunction due to electromagnetic interference or erroneous measurement signals. The harmonic distortion may be found by doing either time domain simulation or frequency domain simulation. The calculation time of large systems is usually much shorter when simulating in the frequency domain, but the accuracy is normally lower. The lower accuracy is a consequence of the fact that the harmonic content of load current has to be estimated. The harmonic content of load current is dependent on the network configuration and may only be determined by equivalent figures from similar system or by time domain simulations.

Voltage drop calculations are done to make sure that the voltage drop does not exceed predefined limits for acceptable transient voltage variations set by class requirements. Voltage drop may be caused by start-up transient current that is several times larger than nominal rated current for e.g. heavy motor consumers. The voltage drop may be calculated using analytical methods, but the most accurate result is often found using numerical simulation.

Sometimes it is necessary to do additional analyses of transient behavior during faults and after fault correction. They include voltage and frequency stability and re-acceleration of motor loads. This kind of analyses require accurate modeling of the network and regulators for voltage and frequency to be reliable.

Reliability analysis or Failure mode and effects (criticality) analysis (FMEA/FMECA) may be done for ships where the availability of the power system is essential and when there are redundancy requirements. The analysis is done to find the consequences of faults in components or system, their criticality and the probability for such events.

### 1.3.2 Numerical simulation tools

Numerical simulation tools may be used in several of the phases mentioned above. Today, determination of harmonic distortion, calculation of voltage drops and analyzing transient behavior of power systems, are done using numerical simulation tools. In addition, also necessary thrust based on the planned operational profile may be determined using simulations. In the past, it has been common to equip vessels with more machinery power than absolutely required. By using system simulation tools where different kinds of extreme loads may be applied, the overall system performance may be simulated and evaluated. Sufficient installed power together with optimized combination, number and size of prime movers may then be chosen based on more realistic grounds.

Today, there are several simulation tools on the market for simulating dynamic behavior of large systems. Some of the tools are developed especially for describing electric components, e.g. Spice, PSCAD and Kream. Spice and PSCAD may also be used to simulate other energy domains but only by use of equivalent mode description. Other alternatives are multi-domain simulation tools, e.g. Saber, MATLAB/Simulink and 20-sim which models each component in their native energy domain. Spice, PSCAD, Kream, Saber, MATLAB/Simulink and 20-sim are discussed in the following.

#### **Spice**

Spice, Simulation Program with Integrated Circuit Emphasis [Nagel 2004], is a general-purpose circuit simulation program for nonlinear dc, nonlinear transient and linear ac analysis developed at Electronics Research Laboratory of the University of California, Berkeley. Spice3 was released in 1993 and has built-in models for diodes, bipolar transistors, MOSFETs and JFETs. The electronic switch models are detailed. It is also easy to add device models. Spice uses nodal analysis or modified nodal analysis where the voltage between nodes in an electric circuit are determined.

#### **PSCAD**

PSCAD® [Manitoba HVDC 2006] is used for studying transient behavior of electric systems in the time domain. The simulation program was first conceptualized in 1988. It comes with a comprehensive library of models managing all aspects of AC and DC power systems and control. The built-in graphical Component Workshop may be used to create own models and libraries. It also supports models written in Fortran/C/C++ and the MATLAB interface makes it possible to use MATLAB m-files. PSCAD uses modified nodal analysis, and the “Interpolated Network Solution and Chatter Removal Technology” gives high speed simulations with switching accuracy of infinitely small time steps. PSCAD has graphical interfaces for circuit assembly, data entry, run, control and analysis and its modular structure enables the user to schematically construct a circuit system

model.

### **Krean**

Krean was developed at the Department of Electric Power Engineering of the Norwegian University of Science and Technology [Nilssen and Mo 1990], [Krean 1995]. The intention for writing Krean was to develop a special purpose program, and not a general purpose programs like Spice and PSCAD. Typical drawbacks for general purpose programs, at that time, was the use of very complex models of circuit components or constant integration step length. In addition, the characteristic discontinuities that occurs in switched power electronic circuits was often not treated in a good way.

The program is especially well suited for principal study of converters and drives, and typical projects where Krean has been used are: interaction between converters, motor drives and power supply systems (harmonics, control strategy etc.), converter design, controlled resonant converter simulations and motor drives with long cable between converter and motor.

The basic models are ideal, but more advanced models are also available and it is possible to include nonlinear models. The numerical methods used and breakpoint detection methods are accurate. Main output results are time domain plots and harmonic information.

### **Saber**

The Saber® [Synopsys 2006] software may be used to simulate physical effects in different engineering domains, e.g. hydraulic, electronic, mechanical and thermal, as well as signal flow algorithms and software control. Saber models these engineering disciplines in their native domains [Chwirka 2000]. It solves nonlinear differential equations as long as the models are expressed in terms of linear or nonlinear algebraic or integro-differential equations<sup>1</sup> [Getreu 1990]. SaberSketch contains a schematic editor and symbol editor used for the modeling, while MAST is Saber's modeling language and allow users to create models based on a set of characteristic equations directly. Saber is also able to read C and Fortran programs together with several versions of spice netlists [Chwirka 2000]. SaberScope is used for post processing and viewing of the simulation results. Modified nodal analysis is used in Saber.

### **MATLAB/Simulink**

Matlab/Simulink® [MathWorks 2007] is a software package for modeling, simulating and analyzing both linear and nonlinear dynamic systems The systems may be modeled in continuous time, sampled time, or a hybrid of the two. Systems

---

1. An Integro-differential equations involves both integrals and derivatives of an unknown function.

can also be multi rate, i.e., have different parts that are sampled or updated at different rates.

Simulink provides a graphical user interface (GUI) for building models as block diagrams, using click-and-drag mouse operations, such that it is not necessary to formulate differential equations and difference equations in a language or program. Simulink includes a comprehensive block library of sinks, sources, linear and nonlinear components, and connectors. The library may be enlarged with personal blocks.

The model may be simulated using different choices of integration methods and scopes and other display blocks shows simulation results while the simulation is running. By putting the result in the Matlab workspace, the result may be analyzed using desired analyzing tools in Matlab.

## 20-sim

20-sim, developed by Controllab Products B.V [20-sim 2006], is a software package for modeling and simulation of the behavior of dynamic systems, such as electrical, mechanical, thermal and hydraulic systems or any combination of these. The modeling may be performed using equations, block diagrams, bond graphs, iconic diagrams or combinations of these representations. 20-sim comes with a large number of predefined components which also may be extended by personal building blocks. The model is debugged and compiled before simulated, thus increasing the simulation speed. The simulation results may be analyzed using various tools such as FFT-analysis, optimization, tolerance analysis and many more. It is possible to generate ANSI c-code of models or sub models such that the model may be used in other simulation packages.

### 1.3.3 Is bond graph modeling a way to go?

Krean, Spice, PSCAD and Saber are using either nodal analysis or modified nodal analysis for simulating electrical networks. The nodal analysis is often used when analyzing large network applications, but is a little limited in its treatment of voltage sources and branch dependent functions [Mahseredjian et al. 2001]. Modified nodal analysis on the other hand is more flexible.

The nodal analysis is used to find a set of equations describing the electric circuit. At each principle node, where 3 or more wires meet, the Kirchoff's Current Law (KCL) stating that the algebraic sum of the currents flowing out of a node equals zero, is applied. The dependency between different components in the circuit is not an issue. The result after applying KCL, is a set of  $n - 1$  equations for  $n - 1$  unknown nodal voltages, where  $n$  is number of principle nodes. The system may be solved using e.g. Gaussian elimination or some other method.

The MATLAB/Simulink is based on state variables instead of nodal analysis. It is

well suitable for solving problems with time-varying nonlinearities, especially power electronic devices with frequent switching [Fuentes et al. 2007]. According to [Arrillaga and Watson 2002], the state variable method may be unsuited for large electrical systems, since it is necessary to recognize dependability between system variables, which reduces the effectiveness of the method.

Bond graph is a powerful method when it comes to modeling electric circuits since it combines both nodal analysis and the advantage of state variables. In addition, the dependency between different components is recognized using causal analysis, see Appendix A.4. If there should be problems in a circuit model, e.g. algebraic constraints that can not be satisfied because the constraints are not dependent on system variables, this will not be detected if using (modified) nodal analysis, ((m)na). Instead the simulators using (m)na will find inconsistent differential and algebraic equations. Then, when doing simulation an error message like “Singular Jacobian Matrix” may appear, and the work for finding what caused the error may be tremendous [Morel et al. 1999]. On the other hand, if modeling using bond graphs, the causality analysis will reveal if there are any problems within the circuit, and the problems may be solved before the simulation is started. The causality analysis may even be used at the single component and sub component level to set requirements to their interface ports. Dependent on the simulation tool where the bond graph model is implemented, a set of state equations will be automatically generated and used for the simulation. 20-sim is such a simulation tool.

Tools that are developed especially for describing electric components are often used for analyzing e.g. a semiconductor device and the device transients are constraining the integration time step to a small value. But it may be impractical and undesirable to use component models constraining the time step to e.g.  $10^{-9}$  when doing simulation of large systems, the simulation cost is all too high. Instead, the bond graph methodology may aid the development of advanced average models of power converters, where e.g. the device transients are taken care of by virtual switching delays, see [Allard et al. 1997], [Allard et al. 1999], [LIN-SHI et al. 2001] and the references therein. By using advanced average models in system simulation, the simulation cost is reduced.

## 1.4 Motivations

It is important to carefully analyze complex machinery systems with regard to performance, safety and reliability. Only optimizing steady state performance may be insufficient and analyzing dynamic behavior of the machinery system in extreme operation should also be considered. In order to design and analyze even more complex systems, it is desirable to have a set of component models that may easily be combined to model the system of interest and that supports system analysis.

The main motivation for writing this thesis is to develop a model library that gives the opportunity to simulate both existing and new machinery systems without

having to remodel the entire system each time. The library should exist of models with different levels of accuracy and it should support the process of modeling and reuse, and also emphasize openness to brace the modeler during the development and refinement phase.

Bond graph modeling allows for such a modular approach, it may help understanding the system and it is a good tool for combining different energy domains.

Based on the motivation, the following set of specifications can be made

- The component library should be flexible, thus supporting modulability and reuse of models.
- The library should increase the understanding of system simulation across modeling disciplines.
- The library should be used to develop system models and simulations should be carried out to evaluate the characteristics of the models.

## 1.5 Previous work

Since the first generation of electric propulsion was taken into use in 1920s [Ådnanes 2003], numerous of publications have treated the subject. Description of the system and implementation on actual ships are discussed in [Hopkins 1991], [Hill et al. 1992] and [Schriek and de Nijs 1991]. Discussions concerning electric equipment as an integrated part of marine systems are found in [Ådnanes et al. 1997] and [Doerry and Davis 1994]. An overview of applications and solutions together with an introduction to components used in vessels with electric propulsion are given in [Ådnanes 2003].

Modeling and control of landbased power systems are treated in e.g. [Ordys et al. 1994], [Kwatny et al. 1996] and [Mariani and Murthy 1997]. There is however a big difference between a stiff landbased network and weak networks (also called buses) such as marine power systems, so the references may not be fully utilized. In landbased networks, voltage and frequency remain constant when connecting and disconnecting large power consumers, while the voltage and frequency are not constant for so called weak networks. Some of the power consumers are big compared to generator capacity and the network will experience voltage dips when starting e.g. a big asynchronous motor.

There exists several research groups working with the concept of All Electric Ship and marine power systems. Royal Institute of Technology, Department of Electrical Engineering in Sweden and University of Wisconsin - Madison, Department of Electrical and Computer Engineering, University of Texas at Austin, The Center for Electromechanics and University of South Carolina, Department of Electrical Engineering, all in the US, are just a few examples.

The main focus of the Department of Electrical Engineering at Royal Institute of Technology is analysis, simulation, and control of electric and integrated energy systems, mostly for landbased systems, but they have also been doing some research treating marine power systems [Jonasson and Soder 2001].

At University of Wisconsin - Madison, a group of researchers are working on power electronics and electric machinery related to next generation ship propulsion [Tenca et al. 2005] and they are an active participant in development of new naval electrical shipboard applications.

At the University of Texas, they are developing a model of the electric ship power system [Ouroua et al. 2005]. They started up making the model using predefined blocks from the Matlab/Simulink toolbox SimPowerSystems, but they are now concentrating on re-building the power system without using predefined “black box” components, in order to have more flexibility, improved model performance and to have more control with possible simulation errors [Ouroua 2007].

The last research group mentioned here is working at the Electrical Engineering department at University of South Carolina. They have developed a Virtual Test Bed (VTB) which is a software for prototyping of large-scale, multi-technical dynamic systems [Dougal 2003]. One of the most important features of the VTB is the possibility of including component models developed in other modeling environments, e.g. VTB, MATLAB, Simulink, ACSL, Paragon, Modelica, Spice and Fortran. In that way, the VTB enables closer collaboration among experts in different fields [Broughton et al. 2004].

## 1.6 Main contribution

One of the main purposes for writing this thesis, was to develop a flexible model library that should assist the modeler in the process of modeling a complete power system and at the same time increase the knowledge and understanding of the system. Increased knowledge and understanding of the system may necessarily not be the case when using predefined blocks in a commercial toolbox, e.g. SimPowerSystems in MATLAB/Simulink, where parts of the code are hidden and inaccessible for the modeler. Using hand written code hidden inside S-functions in MATLAB/Simulink will also be a problem in that respect. When including component models in the VTB, the models have to be either interactive signal or interactive natural VTB models or compiled signal or compiled natural VTB models. If choosing the interactive method which applies to MATLAB and Simulink models, MATLAB/Simulink needs to run concurrently with the VTB software. The other method of including component models demand compilation of the models in their native development language and then import the compiled code in the VTB using the VTB wrapper entity. Using the VTB, the component models becomes more like “black boxes” which may not be desirable when increased understanding of the system is a request.

The main contributions of the thesis are:

- Development of a flexible component library used for modeling and simulation of existing and new marine power plants.
- Component models are verified using test measurements performed by manufacturer and full-scale measurements from a supply-vessel.
- Simulation of selected cases of combined power plants during extreme dynamic loads are conducted.
- Development of a hybrid causality generator model for increased flexibility when simulating combined power plants.

## 1.7 Bond graph modeling

Bond graphs were invented by professor H. M. Paytner, who was a professor at MIT & UT Austin, in 1959, but it took almost 20 years before bond graphs became widely known and practiced. Several people have contributed to increased knowledge and use of bond graphs as a modeling tool. Dean C. Karnopp and Ronald C. Rosenberg [Karnopp and Rosenberg 1968], [Karnopp and Rosenberg 1970], [Rosenberg and Karnopp 1972] and [Karnopp et al. 2000], Donald L. Margolis [Margolis 1985], Jan J. Dixhoorn [Dixhoorn 1972] and Jean U. Thoma [Thoma 1976] are only some examples.

Bond graph is a graphical tool for comprehending the energetic structure of a physical system by representing the system by symbols and lines, thus identifying the power flow paths. The bond graph modeling language consists of power bonds with power direction, power variables, signal bonds, nine standard elements, causality analysis and much more. A short introduction to the bond graph modeling is given in Appendix A.

## 1.8 Organization of the thesis

The organization of the thesis is as follows:

**Chapter 2** starts with a discussion about modeling environments before a template for model documentation is given.

**Chapter 3** presents mathematical description and bond graph models of the most important components in a marine power system. It has been emphasized that the model library should support the process of modeling. Library openness is also important.

Major component models are verified using test measurements of components given by manufacturers and with full-scale measurements from a supply vessel operated

in the North Sea in **chapter 4**.

**Chapter 5** presents a system evaluation of combined power plants. Extreme dynamic loads are large thruster loads, damaged generator sets and system error on generator connected to grid.

A modified version of a synchronous generator is presented in **Chapter 6**. The modified generator increases the flexibility when it comes to modeling combined power plants.

Concluding remarks are given in **chapter 7**.

**Appendix A** gives a short introduction to Bond Graph modeling, while the content of the All Electric Ship library is presented in **Appendix B**. A description of per unit (pu) system is given in **Appendix C** together with calculation of generator parameters. Calculation of model parameters for the asynchronous motor are given in **Appendix D**. **Appendix E** tabulates full scale measurements obtained from the supply ship Viking Energy operated by Eidesvik.



## Chapter 2

### **AES library**

It has been desirable to develop a flexible component model library used for building system models of combined power plants. The system models are then used for prediction of the dynamic performance of combined power plants with required accuracy. The modeling phase should aid the understanding of the overall system and increase the knowledge of the system components. Each component model should be sufficient open and readable, thus supporting the modeler during the system development and refinement phase.

It is important that the documentation of each component model provide adequate information to the modeler. The documentation should include information about how the model is intended to be used, if there are any restrictions to what phenomena the model may capture, if any assumptions are made in the modeling phase and if and how the model has been validated.

The model library is discussed in the following chapter.

#### 2.1 Modeling environments

The objective of developing a complete flexible component model library may possibly be easier to achieve if developing a platform independent model library. The process of modeling and simulating using such a library may be divided into 5 levels. The first and second level are the component model developing level, where the different component models are developed and stored using appropriate modeling tools. The next level is the platform independent library level, where generic component models are stored. The fourth level is the system modeling environment where system models are developed using the independent library and the last level is the system simulation level. Figure 2.1 shows the five level configuration. Different component models could then be modeled in the modeling language the modeler is used to together with the modelers own libraries, e.g. using 20-sim [20-sim 2006] to develop component models of the machinery system, using PSCAD [PSCAD 2005] for modeling electrical components and using Matlab/Simulink [MathWorks 2007] for modeling the controller, see 1) and 2) in Figure 2.1. After finishing the development phase of the models and after the models are

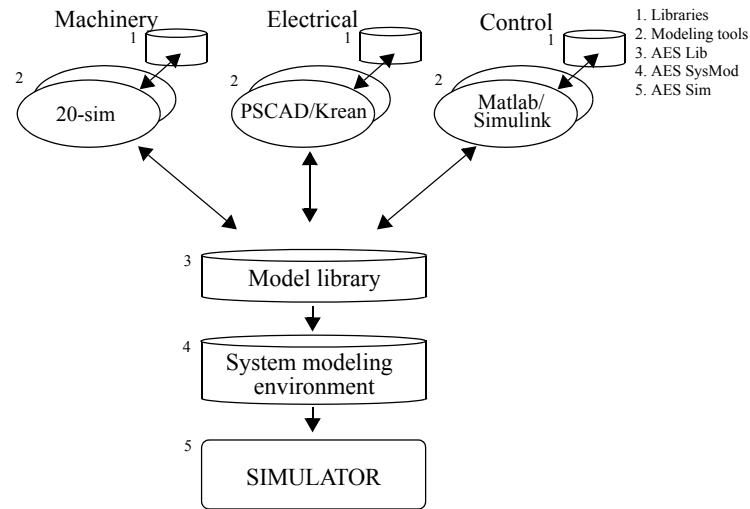


Figure 2.1: Common modeling environment.

thoroughly tested, generic platform independent component models could be generated, see 3) in Figure 2.1. The platform independent component library could then be used for developing combined power plants for simulation purposes using any suitable simulation tool, see 4) in Figure 2.1. At last, the combined power plant is simulated, see 5) in Figure 2.1. If having an independent library, generic component models first developed using PSCAD could also be used in e.g. 20-sim.

Development of a truly platform independent library is quite ambitious. In principle, it is not too difficult to develop a translator which will generate platform independent code, but the translator must be capable of handling all possibilities when it comes to the written code. Many of today translators support most of the modeling methods available in a given modeling language, but if they do not support all, a lot of effort may be necessary to implement the methods not supported. Another problem that may arise, is that the new platform independent code is difficult to read and understand. Getting a good overview of the system model and its model components may also be hard. If this is the case, the platform independent library will not help increasing the understanding of the system that is to be modeled.

The objective of developing a flexible component library supporting the modeler during the modeling phase with well arranged component models ready for reuse or further development, has been assumed more important than developing a complete platform independent library. The bond graph methodology has therefore been chosen as the main modeling language for this “All Electric Ship” (AES) library. It combines different energy domains by using nine basic building blocks in the mechanical, thermal and electrical energy domain and modeling based on a modular approach is supported.

## 2.2 Model structure

According to [Borutzky 1999], object oriented modeling (OOM) has become more and more popular due to modeling of more complex systems. OOM supports safe reuse of models because of encapsulation and inheritance, such that the model knowledge is encapsulated inside the model and submodels instantiated from a generic model will inherit the properties of the generic model. Another feature with OOM is model hierarchy, meaning that a model may be composed of submodels which in turn contains sub models as well.

The bond graph methodology was invented in 1959 and at that time, the notions of knowledge encapsulation and inheritance were not used. Still, bond graph modeling may be thought of as object oriented modeling. Bond graph modeling supports inheritance, and knowledge encapsulation is also employed. Using a storage element as an example, the inheritance is explained as follows. The storage element includes the properties of passivity, of storing a physical quantity given by the state variable and of being energy conservative. This properties are inherited by any instantiation of the model class called store. Concerning knowledge encapsulation, submodels representing either components or elementary physical processes, may only be accessed through their interfaces. For a storage element, the state variable is encapsulated and surrounding objects will not have information about the state of this storage element.

The bond graph methodology also supports hierarchical models. Normally, the bond graph building blocks consist of two layers, The first layer is the physical layer describing the dynamic behavior, e.g. friction. The next layer is the mathematical layer which consists of the mathematical relations describing the dynamic behavior, e.g.  $F = rv$ , where  $F$  is the friction force,  $r$  is the friction coefficient and  $v$  is the velocity of the mass. After realizing the two layer configuration of the bond graph method, it has been natural to partially use the structure of the OLMECO library [Breunese et al. 1998], see Figure 2.2, when developing the AES library. The structure of the OLMECO library adds another layer on top of the physical concept layer and the mathematical layer. The top layer is the technical component layer, which specifies real world objects, e.g. actuators, amplifiers, motors and so on. The three layers will be described next.

### 2.2.1 Technical component layer

Actual systems are modeled in the technical component layer. It may consist of subcomponents recognizable in a real system and it may be used to model larger components. An important property of a component within this layer is the description the components interface, which enables the possibility to connect to other components. The interface states what energy and information that may be exchanged with other components in this layer.



layer become port variables in the mathematical layer. A signal port is associated with one mathematical port variable while a power port is associated with two conjugate port variables, namely effort and flow.

The link between different layers is well defined, so a system build up from small, reusable sets of equations specified in the mathematical layer may be assembled to give a complete set of equations describing the behavior of the system modeled, using automated tools like 20-sim [20-sim 2006] or Modelica [Modelica 2007].

## 2.3 Model documentation

*“Flawed or outdated documentation is more costly than no documentation”* [Posten 1984].

The importance of having the documentation of a component model up to date and accurate, is obvious. For the modeler building the component, it may be enough just knowing how the component model is working and what assumptions that were made when the model was developed, but when storing the component model in a library for reuse by others, it is not enough. The model documentation should include what assumptions and constrains applying to the model, if and how the model is verified and free form comments could for instance be used to describe usage of the model, possible extensions and so on. The model documentation for the AES library includes the following sections: model name, description, parameters, input, output, limitation, validation, comments and reference, see Table 2.1.

<b>Model name:</b> The name of the model together with a short description (one sentence).	<b>Output</b> Model output interface with description of output ports and variable units.
<b>Description</b> This section include the mathematical equations used in the model together with the bond graph representation of the system component.	<b>Limitation</b> Description of what assumptions and constrains which applies to the model.
<b>Parameters</b> The model parameters are given in this section.	<b>Validation</b> Description of if and how the model has been validated.
<b>Input</b> Model input interface with description of input ports and variable units.	<b>Comments</b> This section may be used for comments that may not be entered in the above sections.
	<b>Reference</b> References used for developing the model are included in this section.

Table 2.1: Model documentation for the AES component model library.

An example of the documentation for a synchronous generator is shown next.

### Synchronous generator

- Synchronous generator with 3 phase voltage as output

### Description:

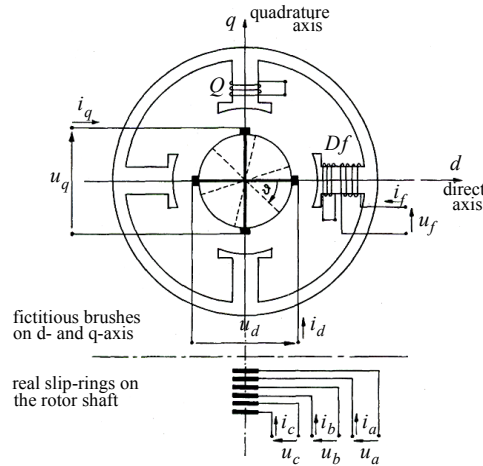


Figure 1: The model machine of the two reaction theory [Sahm 1979].

The synchronous generator is modeled according to “the two-axis theory” [Doherty and Nickle 1926], [Park 1929] and [Sahm 1979]. The usual configuration of the theory is shown in Figure 1. The three phase armature winding is shown as a rotor winding and the axis of the three windings  $a$ ,  $b$  and  $c$  are indicated by thin lines. The real armature windings are replaced by two sets of fictitious commutator windings  $d$  and  $q$ , orthogonal to each other along the  $d$ - and  $q$ -axis indicated by thick lines on the reference axis. Power invariant transformation (PIT) between  $abc$ -frame and  $dq$ - frame rotating at synchronous speed is accomplished using

$$A = \frac{\sqrt{2}}{\sqrt{3}} \begin{bmatrix} \cos(\theta) & \cos\left(\theta - \frac{2}{3}\pi\right) & \cos\left(\theta - \frac{4}{3}\pi\right) \\ -\sin(\theta) & -\sin\left(\theta - \frac{2}{3}\pi\right) & -\sin\left(\theta - \frac{4}{3}\pi\right) \\ \frac{1}{\sqrt{2}} & \frac{1}{\sqrt{2}} & \frac{1}{\sqrt{2}} \end{bmatrix} \text{ and}$$

$B = A^{-1}$ , such that

$$\mathbf{u}_{d,q,0} = A \cdot \mathbf{u}_{a,b,c}, \quad \mathbf{u}_{a,b,c} = A^{-1} \cdot \mathbf{u}_{d,q,0}$$

$$\mathbf{i}_{a,b,c} = B \cdot \mathbf{i}_{d,q,0}, \quad \mathbf{i}_{d,q,0} = B^{-1} \cdot \mathbf{i}_{a,b,c}$$

The voltage balance for the synchronous generator is given as

$$u_d = \dot{\psi}_d - \omega_r n_p \psi_q + R_d i_d,$$

$$u_q = \dot{\psi}_q + \omega_r n_p \psi_d + R_q i_q,$$

$$\dot{\psi}_f = u_f - R_f i_f,$$

$$\dot{\psi}_D = -R_D i_D \text{ and}$$

$$\dot{\psi}_Q = -R_Q i_Q,$$

and the flux linkages are given, when solving with regard to  $[\psi_d \ \psi_q \ i_f \ i_D \ i_Q]^T$ , as

$$\begin{bmatrix} \psi_d \\ \psi_q \\ i_f \\ i_D \\ i_Q \end{bmatrix} = \begin{bmatrix} Z_{11} & 0 & Z_{13} & Z_{14} & 0 \\ 0 & Z_{22} & 0 & 0 & Z_{25} \\ Z_{31} & 0 & Z_{33} & Z_{34} & 0 \\ Z_{41} & 0 & Z_{43} & Z_{44} & 0 \\ 0 & Z_{52} & 0 & 0 & Z_{55} \end{bmatrix} \begin{bmatrix} i_d \\ i_q \\ \psi_f \\ \psi_D \\ \psi_Q \end{bmatrix},$$

where

$$Z_{11} = -\frac{(-L_{fD}^2 L_d - L_D L_{df}^2 - L_f L_{dD}^2 + 2L_{dD} L_{fD} L_{df} + L_f L_D L_d)}{L_f L_D - L_{fD}^2},$$

$$Z_{13} = Z_{31} = \frac{(L_D L_{df} - L_{dD} L_{fD})}{L_f L_D - L_{fD}^2},$$

$$Z_{14} = Z_{41} = \frac{(L_f L_{dD} - L_{df} L_{fD})}{L_f L_D - L_{fD}^2},$$

$$Z_{22} = -\frac{(L_q L_Q - L_{qQ}^2)}{L_Q},$$

$$Z_{25} = Z_{52} = \frac{L_{qQ}}{L_Q},$$

$$Z_{33} = \frac{L_D}{L_f L_D - L_{fD}^2},$$

$$Z_{34} = Z_{43} = -\frac{L_{fD}}{L_f L_D - L_{fD}^2},$$

$$Z_{44} = \frac{L_f}{L_f L_D - L_{fD}^2} \text{ and}$$

$$Z_{55} = \frac{1}{L_Q}.$$

The electromechanical torque is given by

$$T_e = \psi_d i_q - \psi_q i_d.$$

Knowledge about the derivative of  $\psi_d$  and  $\psi_q$  are required when calculating  $u_d$  and  $u_q$ . The derivative are found by numerical differentiation. Since numerical differentiation may cause problems when simulating dynamic systems, a first order filter is used to filtrate the variable before differentiation. The transfer function for the filter and the derivative is given as

$$h(s) = \frac{y(s)}{u(s)} = \frac{s}{1 + Ts} \Leftrightarrow y(s) = \frac{1}{T} \left( u(s) - \frac{1}{s} y(s) \right),$$

where  $T$  is a small time constant.

The bond graph representation of the synchronous generator and the PIT may be seen in Figure 2 and Figure 3.

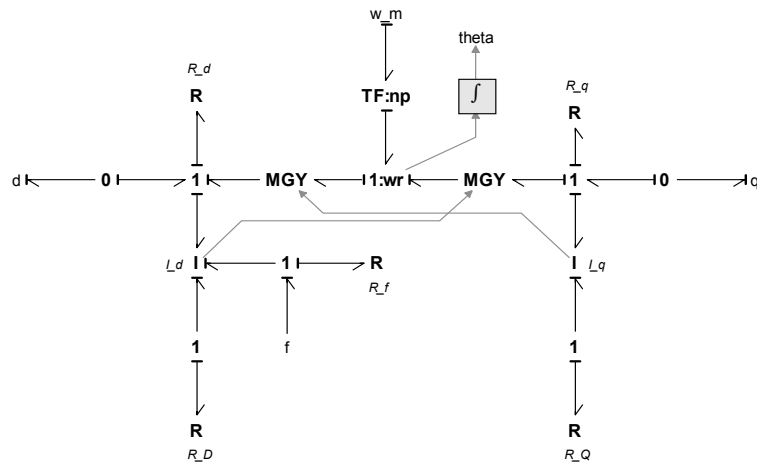


Figure 2:  $dq$ -model of generator with current as output.

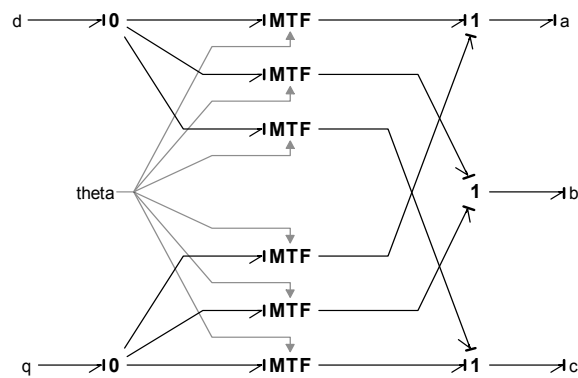


Figure 3: Power invariant transformation between  $dq$ -frame and  $abc$ -frame.

#### Parameters:

The parameters of the generator are given in real values.  $L_d$ ,  $L_f$  and  $L_q$  are constant self inductances while  $L_{df}$ ,  $L_{dD}$ ,  $L_{fD}$  and  $L_{qQ}$  are constant mutual inductances.  $R_d$ ,  $R_q$ ,  $R_f$ ,  $R_D$  and  $R_Q$  are constant resistance coefficients in the  $d$ -,  $q$ -,  $field$ -,  $D$ - and  $Q$ -winding.  $n_p$  is number of pole pairs.  $T$  is a small time constant.

#### Inputs:

$i = [i_a \ i_b \ i_c]^T$  - 3 phase current [A].  
 $u_f$  - field voltage [V].  
 $\omega$  - rotational speed of shaft [rad/s].

#### Outputs:

$u = [u_a \ u_b \ u_c]^T$  - 3 phase network voltage [V].  
 $i_f$  - field current [A].  
 $T_e$  - generator torque [Nm].

**Limitations:**

- Saturation, hysteresis and mechanical losses are neglected.
- The armature windings  $a$ ,  $b$ ,  $c$  are sinusoidal distributed around the circumference of the rotor resulting in uniformly distributed fictitious commutator windings.

**Validation:**

The generator model has been validated using test measurements received from manufacturer [ABB 2002] and using full scale measurements obtained from the supply vessel Viking Energy [Eidesvik 2008].

**Comments:**

For system simulation, this generator model is used in parallel with other generator models which have 3 phase current as output.

**Reference:**

- [ABB 2002] ABB Automation AC Machines, *Generators Technical Specification*, Generator type: AMG 630 S 10, 2002
- [Doherty and Nickle, 1926] R. E. Doherty and C. A. Nickle, "Synchronous machines I and II, an extension of Blondel's two reaction theory", AIEE trans, Vol. 45, pp 912-947, 1926.
- [Eidesvik 2008] Eidesvik Offshore ASA, Bømlo, Norway, web: <http://www.eidesvik.no/Fleet/PDF%20-%20Full%20Spec/Viking%20Energy.pdf>.
- [Park 1929] R. H. Park, "Two reaction theory of synchronous machines, generalized method of analysis - part I", AIEE Trans, Vol. 48, pp. 716-727, 1929.
- [Sahm 1979] Sahm, D., *A Two-Axis, Bond Graph Model of the Dynamics of Synchronous Electrical Machines*, Journal of The Franklin Institute, vol 308, No. 3, pp. 205-218, 1979.



## Chapter 3

### System modeling

The main motivation for writing this thesis is to develop a model library supporting the process of modeling, reuse and further development of component models. The library will include bond graph representation of system components at different levels of complexity.

In the following, mathematical description together with bond graph representation of the different system components are given.

#### 3.1 Diesel and gas engine

##### 3.1.1 Mathematical description

The model of the 4 stroke gas and diesel engine is a basic model, consisting of one rotating mass, represented by an I-element, and mechanical losses represented by a R-element. The rotating mass includes moment of inertia of shaft, piston rod, connecting rod and other rotating masses.

Fuel and air are injected into the cylinders of the diesel engine and a combustion process starts, releasing heat and producing higher pressure inside the cylinders. The increased pressure acts on the piston producing torque on the crank shaft. Assuming sufficient air in the combustion process, the relationship between injected fuel and produced torque may easily be found. The power produced by the engine is given as, see e.g. [Heywood 1988],

$$P_{engine} = \dot{m}_f \cdot h_n \cdot \eta = T \cdot \omega_r, \quad (3.1)$$

where  $\dot{m}_f$  is fuel flow rate,  $h_n$  is lower heat value of fuel,  $\eta$  is thermal efficiency,  $T$  is torque and  $\omega_r$  is rotating speed of shaft.

Rewriting (3.1) gives

$$T = \frac{\dot{m}_f \cdot h_n \cdot \eta}{\omega_r}. \quad (3.2)$$

The fuel flow rate for a 4 stroke engine may be given as

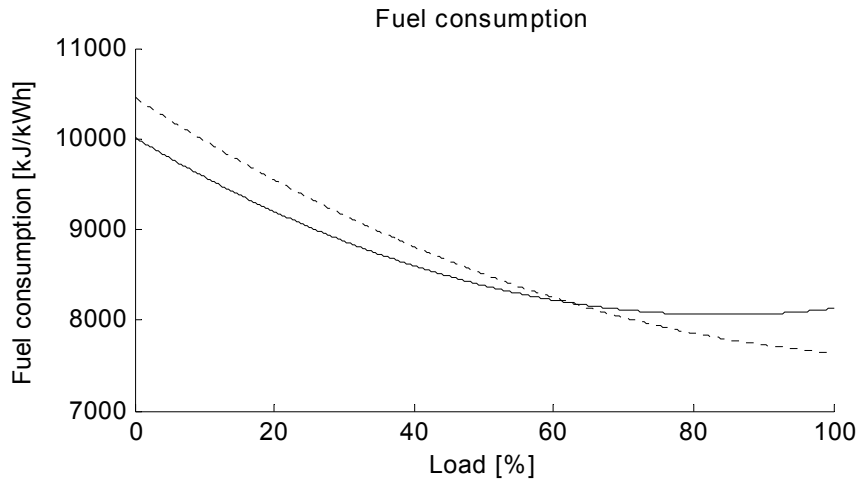


Figure 3.1: Specific fuel consumption for a typical dual fuel engine. The dotted line shows fuel consumption for the engine when gas is used as fuel, while solid line shows fuel consumption when diesel is used.

$$\dot{m}_f = m_{inj} \cdot \frac{\omega_r}{4\pi}, \quad (3.3)$$

where injected fuel,  $m_{inj}$ , is controlled by the engine governor, a PI-controller using shaft speed as control parameter.

The thermal efficiency is related to specific fuel consumption,  $b_e(P)$  tabulated for different powers, and lower heat value in the following way:

$$\eta = \frac{1}{b_e(P) \cdot h_n}. \quad (3.4)$$

$P$  is engine power. Inserting (3.3) and (3.4) into (3.2) gives the relationship between torque and injected fuel,

$$T = \frac{m_{inj}}{4\pi \cdot b_e(P)}. \quad (3.5)$$

Figure 3.1 shows specific fuel consumption for a typical dual fuel engine.

The rotational losses of motor and shaft are given as

$$T_R = c_R \omega_r, \quad (3.6)$$

where  $c_R$  is rotational losses coefficient.

The speed of the engine is controlled by a governor by changing the commanded fuel input, and the control mode may be either speed droop or isochronous. Speed droop is a simple and effective method for ensuring load sharing between generator sets that are connected to the same bus. When using speed droop, the steady state frequency will drop dependent on active load, and this may cause

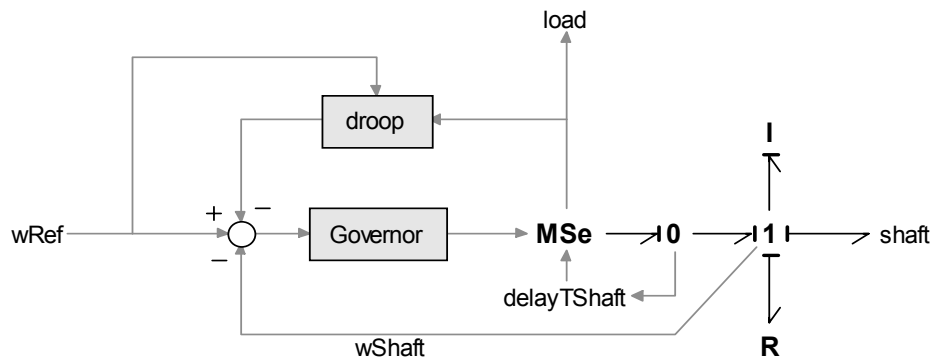


Figure 3.2: Bond graph representation of the engine.

problems if another generator is synchronizing to the bus, or two buses are synchronized.

Isochronous control of the engine ensures generator frequency at setpoint. A signal between governors handles load sharing between generator sets.

Both methods for controlling the governor are often included in electric propulsion plants [Ådnanes 2003]

### 3.1.2 Bond graph representation of the engine model

Figure 3.2 shows the model of the 4 stroke diesel engine. The modulated effort source, MSe, sets torque using (3.5), while the I-and R- element sets shaft speed and mechanical losses, respectively. Since the thermal efficiency is dependent on engine power, a first order transfer function with a small time constant is used on the engine torque to avoid algebraic loops.

## 3.2 Synchronous generator

The synchronous generator is modeled according to “the two-axis theory” [Sahm 1979] where the mathematical description of the dynamics of the generator is simplified. The usual configuration of the theory is shown in Figure 3.3. The three phase armature winding is shown as a rotor winding and the axis of the three windings  $a$ ,  $b$  and  $c$  are indicated by thin lines. The real armature windings are replaced by two sets of fictitious commutator windings  $d$  and  $q$ , orthogonal to each other along the  $d$ - and  $q$ -axis indicated by thick lines on the reference axis.

This model, its validity and simplifying assumptions, have been the subject of numerous publications, see for instance [Doherty and Nickle 1926], [Park 1929] and [Kron 1935].

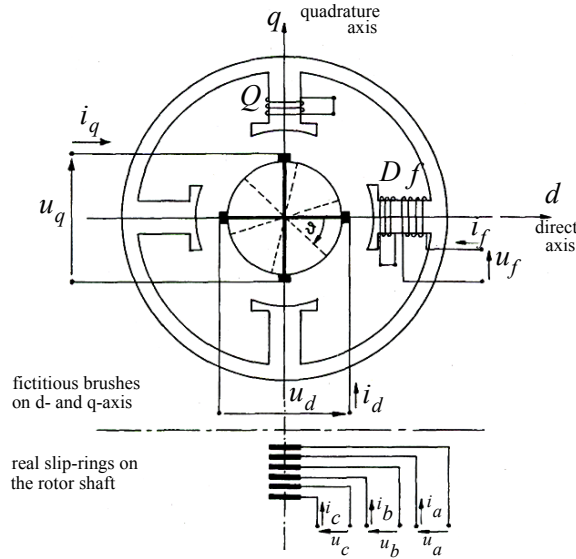


Figure 3.3: The model machine of the two reaction theory [Sahm 1979].

### 3.2.1 Mathematical description

The physical model gives the following voltage balance for the synchronous generator

$$\mathbf{U}^{SR} = \mathbf{R}^{SR} \mathbf{I}^{SR} + \frac{d}{dt} \psi^{SR}, \quad (3.7)$$

where  $\mathbf{R}^{SR}$  is the resistance matrix and  $\mathbf{I}^{SR}$  is the current matrix. The flux linkage  $\psi^{SR}$  may be written as

$$\psi^{SR} = \mathbf{L}^{SR} \mathbf{I}^{SR}. \quad (3.8)$$

The physical inductance matrix  $\mathbf{L}^{SR}$  is a non-diagonal matrix where the self inductances and mutual inductances are not constant, but dependent on the position of the rotor. The voltage balance may be simplified by referring the voltage balance to the synchronously rotating  $dq$  - frame instead of the  $abc$  - frame by a power invariant transformation, see Chapter 3.4.

The voltage balance for the transformed model may be given as

$$\dot{\psi}_d = u_d - R_d i_d + \psi_q n_p \omega_r, \quad (3.9)$$

$$\dot{\psi}_q = u_q - R_q i_q - \psi_d n_p \omega_r, \quad (3.10)$$

$$\dot{\psi}_f = u_f - R_f i_f, \quad (3.11)$$

$$\dot{\psi}_D = -R_D i_D \text{ and} \quad (3.12)$$

$$\dot{\psi}_Q = -R_Q i_Q. \quad (3.13)$$

where the flux linkages are

$$\psi_d = -L_d i_d + L_{df} i_f + L_{dD} i_D, \quad (3.14)$$

$$\psi_q = -L_q i_q + L_{qQ} i_Q, \quad (3.15)$$

$$\psi_f = -L_{df} i_d + L_f i_f + L_{fD} i_D, \quad (3.16)$$

$$\psi_D = -L_{dD} i_d + L_{fD} i_f + L_D i_D \text{ and} \quad (3.17)$$

$$\psi_Q = -L_{qQ} i_q + L_Q i_Q. \quad (3.18)$$

$L_d$ ,  $L_f$  and  $L_q$  are constant self inductances while  $L_{df}$ ,  $L_{dD}$ ,  $L_{fD}$  and  $L_{qQ}$  are constant mutual inductances.

$$\boldsymbol{\psi} = [\psi_d \ \psi_q \ \psi_f \ \psi_D \ \psi_Q]^T,$$

$$\mathbf{I} = [i_d \ i_q \ i_f \ i_D \ i_Q]^T \text{ and}$$

$$\mathbf{R} = [R_d \ R_q \ R_f \ R_D \ R_Q]^T,$$

are flux linkage, currents and resistances given in the  $d$ -,  $q$ -,  $field$ -,  $D$ - and  $Q$ -winding.  $n_p$  is number of generator pole pairs.

The electromechanical torque is given by

$$T_e = \psi_d i_q - \psi_q i_d. \quad (3.19)$$

(3.9) to (3.18) may be given in state-space form as

$$\dot{\boldsymbol{\psi}} = -\omega_r \mathbf{D} \boldsymbol{\psi} - \mathbf{R} \mathbf{i} + \mathbf{E} \mathbf{u}_s + \mathbf{b} u_f \text{ and} \quad (3.20)$$

$$\boldsymbol{\psi} = \mathbf{L} \mathbf{i} \Leftrightarrow \mathbf{i} = \mathbf{L}^{-1} \boldsymbol{\psi}, \quad (3.21)$$

where

$$\mathbf{D} = \begin{bmatrix} 0 & -n_p & 0 & 0 & 0 \\ n_p & 0 & 0 & 0 & 0 \\ 0 & 0 & 0 & 0 & 0 \\ 0 & 0 & 0 & 0 & 0 \\ 0 & 0 & 0 & 0 & 0 \end{bmatrix}, \quad \mathbf{L} = \begin{bmatrix} -L_d & 0 & L_{fD} & L_{dD} & 0 \\ 0 & -L_q & 0 & 0 & L_{qQ} \\ -L_{fD} & 0 & L_f & L_{fD} & 0 \\ -L_{dD} & 0 & L_{fD} & L_D & 0 \\ 0 & -L_{qQ} & 0 & 0 & L_Q \end{bmatrix},$$

$$\mathbf{E} = \begin{bmatrix} 1 & 0 & 0 & 0 & 0 \\ 0 & 1 & 0 & 0 & 0 \end{bmatrix}^T, \quad \mathbf{b} = [0 \ 0 \ 1 \ 0 \ 0]^T.$$

and the electromechanical torque may be given as

$$T_e = [\psi_d \ \psi_q] \begin{bmatrix} 0 & 1 \\ -1 & 0 \end{bmatrix} \begin{bmatrix} i_d \\ i_q \end{bmatrix} = \boldsymbol{\psi}_s^T \mathbf{H} \mathbf{i}_s = \boldsymbol{\psi}_s^T \mathbf{G}^T \mathbf{H} \mathbf{G} \mathbf{i}, \quad (3.22)$$

when defining  $\mathbf{i}_s = [i_d \ i_q]^T$  and  $\boldsymbol{\psi}_s = [\psi_d \ \psi_q]^T$  as stator currents and flux linkages and

$$\mathbf{H} = \begin{bmatrix} 0 & 1 \\ -1 & 0 \end{bmatrix}, \quad \mathbf{G} = \begin{bmatrix} 1 & 0 & 0 & 0 & 0 \\ 0 & 1 & 0 & 0 & 0 \end{bmatrix}. \quad (3.23)$$

Active and reactive power are written as

$$P = u_d i_d + u_q i_q \quad \text{and} \quad Q = u_q i_d - u_d i_q, \quad (3.24)$$

which in vector notation become

$$P = \boldsymbol{\psi}_s^T \mathbf{i}_s = \boldsymbol{\psi}_s^T \mathbf{G} \mathbf{i} \quad \text{and} \quad Q = -\boldsymbol{\psi}_s^T \mathbf{H} \mathbf{i}_s^T = -\boldsymbol{\psi}_s^T \mathbf{H} \mathbf{G} \mathbf{i}. \quad (3.25)$$

Marine power systems are weak networks meaning that voltage and frequency are not constant. In this thesis, one generator is chosen as primary generator, setting voltage and frequency on the grid, while other generators connected to the bus are secondary generators having phase current as output.

The generator model described by (3.20) and (3.21) has current as output. Another generator model with voltage as output is therefor developed. Rewriting (3.9)-(3.10) give

$$\mathbf{u}_s = \boldsymbol{\psi}_s + \omega_r \mathbf{D}_s \boldsymbol{\psi}_s + \mathbf{R}_s \mathbf{i}_s, \quad (3.26)$$

where  $\mathbf{u}_s = [u_d \ u_q]^T$  and

$$\mathbf{R}_s = \begin{bmatrix} R_d & 0 \\ 0 & R_q \end{bmatrix}, \quad \mathbf{D}_s = \begin{bmatrix} 0 & -n_p \\ n_p & 0 \end{bmatrix}. \quad (3.27)$$

Solving (3.14)-(3.18) with regard to  $[\psi_d \ \psi_q \ i_f \ i_D \ i_Q]^T$  give,

$$\begin{bmatrix} \psi_d \\ \psi_q \\ i_f \\ i_D \\ i_Q \end{bmatrix} = \begin{bmatrix} Z_{11} & 0 & Z_{13} & Z_{14} & 0 \\ 0 & Z_{22} & 0 & 0 & Z_{25} \\ Z_{31} & 0 & Z_{33} & Z_{34} & 0 \\ Z_{41} & 0 & Z_{43} & Z_{44} & 0 \\ 0 & Z_{52} & 0 & 0 & Z_{55} \end{bmatrix} \begin{bmatrix} i_d \\ i_q \\ \psi_f \\ \psi_D \\ \psi_Q \end{bmatrix}, \quad (3.28)$$

where

$$Z_{11} = \frac{-L_{fD}^2 L_d - L_D L_{df}^2 - L_f L_{dD}^2 + 2L_{dD} L_{fD} L_{df} + L_f L_D L_d}{L_f L_D - L_{fD}^2},$$

$$Z_{13} = Z_{31} = \frac{L_D L_{df} - L_{dD} L_{fD}}{L_f L_D - L_{fD}^2},$$

$$\begin{aligned}
Z_{14} = Z_{41} &= \frac{L_f L_{dD} - L_{df} L_{fD}}{L_f L_D - L_{fD}^2}, \\
Z_{22} &= \frac{L_q L_Q - L_{qQ}^2}{L_Q}, \\
Z_{25} = Z_{52} &= \frac{L_{qQ}}{L_Q}, \\
Z_{33} &= \frac{L_D}{L_f L_D - L_{fD}^2}, \\
Z_{34} = Z_{43} &= -\frac{L_{fD}}{L_f L_D - L_{fD}^2}, \\
Z_{44} &= \frac{L_f}{L_f L_D - L_{fD}^2} \text{ and} \\
Z_{55} &= \frac{1}{L_Q}.
\end{aligned}$$

(3.11) to (3.13) are still used for calculating  $\dot{\psi}_f$ ,  $\dot{\psi}_D$  and  $\dot{\psi}_Q$ . (3.26) requires knowledge about the derivative of  $\psi_s$  which may either be found by solving a set of differential-algebraic equations using an implicit solver, or the derivative of  $\psi_s$  may be found by numerical differentiation of  $\psi_d$  and  $\psi_q$  in (3.28). Numerical differentiation may cause problems when simulating dynamic systems, therefore a first order filter is used to filtrate the signal before differentiation. The transfer function for the derivative is  $h(s) = s$ , and the transfer function for the filter and the derivative may then be given as

$$h(s) = \frac{y(s)}{u(s)} = \frac{s}{1 + Ts} \Leftrightarrow y(s) = \frac{1}{T} \left( u(s) - \frac{1}{s} y(s) \right), \quad (3.29)$$

where  $T$  is a small time constant.

### 3.2.2 Bond graph representation of the generator model

Figure 3.4 shows the generator modeled in the  $dq$ -frame using (3.20) and (3.21). The  $I$ -fields represent (3.21). The  $R$ -elements represent  $d$ - and  $q$ -axis resistances, field resistance and amortisseur winding resistance on  $d$ - and  $q$ -axis. The term  $\mathbf{K}(\omega_s)\psi$  is represented by the modulated gyrators and the transformer represents the number of pole pairs.

The model of the generator with  $dq$ -voltage as output, which represents (3.26) and (3.28), is presented in Figure 3.5.

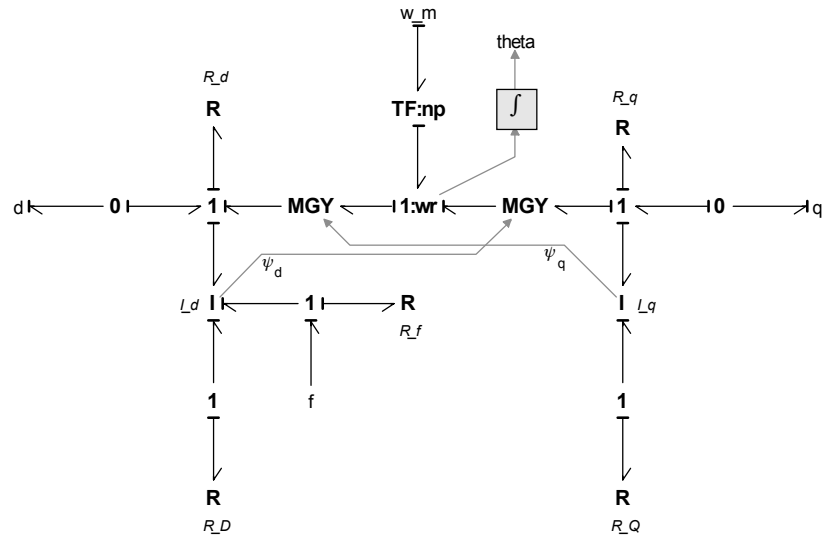


Figure 3.4:  $dq$ -model of generator with current as output.

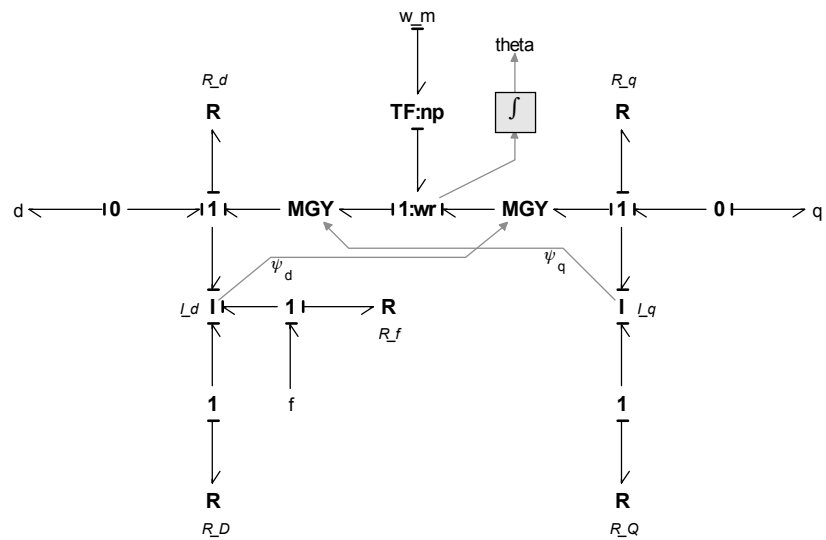


Figure 3.5:  $dq$ -model of generator with voltage as output.

### 3.3 Magnetic saturation in the generator model

Magnetic saturation was neglected in the synchronous generator model presented in previous chapter. However, magnetic saturation may influence the performance of the generator due to large impact on torque angle and field current of the generator [Hirayama 1995].

When including magnetic saturation in the  $dq$ -model, it is favorable to transform the model into a per unit, pu, system. The pu system used here deviates a little from the pu system normally used because of the power invariant transformation. The pu system is described in Appendix C.

Next, two methods for including magnetic saturation are presented.

#### 3.3.1 Method I

Kaiichiro Hirayama [Hirayama 1995] has the following proposal for including saturation in the generator model. Assuming flux saturation only occurring in  $L_{dh_{pu}}$  and  $L_{qh_{pu}}$ , see Appendix C.1, the flux saturation may be expressed by using  $x_{dhs_{pu}}$  and  $x_{qhs_{pu}}$ , such that

$$\begin{bmatrix} \psi_{d_{pu}} \\ \psi_{q_{pu}} \\ \psi_{f_{pu}} \\ \psi_{D_{pu}} \\ \psi_{Q_{pu}} \end{bmatrix} = \begin{bmatrix} -x_{ds_{pu}} & 0 & x_{dhs_{pu}} & x_{dhs_{pu}} & 0 \\ 0 & -x_{qs_{pu}} & 0 & 0 & x_{qhs_{pu}} \\ -x_{dhs_{pu}} & 0 & x_{fs_{pu}} & x_{dhs_{pu}} & 0 \\ -x_{dhs_{pu}} & 0 & x_{dhs_{pu}} & x_{Ds_{pu}} & 0 \\ 0 & x_{qhs_{pu}} & 0 & 0 & x_{Qs_{pu}} \end{bmatrix} \begin{bmatrix} i_{d_{pu}} \\ i_{q_{pu}} \\ i_{f_{pu}} \\ i_{D_{pu}} \\ i_{Q_{pu}} \end{bmatrix}. \quad (3.30)$$

$\psi_{d_{pu}}$  may be found from (3.30) as

$$\begin{aligned} \psi_{d_{pu}} &= -x_{ds_{pu}} i_{d_{pu}} + x_{dhs_{pu}} i_{f_{pu}} + x_{dhs_{pu}} i_{D_{pu}} \\ &= -x_{s\sigma_{pu}} i_{d_{pu}} + x_{dhs_{pu}} (-i_{d_{pu}} + i_{f_{pu}} + i_{D_{pu}}) \end{aligned} \quad (3.31)$$

By choosing

$$\psi_{md_{pu}} = x_{dhs_{pu}} (-i_{d_{pu}} + i_{f_{pu}} + i_{D_{pu}}), \quad (3.32)$$

then  $\psi_{f_{pu}}$  and  $\psi_{D_{pu}}$  may be expressed as

$$\psi_{f_{pu}} = x_{fs_{pu}} i_{f_{pu}} - x_{dhs_{pu}} i_{d_{pu}} + x_{dhs_{pu}} i_{D_{pu}} = x_{f\sigma_{pu}} i_{f_{pu}} + \psi_{md_{pu}} \quad \text{and} \quad (3.33)$$

$$\psi_{D_{pu}} = x_{Ds_{pu}} i_{D_{pu}} - x_{dhs_{pu}} i_{d_{pu}} + x_{dhs_{pu}} i_{f_{pu}} = x_{D\sigma_{pu}} i_{D_{pu}} + \psi_{md_{pu}}, \quad (3.34)$$

thus,  $i_{f_{pu}}$  and  $i_{D_{pu}}$  are given as

$$i_{f_{pu}} = \frac{\psi_{f_{pu}} - \psi_{md_{pu}}}{x_{f\sigma_{pu}}} \quad \text{and} \quad (3.35)$$

$$i_{D_{pu}} = \frac{\psi_{D_{pu}} - \psi_{md_{pu}}}{x_{D\sigma_{pu}}}. \quad (3.36)$$

Inserting (3.35) and (3.36) in (3.32) gives

$$\psi_{md_{pu}} = \frac{\psi_{f_{pu}}/x_{f\sigma_{pu}} + \psi_{D_{pu}}/x_{D\sigma_{pu}} - i_{d_{pu}}}{1/x_{f\sigma_{pu}} + 1/x_{D\sigma_{pu}} + 1/x_{dhs_{pu}}}. \quad (3.37)$$

For the  $q$ -axis, the following relations are given

$$\begin{aligned} \psi_{q_{pu}} &= -x_{qs_{pu}} i_{q_{pu}} + x_{qhs_{pu}} i_{Q_{pu}} \\ &= -x_{s\sigma_{pu}} i_{q_{pu}} + x_{qhs_{pu}} (-i_{q_{pu}} + i_{Q_{pu}}) = -x_{s\sigma_{pu}} i_{q_{pu}} + \psi_{mq_{pu}} \end{aligned} \quad (3.38)$$

$$\psi_{Q_{pu}} = -x_{qhs_{pu}} i_{q_{pu}} + x_{Qs_{pu}} i_{Q_{pu}} = x_{Q\sigma_{pu}} i_{Q_{pu}} + \psi_{mq_{pu}}, \quad (3.39)$$

such that

$$i_{Q_{pu}} = \frac{\psi_{Q_{pu}} - \psi_{mq_{pu}}}{x_{Q\sigma_{pu}}} \quad \text{and} \quad (3.40)$$

$$\psi_{mq_{pu}} = \frac{\psi_{Q_{pu}}/x_{Q\sigma_{pu}} - i_{q_{pu}}}{1/x_{Q\sigma_{pu}} + 1/x_{qhs_{pu}}}. \quad (3.41)$$

Although reactances are constant, Hirayama treats  $x_{dhs_{pu}}$  and  $x_{qhs_{pu}}$  as variables that changes with  $\psi_{md_{pu}}$  and  $\psi_{mq_{pu}}$ . The magnetic fluxes and reactances that do not change instantaneously during transient periods, are given as

$$a = \psi_{f_{pu}}/x_{f\sigma_{pu}} + \psi_{D_{pu}}/x_{D\sigma_{pu}}, \quad (3.42)$$

$$b = 1/x_{f\sigma_{pu}} + 1/x_{D\sigma_{pu}}, \quad (3.43)$$

$$c = \psi_{Q_{pu}}/x_{Q\sigma_{pu}} \quad \text{and} \quad (3.44)$$

$$d = 1/x_{Q\sigma_{pu}}. \quad (3.45)$$

The saturated reactances  $x_{dhs_{pu}}$  and  $x_{qhs_{pu}}$  vary with the degree of flux saturation, expressed using the saturation factor  $k$ , as

$$x_{dhs_{pu}} = kx_{dh_{pu}} \quad \text{and} \quad (3.46)$$

$$x_{qhs_{pu}} = kx_{qh_{pu}}. \quad (3.47)$$

Recall that  $x_{dh_{pu}}$  and  $x_{qh_{pu}}$  are unsaturated reactances.  $\psi_{md_{pu}}$  and  $\psi_{mq_{pu}}$  may now be given as

$$\psi_{md_{pu}} = \frac{kx_{dh_{pu}}(a - i_{d_{pu}})}{1 + bkx_{dh_{pu}}} \quad \text{and} \quad (3.48)$$

$$\psi_{mq_{pu}} = \frac{kx_{qh_{pu}}(c - i_{q_{pu}})}{1 + dkx_{qh_{pu}}}, \quad (3.49)$$

where  $k$  is a function of  $\psi_{m_{pu}}$ ,

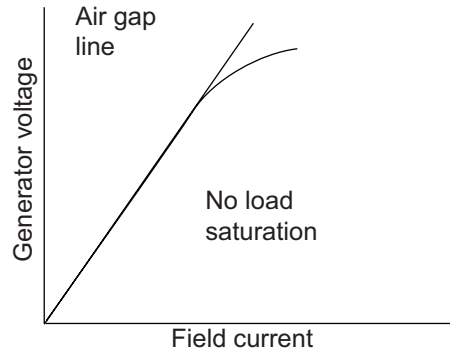


Figure 3.6: Saturation curve of unloaded generator [Hirayama 1995].

$$k = f(\psi_{m_{pu}}), \quad (3.50)$$

$$\psi_{m_{pu}} = \sqrt{\psi_{md_{pu}}^2 + \psi_{mq_{pu}}^2}. \quad (3.51)$$

The relationship between the saturation factor  $k$  and the magnetic flux  $\psi_{m_{pu}}$  is calculated from the saturation curve of the unloaded generator shown in Figure 3.6. It is assumed that the  $d$ -axis and  $q$ -axis are equally saturated.

When the generating unit is not loaded, the generator terminal voltage is equal to the  $q$ -axis voltage, and if the generator is running under no load and at rated speed, the following holds

$$u_{t_{pu}} = u_{q_{pu}} = \psi_{md_{pu}}. \quad (3.52)$$

If the ratio between the generator voltage and the field current read from the saturation curve of an unloaded generator in Figure 3.6 is taken to be  $k'$ , then  $k'$  may be expressed as

$$k' = \frac{u_{t_{pu}}}{i_{f_{pu}}} = \frac{\psi_{md_{pu}}}{i_{f_{pu}}}. \quad (3.53)$$

Let the maximum value of  $k'$  be  $k''$ . Assuming  $k''$  to be 1 when the generator is not saturated, then the saturation factor  $k$  is determined by

$$k = \frac{k'}{k''} \quad (3.54)$$

Hirayama proposes that the saturation factor can be approximated by the second order algebraic equation

$$k = \alpha + \beta\psi_{md_{pu}} + \gamma\psi_{md_{pu}}^2 \quad (3.55)$$

where  $\alpha$ ,  $\beta$  and  $\gamma$  are constants determined from (3.52) to (3.54). The generator voltage is  $u_t = \psi_{md}$  from (3.52) when the generating unit is not loaded, while the saturation factor  $k$ , when the generating unit is loaded, is obtained by substituting  $\psi_m$  of (3.50) instead of  $\psi_{md}$  into (3.55). Performing iterative calculations with  $k$  taken as a parameter so that (3.48) to (3.50) are met, gives the saturation factor  $k$

and the magnetic fluxes  $\psi_{md}$  and  $\psi_{mq}$ .

### 3.3.2 Method II

[Corzine et al. 1998] propose another method for incorporating magnetic saturation not requiring iterative procedures, instead the magnetic flux is chosen as a state variable. It has been common to consider q-axis saturation in the literature, see [Boldea and Nasar, 1988], [Harley et al 1995], [Hirayama 1995] and [Krause et al, 1995], but some experimentally work done by Corzine et al. show that the power system transients calculated for salient machines were sufficiently accurate when only incorporating magnetic saturation in the  $d$ -axis.

When using the magnetic flux as a state variable, it is necessary to reformulate the expressions normally used for the generator. An expression for the time derivative of the magnetizing flux given as a function of the input variables and the remaining state variables, has to be found.

First, the  $d$ -axis magnetizing current is written as

$$i_{md_{pu}}(\psi_{md_{pu}}) = F(\psi_{md_{pu}}), \quad (3.56)$$

where  $\psi_{md_{pu}}$  is the magnetizing flux linkage.

The  $d$ -axis rotor current vector may be expressed as

$$i_{D_{pu}} = \frac{1}{x_{D\sigma_{pu}}}(\psi_{D_{pu}} - \psi_{md_{pu}}), \quad (3.57)$$

and the field current is written as

$$i_{f_{pu}} = \frac{1}{x_{f\sigma_{pu}}}(\psi_{f_{pu}} - \psi_{md_{pu}}). \quad (3.58)$$

By letting  $i_{md_{pu}} = -i_{d_{pu}} + i_{f_{pu}} + i_{D_{pu}}$ , the  $d$ -axis stator current may be written as

$$\begin{aligned} i_{d_{pu}} &= -i_{md_{pu}} + i_{f_{pu}} + i_{D_{pu}}, \quad (3.59) \\ &= -F(\psi_{md_{pu}}) + \frac{1}{x_{f\sigma}}(\psi_{f_{pu}} - \psi_{md_{pu}}) + \frac{1}{x_{D\sigma_{pu}}}(\psi_{D_{pu}} - \psi_{md_{pu}}) \end{aligned}$$

and the  $d$ -axis stator flux linkage may becomes

$$\begin{aligned} \psi_{d_{pu}} &= -x_{s\sigma_{pu}} \left( -F(\psi_{md_{pu}}) + \frac{1}{x_{f\sigma_{pu}}}(\psi_{f_{pu}} - \psi_{md_{pu}}) \right. \\ &\quad \left. + \frac{1}{x_{D\sigma_{pu}}}(\psi_{D_{pu}} - \psi_{md_{pu}}) \right) + \psi_{md_{pu}} \quad (3.60) \\ &= x_{s\sigma_{pu}} F(\psi_{md_{pu}}) - \frac{x_{s\sigma_{pu}}}{x_{f\sigma_{pu}}} \psi_{f_{pu}} + \frac{x_{s\sigma_{pu}}}{x_{f\sigma_{pu}}} \psi_{md_{pu}} \\ &\quad - \frac{x_{s\sigma_{pu}}}{x_{D\sigma_{pu}}} \psi_{D_{pu}} + \frac{x_{s\sigma_{pu}}}{x_{D\sigma_{pu}}} \psi_{md_{pu}} + \psi_{md_{pu}} \end{aligned}$$

The time derivative of (3.60) is

$$\begin{aligned} \frac{d\psi_{d_{pu}}}{dt} = & x_{s\sigma_{pu}} \frac{\partial F}{\partial \psi_{md_{pu}}} \frac{\partial \psi_{md_{pu}}}{\partial t} - \frac{x_{s\sigma_{pu}}}{x_{f\sigma_{pu}}} \frac{d\psi_{puf}}{dt} + \frac{x_{s\sigma_{pu}}}{x_{f\sigma_{pu}}} \frac{d\psi_{md_{pu}}}{dt}, \\ & - \frac{x_{s\sigma_{pu}}}{x_{D\sigma_{pu}}} \frac{d\psi_{D_{pu}}}{dt} + \frac{x_{s\sigma_{pu}}}{x_{D\sigma_{pu}}} \frac{d\psi_{md_{pu}}}{dt} + \frac{d\psi_{md_{pu}}}{dt} \end{aligned} \quad (3.61)$$

which may be solved for the time derivative of the magnetizing flux linkage as,

$$\dot{\psi}_{md_{pu}} = \quad (3.62)$$

$$\frac{1}{1 + x_{s\sigma_{pu}} \frac{\partial F}{\partial \psi_{md_{pu}}} + \frac{x_{s\sigma_{pu}}}{x_{f\sigma_{pu}}} + \frac{x_{s\sigma_{pu}}}{x_{D\sigma_{pu}}}} \left( \dot{\psi}_{d_{pu}} + \frac{x_{s\sigma_{pu}}}{x_{f\sigma_{pu}}} \dot{\psi}_{f_{pu}} + \frac{x_{s\sigma_{pu}}}{x_{D\sigma_{pu}}} \dot{\psi}_{D_{pu}} \right).$$

The relationship between the magnetizing flux linkage and magnetizing current is linear for both unsaturated and highly saturated conditions, although the slopes and intercepts of the two regions are different. Since the slope is initially constant, undergoes a transition, before becoming constant again, Corzine et al. proposed to represent the slope of the saturation function by the following arctangent function,

$$\frac{\partial F(\psi_{md_{pu}})}{\partial \psi_{md_{pu}}} = \frac{2}{\pi} M_d \text{atan}(\tau_T(\psi_{md_{pu}} - \psi_{T_{pu}})) + M_a, \quad (3.63)$$

where  $M_d$  and  $M_a$  are related to the initial and final slopes of the saturation function,

$$M_d = \frac{M_f - M_i}{2} \quad \text{and} \quad (3.64)$$

$$M_a = \frac{M_f + M_i}{2}. \quad (3.65)$$

$\tau_T$  is the tightness of the transition from initial slope to final slope with respect to  $\psi_{md_{pu}}$  and  $\psi_T$  is the point of transition. When zero magnetizing current corresponds to zero magnetizing flux linkage, integration of  $\partial F(\psi_{md_{pu}})/(\partial \psi_{md_{pu}})$  yields,

$$\begin{aligned} F(\psi_{md}) = & \frac{2M_d}{\pi} \left[ (\psi_{md} - \psi_T) \text{atan}(\tau_T(\psi_{md} - \psi_T)) - \psi_T \text{atan}(\tau_T \psi_T) \right] \\ & + \frac{M_d}{\pi \tau_T} \left[ \ln(\tau_T^2 \psi_T^2 + 1) - \ln((\tau_T(\psi_{md} - \psi_T))^2 + 1) \right] + M_a \psi_{md} \end{aligned} \quad (3.66)$$

Figure 3.7 shows a comparison between measured laboratory data and the arctangent saturation function [Corzine et al. 1998].

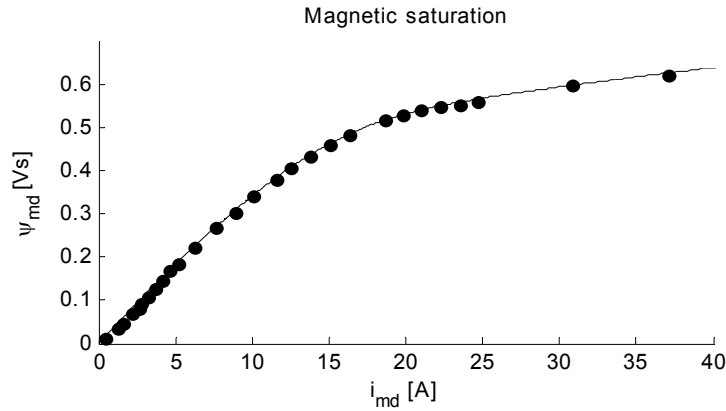


Figure 3.7: Measured and arctangent function saturation curves [Corzine et al. 1998].

### 3.3.3 Procedure for calculating saturation using method II

Two generator models have been presented using bond graphs, one model having all integral causality and one having derivative causality. Next follows the procedures for calculating saturation for both models. Calculation of saturation is done for the  $d$ -axis only, but saturation may also be included in the  $q$ -axis using the same procedure, but cross coupling effects are neglected.

#### Generator model with integral causality

Figure 3.4 shows a bond graph model of a generator with integral causality. The input variables for the  $d$ -axis are:  $\dot{\psi}_{d_{pu}}$ ,  $\dot{\psi}_{f_{pu}}$  and  $\dot{\psi}_{D_{pu}}$  and the state variables for the same axis are  $\psi_{md_{pu}}$ ,  $\psi_{f_{pu}}$  and  $\psi_{D_{pu}}$ . First, the magnetizing flux linkage is calculated as

$$\dot{\psi}_{md_{pu}} = \frac{1}{1 + x_{s\sigma_{pu}} \frac{\partial F}{\partial \psi_{md_{pu}}} + \frac{x_{s\sigma_{pu}}}{x_{f\sigma_{pu}}} + \frac{x_{s\sigma_{pu}}}{x_{D\sigma_{pu}}}} \left( \dot{\psi}_{d_{pu}} + \frac{x_{s\sigma_{pu}}}{x_{f\sigma_{pu}}} \dot{\psi}_{f_{pu}} + \frac{x_{s\sigma_{pu}}}{x_{D\sigma_{pu}}} \dot{\psi}_{D_{pu}} \right).$$

Then the state variables are calculated as

$$\psi_{md_{pu}} = \int \dot{\psi}_{md_{pu}} dt,$$

$$\psi_{f_{pu}} = \int \dot{\psi}_{f_{pu}} dt \text{ and}$$

$$\psi_{D_{pu}} = \int \dot{\psi}_{D_{pu}} dt,$$

and eventually the currents,

$$i_{D_{pu}} = \frac{1}{x_{D\sigma_{pu}}} (\psi_{D_{pu}} - \psi_{md_{pu}}),$$

$$i_{f_{pu}} = \frac{1}{x_{f\sigma_{pu}}}(\psi_{f_{pu}} - \psi_{md_{pu}}) \text{ and}$$

$$i_{d_{pu}} = i_{f_{pu}} + i_{D_{pu}} - F(\psi_{md_{pu}}),$$

where  $F(\psi_{md_{pu}})$  is given by (3.66).

### Generator model with derivative causality

The input variables for the  $d$ -axis for the generator with derivative causality, see Figure 3.5, are  $i_{d_{pu}}$ ,  $\dot{\psi}_{f_{pu}}$  and  $\dot{\psi}_{D_{pu}}$ , and the state variables are  $\psi_{md_{pu}}$ ,  $\psi_{f_{pu}}$  and  $\psi_{D_{pu}}$ . The constitutive equations for the  $d$ -axis are

$$\dot{\psi}_{d_{pu}} = x_{s\sigma_{pu}} i_{d_{pu}} + \dot{\psi}_{md_{pu}}$$

$$i_{f_{pu}} = \frac{1}{x_{f\sigma_{pu}}}(\psi_{f_{pu}} - \psi_{md_{pu}}) \text{ and}$$

$$i_{D_{pu}} = \frac{1}{x_{D\sigma_{pu}}}(\psi_{D_{pu}} - \psi_{md_{pu}}).$$

Calculation of  $\dot{\psi}_{md_{pu}}$  requires the derivative of  $\psi_{d_{pu}}$ , which may be approximated by using the transfer function given by (3.29). Next,  $\dot{\psi}_{md_{pu}}$  is calculated using (3.62). The output from the  $d$ -axis  $I$ -field are  $\dot{\psi}_{d_{pu}}$  together with the currents  $i_{D_{pu}}$  and  $i_{f_{pu}}$ .

## 3.4 Power invariant transformation

The physical inductance matrix of synchronous and asynchronous motor or generator is a non-diagonal matrix where self and mutual inductances are dependent on the position of the rotor. The induction matrix may however be done symmetric and constant by accomplishing a transformation that refer the voltage balance to the  $dq$ -frame instead of the  $abc$ -frame, see Chapter 3.2.

### 3.4.1 Mathematical description

The transformation between the  $abc$ -frame and the  $dq$ -frame is usually given as

$$\begin{bmatrix} u_d \\ u_q \\ u_0 \end{bmatrix} = \frac{2}{3} \begin{bmatrix} \cos(\theta) & \cos\left(\theta - \frac{2}{3}\pi\right) & \cos\left(\theta - \frac{4}{3}\pi\right) \\ -\sin(\theta) & -\sin\left(\theta - \frac{2}{3}\pi\right) & -\sin\left(\theta - \frac{4}{3}\pi\right) \\ \frac{1}{2} & \frac{1}{2} & \frac{1}{2} \end{bmatrix} \begin{bmatrix} u_a \\ u_b \\ u_c \end{bmatrix} \text{ and} \quad (3.67)$$

$$\begin{bmatrix} i_a \\ i_b \\ i_c \end{bmatrix} = \begin{bmatrix} \cos(\theta) & -\sin(\theta) & 1 \\ \cos\left(\theta - \frac{2}{3}\pi\right) & -\sin\left(\theta - \frac{2}{3}\pi\right) & 1 \\ \cos\left(\theta - \frac{4}{3}\pi\right) & -\sin\left(\theta - \frac{4}{3}\pi\right) & 1 \end{bmatrix} \begin{bmatrix} i_d \\ i_q \\ i_0 \end{bmatrix}, \quad (3.68)$$

which in vector notation becomes

$$\mathbf{u}_{d,q,0} = \mathbf{A} \cdot \mathbf{u}_{a,b,c}, \quad \mathbf{u}_{a,b,a} = \mathbf{A}^{-1} \cdot \mathbf{u}_{d,q,0}, \quad (3.69)$$

$$\mathbf{i}_{a,b,c} = \mathbf{B} \cdot \mathbf{i}_{d,q,0}, \quad \mathbf{i}_{d,q,0} = \mathbf{B}^{-1} \cdot \mathbf{i}_{a,b,c}, \quad (3.70)$$

hence  $\mathbf{B} = \mathbf{A}^{-1}$ , but  $\mathbf{B}^T \neq \mathbf{A}$ .

The power before and after the transformation is given as

$$P_{a,b,c} = \begin{bmatrix} i_a & i_b & i_c \end{bmatrix} \begin{bmatrix} u_a \\ u_b \\ u_c \end{bmatrix} = \mathbf{B} \begin{bmatrix} i_d \\ i_q \\ i_0 \end{bmatrix} \mathbf{A}^{-1} \begin{bmatrix} u_d \\ u_q \\ u_0 \end{bmatrix} = \begin{bmatrix} i_d & i_q & i_0 \end{bmatrix} \mathbf{B} \mathbf{B}^T \begin{bmatrix} u_d \\ u_q \\ u_0 \end{bmatrix}, \quad (3.71)$$

but because  $\mathbf{B}^T \neq \mathbf{A} \wedge \mathbf{B} = \mathbf{A}^{-1}$  gives  $\mathbf{B} \mathbf{B}^T \neq 1$ , then  $P_{a,b,c} \neq P_{d,q,0}$ , thus the transformation is not power invariant. In bond graphs, the transformation must be power invariant and for that reason, another transformation matrix is used. By letting

$$\mathbf{C} = \sqrt{\frac{2}{3}} \begin{bmatrix} \cos(\theta) & \cos\left(\theta - \frac{2}{3}\pi\right) & \cos\left(\theta - \frac{4}{3}\pi\right) \\ -\sin(\theta) & -\sin\left(\theta - \frac{2}{3}\pi\right) & -\sin\left(\theta - \frac{4}{3}\pi\right) \\ \frac{1}{\sqrt{2}} & \frac{1}{\sqrt{2}} & \frac{1}{\sqrt{2}} \end{bmatrix} \text{ and} \quad (3.72)$$

$\mathbf{D} = \mathbf{C}^{-1}$  gives  $\mathbf{D}^T = \mathbf{C}$ , such that

$$\mathbf{u}_{d,q,0} = \mathbf{C} \cdot \mathbf{u}_{a,b,c}, \quad \mathbf{u}_{a,b,a} = \mathbf{C}^{-1} \cdot \mathbf{u}_{d,q,0}, \quad (3.73)$$

$$\mathbf{i}_{a,b,c} = \mathbf{D} \cdot \mathbf{i}_{d,q,0}, \quad \mathbf{i}_{d,q,0} = \mathbf{D}^{-1} \cdot \mathbf{i}_{a,b,c}. \quad (3.74)$$

Since  $\mathbf{C}$  and  $\mathbf{D}$  are orthogonal matrices, the power before and after the transformation will be the same, thus this transformation is power invariant and the bond graph methodology can be utilized.

### 3.4.2 Bond graph representation of power invariant transformation

The bond graph models representing (3.73) and (3.74) are presented in Figure 3.8 and Figure 3.9, respectively.

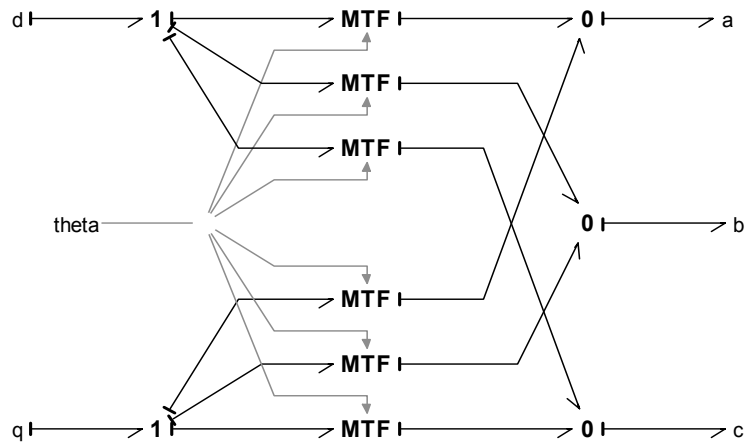


Figure 3.8: Power invariant transformation between dq-frame and abc-frame, the  $C$ -matrix from (3.73).

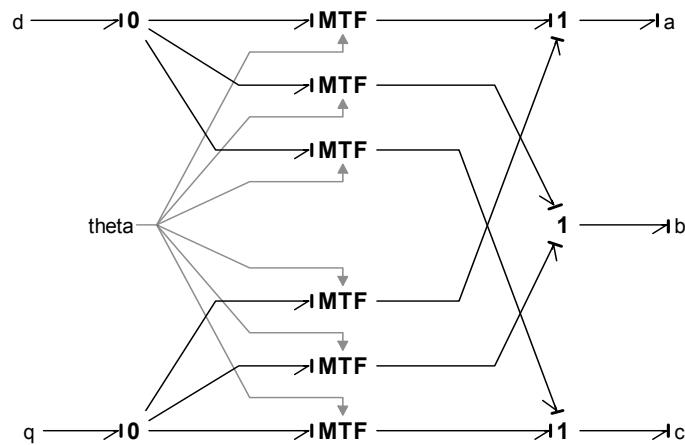


Figure 3.9: Power invariant transformation between dq-frame and abc-frame, the  $D$ -matrix from (3.74).

The power invariant transformation modules will be used between energy producers and consumers modeled in the  $dq$ -frame and the 3 phase bus voltages and currents.

### 3.5 Circuit breaker

The power system on board offshore applications consist of power producers, power distributors and power consumers. Power producers may be different kinds of engines connected to generators or other power producing equipments, while

consumers may be thrusters, pumps, hotel loads and so on. A marine power system is an isolated system, a so called weak network, where voltage and frequency are not constant, but highly dependent on the network loading. In this thesis one generator is chosen as primary generator setting voltage and frequency on the bus, while the other generators that will be connected to the bus will have current as output, see Chapter 3.2. Before connecting a generator to the bus, the generator must have the same voltage, frequency and phase as the bus to prevent disturbances. A circuit breaker is used between generators and the bus and the modeling of such a circuit breaker is the topic next.

In the literature there are several proposals concerning modeling of switching systems using bond graphs. [Karnopp et al. 1992] and [Asher 1993] propose a method using modulated transformer, MTF, to model the discontinuity. Using a modulated transformer makes it necessary to reassign causality when switching. [Borutzky et al. 1995] proposed the use of a combination of a MTF and a resistance element,  $R$ , allowing a fixed causality bond graph. However, the switching is non-ideal since the  $R$ -element brings dissipation, and it can also increase simulation time since the resistance may contribute to a numerically stiff system. Yet another method is proposed by [Top et al. 1993] by introducing an ideal switch as a new bond graph element which enforces zero effort on the junction if switch is ON and zero flow when switch is OFF. A problem with this method is that the causality and hence the model structure will change when mode of operation changes.

The method, switched power junction (SPJ) used in this thesis, is proposed by [Umarikar and Umanand 2005]. It models ideal switching eliminating the problem of stiff systems and numerical stability problems during simulation. The causality invariance is also maintained for the whole system.

### 3.5.1 Theory of switched power junction

An ideal junction will neither store nor dissipate energy, but transmit power instantaneously between its ports. In Chapter A.3 it was shown that there are two standard junction elements: 0- and 1- junctions, where the 0-junction defines a unique common effort on all the bonds connected to the junction, while summation of flows of all bonds are zero. The 1-junction on the other hand defines a unique common flow on all the bonds, while summation of efforts of all bond are zero. The definition of the 0- and 1- junctions give the causality structures of the junctions. For a 0-junction the efforts on all the bonds are equal, thus only one effort bond may be an independent variable and only one causality stroke is placed on the junction side of the bond. For the 1-junction where flows on all bonds are equal, all strokes will be on junction side except for one, see Figure 3.10.

In [Umarikar and Umanand 2005] a method called switched power junction is introduced, which allow several bonds deciding effort on a 0-junction and flow on a 1-junction, but only one of the deciding bonds is active at any instant of time. The

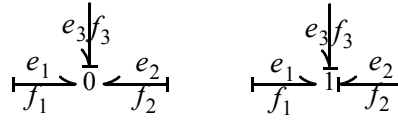
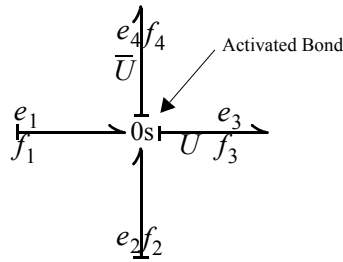


Figure 3.10: 0- and 1- junction with causal strokes.

Figure 3.11:  $0_s$ -junction with two effort deciding bonds [Umarikar and Umanand 2005].

switched power 0-junction is denoted as  $0_s$  and the switched power 1-junction is denoted as  $1_s$ . A  $0_s$ -junction with two deciding bonds is shown in Figure 3.11.  $U$  and  $\bar{U}$  are integer variables (either 0 or 1) associated with bond 3 and 4 which are dependent of the system switching bond, i.e. the activated bond shown in the figure. When  $U$  is 1, the effort on bond 3 is the unique effort shared by the other bonds connected to the  $0_s$ -junction, while when  $\bar{U}$  is 1, the effort of bond 4 is the junction effort. The constitutive relations for the  $0_s$ -junction may be written as:

$$\text{Junction effort} = Ue_3 + \bar{U}e_4$$

$$f_3 = U(f_1 + f_2), f_4 = \bar{U}(f_1 + f_2)$$

$$f_1 + f_2 - f_3 - f_4 = 0.$$

The constitutive relations for the  $1_s$ -junction may be written in a similar way.

$0_s$ - and  $1_s$ -junctions may easily be generalized to include  $n$  effort or flow deciding bonds. The relations for generalized switched power bonds are given (bond 3 to  $n$  are deciding bonds),

for  $0_s$ -junction:

$$\text{Junction effort} = U_3e_3 + \dots + U_n e_n$$

$$f_3 = U_3(f_1 + f_2)$$

.

$$f_n = U_n(f_1 + f_2)$$

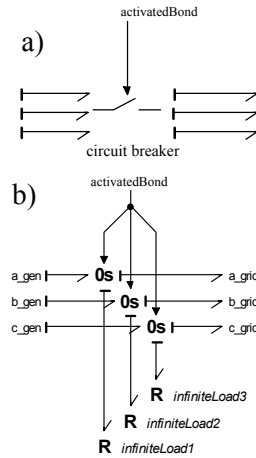


Figure 3.12:  $0_s$ -junction used as switch between generator and grid, a) the overall model and b) the bond graph model of the switch using SPJ.

for  $1s$ -junction:

$$\text{Junction flow} = U_3 f_3 + \dots + U_n f_n$$

$$e_3 = U_3(e_1 + e_2)$$

.

.

$$e_n = U_n(e_1 + e_2)$$

### 3.5.2 Bond graph representation of the circuit breaker

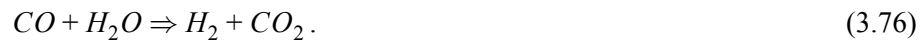
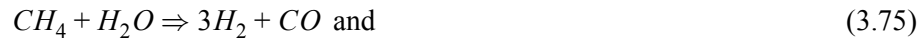
Figure 3.12 shows a) the overall model of the circuit breaker used between a generator and the grid and b) the bond graph representation of the circuit breaker using SPJ. When the generator is not connected to the grid, a R-element sets the effort on each junction, while the grid is setting the effort when the generator is connected.  $a\_gen$ ,  $b\_gen$  and  $c\_gen$  and  $a\_grid$ ,  $b\_grid$  and  $c\_grid$  are the 3 phase voltage of generator and grid, respectively. The signal bond called *activatedBond* decides which of the two bonds that are setting effort on the switched  $0$ -junctions. When the bond, which is an integer, has the value 1, the generator is connected and voltage is set by the grid while the voltages are set by the resistance elements when the value of the *activatedBond* is 0.

## 3.6 Fuel cell

### 3.6.1 Mathematical description

An illustration of a solid oxide fuel cell, SOFC, is shown in Figure 3.13, which is built up by a membrane-electrolyte assembly (MEA) consisting of a solid oxide electrolyte that conducts oxide ions from the cathode to the anode. The electrochemical reactions take place at the triple phase boundary (TPB).

The following is taken from [Stiller 2006]. Fuel is passed over the anode surface and anode exhaust gas is recycled to provide heat and steam for shift and reforming reactions in the fuel processing system. Thus, the anode gas flow consists of steam, carbon dioxide, carbon monoxide, methane and hydrogen. High temperature causes most of the carbon to be reduced to carbon dioxide through the reforming and shift reactions given as



The electrochemical reaction is written as



The reversible voltage potential,  $U_{rev}$ , supplied by the electrodes, is given by the Nernst equation

$$U_{rev} = U_0 + \frac{R_0 T}{2F} \ln \left( \frac{p_{H_2} p_{O_2}^{1/2}}{p_{H_2O}} \right), \quad (3.79)$$

where  $U_0$  is the reversible open circuit voltage,  $R_0$  is universal gas constant,  $T$  is temperature and  $F$  is Faraday's constant.  $p_{H_2}$ ,  $p_{O_2}$  and  $p_{H_2O}$  are partial pressures of hydrogen, oxygen and water, respectively.

The SOFC is modeled according to [Padullés et al. 2000] where the model is based on the following assumptions;

- The gases are ideal.
- The channels that transport gases along the electrodes have fixed volume, and their lengths are small, thus it is only necessary to define one single pressure value in their interior.
- The exhaust of each channel is via a single orifice. The ratio of pressures between the interior and exterior of the channel is large enough to consider that the orifice is choked.
- The temperature is stable at all times.
- The only source of losses is ohmic, since this is the most dominant voltage loss. At small initial current densities and large current densities, also

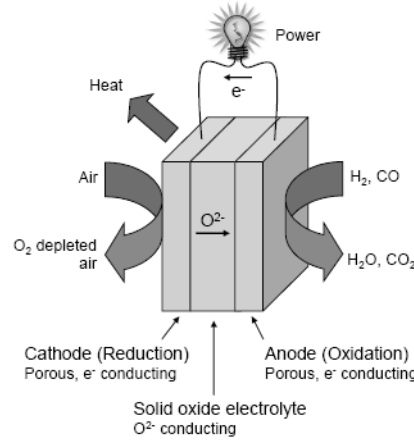


Figure 3.13: Solid oxide fuel cell [Stiller 2006].

activation and concentration losses are of importance, but the working conditions of interest are not close to upper and lower extremes of current.

- The Nernst equation can be applied.

The stack voltage may be written as

$$U = N_0 U_{rev} - rI, \quad (3.80)$$

where  $N_0$  is number of cells in series in the stack and the term  $rI$  represents ohmic losses.  $U_{rev}$  is given by (3.79).

The partial pressure of hydrogen is given as

$$p_{H_2} = \frac{1/K_{H_2}}{1 + \tau_{H_2} s} (q_{H_2}^{in} - 2K_r I_{fc}), \quad (3.81)$$

where  $K_{H_2} = q_{H_2}/p_{H_2}$ ,  $\tau_{H_2} = V_{an}/(K_{H_2}RT)$ ,  $q_{H_2}$  is molar flow of hydrogen,  $V_{an}$  is volume of the anode,  $K_r = N_0/(2F)$  and  $I_{fc}$  is stack current. The partial pressures of oxygen and water are given in a similar way,

$$p_{O_2} = \frac{1/K_{O_2}}{1 + \tau_{O_2} s} (q_{O_2}^{in} - K_r I_{fc}) \quad \text{and} \quad (3.82)$$

$$p_{H_2O} = \frac{1/K_{H_2O}}{1 + \tau_{H_2O} s} (2K_r I_{fc}), \quad (3.83)$$

where

$$K_{O_2} = q_{O_2}/p_{O_2},$$

$$\tau_{O_2} = V_{an}/(K_{O_2}R_0T),$$

$$K_{H_2O} = q_{H_2O}/p_{H_2O} \text{ and}$$

$$\tau_{H_2O} = V_{an}/(K_{H_2O}R_0T).$$

$q_{O_2}^{in}$  is molar flow of oxygen.

Fuel utilization describes the ratio between the hydrogen flow that reacts,  $q_{H_2}^r$ , and the input hydrogen flow,  $q_{H_2}^{in}$ , and is written as

$$U_f = \frac{q_{H_2}^r}{q_{H_2}^{in}}. \quad (3.84)$$

According to [Padullés et al. 2000], the molar flow of hydrogen that reacts, may be given as

$$q_{H_2}^r = \frac{N_0 I}{2F} = 2K_r I, \quad (3.85)$$

thus

$$q_{H_2}^{in} = \frac{2K_r I}{U_f}. \quad (3.86)$$

The fuel processor is modeled as a first order transfer function with  $T_f$  as the response time, which is often slow since it is associated with the time to change chemical reaction parameters after a change in flow of reactants [Zhu and Tomosovic 2002].

The oxygen flow is found using the hydrogen - oxygen flow ratio,  $r_{H-O}$ .

### Connecting the fuel cell to the bus

There exists at least two possibilities for using fuel cell as power producer on board offshore vessels. The fuel cell generates DC voltage and one possibility is to let the fuel cell be connected to a DC network with DC loads. Another possibility is to use a DC to AC conversion of the power before distributing the power on AC bus. Then the fuel cell is connected to a bus using a power conditioning unit (PCU), see Figure 3.14. The PCU includes pulse width modulated (PWM) dc to ac inverter to convert DC grid voltage to AC voltage and a transformer. Two control loops are utilized to control the output AC voltage and power.

From [Krause et al. 2002] it is found that the fast average value of the converter voltage  $\mathbf{u}_c^c = \begin{bmatrix} u_{cd}^c & u_{cq}^c \end{bmatrix}^T$  may be given in the converter reference frame as

$$\begin{bmatrix} u_{cd}^c \\ u_{cq}^c \end{bmatrix} = \begin{bmatrix} 0 \\ m_c u_{fc} \end{bmatrix}, \quad (3.87)$$

when assuming that the switching frequency of the converter is much higher than the system fundamental frequency.  $u_{fc}$  is the fuel cell voltage and  $m_c$  is the

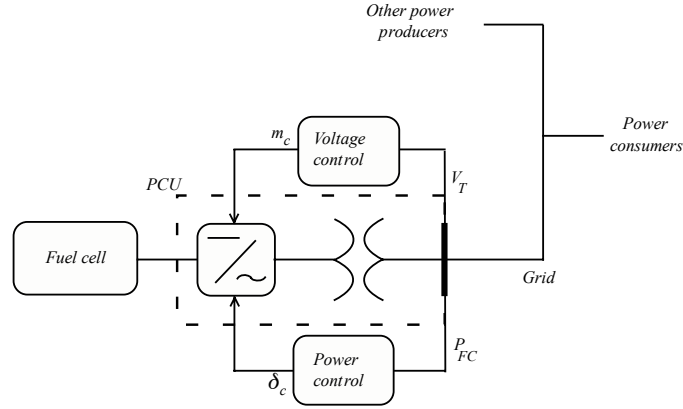


Figure 3.14: Single line diagram of fuel cell connected to grid [Stevandic and Jiang 2003].

amplitude modulation index.

Vectors may be transformed between orthogonal coordinate systems with an angle difference  $\phi = \theta_y - \theta_x$  by using

$$\begin{bmatrix} f_d^y \\ f_q^y \end{bmatrix} = \begin{bmatrix} \cos \phi & -\sin \phi \\ \sin \phi & \cos \phi \end{bmatrix} \begin{bmatrix} f_d^x \\ f_q^x \end{bmatrix}, \quad (3.88)$$

such that the converter voltage may be represented in the  $dq$ -reference frame by

$$\begin{bmatrix} u_{cd} \\ u_{cq} \end{bmatrix} = \begin{bmatrix} -m_c u_{fc} \sin(\theta_{ce}) \\ m_c u_{fc} \cos(\theta_{ce}) \end{bmatrix}. \quad (3.89)$$

$\theta_{ce}$  is angular displacement of the converter reference frame from the synchronous reference frame,

$$\theta_{ce} = \theta_c - \theta. \quad (3.90)$$

$\theta_c$  and  $\theta$  are the angular position of converter reference frame and synchronously rotating reference frame, respectively.

The converter is assumed free of any losses, thus active power must be the same on both sides of the converter.

$$P_{fc} = P_c \Leftrightarrow u_{fc} i_{fc} = u_{cd} i_{cd} + u_{cq} i_{qc}, \quad (3.91)$$

and the fuel cell current is given by

$$i_{fc} = m_c (-i_d \sin(\theta_{ce}) + i_q \cos(\theta_{ce})). \quad (3.92)$$

The voltage balance of the 3 phase RL transformer circuit may be expressed in  $dq$  reference frame as [Krause et al. 2002]

$$\begin{bmatrix} u_{cd} - u_{td} \\ u_{cq} - u_{tq} \end{bmatrix} = R_t \begin{bmatrix} i_d \\ i_q \end{bmatrix} + \begin{bmatrix} 0 & -\omega \\ \omega & 0 \end{bmatrix} \begin{bmatrix} \psi_d \\ \psi_q \end{bmatrix} + \begin{bmatrix} \dot{\psi}_d \\ \dot{\psi}_q \end{bmatrix}, \quad (3.93)$$

where  $\psi_d = Li_d$  and  $\psi_q = Li_q$ .  $R_t$  and  $L$  are resistance and inductance parameters of the transformer and  $\omega$  is the bus frequency.

### Controlling the fuel cell

[Stevandic and Jiang 2003] propose a decoupled feedback control strategy for the fuel cell where a decoupling feedback branch is added to a feedback controller. The  $dq$  reference voltage signals are given as

$$u_{cd}^* = u_{cd_{FB}}^* + u_{cd_{DF}}^* \quad \text{and} \quad (3.94)$$

$$u_{cq}^* = u_{cq_{FB}}^* + u_{cq_{DF}}^*, \quad (3.95)$$

where

$$u_{cd_{FB}}^* = K_p(i_d^* - i_d) + K_i \int (i_d^* - i_d) dt, \quad (3.96)$$

$$u_{cq_{FB}}^* = K_p(i_q^* - i_q) + K_i \int (i_q^* - i_q) dt \quad \text{and} \quad (3.97)$$

$$\begin{bmatrix} u_{cd_{DF}}^* \\ u_{cq_{DF}}^* \end{bmatrix} = \begin{bmatrix} R_t & -\omega L \\ \omega L & R_t \end{bmatrix} \begin{bmatrix} i_d \\ i_q \end{bmatrix} + \begin{bmatrix} u_{td} \\ u_{tq} \end{bmatrix}. \quad (3.98)$$

The command signal for the phase angle  $\delta_c$  and the amplitude modulation index  $m_c$  can be calculated as follows [Krause et al. 2002],

$$m_c^* = \frac{\sqrt{(u_{cd}^*)^2 + (u_{cq}^*)^2}}{u_{fc}} \quad \text{and} \quad (3.99)$$

$$\delta_c^* = \theta_{ce}^* = \text{angle}(u_{cq_{DF}}^* - ju_{cd_{DF}}^*). \quad (3.100)$$

The combined state equations for the transformer and the control system may be expressed by

$$\begin{bmatrix} \dot{i}_d \\ \dot{i}_q \\ \dot{x}_d \\ \dot{x}_q \end{bmatrix} = \begin{bmatrix} -\frac{K_p}{L} & 0 & \frac{K_i}{L} & 0 \\ 0 & -\frac{K_p}{L} & 0 & \frac{K_i}{L} \\ -1 & 0 & 0 & 0 \\ 0 & -1 & 0 & 0 \end{bmatrix} \begin{bmatrix} i_d \\ i_q \\ x_d \\ x_q \end{bmatrix} + \begin{bmatrix} \frac{K_p}{L} & 0 \\ 0 & \frac{K_p}{L} \\ 1 & 0 \\ 0 & 1 \end{bmatrix} \begin{bmatrix} i_d^* \\ i_q^* \end{bmatrix}, \quad (3.101)$$

and the characteristic polynomials for the  $d$ - and  $q$ -axes becomes

$$\Delta_d = \Delta_q = \lambda^2 + \frac{K_p}{L}\lambda + \frac{K_i}{L} = 0, \quad (3.102)$$

which have the eigenvalues

$$\lambda_{1,2}^d = \lambda_{1,2}^q = \frac{1}{2L}(-K_p \pm \sqrt{K_p^2 - 4LK_i}). \quad (3.103)$$

When using decoupled feedback together with a normal feedback controller, it is possible to place the closed-loop poles at any location. In addition, the fuel cell power plant is also insensitive to the variations of the grid parameters [Stevandic and Jiang 2003].

Active and reactive power are given in the  $dq$ -frame as

$$P = u_d i_d + u_q i_q \quad \text{and} \quad (3.104)$$

$$Q = -u_d i_q + u_q i_d \quad (3.105)$$

Solving (3.104) and (3.105) with respect to  $i_d$  and  $i_q$  gives

$$i_d = \frac{1}{u_d^2 + u_q^2}(u_d P + u_q Q) \quad \text{and} \quad (3.106)$$

$$i_q = \frac{1}{u_d^2 + u_q^2}(u_q P - u_d Q), \quad (3.107)$$

which are used to determine the current references  $i_d^*$  and  $i_q^*$ .  $P$  and  $Q$  are desired output of active and reactive power from the fuel cell power plant while  $\mathbf{u} = [u_d \ u_q]^T$  are network voltages.

### 3.6.2 Bond graph representation of a fuel cell power plant

Figure 3.15 presents a bond graph representation of a fuel cell power plant modeled in the  $dq$ -reference frame. It is assumed that the power plant consist of one or more generator sets of which one generator set sets voltage. Power consumers may include loads from thrusters, winches, pumps and so on.

A model of the solid oxide fuel cell is shown in Figure 3.16. Equation (3.80) to (3.86) are modeled using block diagram, while a modulated effort source is used to set the calculated stack voltage. Block diagram implementation is chosen since the fuel cell performance calculation is done using only transfer-functions. A bond graph model of a SOFC is presented in [Bruun and Pedersen 2007].

The power conditioning unit (PCU) holds a converter/booster and a transformer. Equation (3.89) and (3.92) are used for the converter/booster which is modeled using a modulated transformer. The converter control variables  $m_c^*$  and  $\delta_c^*$  are calculated using (3.99) and (3.100). The bond graph representation of the 3 phase RL transformer is shown in Figure 3.17 and is given by (3.93). The block *Reference current* calculates required current based on (3.106) and (3.107) and desired active and reactive power. The feedback controller and decoupling controller are given by (3.96) to (3.98).

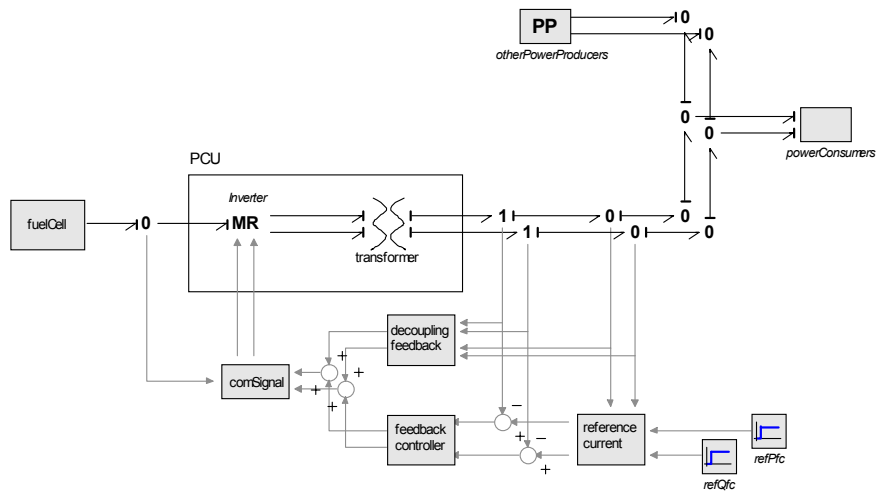


Figure 3.15: Fuel cell power plant including control system connected to grid.

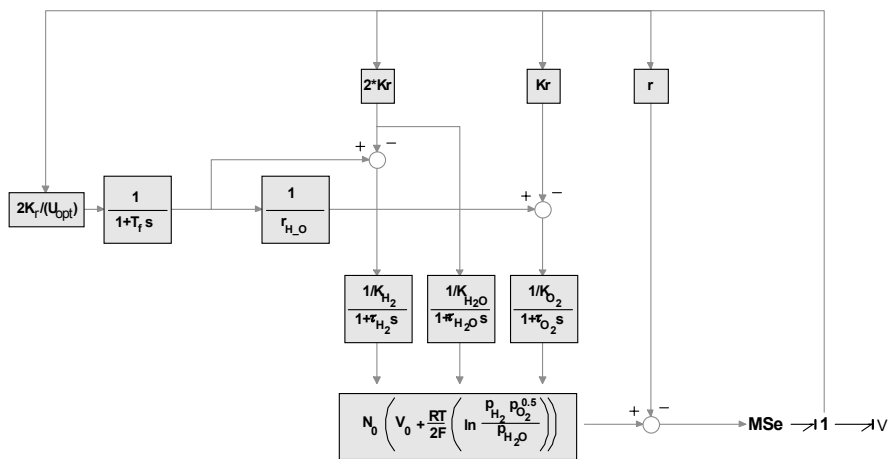


Figure 3.16: Dynamic model of SOFC.

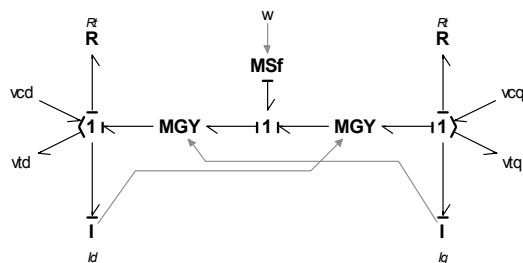


Figure 3.17: Bond graph model of the transformer.

## 3.7 Asynchronous motor

### 3.7.1 Mathematical description

The asynchronous motor is modeled using the same approach as the synchronous generator, that is the two reaction theory.

The voltage balance may be given from the physical model as

$$\mathbf{U}^{SR} = \mathbf{R}^{SR} \mathbf{I}^{SR} + \frac{d}{dt} \psi^{SR} \quad (3.108)$$

where

$$\mathbf{U}^{SR} = [u_a \ u_b \ u_c \ u_D \ u_Q]^T,$$

$$\mathbf{I}^{SR} = [i_a \ i_b \ i_c \ i_D \ i_Q]^T \text{ and}$$

$$\mathbf{R}^{SR} = \text{diag}[r_a, r_b, r_c, r_D, r_Q]$$

are the voltages, currents and resistances in the stator windings and damper windings.  $\psi^{SR}$  represents the flux linkage given as

$$\psi^{SR} = \mathbf{L}^{SR} \mathbf{I}^{SR}. \quad (3.109)$$

$\mathbf{L}^{SR}$  is the physical inductance matrix which is non-linear and a function of rotor position angle. As for the inductance matrix of the generator, the physical inductance matrix may be done independent of rotor angle by using power invariant transformation, see Chapter 3.4.

The voltage balance  $\mathbf{u} = [u_{ds} \ u_{qs} \ u_{dr} \ u_{qr}]^T$  for the induction motor using transformed variables, is given as

$$\mathbf{u} = \mathbf{R} \mathbf{i} + \frac{d}{dt} \psi, \quad (3.110)$$

where

$$\mathbf{R} = \text{diag}[r_s, r_s, r_r, r_r],$$

$$\mathbf{i} = [i_{ds} \ i_{qs} \ i_{dr} \ i_{qr}]^T \text{ and}$$

$$\psi = [\psi_{ds} \ \psi_{qs} \ \psi_{dr} \ \psi_{qr}]^T$$

are stator and rotor resistances, currents and flux linkages, respectively. The flux linkage is expressed as

$$\psi = \mathbf{L} \mathbf{i}, \quad (3.111)$$

where the inductance matrix  $\mathbf{L}$  is independent of rotor position angle and written as

$$\mathbf{L} = \begin{bmatrix} L_s & 0 & L_m & 0 \\ 0 & L_s & 0 & L_m \\ L_m & 0 & L_r & 0 \\ 0 & L_m & 0 & L_r \end{bmatrix} \quad (3.112)$$

The diagonal terms of the inductance matrix are self inductances, while the off-diagonal terms are mutual inductances. The currents  $\mathbf{i}$  may now be found as

$$\mathbf{i} = \mathbf{L}^{-1}\boldsymbol{\psi}, \quad (3.113)$$

which gives

$$i_{ds} = \frac{-(-L_r\psi_{ds} + L_m\psi_{dr})}{L_sL_r - L_m^2}, \quad (3.114)$$

$$i_{qs} = \frac{-(-L_r\psi_{qs} + L_m\psi_{qr})}{L_sL_r - L_m^2}, \quad (3.115)$$

$$i_{dr} = \frac{L_s\psi_{dr} - L_m\psi_{ds}}{L_sL_r - L_m^2} \text{ and} \quad (3.116)$$

$$i_{qr} = \frac{L_s\psi_{qr} - L_m\psi_{qs}}{L_sL_r - L_m^2}. \quad (3.117)$$

The stator voltages given in the  $dq$ -reference frame rotating with the rotor angular velocity  $\omega_r$  are written as

$$u_{ds} = r_s i_{ds} - \omega_r \psi_{qs} + \dot{\psi}_{ds} \text{ and} \quad (3.118)$$

$$u_{qs} = r_s i_{qs} + \omega_r \psi_{ds} + \dot{\psi}_{qs}, \quad (3.119)$$

while the rotor voltages are

$$0 = r_r i_{dr} + \dot{\psi}_{dr} \text{ and} \quad (3.120)$$

$$0 = r_r i_{qr} + \dot{\psi}_{qr}. \quad (3.121)$$

The electromechanical torque is given by

$$T_e = \psi_{ds} i_{qs} - \psi_{qs} i_{ds}. \quad (3.122)$$

When letting the reference frame rotate with the angular velocity  $\omega_r$ , the  $ds$ -,  $qs$ -,  $dr$ - and  $qr$ - voltages, currents and flux linkages will not be constant, but vary as a sinusoidal dependent on  $\omega_s \cdot s \cdot t$ , where  $\omega_s$  is synchronous speed,  $s$  is the slip and  $t$  is time.

By letting the reference frame rotate at synchronous speed  $\omega_s$  instead of angular velocity  $\omega_r$ , the stator and rotor voltages may given as

$$u_{ds} = r_s i_{ds} - \omega_s \psi_{qs} + \dot{\psi}_{ds}, \quad (3.123)$$

$$u_{qs} = r_s i_{qs} + \omega_s \psi_{ds} + \dot{\psi}_{qs}, \quad (3.124)$$

$$0 = r_r i_{dr} - s \omega_s \psi_{qr} + \dot{\psi}_{dr} \text{ and} \quad (3.125)$$

$$0 = r_r i_{qr} + s \omega_s \psi_{dr} + \dot{\psi}_{qr}. \quad (3.126)$$

The slip is given as

$$s = \frac{\omega_s - \omega_r}{\omega_s}. \quad (3.127)$$

Using (3.127) in (3.125) and (3.126), gives the following equations for the rotor voltages

$$0 = r_r i_{dr} - (\omega_s - \omega_r) \psi_{qr} + \dot{\psi}_{dr} \text{ and} \quad (3.128)$$

$$0 = r_r i_{qr} + (\omega_s - \omega_r) \psi_{dr} + \dot{\psi}_{qr}. \quad (3.129)$$

The electromechanical torque is given by

$$Q_e = \psi_{qr} i_{dr} - \psi_{dr} i_{qr}. \quad (3.130)$$

Defining  $\mathbf{u}_s = [u_{ds} \ u_{qs}]^T$ , then stator and rotor voltages may be given in state space form as

$$\dot{\psi} = \mathbf{K}(\omega_s, \omega_r) \psi + \mathbf{R} \mathbf{i} + \mathbf{E} \mathbf{u}_s, \quad (3.131)$$

where

$$\mathbf{K}(\omega_s, \omega_r) = \begin{bmatrix} 0 & n_p \omega_s & 0 & 0 \\ -n_p \omega_s & 0 & 0 & 0 \\ 0 & 0 & 0 & n_p (\omega_s - \omega_r) \\ 0 & 0 & -n_p (\omega_s - \omega_r) & 0 \end{bmatrix}, \quad \mathbf{E} = \begin{bmatrix} 1 & 0 \\ 0 & 1 \\ 0 & 0 \\ 0 & 0 \end{bmatrix} \text{ and}$$

$$\mathbf{R} = \begin{bmatrix} -r_s & 0 & 0 & 0 \\ 0 & -r_s & 0 & 0 \\ 0 & 0 & -r_r & 0 \\ 0 & 0 & 0 & -r_r \end{bmatrix}.$$

The electromechanical torque may be written as

$$T = [\psi_{dr} \ \psi_{qr}] \begin{bmatrix} 0 & -1 \\ 1 & 0 \end{bmatrix} \begin{bmatrix} i_{dr} \\ i_{qr} \end{bmatrix} = \psi_r^T \mathbf{H} \mathbf{i}_r = \psi^T \mathbf{G}_r^T \mathbf{H} \mathbf{G}_r \mathbf{i} \quad (3.132)$$

when defining  $\mathbf{i}_r = [i_{dr} \ i_{qr}]^T$  and  $\psi_r = [\psi_{dr} \ \psi_{qr}]^T$  and  $\mathbf{H}$  and  $\mathbf{G}_r$  are given as

$$\mathbf{H} = \begin{bmatrix} 0 & -1 \\ 1 & 0 \end{bmatrix} \text{ and} \quad (3.133)$$

$$\mathbf{G}_r = \begin{bmatrix} 0 & 0 & 1 & 0 \\ 0 & 0 & 0 & 1 \end{bmatrix} \quad (3.134)$$

Active and reactive power may be given in the  $dq$ -frame as

$$P = u_{ds}i_{ds} + u_{qs}i_{qs} \text{ and } Q = -u_{ds}i_{qs} + u_{qs}i_{ds}, \quad (3.135)$$

which in vector notation becomes

$$P = \mathbf{u}_s^T \mathbf{i}_s = \mathbf{u}_s^T \mathbf{G}_s \mathbf{i} \text{ and } Q = \mathbf{u}_s^T \mathbf{H} \mathbf{i}_s = \mathbf{u}_s^T \mathbf{H} \mathbf{G}_s \mathbf{i}, \quad (3.136)$$

when

$$\mathbf{G}_s = \begin{bmatrix} 1 & 0 & 0 & 0 \\ 0 & 1 & 0 & 0 \end{bmatrix} \quad (3.137)$$

### 3.7.2 Bond graph representation of the induction motor

The bond graph model representing equation (3.114) to (3.122) may be seen in Figure 3.18. The  $I$ -fields,  $I_d$  and  $I_q$ , represent equation (3.114) to (3.117), while the  $R$ -elements represent stator and rotor resistances. The modulated gyrators represent the terms  $\omega_r \psi_{ds}$  and  $\omega_r \psi_{qs}$  in (3.118) and (3.119) and the transformer represents the number of pole pairs for the induction motor.

The next figure, Figure 3.19, shows the bond graph model of the induction motor with the reference frame rotating at synchronous speed. The  $I$ -fields,  $I_d$  and  $I_q$ , are still representing equation (3.114) to (3.117), and the  $R$ -elements are representing stator and rotor resistances. The main differences between the two models are the modulated gyrators which represents the terms  $\omega_s \psi_{ds}$ ,  $\omega_s \psi_{qs}$ ,  $(\omega_s - \omega_r) \psi_{qr}$  and  $(\omega_s - \omega_r) \psi_{dr}$  in (3.123), (3.124), (3.128) and (3.129)

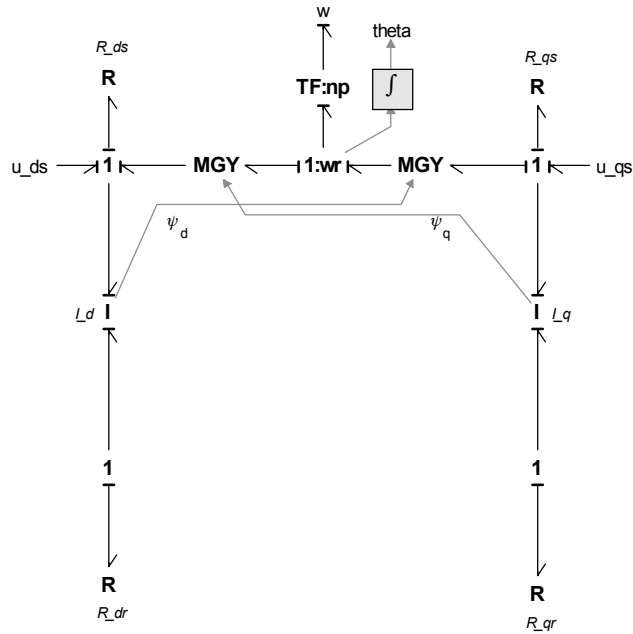


Figure 3.18: Induction motor model in  $dq$ -frame rotation at rotor angular speed.

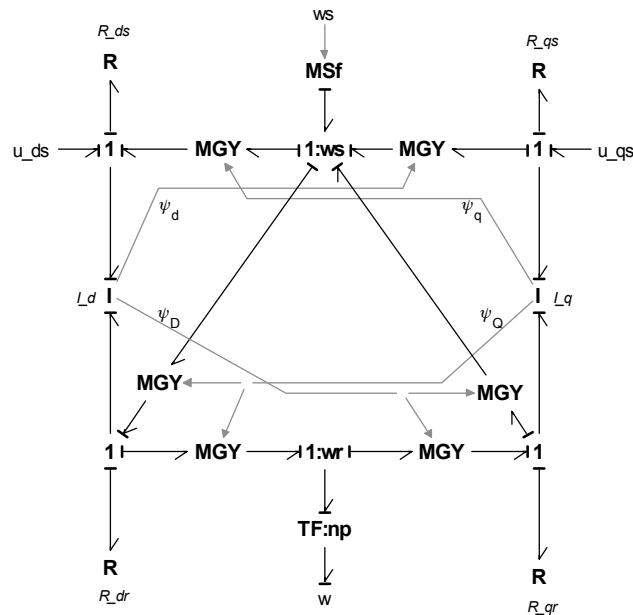


Figure 3.19: Induction motor model in  $dq$ -frame rotation at synchronous speed.

## 3.8 Power converters

The speed of the synchronous and asynchronous motors are given by the frequency of the applied voltage. Since it is desirable to have approximately constant voltage and frequency on the switchboard, a motor drive is used to control the speed of the electrical motor.

The main scope of the power converter is to change the frequency of the AC, but it may also alter the amplitude. Power semiconductors are used to convert the fixed network AC voltage to desired amplitude and frequency. There are three types of semiconductors [Ådnanes 2003].

- uncontrolled components,
- controllable turn-on components and
- controllable turn-on and turn-off components.

The diode is an uncontrolled component and conducts current if positively biased while blocking current if negatively biased. The thyristor is a controllable turn-on component which will block current in both directions without a gate firing signal. If the thyristor is positively biased and a gate firing signal is given, it will conduct until the surrounding circuits forces the current to reverse. An example of the last group of components is the transistor which may be turned on while blocked if it is positively biased using a continuous gate firing signal. If the signal is stopped, the transistor will block even though it is still positively biased.

There are two groups of AC to AC converters, the first group, cyclo converters, changes the AC directly to a new AC without a DC link. The motor frequency is controllable up to about one third of the supply frequency [Ådnanes 2003] and is therefore most suitable for direct shaft drives. The cyclo converter is normally used together with synchronous motors and due to low output frequency it is normally used for slow speed and very high power applications, e.g. icebreakers.

The second group of AC to AC converters are frequency converters using a DC-link. Voltage source inverter (VSI) and current source inverter (CSI) are both in the second group. The CSI converter is mainly used with synchronous motors, but if making a few modifications to an asynchronous motor, the CSI converter may also be used together with the modified asynchronous motor. As the name imply, the current source inverter is fed by DC current fed by a thyristor-controlled rectifier and smoothed by an inductor.

The VSI converter is today the most used frequency converter. It can be used together with an asynchronous engine and at the same time give much better performance than other alternatives for synchronous and permanent magnet machines. The most common method to control the voltage output to the electrical motor is to use a variant of pulse width modulation (PWM). Therefore, a VSI-PWM converter consisting of a diode rectifier, DC-link and a inverter, see Figure 3.20, is the only converter modeled here. The rectifier and the inverter are discussed next.

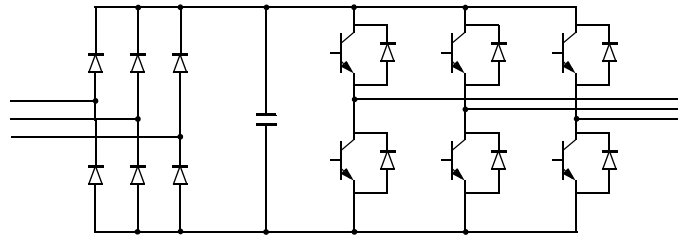


Figure 3.20: PWM-VSI converter.

### 3.8.1 A basic rectifier

#### Mathematical description

The analyze of the three phase diode rectifier shown in Figure 3.21 may be simplified by obtaining an equivalent circuit of the rectifier. According to [Mohan et al. 1989], the equivalent circuit is found by first obtaining the DC output voltage under an open circuit condition. The capacitor,  $C_{DC}$ , is replaced by a large resistance,  $R_{DC} \rightarrow \infty$ , across the rectifier output such that the current,  $i_{DC}$ , is approximately 0. The diodes 1, 3 and 5 have common cathode connections, and the diode with highest positive phase voltage conducts. The same applies for the diodes 2, 4 and 6, which also have common cathode connections, but now the diode with the most negative phase voltage will conduct.  $u_{Pn}$  is the voltage of the top terminal  $P$  on the DC side of the rectifier, with respect to the AC source neutral  $n$ . For the bottom terminal  $N$ ,  $u_{Nn}$  is the voltage on the DC side of the rectifier with respect to  $n$ , see Figure 3.22. By investigating Figure 3.22, it is clear that at any instant of time two diodes conduct, one from the top group 1, 3 and 5, and one from the bottom group 2, 4 and 6. Each diode conducts for  $120^\circ$  per cycle and a new diode begins to conduct after a interval of  $60^\circ$ . By using Figure 3.22, a simple equivalent circuit is derived, see Figure 3.23. A diode is used in series with  $u_{DC}$  to ensure that  $i_{DC}$  through the circuit cannot reverse. Since two phases are conducting when current is flowing, the series inductance is  $2L_s$ . This equivalent circuit can be used, provided that the current  $i_{DC}$  through the rectifier becomes zero prior to each  $60^\circ$  interval. Because of a large  $C_{DC}$ , the DC side voltage is approximated as  $u_{DC}(t) \approx U_{DC}$ .

Often in three-phase rectifiers, if an inductor is used to improve the current waveforms and the ripple in the DC voltage output, it is placed on the DC side between the rectifier and the filter capacitor, see Figure 3.24. In this circuit, even if  $i_{DC}$  flows continuously, the equivalent circuit of Figure 3.23 can be modified and used as shown in Figure 3.25, assuming  $L_s$  to be negligibly small.

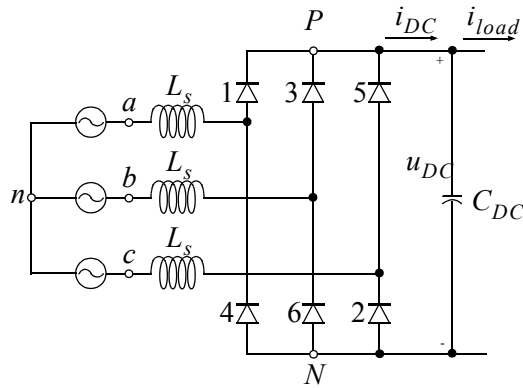


Figure 3.21: Three phase diode rectifier [Mohan et al. 1989].

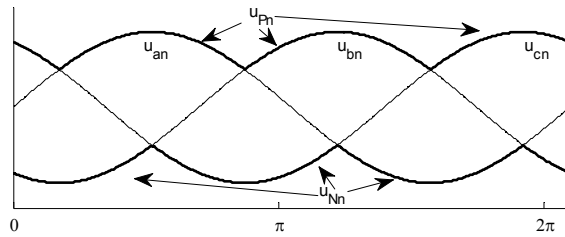


Figure 3.22: Open circuit waveform with  $R_{DC} \rightarrow \infty$  and  $i_{DC} \approx 0$ .

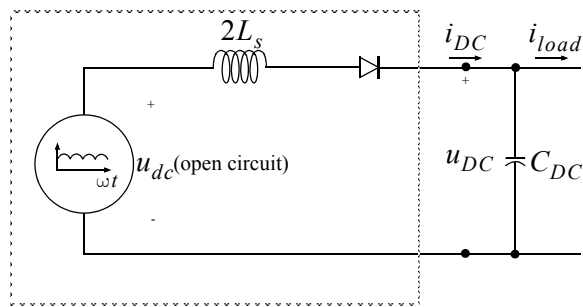


Figure 3.23: 3 Equivalent circuit [Mohan et al. 1989].

With a continuously flowing  $i_{DC}$ , the average value of the output voltage can be calculated from Figure 3.26. The area under the  $u_{DC}$  waveform during a  $60^\circ$  interval is given as

$$A_{DC} = \int_{-\frac{\pi}{6}}^{\frac{\pi}{6}} \sqrt{2} U_{LL} \cos(\omega t) d(\omega t) = \sqrt{2} U_{LL}, \quad (3.138)$$

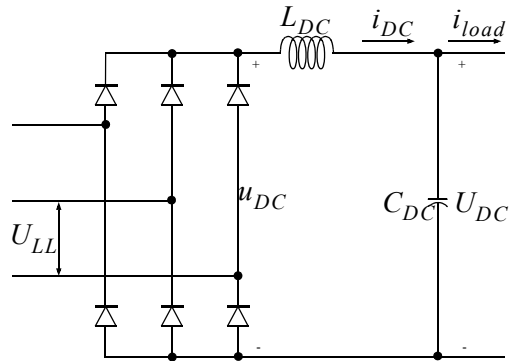


Figure 3.24: Three phase rectifier with an inductor  $L_{DC}$  [Mohan et al. 1989].

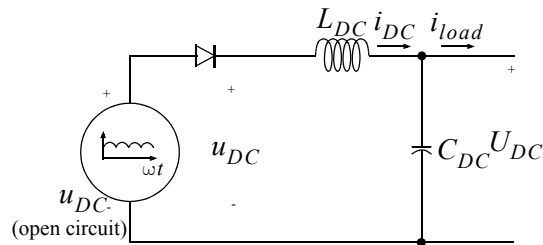


Figure 3.25: Equivalent circuit [Mohan et al. 1989].

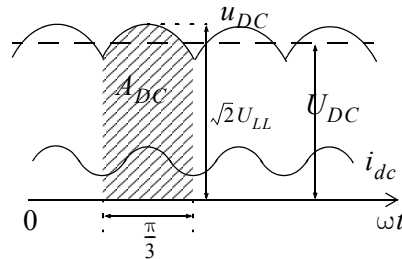


Figure 3.26: DC link voltage and current waveform [Mohan et al. 1989].

such that

$$U_{DC} = \frac{A_{DC}}{\pi/3} = \frac{3\sqrt{2}}{\pi} U_{LL}. \quad (3.139)$$

$U_{LL}$  is the rms line to line voltage.

According to [Mohan et al. 1989], the AC-side inductance  $L_s$  will affect the average DC-link output voltage. Thus, by accounting for the inductance,  $L_s$ , the reduced DC-link voltage is given as

$$U_{DC} = \frac{3\sqrt{2}}{\pi} U_{LL} - \frac{3\omega L_s}{\pi} I_{DC} \quad (3.140)$$

$I_{DC}$  is the average DC link current.

The rectifier currents on the AC side are calculated as

$$i_d = \frac{1}{u_d^2 + u_q^2} (u_d P_{rectifier} + u_q Q_{rectifier}) \quad \text{and} \quad (3.141)$$

$$i_q = \frac{1}{u_d^2 + u_q^2} (u_q P_{rectifier} - u_d Q_{rectifier}), \quad (3.142)$$

where  $P_{rectifier}$  and  $Q_{rectifier}$  are active and reactive power of the rectifier and  $u_d$  and  $u_q$  are network voltages given in the  $d$ - and  $q$ -windings. Active power through the rectifier is found as

$$P_{rectifier} = \frac{I_{DC} U_{DC}}{\eta}, \quad (3.143)$$

where  $\eta$  is rectifier efficiency.

The reactive power is then given as

$$Q_{rectifier} = \sqrt{\left(\frac{P_{rectifier}}{PF}\right)^2 - P_{rectifier}^2}, \quad (3.144)$$

where  $PF$  is rectifier power factor.

### 3.8.2 DC-link with brake

#### Mathematical description

The DC-link consists of a large capacitance and a brake used for burning of excessive energy in the DC-link.

The DC-link voltage is calculated as

$$u_{DC} = \frac{1}{C_{DC}} \int i_{DC} dt, \quad (3.145)$$

where  $C_{DC}$  is the capacitance and  $i_{DC}$  is sum of current going in to and out from the DC-link.

The DC-link brake is necessary to avoid high voltages in the DC-link caused by sudden load changes or regenerative use of the inverters when stopping thrusters or other rotating equipment. The brake current is calculated as

$$i_{brake} = \frac{P_{brake}}{u_{DC}}, \quad (3.146)$$

where the braking power  $P_{brake}$  is limited by maximum braking power,  $P_{brake_{max}}$ . The DC-link brake is inactive when the DC-link voltage is below a predefined

maximum value.

### 3.8.3 The inverter

#### Advanced inverter model

A three phase transistor inverter is shown in Figure 3.27. Each inverter half-bridge consist of two transistor-diode pairs which will be opened and closed alternatively, meaning whenever  $S_1$  is open  $S_4$  is closed and vice versa

Assuming that each transistor-diode pair behaves like an ideal switch, they may be modeled using  $1_s$ -junctions while  $0_s$ -junctions are used to model the switching of the terminal voltages between the DC-link voltages  $u_{DC}/2$  and  $-u_{DC}/2$  [Junco et al. 2007], see Chapter 3.5.1 for switching power junction. A bond graph representation of the inverter is shown in Figure 3.28.

There are several ways of controlling the switching of the inverter, but the two far most used methods today are Direct Torque Control (DTC) and Field Oriented Control (FOC).

#### Controlling the inverter - Direct torque control

The purpose of the DTC is to control both torque and flux of the induction motor within a set of lower and upper limits. This is done by controlling the opening and closing of the 6 switches  $S_1$  to  $S_6$  according to a predefined switching table, see Table 3.1 [Buja and Kazmierkowski 2004]. The control parameters for finding the right switching sequence are error in flux and torque together with position of stator flux, thus the three variables used in the look-up table are,  $S_\psi$ ,  $S_T$  and  $S_\theta$ . When  $S_\psi = 1$ , the flux in stator windings are too low, and an increase in flux magnitude is needed, while if  $S_\psi = 0$ , the flux is too high and the magnitude has to be lowered. The torque logic variable,  $S_T$ , may have the following values, 1, 0 and  $-1$ , which represents an increase, maintain as is or a decrease in motor torque. The last variable  $S_\theta$  indicates which sector the stator flux linkage is, see Figure 3.29.

The six switches gives a total of  $2^3 = 8$  different voltage vectors, six active voltage vectors and two null vectors.

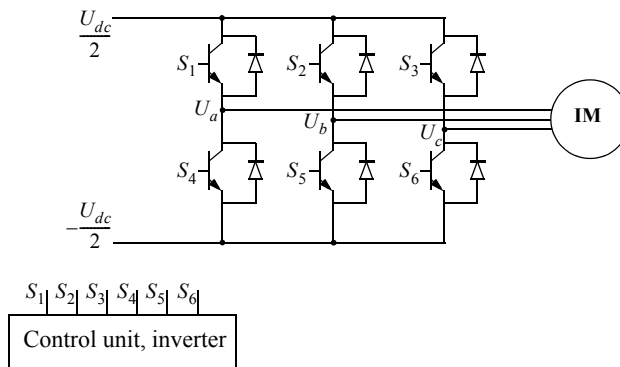


Figure 3.27: Three phase transistor inverter.

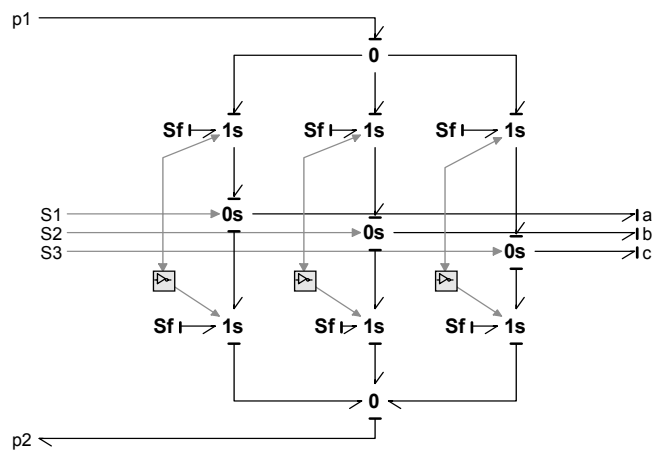


Figure 3.28: Bond graph model of the inverter [Junco et al. 2007].

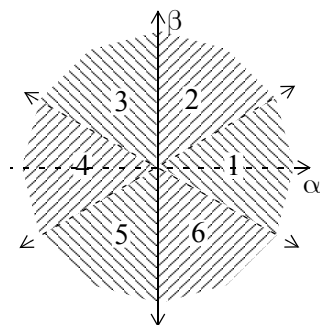


Figure 3.29: Flux linkage sectors in the  $\alpha\beta$ -frame.

$S_\psi$	$S_T$	$S_\theta$					
		1	2	3	4	5	6
1	1	(1, 1, 0)	(0, 1, 0)	(0, 1, 1)	(0, 0, 1)	(1, 0, 1)	(1, 0, 0)
1	0	(1, 1, 1)	(0, 0, 0)	(1, 1, 1)	(0, 0, 0)	(1, 1, 1)	(0, 0, 0)
1	-1	(1, 0, 1)	(1, 0, 0)	(1, 1, 0)	(0, 1, 0)	(0, 1, 1)	(0, 0, 1)
0	1	(0, 1, 0)	(0, 1, 1)	(0, 0, 1)	(1, 0, 1)	(1, 0, 0)	(1, 1, 0)
0	0	(0, 0, 0)	(1, 1, 1)	(0, 0, 0)	(1, 1, 1)	(0, 0, 0)	(1, 1, 1)
0	-1	(0, 0, 1)	(1, 0, 1)	(1, 0, 0)	(1, 1, 0)	(0, 1, 0)	(0, 1, 1)

Table 3.1 : Predefined switching table [Buja and Kazmierkowski 2004].

The three phase line voltages may be calculated and transformed to the  $\alpha\beta$ -frame by using measurement of the DC link voltage together with switch position and power invariant transformation. The  $\alpha\beta$ -frame is a two-phase stationary reference frame. Thus,  $u_{\alpha s}$  and  $u_{\beta s}$  may be written as

$$u_{\alpha s} = \sqrt{\frac{2}{3}}u_{ab} + \frac{1}{\sqrt{6}}u_{bc} \text{ and} \quad (3.147)$$

$$u_{\beta s} = \frac{1}{\sqrt{2}}u_{bc}, \quad (3.148)$$

where  $u_{ab} = u_{as} - u_{bs}$  and  $u_{bc} = u_{bs} - u_{cs}$  and  $u_{as}$ ,  $u_{bs}$  and  $u_{cs}$  are 3 phase stator voltages given in  $abc$ -frame. The currents are given in  $\alpha\beta$ -frame as

$$i_{\alpha s} = \sqrt{\frac{2}{3}}\left(i_{as} - \frac{1}{2}i_{bs} - \frac{1}{2}i_{cs}\right) \text{ and} \quad (3.149)$$

$$i_{\beta s} = \frac{1}{\sqrt{2}}(i_{bs} - i_{cs}). \quad (3.150)$$

$i_{as}$ ,  $i_{bs}$  and  $i_{cs}$  are stator currents given in  $abc$ -frame.

Compensating for the stator resistance drop, the  $\alpha$ -axis and  $\beta$ -axis stator flux linkages may be given as

$$\psi_{\alpha s} = \int(u_{\alpha} - R_s i_{\alpha s})dt \text{ and} \quad (3.151)$$

$$\psi_{\beta s} = \int(u_{\beta} - R_s i_{\beta s})dt. \quad (3.152)$$

The electromagnetic torque may then be written as

$$T_e = 3(\psi_{\alpha s} i_{\beta s} - \psi_{\beta s} i_{\alpha s}) \quad (3.153)$$

Comparing the resultant stator flux linkage  $\psi_s = \sqrt{\psi_{\alpha s}^2 + \psi_{\beta s}^2}$  with the reference value  $\psi_{s_{ref}}$  gives  $S_\psi$ .  $S_T$  is found by comparing the torque reference with the electromagnetic torque found in (3.153).  $S_\theta$  is found by using Table 3.2. [Panigrahi et al. 2006].

$A_2$	$A_1$	$A_0$	$S_\theta$
0	0	0	4
0	0	1	5
0	1	0	1
0	1	1	6
1	0	0	4
1	0	1	3
1	1	0	1
1	1	1	2

Table 3.2 : Sector look-up table [Panigrahi et al. 2006].

$A_0$ ,  $A_1$  and  $A_2$  are given as

$$A_0 = \begin{cases} 1, & |\psi_{\beta s}/\psi_{\alpha s}| \geq 1/\sqrt{3} \\ 0, & |\psi_{\beta s}/\psi_{\alpha s}| < 1/\sqrt{3} \end{cases}, \quad (3.154)$$

$$A_1 = \begin{cases} 1, & \psi_{\alpha s} > 0 \\ 0, & \psi_{\alpha s} \leq 0 \end{cases} \text{ and} \quad (3.155)$$

$$A_2 = \begin{cases} 1, & \psi_{\beta s} > 0 \\ 0, & \psi_{\beta s} \leq 0 \end{cases}. \quad (3.156)$$

The block diagram description of the controller based on direct torque control is shown in Figure 3.30 together with a bond graph representation of an inverter and an asynchronous motor including shaft, gear and propeller. The bond graph representation of the inverter is shown in Figure 3.28. For simplicity, it is assumed that the DC-link voltage is approximately constant, thus two effort sources are used to set DC-link voltage. The *Flux and torque estimator* calculates motor flux and torque using (3.151) to (3.153), while *Sector determination* is done using (3.154) to (3.156) together with Table 3.2. The motor flux and torque are compared to the reference flux and torque and the results are used together with determined sector to set desired switching pattern using Table 3.1.

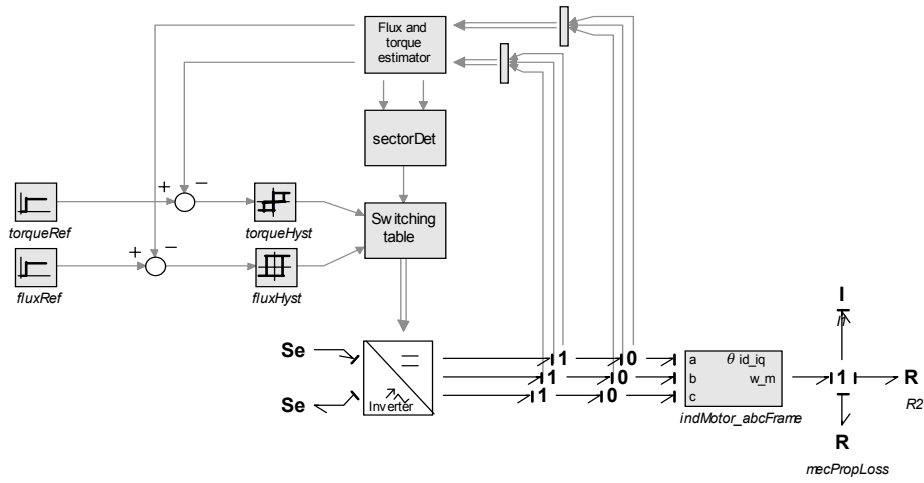


Figure 3.30: Direct torque control of an induction motor.

### Controlling the inverter - Field oriented control

Field oriented control (FOC) is another way of controlling the opening and closing of the 6 switches  $S_1$  to  $S_6$ , see e.g. [Singh et al. 2005]. By controlling the stator current and maintaining constant amplitude of rotor flux, the torque may be controlled by the torque component of the stator current.

Letting the  $dq$ -frame be fixed to the rotor flux vector rotating at synchronous speed, the equations describing the induction motor are given as (taken from Chapter 3.7),

$$u_{ds} = r_s i_{ds} - \omega_s \psi_{qs} + \dot{\psi}_{ds}, \quad (3.157)$$

$$u_{qs} = r_s i_{qs} + \omega_s \psi_{ds} + \dot{\psi}_{qs}, \quad (3.158)$$

$$0 = r_r i_{dr} - (\omega_s - \omega_r) \psi_{qr} + \dot{\psi}_{dr} \text{ and} \quad (3.159)$$

$$0 = r_r i_{qr} + (\omega_s - \omega_r) \psi_{dr} + \dot{\psi}_{qr}. \quad (3.160)$$

The flux linkages are given as

$$\psi_{ds} = L_s i_{ds} + L_m i_{dr}, \quad (3.161)$$

$$\psi_{qs} = L_s i_{qs} + L_m i_{qr}, \quad (3.162)$$

$$\psi_{dr} = L_r i_{dr} + L_m i_{ds} \text{ and} \quad (3.163)$$

$$\psi_{qr} = L_r i_{qr} + L_m i_{qs}. \quad (3.164)$$

Assuming that the resultant rotor flux  $\psi_r$  is on the direct axis only gives

$$\psi_r = \psi_{dr} \quad (3.165)$$

$$\psi_{qr} = 0 \text{ and} \quad (3.166)$$

$$\dot{\psi}_{qr} = 0. \quad (3.167)$$

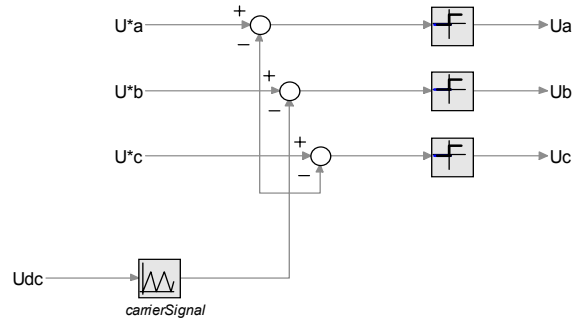


Figure 3.31: Signal flow diagram of Sub oscillation method [Schonung and Stemmler 1964].

Using (3.165) to (3.167) in (3.159) and (3.160) and letting  $\omega_{sr} = \omega_s - \omega_r$ , gives

$$r_r i_{dr} + \dot{\psi}_{dr} = 0 \quad \text{and} \quad (3.168)$$

$$r_r i_{qr} + \omega_{sr} \psi_r = 0. \quad (3.169)$$

Rewriting (3.163) and (3.164) and inserting (3.165) and (3.166) gives the rotor currents in terms of the stator currents as

$$i_{dr} = \frac{\psi_r}{L_r} - \frac{L_m}{L_r} i_{ds} \quad \text{and} \quad (3.170)$$

$$i_{qr} = -\frac{L_m}{L_r} i_{qs}. \quad (3.171)$$

Now, inserting (3.170) and (3.171) into (3.168) and (3.169) yields

$$i_{ds} = \frac{1}{L_m} \left( \psi_r + \frac{L_r}{r_r} \dot{\psi}_r \right) \quad \text{and} \quad (3.172)$$

$$\omega_{sl} = r_r \frac{L_m i_{ds}}{L_r \psi_r}. \quad (3.173)$$

Substituting the rotor currents given by (3.170) and (3.171) into the torque expression gives the electromagnetic torque as

$$T_e = \frac{L_m}{L_r} \psi_r i_{qs}. \quad (3.174)$$

The output from the FOC are  $u_a^*$ ,  $u_b^*$  and  $u_c^*$ , which are found by power invariant transformation of the controller output  $u_d^*$  and  $u_q^*$ . Next, “Sub oscillation method” [Schonung and Stemmler 1964] may be used to provide the control signal to the transistor bases  $S_1$  to  $S_6$ .  $u_a^*$ ,  $u_b^*$  and  $u_c^*$  are sinusoidal in steady state and forms a symmetrical three phase system. The three reference signals and the triangular carrier signal are compared and the logic signals  $S_1$ ,  $S_2$  and  $S_3$  are generated, see Figure 3.31.  $S_4$  to  $S_6$  are found by letting  $S_4 = 1 - S_1$ ,  $S_5 = 1 - S_2$  and  $S_6 = 1 - S_3$ .

Figure 3.32 and Figure 3.33 a) shows the reference signals together with the carrier

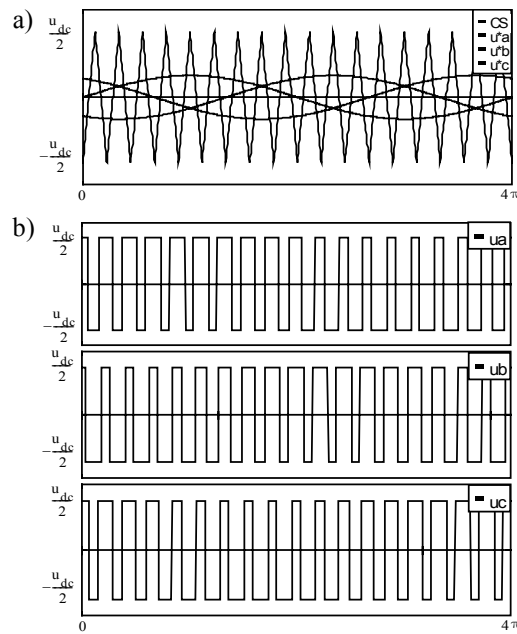


Figure 3.32: a) Reference signals and carrier signals (CS) modulation index  $m = 1/3 \cdot m_{max}$  and b) 3 phase output,  $U_a$ ,  $U_b$  and  $U_c$  from the inverter. [Schonung and Stemmler 1964].

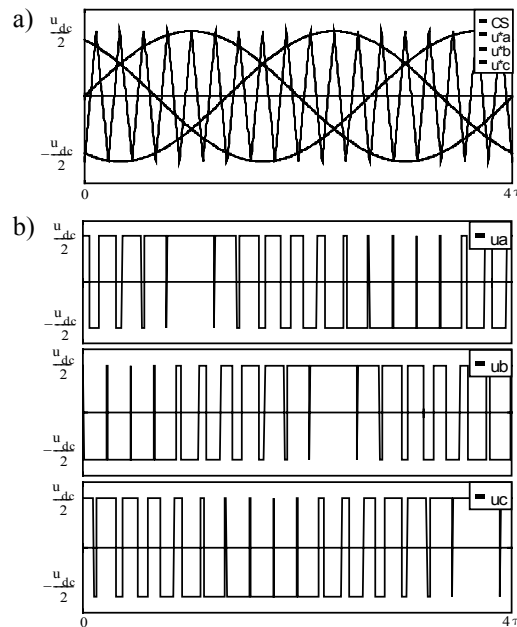


Figure 3.33: a) Reference signals and carrier signals (CS) modulation index  $m = m_{max}$  and b) 3 phase output,  $U_a$ ,  $U_b$  and  $U_c$  from the inverter [Schonung and Stemmler 1964].

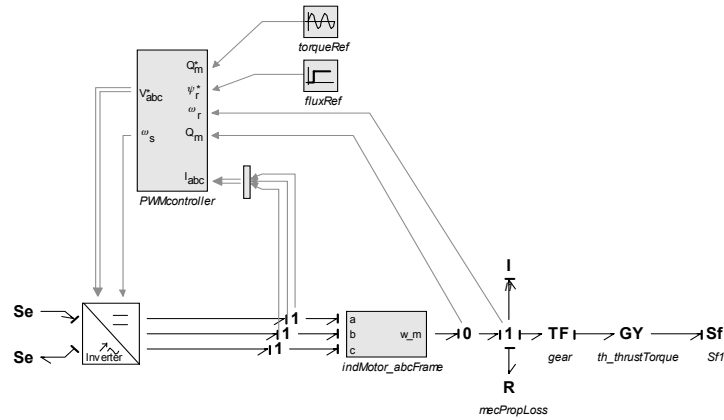


Figure 3.34: Field oriented control of an induction motor.

signal for modulation index  $m = 1/3 \cdot m_{max}$  and  $m = m_{max}$  and b) 3 phase output from the inverter. Whenever  $u_a^*$  lies above the carrier signal, the output  $u_a$  from the inverter is  $u_{dc}/2$ , otherwise it is  $-u_{dc}/2$ . The same applies for  $u_b$  and  $u_c$ .

In Figure 3.34 the direct torque controller is replaced with a controller based on field oriented control. A tachometer is necessary to determine shaft speed, while motor torque is either determined using sensors on the motor or estimated using (3.174)

Figure 3.35 shows the controller based on FOC. Three phase currents are transformed using power invariant transformation, then  $\psi_r$  is calculated using (3.172) when not accounting for flux dynamics, thus  $\dot{\psi}_r = 0$ .  $\omega_s$  is determined using rotor speed and (3.173), while  $\theta_s$  is the time integral of  $\omega_s$ . The references  $i_d^*$  and  $i_q^*$  are either found using flux and torque controllers or estimated using (3.172) and (3.174). Both flux and torque controllers are proportional integral (PI)-controllers. Two PI-controllers are used to minimize the errors in stator currents. The reference voltages  $u_d^*$  and  $u_q^*$  are transformed to three phase voltages using power invariant transformation.

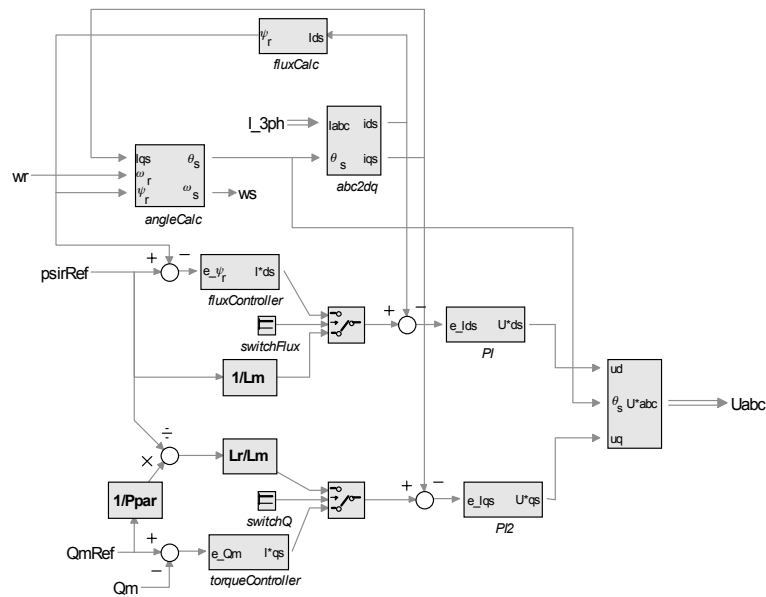


Figure 3.35: Block diagram of the field oriented controller.

### Inverter with filters

The stress on the motor increases with increasing switching frequencies which may contribute to premature winding failures and bearing currents. A lot of research have been performed and several methods have been proposed to solve the problem, see e.g. [Erdman et al. 1996], [Chen et al. 1996] and [Rendusara and Enjeti 1997]. The most common approach to overcome the problem is to use a resistance, inductance and capacitance (RLC) network at the output of the inverter, see Figure 3.36 and Figure 3.37a).

The amount of stress applied to the motor may be found by calculating the voltage harmonics at multiples of the switching frequency. By using a RLC network, the harmonics may be reduced dependent on the cut-off frequency and amount of damping added by the resistor. Increased and better filtering is obtained by reducing the cut-off frequency and increasing the damping resistance, but this will cause delays in the outer and inner control loops and reduces the system efficiency.

Another proposed method for reducing the stress on the motor is to use a inductance and capacitance (LC) trap filter in cascade with the RLC network [Sozer et al. 2000], see Figure 3.37 b). By tuning the LC trap filter to the inverter switching frequency, the filtering of the voltage harmonics at the switching frequency will become very effective, and the RLC network may then have a higher cut-off frequency and lower damping resistance. The RLC network will reduce the voltage harmonics above the switching frequency, and the output from the inverter are approximately sinusoidal voltages.

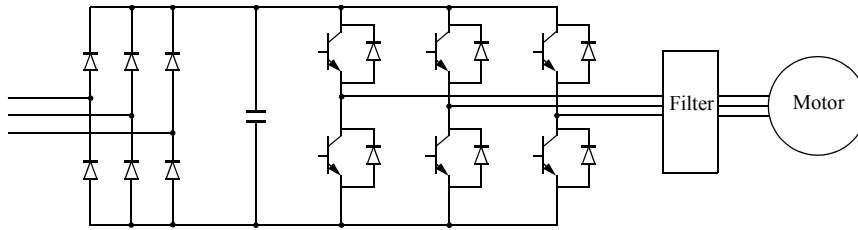


Figure 3.36: PWM converter with output filter.

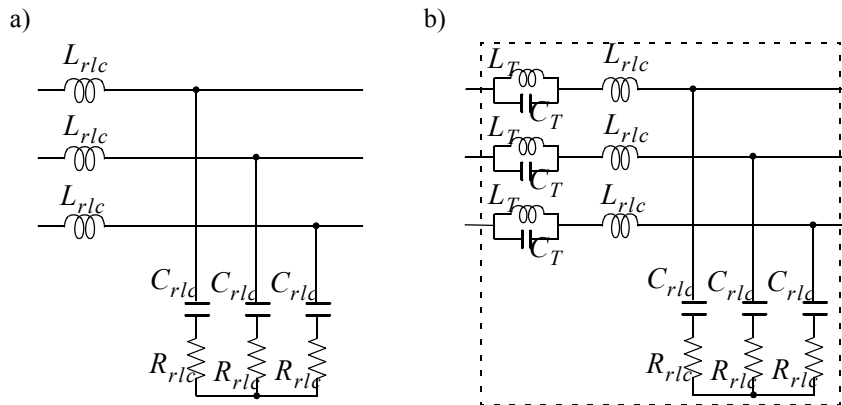


Figure 3.37: a) RLC network and b) LC trap filter in cascade with RLC network.

Assuming sinusoidal voltages leads to the average model of the inverter.

### Average model of the inverter

Using well tuned filters after the inverter gives approximately sinusoidal voltages, but the voltages will have a small phase angle compared to the reference voltages. Assuming small angles and that the thruster controller is capable of handling this phase angle, the output voltages from the average inverter will in the following be the same as the reference voltages.

Letting the inverter efficiency be a function of the power flow through the inverter and the motor rotor speed,  $\eta(P_{inv}, \omega_r)$ , the DC-link inverter current is expressed as

$$i_{DC} = \frac{P_{inv}}{u_{DC}\eta(P_{inv}, \omega_r)}, \quad (3.175)$$

when the active power of the inverter is given as

$$P_{inv} = u_d i_d + u_q i_q. \quad (3.176)$$

$u_d$ ,  $u_q$ ,  $i_d$  and  $i_q$  are inverter voltages and currents.

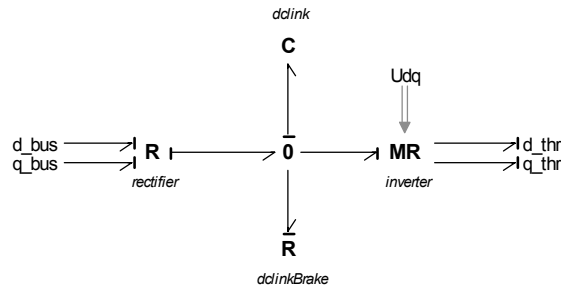


Figure 3.38: Complete model of a PWM converter.

### 3.8.4 VSI-PWM converter

#### Bond graph representation of the VSI-PWM converter

The bond graph representation of the VSI-PWM converter is shown in Figure 3.38.  $u_{dq}$ , which is the inverter output voltage vector, is the same as the reference voltage  $u^*_{dq}$  given by the FOC, when omitting transformation between  $u^*_{dq}$  and  $u^*_{abc}$ . The DTC may not be used together with the average model of the inverter since the output from the DTC directly controls the switching pattern of the real inverter and does not use a reference voltage signal to control the switching.

The  $R:rectifier$ -element calculates the current flow through the rectifier. The DC link current is calculated using (3.140), while the currents  $i_d$  and  $i_q$  drawn from the bus are given by (3.141) and (3.142). The DC-link capacitor bank, the  $C$ -element, sets the DC-link voltage using (3.145). The DC-link brake, which is used when DC-link voltage becomes too high, determines necessary brake current using (3.146). The DC-link inverter, which is represented by a  $MR:inverter$ -element, calculates the current drawn from the DC-link using (3.175) and the voltage outputs from the inverter to the thruster are the same as the reference voltage  $u^*_{dq}$  given by the field oriented controller.

## 3.9 Propeller

### 3.9.1 Mathematical description

The propeller thrust and torque are given as

$$T_a = \rho_w D^4 K_T |n|n \text{ and } Q_a = \rho_w D^5 K_Q |n|n, \quad (3.177)$$

where  $\rho_w$  is water density,  $D$  is propeller diameter and  $n$  is propeller speed in revolution per seconds (rps).  $K_T$  and  $K_Q$  are thrust and torque coefficients where the effects of thrust and torque losses are accounted for [Sørensen 2005]. For deeply

submerged propellers, the thrust and torque coefficients are generally found experimentally by open-water tests performed in a cavitation tunnel or a towing tank, and given as a function of the advance number  $J_a$ , the pitch ratio  $P/D$ , the expanded blade-area ratio  $A_e/A_0$ , number of blades  $Z$ , Reynolds number  $R_n$  and the ratio between the maximum thickness  $t$  and the chord length  $c$  of the section. The advance number is given as

$$J_a = \frac{V_a}{nD}, \quad (3.178)$$

where  $V_a$  is the inflow water velocity.

Wageningen B-series from MARIN in the Netherlands, see e.g. [Lammeren et al. 1969] or [Oosterveld and van Oossanen 1975] are probably the most known propeller series.

For a given propeller with a specific geometry, the thrust and torque coefficients may be given as a second order polynomials of  $J_a$  as,

$$K_T = K_{T0} + \alpha_{T1}J_a + \alpha_{T2}J_a|J_a| \text{ and} \quad (3.179)$$

$$K_Q = K_{Q0} + \alpha_{Q1}J_a + \alpha_{Q2}J_a|J_a|. \quad (3.180)$$

$K_{T0}$  and  $K_{Q0}$  are nominal thrust and torque coefficients assumed constant for a given propeller geometry.  $\alpha_{T1}$ ,  $\alpha_{T2}$ ,  $\alpha_{Q1}$  and  $\alpha_{Q2}$  are constants. Inserting (3.179) and (3.180) into (3.177) gives

$$T_a = T_{nn}n|n| + T_{nv}|n|V_a + T_{vv}V_a|V_a| \text{ and} \quad (3.181)$$

$$Q_a = Q_{nn}n|n| + Q_{nv}|n|V_a + Q_{vv}V_a|V_a|, \quad (3.182)$$

with

$$T_{nn} = \rho D^4 K_{T0}, \quad Q_{nn} = \rho D^5 K_{Q0},$$

$$T_{nv} = \rho D^3 \alpha_{T1}, \quad Q_{nv} = \rho D^4 \alpha_{Q1},$$

$$T_{vv} = \rho D^2 \alpha_{T2}, \quad Q_{vv} = \rho D^3 \alpha_{Q2}.$$

[Smogeli 2006] emphasizes that the quadratic polynomial representation of the propeller characteristics is only applicable in the first quadrant, due to the fact that the drop in  $K_T$  and  $K_Q$  for small negative  $J_a$  are not captured. In addition, the open water characteristics for a ducted propeller is significantly different, and less linear, than for an open propeller.

There exists various methods for representing the propeller characteristics in all four quadrants. The 4-quadrant model, first defined by [Miniovich 1960], uses the angle of attack,  $\beta$ , of the propeller blade at radius  $0.7R$  to calculate thrust and torque,

$$T_a = \frac{1}{2} \pi C_T(\beta) R^2 \rho_w V_{0.7}^2, \quad (3.183)$$

$$Q_a = \pi C_Q(\beta) R^3 \rho_w V_{0.7}^2. \quad (3.184)$$

where

$$V_{0.7} = \sqrt{V_a^2 + (0.7\omega R)^2},$$

is the undisturbed incident velocity to the propeller at radius  $0.7R$  and  $C_T(\beta)$  and  $C_Q(\beta)$  are given in [Lammeren et al. 1969] as

$$C_T(\beta) = \sum_{k=0}^{20} (A_T(k)\cos(\beta k) + B_T(k)\sin(\beta k)) \text{ and} \quad (3.185)$$

$$C_Q(\beta) = \sum_{k=0}^{20} (A_Q(k)\cos(\beta k) + B_Q(k)\sin(\beta k)). \quad (3.186)$$

$A_T(k)$ ,  $B_T(k)$ ,  $A_Q(k)$  and  $B_Q(k)$  are coefficients of a 20<sup>th</sup> order Fourier series. This representation has many advantages over the above open water characteristic, but requires much more model knowledge and necessary data may not be available. By using only the first terms in the Fourier series, a simplified 4-quadrant model may be obtained.

Overshoot in thrust and torque during transient operation are not captured by steady state theory, and for small vehicles like remotely operated vehicles (ROVs) and autonomous underwater vehicles (AUVs) this overshoot may be very important to foresee when designing efficient motion controllers [Yoerger et al. 1991]. In [Healy et al. 1995] a nonlinear thruster model is developed which capture overshoot in thrust and torque and is valid in all 4-quadrants. The ambient fluid velocity is assumed zero, then the axial thrust force on a ducted propeller in steady state operation is given as

$$T = \rho_w A l \gamma \dot{V}_p + \Delta\beta \rho_w A V_p |V_p|, \quad (3.187)$$

where  $A$  is thruster duct area,  $l$  is thruster duct length,  $\gamma$  is an added mass coefficient,  $V_p$  is axial fluid velocity at propeller and  $\Delta\beta$  is flux coefficient. The propeller thrust,  $T$ , and torque,  $Q$ , are related to propeller blade lift,  $L$ , and drag,  $D$ , as

$$T = L \cos(\theta) - D \sin(\theta) \text{ and} \quad (3.188)$$

$$Q = 0.7r(L \sin(\theta) + D \cos(\theta)), \quad (3.189)$$

where

$$\theta = \text{atan2}(V_p, V_t),$$

$$V_t = 0.7R\omega \text{ and}$$

$$\alpha = p - \theta.$$

$p$  is propeller blade average pitch. Lift and drag are calculated as

$$L = \frac{1}{2} \rho V_{tot}^2 A C_{L_{max}} \sin(2\alpha) \text{ and} \quad (3.190)$$

$$D = \frac{1}{2} \rho V_{tot}^2 A C_{D_{max}} (1 - \cos(2\alpha)), \quad (3.191)$$

when  $V_{tot} = \sqrt{V_p^2 + V_t^2}$  and  $C_{L_{max}}$  and  $C_{D_{max}}$  are lift and drag coefficients

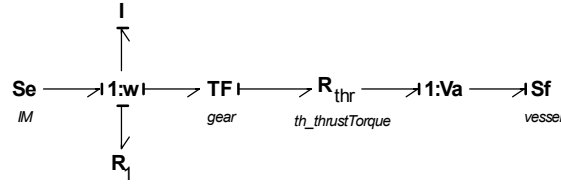


Figure 3.39: One and four quadrant propeller model based on steady state theory.

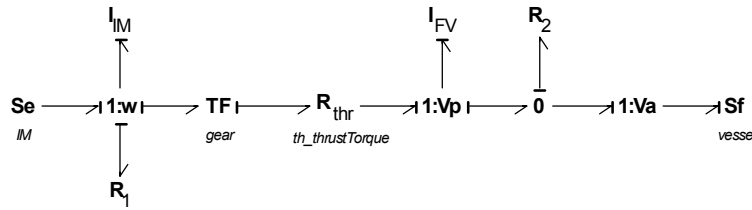


Figure 3.40: Nonlinear dynamic propeller model.

experimentally determined.

### 3.9.2 Bond graph representation of the propeller

Figure 3.39 shows a bond graph representation of one and four quadrant propeller model based on steady state theory. For simplicity, the induction motor is displayed as an effort source setting torque,  $Se_{IM}$ . The  $I_{IM}$ -element includes inertia of induction motor, shaft, gear and propeller. The  $R_1$ -element includes rotational resistances of induction motor, shaft and propeller, while the gear,  $TF$ , is assumed lossless. Thrust and torque are calculated in  $R_{thr}$  using (3.181) and (3.182) for the one quadrant model or using (3.183) and (3.184) for the four quadrant model. The flow source,  $SF:vessel$ , sets the velocity of the vessel.

The next figure shows the nonlinear dynamic model of the propeller. As for the one and four quadrant model,  $Se_{IM}$  sets torque on the shaft,  $I_{IM}$  includes inertia of induction motor, shaft, gear and propeller,  $R_1$  includes rotational resistances and  $TF$  represents lossless gear. Thrust and torque are calculated by the  $R_{thr}$ -element using (3.188) and (3.189). By rewriting (3.187),

$$\dot{V}_p = \frac{1}{\rho A l \gamma} (T - \Delta \beta \rho A V_p |V_p|), \quad (3.192)$$

and taking the integral of  $\dot{V}_p$ , the axial fluid velocity at propeller is obtained,  $I_{FV}$ . Second term of (3.192) is represented by the  $R_2$ -element. Since  $V_a$  is assumed 0, the dynamic thruster model is only valid for station-keeping operation with small current.

## 3.10 Hotel and auxiliary loads

### 3.10.1 Mathematical description

Active and reactive power may be given in the  $d$ - and  $q$ - frame as, see also Chapter 3.6,

$$P = u_d i_d + u_q i_q \text{ and } Q = -u_d i_q + u_q i_d, \quad (3.193)$$

where  $u_d$ ,  $u_q$ ,  $i_d$  and  $i_q$  are voltages and currents in  $d$ - and  $q$ -windings. Solving (3.193) with respect to  $i_d$  and  $i_q$  gives

$$i_d = \frac{1}{u_d^2 + u_q^2} (u_d P + u_q Q) \text{ and } i_q = \frac{1}{u_d^2 + u_q^2} (u_q P - u_d Q). \quad (3.194)$$

### 3.10.2 Bond graph representation of hotel and auxiliary loads

Figure 3.41 shows a bond graph representation of hotel and auxiliary loads. 3 phase network voltages are transformed to the  $dq$ -reference frame using power invariant transformation, see Chapter 3.4. The modulated resistance element  $MR$  calculates  $i_d$  and  $i_q$  using (3.194).  $u_d$  and  $u_q$  are network voltages given in the  $dq$ -reference frame and  $P$  and  $Q$  are desired active and reactive power generated in the block *loadGenerator*.  $i_d$  and  $i_q$  are transformed to 3 phase currents using power invariant transformation before entering the network.

## 3.11 Ship

### 3.11.1 Mathematical description

A marine vessel will in principle be moving in 6 degrees of freedom (DOF) since 6 independent coordinates are necessary to determine the position and orientation of the ship. It is common to only consider 3 DOF when modeling surface vessels [Fossen 1994] and the 3 degrees of freedom are motions in surge, sway and yaw (motion in x- and y-direction together with rotation about z-axis).

When analyzing the motion of marine vessels, it is convenient to define two coordinate frames, one frame that moves with the vessel, body-fixed coordinate frame, and one frame that is inertial, see Figure 3.42. For marine vessels, it is assumed that acceleration of a point on the surface of the Earth can be neglected, so a Earth-fixed reference frame  $XYZ$  can be considered to be inertial. The earth-fixed reference frame used is the North - East - Down, NED, frame. The x-axis points to the North, the y-axis to the East and the z-axis points downwards. The moving coordinate frame, the body-fixed frame, is normally placed in the centre of gravity



Figure 3.41: Bond graph representation of hotel and auxiliary loads.

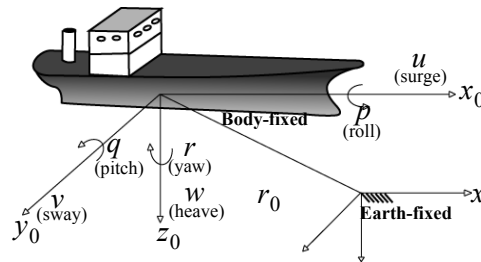


Figure 3.42: Example of earth-fixed frame and body-fixed frame [Fossen 94].

of the vessel. The axes of the body-fixed frame coincide with the principal axes of inertia, meaning that the longitudinal axis is directed from aft to fore, the transverse axis is directed to starboard and the normal axis is directed from top to bottom [Fossen 1994].

The motion of the offshore vessel is described by

$$\mathbf{M}\dot{\mathbf{v}} + \mathbf{D}\mathbf{v} = \boldsymbol{\tau}_E + \boldsymbol{\tau}, \quad (3.195)$$

$$\dot{\boldsymbol{\eta}} = \mathbf{J}(\boldsymbol{\eta})\mathbf{v}, \quad (3.196)$$

where  $\boldsymbol{\eta} = [x, y, \psi]^T$  and  $\mathbf{v} = [u, v, r]^T$ .  $x$  is the  $x$ -position and  $y$  is the  $y$ -position of the ship in earth-fixed frame while  $u$  and  $v$  are the body-fixed velocities.  $r$  is the angular velocity about the  $z$ -axis and  $\psi$  is the ships heading.  $\mathbf{M}$  denotes mass and added mass matrix while  $\mathbf{D}$  is the damping matrix. The  $\mathbf{M}$  and  $\mathbf{D}$  matrixes may be found using ship hull analyzing software like [Veres].  $\boldsymbol{\tau}_E$  is environmental forces and torques caused by wind, currents and waves while  $\boldsymbol{\tau}$  is propulsion forces and torques.  $\mathbf{J}(\boldsymbol{\eta})$  is a rotation matrix given by

$$\mathbf{J}(\boldsymbol{\eta}) = \begin{bmatrix} \cos \psi & -\sin \psi & 0 \\ \sin \psi & \cos \psi & 0 \\ 0 & 0 & 1 \end{bmatrix}. \quad (3.197)$$

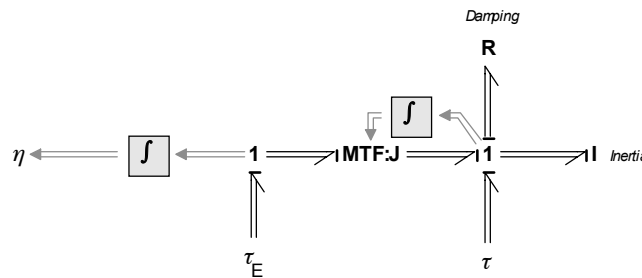


Figure 3.43: Bond graph model of an offshore vessel.

### 3.11.2 Bond graph representation of a ship

A bond graph model of an offshore vessel given by (3.195) is shown in Figure 3.43. The  $R$ -field represents the damping forces given by the damping matrix  $D$ , the  $I$ -field represents mass and added mass given by the matrix  $M$ .  $\tau_E$  and  $\tau$  are environmental forces and torques and propulsion forces and torques, given in earth fixed and body fixed reference frame, respectively. The transformation between the earth fixed and the body fixed reference frame is done with the modulated transformer,  $MTF:J$ .

In the figure, vector power bonds are used instead of single power bonds. When several power bonds are drawn from one component to another and all the bonds have the same power direction and causality, the single power bonds may be replaced by one vector power bond. The  $R$ - and  $I$ -elements are replaced with  $R$ - and  $I$ -fields.

## 3.12 Environmental loads

### 3.12.1 Mathematical description

Environmental loads may consist of loads from waves, current and wind. In this thesis only current and waves are considered, since only propeller loads are of interest.

#### Waves

Irregular waves are usually described by a wave spectrum consisting of a frequency spectrum,  $S(\omega)$ , and a directional spreading function,  $D(\psi, \omega)$  as [Myrhaug 2000]

$$S(\omega, \psi) = S(\omega)D(\psi, \omega), \quad (3.198)$$

where  $\psi$  and  $\omega$  are direction and frequency. The total energy in the sea state is given as

$$S_{tot} = \int_0^\infty \int_0^{2\pi} S(\omega, \psi) d\psi d\omega. \quad (3.199)$$

By assuming linearity it is possible to superimpose the harmonic wave components extracted from the spectrum [Sørensen 2005]. Then, by dividing the frequency spectrum and the directional spreading function using constant frequency and direction intervals, the amplitude of one wave,  $\zeta_{a_{ij}}$ , given by the frequency  $\omega_i$  and direction  $\psi_j$ , is determined by

$$\zeta_{a_{ij}} = \sqrt{2S(\omega_i, \psi_j)\Delta\omega\Delta\psi}. \quad (3.200)$$

The surface elevation may be given in the earth fixed reference frame, see Chapter 3.11, as

$$\zeta_{ij}(x, y, t) = \zeta_{a_{ij}} \sin(\omega_i t + \phi_{ij} - k_i(x \cos(\psi_j) + y \sin(\psi_j))), \quad (3.201)$$

where  $\phi_{ij}$  is the phase angle,  $k_i$  is given by  $k_i = 2\pi/\lambda_i$  where  $\lambda_i$  is the wave length. For deep waters,  $k_i = \omega_i^2/g$  where  $g$  is the acceleration of gravity.  $x$  and  $y$  are wave position in the earth fixed reference frame. By superposition, the total surface elevation may be found as

$$\zeta(x, y, t) = \sum_{i=1}^n \sum_{j=1}^m \zeta_{a_{ij}} \sin(\omega_i t + \phi_{ij} - k_i(x \cos(\psi_j) + y \sin(\psi_j))). \quad (3.202)$$

$n$  and  $m$  are total number of frequencies and directions.

Different wave spectrum may be used for calculating surface elevation, the most common are the Pierson-Moskowitz, PM, spectrum, the ITTC/ISSC spectrum and the JONSWAP spectrum [Sørensen 2005]. For fully developed sea, the frequency spectrum may be written as

$$S(\omega) = \frac{A}{\omega^5} e^{-\frac{B}{\omega^4}}, \quad (3.203)$$

where  $A$  and  $B$  are given as

$$A = 0.0081g^2 \text{ and } B = 0.74\left(\frac{g}{V}\right)^2 \quad (3.204)$$

for the Pierson-Moskowitz spectrum.  $V$  is the average wind velocity at 19.5 m above sea surface. For open seas, ITTC and ISSC recommends the use of Modified Pierson-Moskowitz spectrum that gives the following values for  $A$  and  $B$ ,

$$A = 487H_s^2\omega_p^4 \text{ and } B = \frac{5}{4}\omega_p^4, \quad (3.205)$$

where  $H_s$  is significant wave height and  $\omega_p$  is peak wave frequency.

The last spectrum mentioned here is the JONSWAP spectrum which is a spectrum for not fully developed seas. The peak is sharper than for the PM and Modified PM spectrums. According to [Hasselmann 1973], the JONSWAP spectrum may be written as

$$S(\omega) = \alpha \frac{g^2}{\omega^5} e^{\left(-\frac{5}{4} \left(\frac{\omega_p}{\omega}\right)^4\right)} \gamma e^{-\frac{1}{2} \left(\frac{\omega - \omega_p}{\sigma \omega_p}\right)^2}, \quad (3.206)$$

where  $\alpha$ ,  $\gamma$  and  $\sigma$  are parameters to be determined. The following values are recommended by [Faltinsen 1990],

$$\gamma = 3.3, \sigma = \begin{cases} 0.07 & (\omega \leq \omega_p) \\ 0.09 & (\omega > \omega_p) \end{cases} \text{ and } \alpha = 0.2 \frac{H_s^2 \omega_p^4}{g^2}.$$

A comparison between the PM, the modified PM and the JONSWAP spectrums are shown in Figure 3.44. Significant wave height,  $H_s$ , is set to 7 and peak wave frequency,  $\omega_p$ , is calculated using

$$\omega_p = \frac{2\pi}{(4.883 + 2.68H_s^{0.54})}, \quad (3.207)$$

which are based on statistical North Sea data, NORSOK.

In [Faltinsen 1990] it is found that  $x$ ,  $y$  and  $z$  component of the wave velocity for infinite water depths are given as

$$u = \sum_{i=1}^n \sum_{j=1}^m \sin(\omega_i t + \phi_{ij} - k_i \Psi_j) \cos(\psi_j) \zeta_a e^{-iz} \omega_i, \quad (3.208)$$

$$v = \sum_{i=1}^n \sum_{j=1}^m \sin(\omega_i t + \phi_{ij} - k_i \Psi_j) \sin(\psi_j) \zeta_a e^{-iz} \omega_i \text{ and} \quad (3.209)$$

$$w = -\sum_{i=1}^n \zeta_a e^{-iz} \omega_i \cos(\omega_i t + \phi_{ij} - k_i \Psi_j), \quad (3.210)$$

where  $\Psi_j = x \cos(\psi_j) + y \sin(\psi_j)$  is direction of wave propagation.

## Currents

[Sørensen 2005] states that it is sufficient to use a 2-dimensional current model when modeling surface vessels. Describing the current by magnitude  $V_c$  and direction  $\psi_c$  given in the NED reference frame, the current velocity vector is given as

$$\mathbf{v}_c = \begin{bmatrix} V_c \cos(\psi_c) & V_c \sin(\psi_c) & 0 \end{bmatrix}^T. \quad (3.211)$$

By using a 1st order Gauss-Markov Process with Gaussian white noise,  $\omega$ , and  $\mu \geq 0$ , the variation in current velocity may be given as [Fossen 2002]

$$\dot{V}_c + \mu V_c = \omega. \quad (3.212)$$

$V_c$  should be restricted by saturation elements such that

$$V_{c_{min}} \leq V_c \leq V_{c_{max}}. \quad (3.213)$$

The variation in current direction may be given in a similar way.

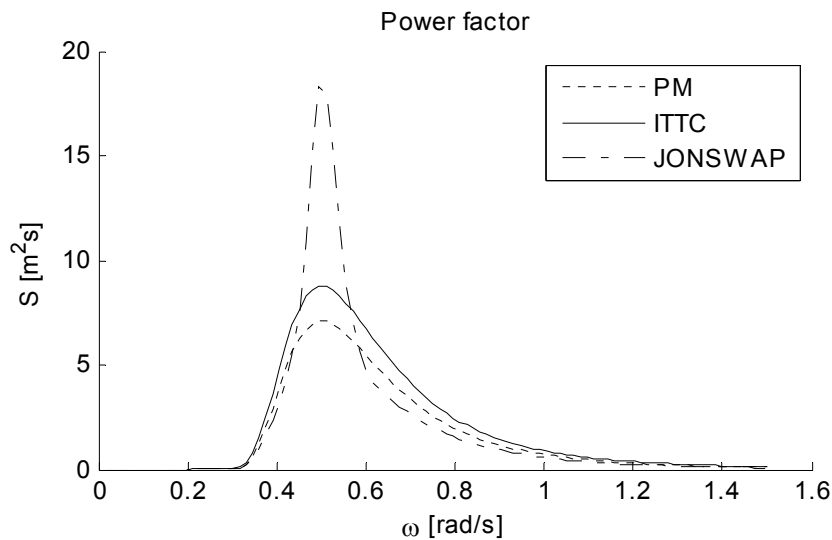


Figure 3.44: Comparison of different spectrums.

### 3.12.2 Bond graph representation of waves and current loads

A bond graph representation of a vessel including thruster and environmental loads is shown in Figure 3.45. Instead of letting the environmental loads be represented by forces and torques given in NED reference frame, the environmental loads is modeled as change in inflow velocity to the propeller. Local wave velocities are given by (3.208) to (3.210), while the currents are given according to (3.211). The stern thruster is normally not placed in the mass center of the ship and a transformation of velocities, rotations, forces and moments must then be done between the local coordinate frame of the stern thruster and the vessel. In addition, if the thrusters are used as steering gear, the thruster is able to rotate an angle  $\delta$  [rad]. The transformer,  $TF$ , and the modulated transformer,  $MTF$ , in Figure 3.45 transform velocities, rotations, forces and moments between the stern thruster and the ship based on placing and rotation of thruster. Input to the modulated transformer will be the thruster angle  $\delta$ .

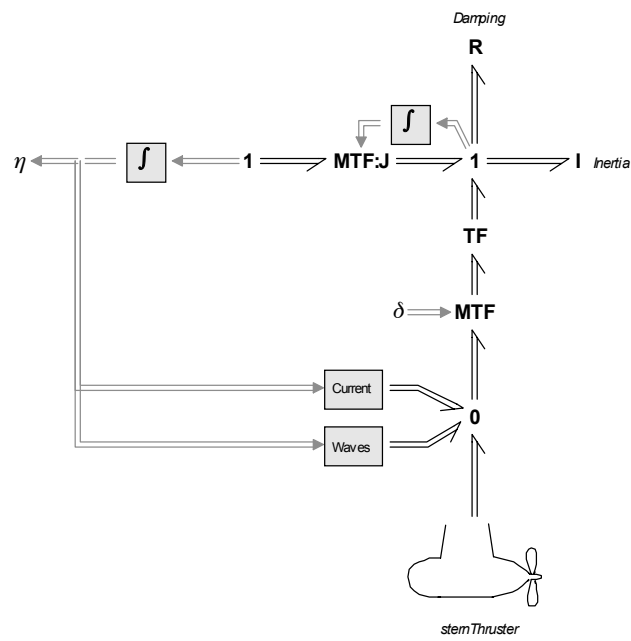


Figure 3.45: Waves and current loads.

## Chapter 4

### Model verification

The model components discussed in Chapter 3 are implemented in 20-sim [20-sim 2006]. Several simulations are accomplished to check the behaviour of the component models. Simulation results are verified using test results obtained from manufacturers. Full scale measurements obtained from Viking Energy, a supply ship operated by Eidesvik [Eidesvik 2008] for StatoilHydro in the North Sea are also used as a reference for the simulations.

Full scale measurements were accomplished during a two day round trip between several oil drilling platforms. The weather was calm and the significant wave height  $H_s$  was not more than 1 [m]. The principal dimensions of the ship are: overall length 94.9 [m], breadth 20.4 [m] and summer draught 7.9 [m]. The full scale measurements are tabulated in Appendix E.

#### 4.1 Generator

##### 4.1.1 Verifying excitation data

The purpose of the first simulation is to verify generator excitation data. The parameters of the generator are calculated using a technical specification scheme of the generator obtained from the manufacturer. Stator and rotor resistances were not found, thus they were assumed.

Appendix C.2 gives a procedure for calculation of generator parameters based on manufacturer data.

##### System setup

The system setup used for verifying excitation data given for a generator is displayed in Figure 4.1. Engine dynamics are not considered, thus a flow source  $Sf:\omega$  sets generator shaft speed. The shaft speed is assumed constant.

The generator model used in this simulation is shown in Figure 3.5, while the block *otherLoads* is modeled according to Chapter 3.10. Reference voltage magnitude is

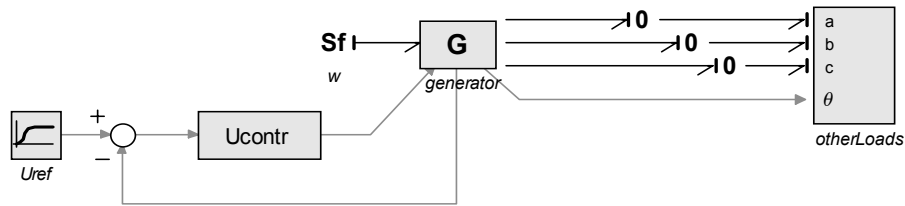


Figure 4.1: System setup for verifying excitation data.

	No load	Rated load
Rated output [kVA]	0	2438
P [kW]	0	1950
Q [kVAr]	0	1463
PF [-]	0	0.8

Table 4.1 : Load data.

DC excitation voltage			
	Given	Simulation	Deviation [%]
No load	38.0	35.6	6.3
Rated load	79.2	78.9	0.4

Table 4.2 : DC excitation voltage.

held constant after an initial startup phase. An ordinary PI controller has been used for controlling the generator voltage.

## Simulation

Generator load data are presented in Table 4.1. The voltage reference used in the simulation is presented in Figure 4.2, while Figure 4.3 shows the amount of active and reactive power drawn from the bus with resulting power factor shown in Figure 4.4.

Table 4.2 and Figure 4.5 present necessary magnetization voltage at zero and rated load. The table show static values. The results show a small deviation of necessary excitation voltage at no load, while the deviation at rated load is insignificant.

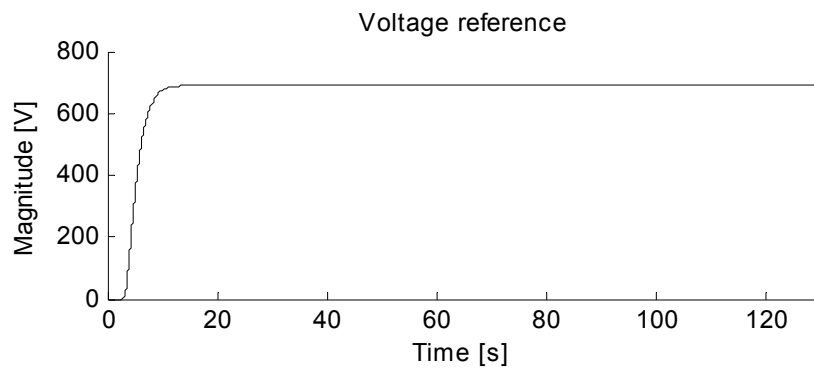


Figure 4.2: Voltage reference.

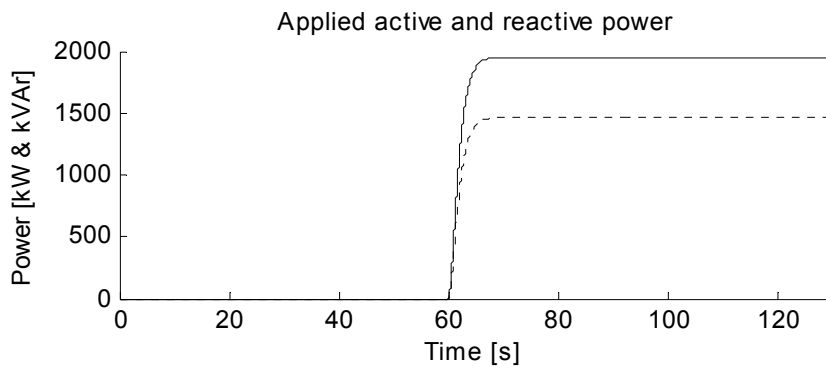


Figure 4.3: Applied active (—) and reactive power (---).

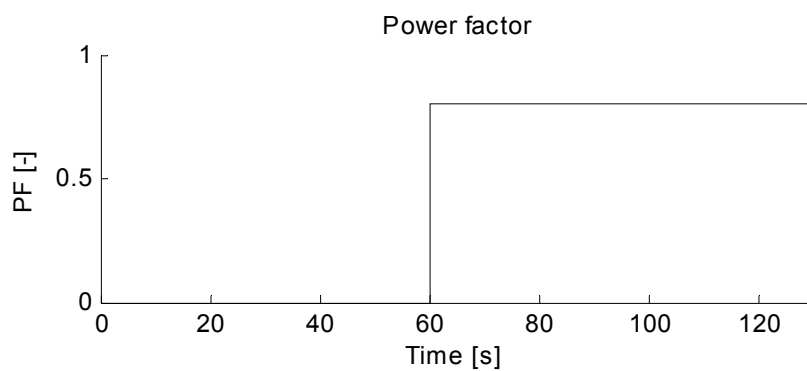


Figure 4.4: Power factor.

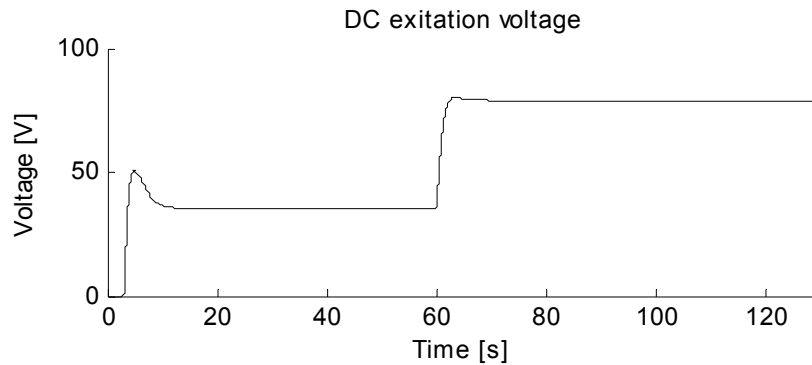


Figure 4.5: DC excitation voltage.

## Conclusion

There may be several reasons for the deviation at no load. Hysteresis and magnetic saturation are not included in the model. In addition, stator and rotor resistances were not given. The resulting excitation voltage is slightly dependent on these resistances.

## 4.1.2 Magnetic saturation

### System setup

Magnetic saturation has been incorporated in the synchronous generator model using method II, see Chapter 3.3.3, proposed by [Corzine et al. 1998]. A comparison between an unsaturated and a saturated generator model has been done using the system setup shown in Figure 4.6. The generators were not loaded and the shaft speed was assumed constant. Several simulations were accomplished where only the DC excitation voltage was altered.

Figure 4.8 shows the same system setup used when the excitation data were verified, but now the unsaturated synchronous generator model has been replaced by the generator model accounting for magnetic saturation. The load profile is the same as used in Chapter 4.1.1.

### Simulation

By accomplishing several simulations with constant shaft speed, no load applied to the generators and only altering the DC excitation voltage between each simulation, it was possible to compare the saturated and unsaturated synchronous generator models with each other. In Figure 4.8, the stator  $\psi_d$  is plotted as a function of field current  $I_f$  for both the unsaturated (—) and the saturated (---) generator model. It

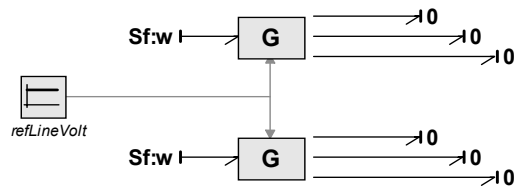


Figure 4.6: Saturated versus unsaturated synchronous generator model.

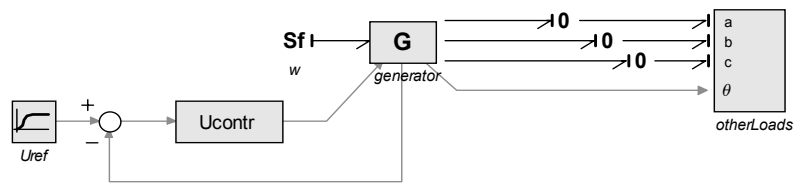


Figure 4.7: Verifying excitation data using saturated synchronous generator model.

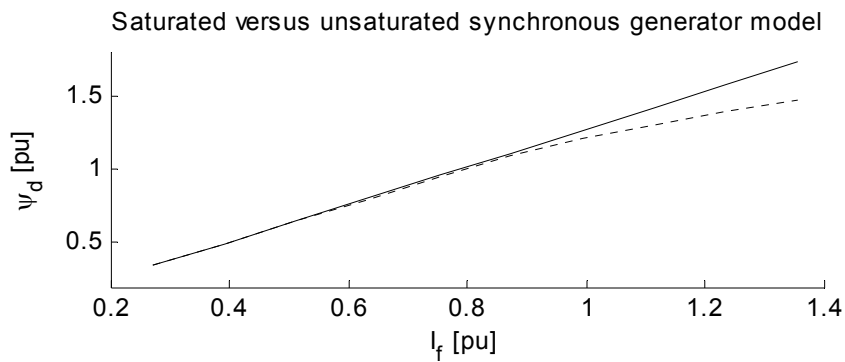


Figure 4.8: Saturated (--) versus unsaturated (—) synchronous generator model.

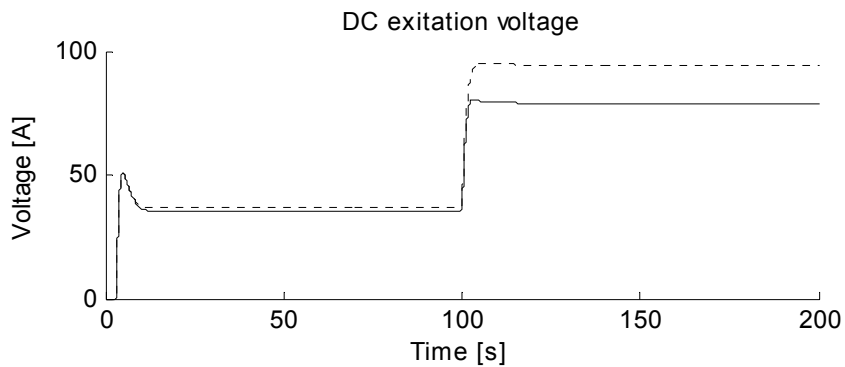


Figure 4.9: DC excitation voltage at 0 and rated load for unsaturated (—) and saturated (--) synchronous generator model.

	Power [kVA]	Given excitation value [V]	Unsaturated excitation voltage [V]/[%]	Saturated excitation voltage [V]/[%]
Zero load	0	38.0	35.6 / 6.3	37.2 / 2.1
Rated output [kVA]	2438	79.2	78.9 / 0.4	94.4 / 16.1

Table 4.3 : DC excitation voltage.

has not been possible to obtain measurements from the actual generator where the saturation effects appear, therefore the saturation shown in Figure 4.8 is based on assumed values only.

Figure 4.9 shows a comparison of DC excitation voltage between the unsaturated (—) and saturated (--) synchronous generator model at 0 and rated load. The comparison is tabulated in Table 4.3.

## Conclusion

The simulations show that magnetic saturation affects both generator flux linkages and excitation voltage, but it is difficult to determine to what the extent the influence will be since only assumed values for the saturation are used in the simulation.

As previous mentioned, stator and rotor resistances were not given by the manufacturer, instead the values were found by trial and error with the unsaturated generator model. If the resistances as an alternative had been found using the saturated generator model, maybe the conformity between given and simulated excitation voltages would have been better.

Since it was uncertainty in connection with both the resistances and saturated values the unsaturated generator model has been used in later simulations, but if better data for resistances and magnetic saturation had been found, the saturated generator model could have been used instead.

### 4.1.3 Synchronization of three phase generator to bus

#### System setup

The system setup used for simulating synchronization of a three phase generator to bus is shown in Figure 4.10. The primary generator, named *G1*, sets voltages which are input to both secondary generator, named *G2*, and the *otherLoads* block. Measurements from a supply vessel are used for the load module. At startup, only *G1* is running. After a while, the power management system will give a start signal to generator set 2. The generator set will start synchronizing to the bus to obtain same frequency, phase voltage and voltage as the bus before connecting to the bus. After the generator is connected, the two generators will start sharing load, both

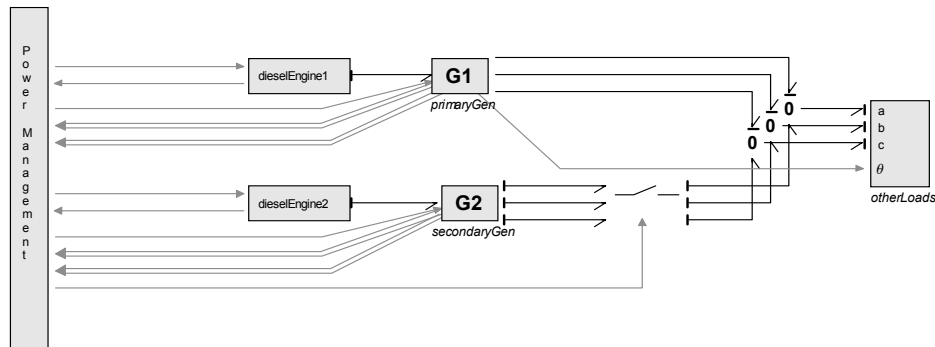


Figure 4.10: System setup for synchronization of three phase generator to bus.

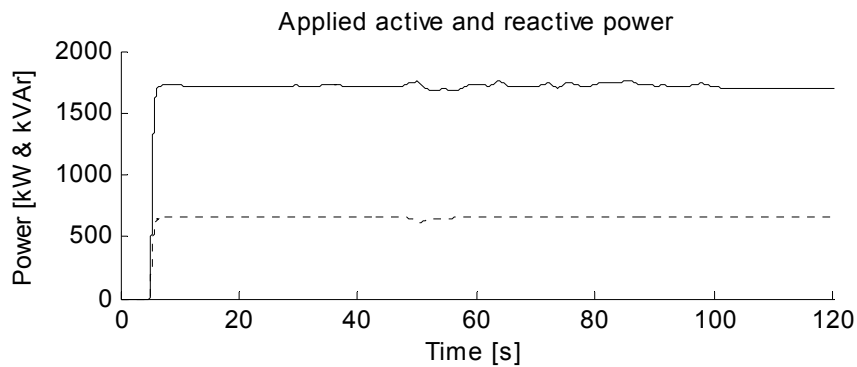


Figure 4.11: Applied active (—) and reactive power (--).

active and reactive. The results are compared with measurements from the supply vessel.

### Simulation

Measurements from a supply vessel, see Appendix E.1, are used as reference for the consumers, see Figure 4.11. Generator set 1 is started at the beginning of the simulation, and active and reactive loads are applied when generator 1 reach rated voltage,  $U = 690$  [V]. After some time, generator set 2 is set to start, it speeds up and the voltage of generator 2 approaches the bus voltage, see Figure 4.12.

The last 2 figures, Figure 4.13 and Figure 4.14, present active and reactive load sharing. The generators start sharing load after generator 2 is connected to the bus.

### Conclusion

The simulation was accomplished to check if the system models are able to reproduce the results from a real system when a generator set is set to synchronize and connect to a bus before load sharing is started.

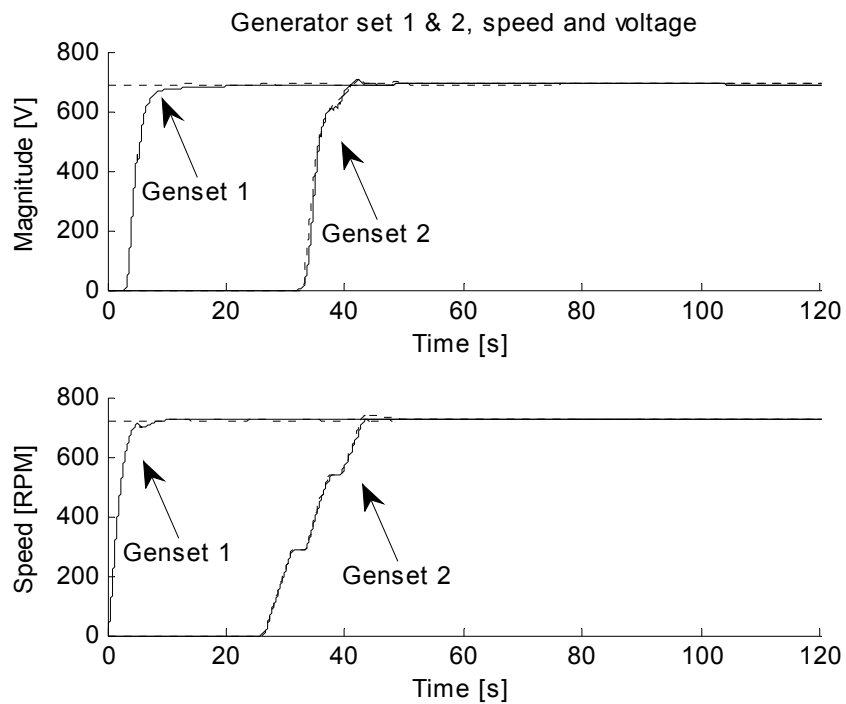


Figure 4.12: Speed and voltage for generator set 1 and 2. Results from simulation (—) and measurements obtained from Viking Energy (--).

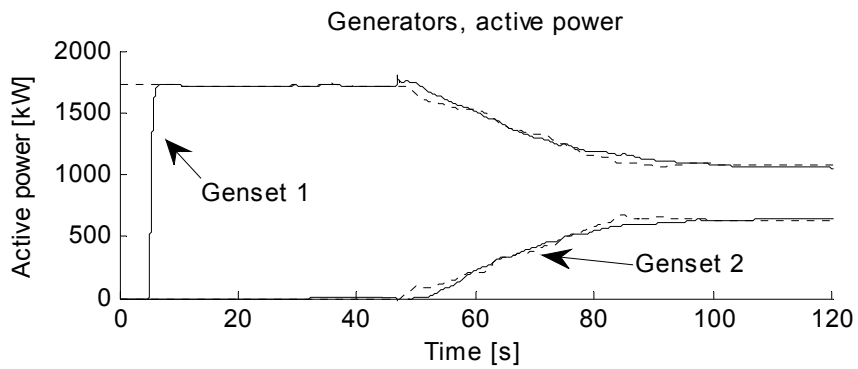


Figure 4.13: Active power sharing between generator 1 and 2. Results from simulation (—) and measurements obtained from Viking Energy (--).

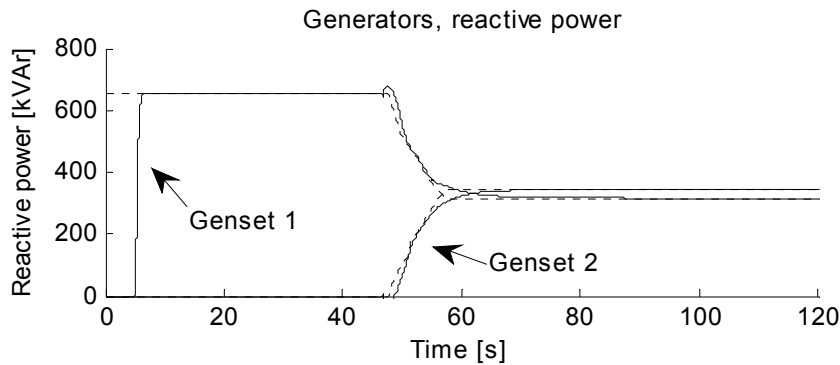


Figure 4.14: Reactive power sharing between generator 1 and 2. Results from simulation (—) and measurements obtained from Viking Energy (--).

The simulation results show good accordance with the full scale measurements. The load sharing between the generator sets on board this supply vessel will normally not be equally just after connection of another generator to the bus. The reason for this is that the newly started generator set is operated on diesel at startup. After synchronization and stable running of the connected generator at some load, the fuelling will change from diesel to gas, then the generator sets connected to the bus will be operated with equally load sharing.

## 4.2 Fuel cell

The purpose of this chapter is to check out the behaviour of the fuel cell model. The first simulation is accomplished with a stand alone fuel cell connected to a slowly varying load. In the second simulation, a generator and a fuel cell is connected to a common bus with a time varying load.

### 4.2.1 Stand alone fuel cell

#### System setup

The system setup for the stand alone fuel cell is presented in Figure 4.15. The fuel cell block contains the fuel cell model presented in Chapter 3.6. The bond graph element *MR* is a modulated resistance element which calculates the stack current based on desired power output of the fuel cell. For simplicity, the stack current is modeled using a first order transfer function which takes the electrical response time of the fuel cell into account.

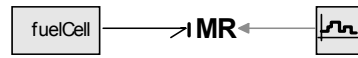


Figure 4.15: System setup for stand alone fuel cell.

Time [sec]	0	500	1000	1500	2000	2500
Power demand [kW]	50	75	100	50	25	35

Table 4.4 : Fuel cell power demand.

### Simulation

The stand alone fuel cell is simulated with varying load demand as shown in Table 4.4 and Figure 4.15. A close-up of the fuel cell output power is shown in lower part of Figure 4.16. At  $t = 500$  [s], the load demand is increased from 50 [kW] to 75 [kW], and the figure shows that the fuel cell needs approximately 40 seconds before delivering desired power.

The next figure, Figure 4.17, shows fuel cell voltage and current. It may be noticed that the voltage decreases as the current and power output increases. Partial pressure of oxygen and hydrogen are presented in Figure 4.18.

### Conclusion

A stand alone fuel cell model has been simulated to investigate the behaviour of the model when varying the load demand. The simulation results have been compared to results presented in several papers, e.g. [EL-Sharkh et al. 2004] and [Zhu and Tomsovic 2002].

The comparison show that the fuel cell model behaves as expected. A fuel cell is not able to increase power output instantly, thus some kind of auxiliary power should be installed together with the fuel cell to take sudden load changes. A decrease in fuel cell voltage when fuel cell current and power output increases, was also observed in the above mentioned papers.

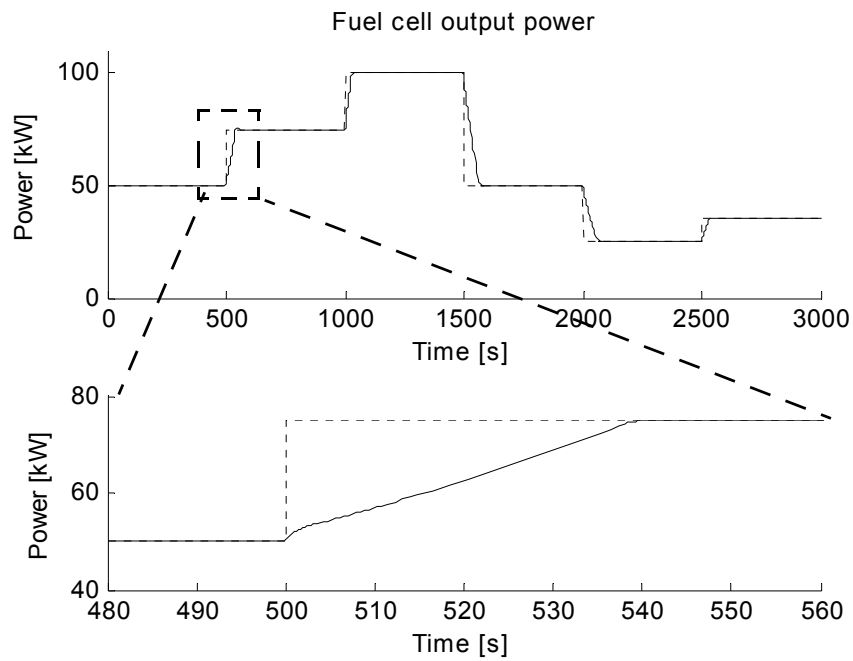


Figure 4.16: Fuel cell output power,  $P_{ref}$  (--) and  $P_{fc}$  (—).

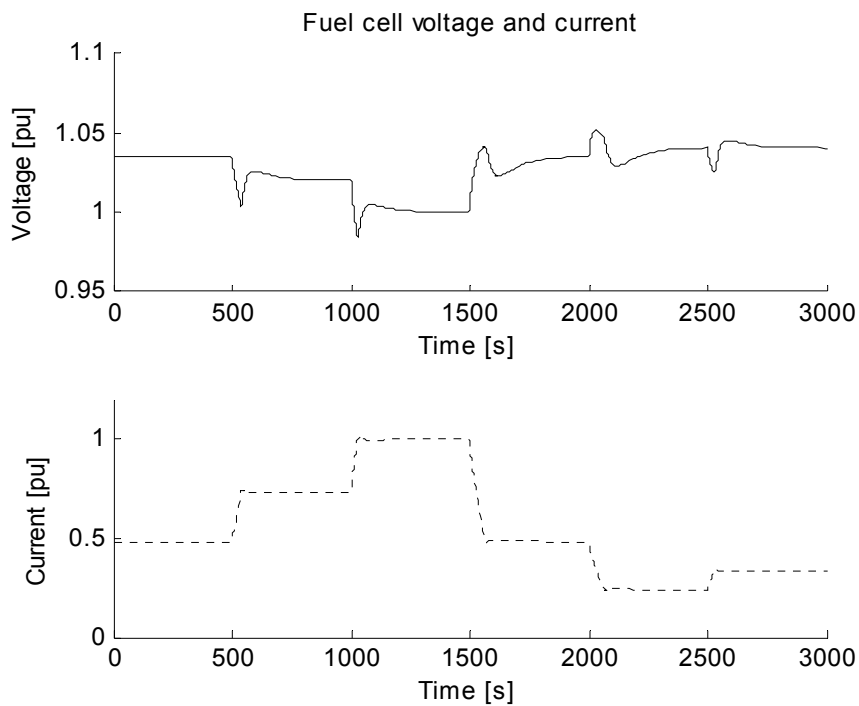


Figure 4.17: Fuel cell voltage (—) and current (--).

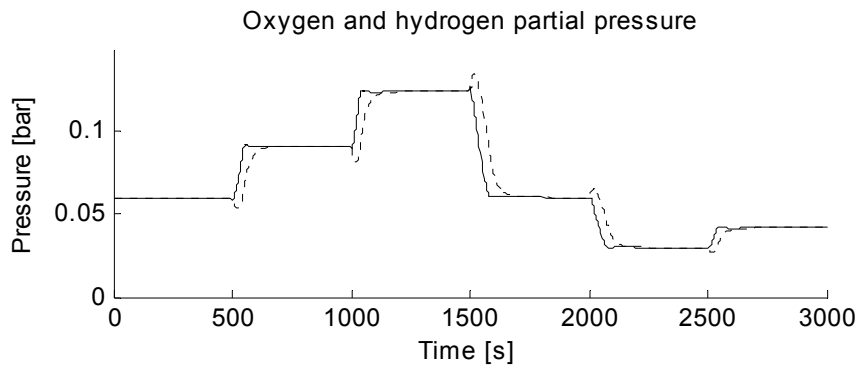


Figure 4.18: Partial pressure of oxygen (—) and hydrogen (--).

## 4.2.2 Fuel cell and grid

### System setup

Figure 4.19 shows a power plant consisting of one generator set and a fuel cell. The power control system ensures desired voltage and frequency on the bus, and at the same time the load allocation between the generator set and the fuel cell. The diesel engine and the generator are modeled according to Chapter 3.1 and Chapter 3.2. The fuel cell together with the converter and transformer are presented in Chapter 3.6, while the *loadModule* is taken from Chapter 3.10. The power system is modeled in the  $dq$  reference frame of the generator.

### Simulation

Maximum power generation using only the generator set is 1950 [kW], while the fuel cell is set to produce between 50 and 400 [kW]. Figure 4.20 to Figure 4.25 show the simulation results when the following events appeared:

From  $t = 0$  [s] to  $t = 1000$  [s] the applied active power consumption is gradually increased such that the generator set is eventually running on optimum loading, 80%, with only minimum power production from the fuel cell. Optimum loading is defined as the loading with minimum fuel consumption per produced kWh.

Between  $t = 1000$  [s] and  $t = 4000$  [s], the power output from the fuel cell is controlled such a way that the generator set is running on 80% loading. If the load demand for the fuel cell is outside the operation range of the fuel cell, the generator will not have optimum loading.

Between  $t = 4000$  [s] and  $t = 6000$  [s], the power output from the fuel cell is controlled independent of the generator loading. The fuel cell follows a predefined power output reference, while the generator must take the load variation.

At last, from  $t = 6000$  [s] to  $t = 8000$  [s], the active power consumption is held constant while the reactive power is changing. The Fuel cell has up to now only produced real power, but it may also deliver reactive power to the bus by controlling

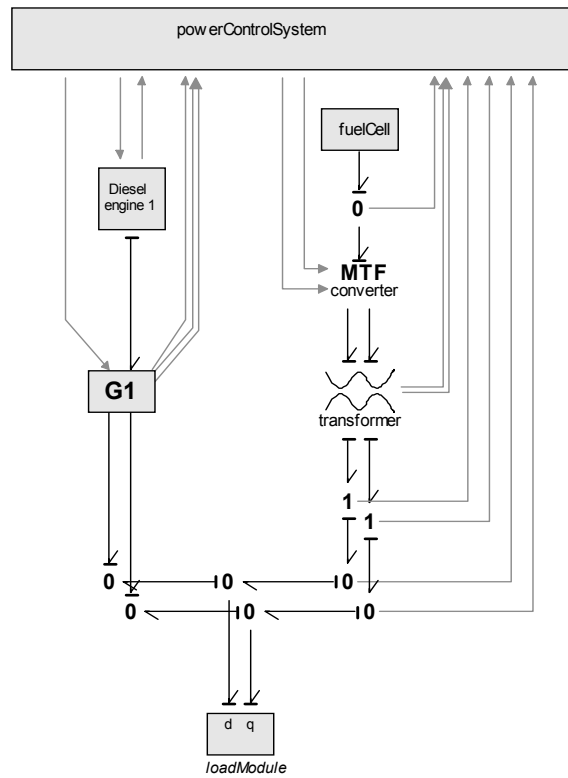


Figure 4.19: System setup for a bus-connected fuel cell.

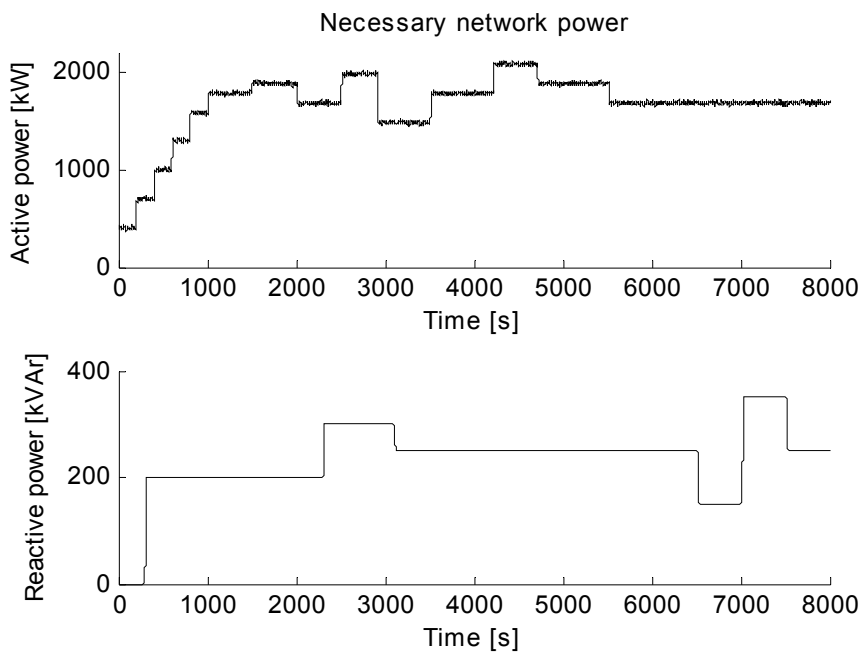


Figure 4.20: Necessary active and reactive network power.

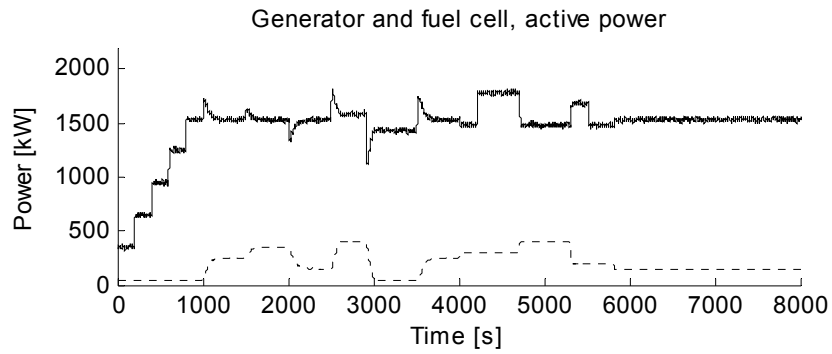


Figure 4.21: Active power production, generator (—) and fuel cell (--).

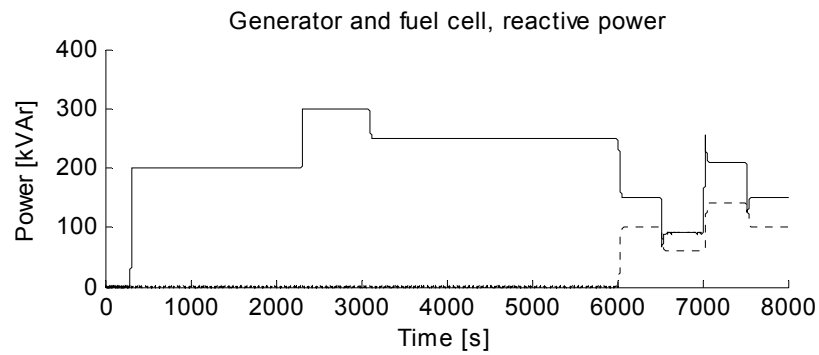


Figure 4.22: Reactive power production, generator (—) and fuel cell (--).

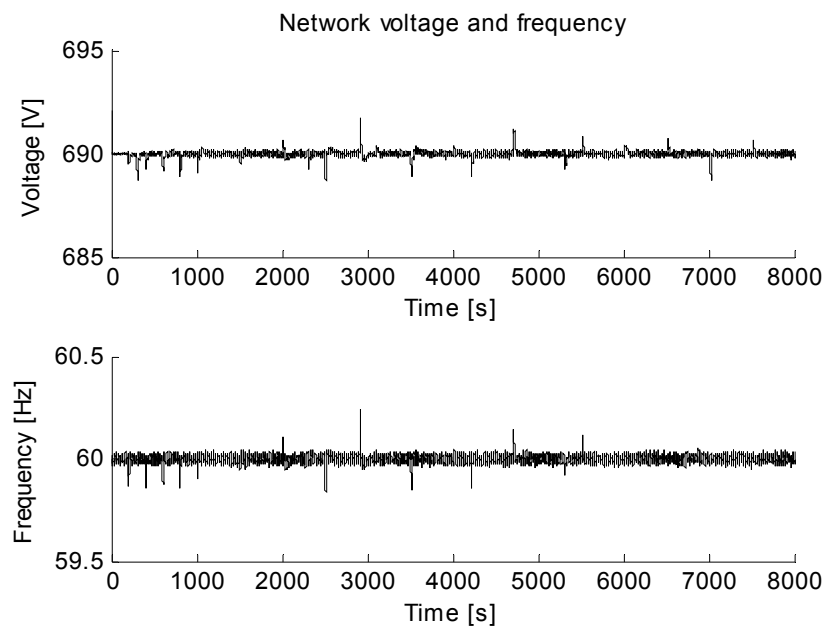


Figure 4.23: bus voltage and frequency.

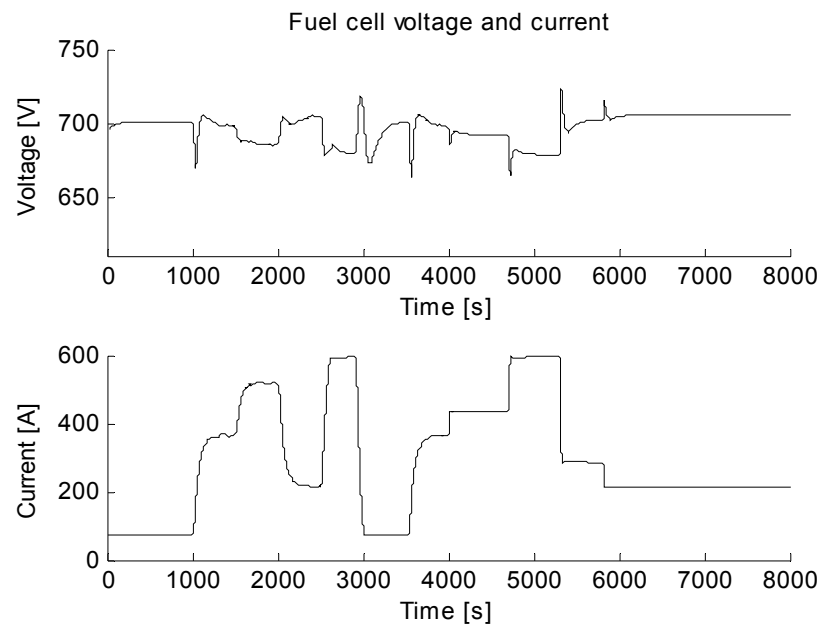
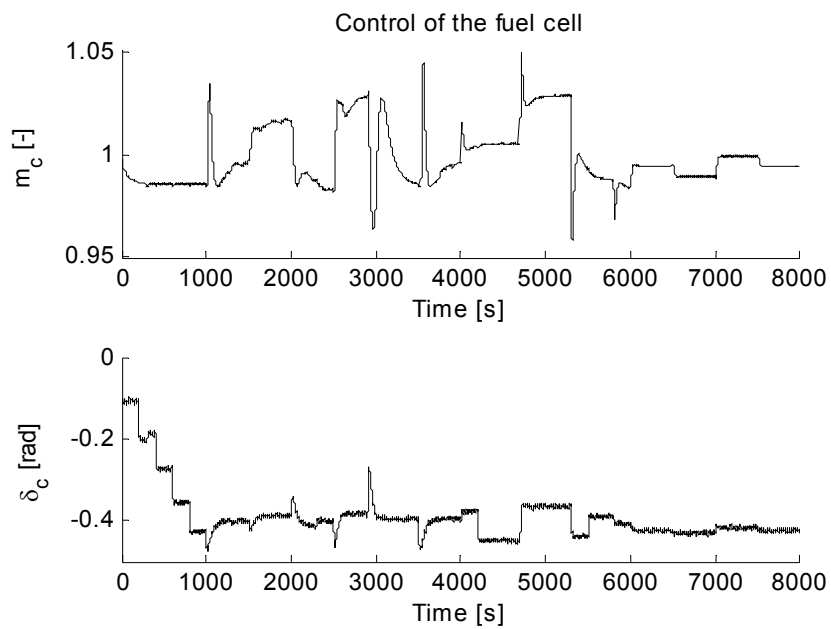


Figure 4.24: Fuel cell voltage and current.

Figure 4.25: Converter modulation index  $m_c$  and phase angle  $\delta_c$ .

the modulation index and phase angle of the converter.

## Conclusion

The motivation for doing the previous simulation was to show how a generator set and a fuel cell could be combined into one power plant and to show different control strategies for the power reference for the fuel cell.

As already mentioned, the fuel cell is unable to take sudden load changes, so fast load transient must be taken by the generator. Still, the fuel cell could be operated to give optimal fuel consumption for the generator. If for example the generator loading is higher than the loading giving lowest fuel consumption per produced kW, the power reference for the fuel cell could be slowly increased, such that the loading on the generator is reduced.

## 4.3 Asynchronous motor

### 4.3.1 Verifying asynchronous motor data

#### System setup

The asynchronous motor has been verified against data from a no-load test, short-circuit test and rated output test of an actual asynchronous motor. The data are obtained from the manufacturer of the selected motor. See Appendix D for a procedure for calculating model parameters based on manufacturer data.

Figure 4.26 shows the system setup. Power invariant transformation is described in Chapter 3.4, while the asynchronous motor is given in Chapter 3.7. The induction motor is modeled in synchronous rotating reference frame. The  $I$ -element represent motor and shaft inertia and the  $R$ -elements *rotLoss* and *load* represent rotational loss and load.

#### Simulation, no-load test

The no-load test is accomplished as follows. The machine runs on no-load with a free shaft extension at rated voltage and frequency. Readings of stator voltage, stator current and active power are measured at nominal voltage and given in Table 4.5.

Figure 4.27 shows the following results from the simulation, motor real power  $P$ , power factor  $PF$ , rms value of motor current  $I_{rms}$  and shaft speed  $\omega$ .

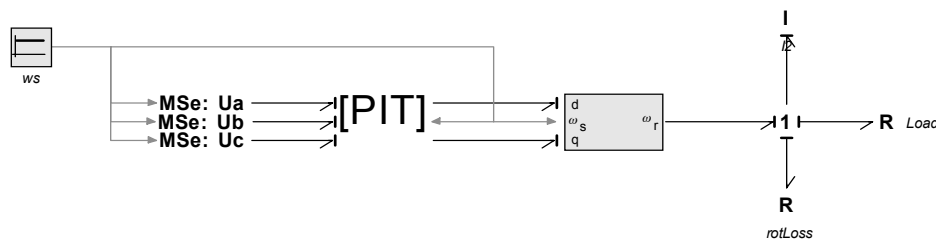


Figure 4.26: System setup for asynchronous motor.

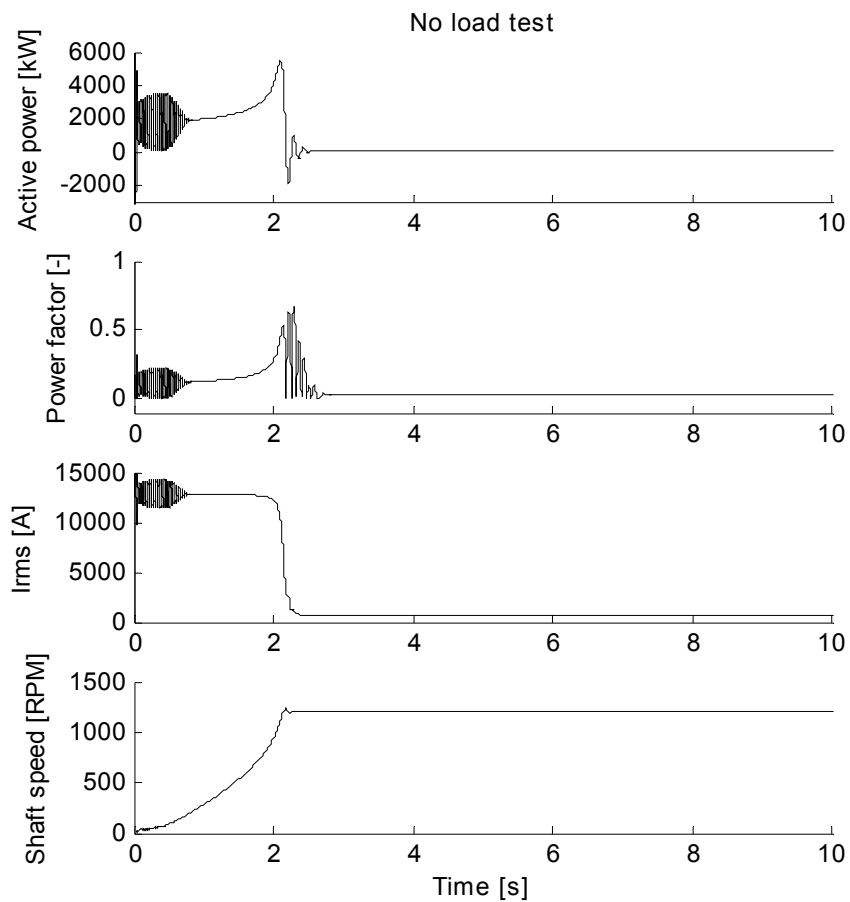


Figure 4.27: No load test.

No-load point				
$f$ [Hz]	$U_1$ [V]	$I_1$ [A]	$P_1$ [kW]	PF
60.3	689.0	672.20	25.40	0.032

Table 4.5 : Reading of frequency, stator voltage, stator current and input power.

	Test	Simulation	Deviation [%]
$I_1$ [A]	672.2	672.7	0.07
$PF$ [-]	0.032	0.0316	1.3
<i>Shaft speed</i> [rpm]		1205.9	
$P$ [kW]	25.4	25.406	0.02

Table 4.6 : No-load test.

Short circuit point				
$f$ [Hz]	$U_1$ [V]	$I_1$ [A]	$P_1$ [kW]	PF
60.3	177.0	3268.5	115.6	0.115

Table 4.7 : Reading of frequency, stator voltage, stator current and input power.

### Conclusion, no-load test

Static values of active power, power factor, Irms and shaft speed are compared to data from the actual no-load test in Table 4.6. The comparison show that the deviations are small. Resulting shaft speed was not given for the no-load test.

### Simulation, short circuit test

The short-circuit test is done by locking the rotor. The readings of stator voltage, stator current and active power at nominal current are given in Table 4.7

The resulting active power, power factor and motor currents are presented in Figure 4.28

### Conclusion, short circuit test

The stationary values are given in Table 4.8 together with a comparison with data from the short circuit test. Again, the comparison show that the deviations are small.

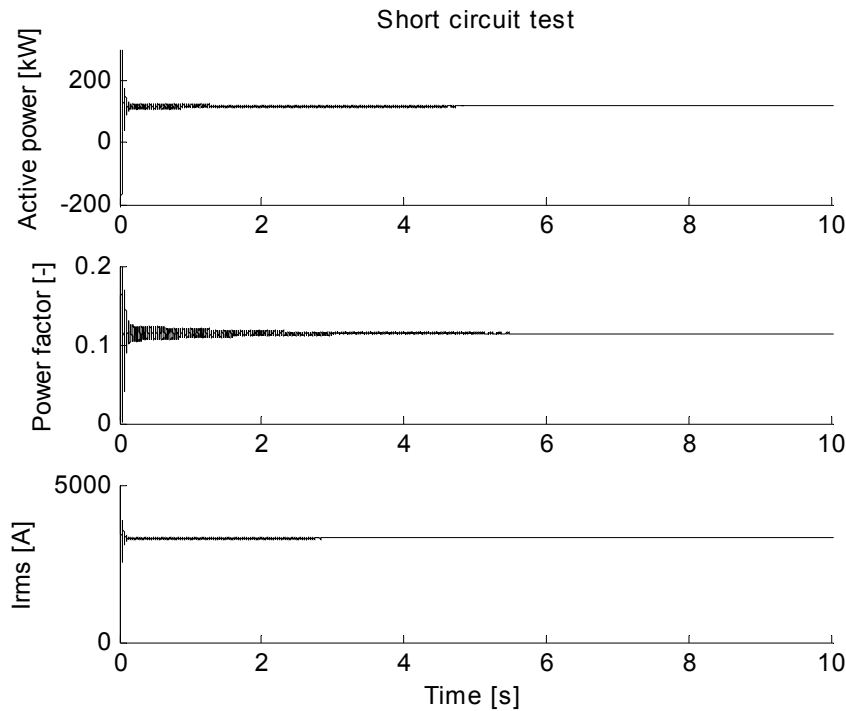


Figure 4.28: Short circuit test.

	Test	Simulation	Deviation [%]
$I_1$ [A]	3268.5	3299.8	1.0
$PF$ [-]	0.115	0.1142	0.7
Shaft speed [rpm]		0	
$P$ [kW]	115.6	115.49	0.1

Table 4.8 : Short circuit test.

### Simulation, rated values

The last verification test is done at rated values of the induction motor. Assuming that the load on the induction motor is given on the form

$$T_{load} = C_{load} \omega_r^2,$$

the coefficient  $C_{load}$  is chosen to give a load of approximately 3300 [kW] at rated speed. The applied voltage is  $U_1 = 690$  [V] and the frequency is  $f = 60,3$  [Hz]. The simulation results are presented in Figure 4.29, while stationary values for current, power factor, shaft speed, real power and output power are given in Table 4.9.

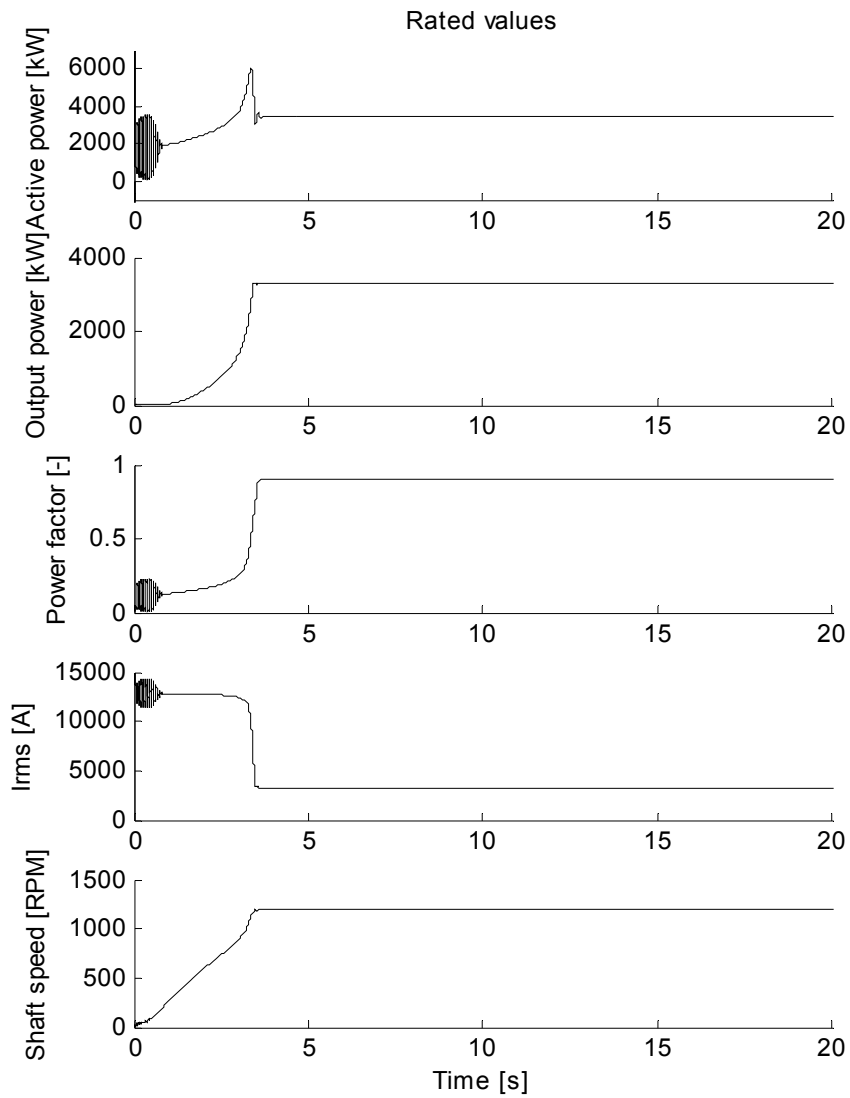


Figure 4.29: Rated values.

	Test	Simulation	Deviation [%]
$I_1$ [A]	3270	3174.7	2.9
$PF$ [-]	0.87	0.9033	3.8
<i>Shaft speed</i> [rpm]	1199	1189.5	0.79
$P$ [kW]		3430	
$P_{output}$ [kW]	3300	3300.01	0.00003

Table 4.9 : Rated values.

### Conclusion, rated values

A comparison between rated values given by manufacturer and results from simulation show only small deviations.

The three simulation cases are accomplished to verify the characteristics of the asynchronous motor model. All tests show only small deviations which demonstrate the goodness of the motor model.

## 4.4 PWM converter

In the following, several simulation have been accomplished using the pulse width modulated converter to verify the characteristics of the converter model. The rectifier has been omitted when testing the inverter with Direct Torque Control (DTC) and Field Oriented Control (FOC). A comparison between average inverter model and the inverter model using ideal switches has also been completed. In the latter simulation case it has been assumed that the inverter model using ideal switches is most accurate, and the simulation is accomplished to check how well the average model follows the model using ideal switches.

Due to long computational time for the advanced PWM converter model, the moment of inertia for the thruster was set small to give fast response when changing commanded torque. However, this do not affect the stationary results.

### 4.4.1 Direct torque control

#### System setup

The system setup for simulating the pulse width modulated converter using direct torque control is shown in Figure 4.30. The DTC method is covered in Chapter 3.8.3. The DC-link voltage is assumed constant, thus the rectifier and DC-link are replaced with two effort sources. The bond graph representation of the inverter using ideal switching is seen in Figure 3.28, while the asynchronous motor is treated in Chapter 3.7. Power invariant transformation, see Chapter 3.4, is used to transform currents and voltages between the  $abc$  frame of the converter to the  $dq$ -frame of the asynchronous motor rotating with rotor angular velocity  $\omega_r$ . The load torque is given as

$$Q_{load} = C_Q \omega_r |\omega_r|,$$

where  $C_Q$  is the torque coefficient.

#### Simulation

The following events appeared during the simulation:  $t = 0$  [s]; the torque reference is increased from 0 to 25 [kNm],  $t = 1$  [s]; torque reference is decreased

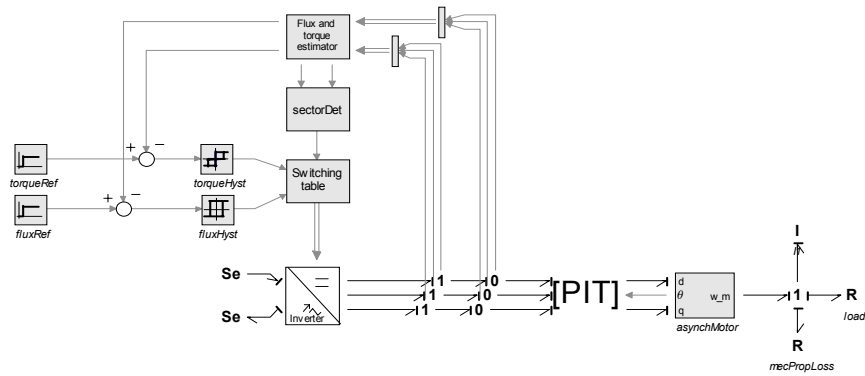


Figure 4.30: System setup for PWM converter with direct torque control.

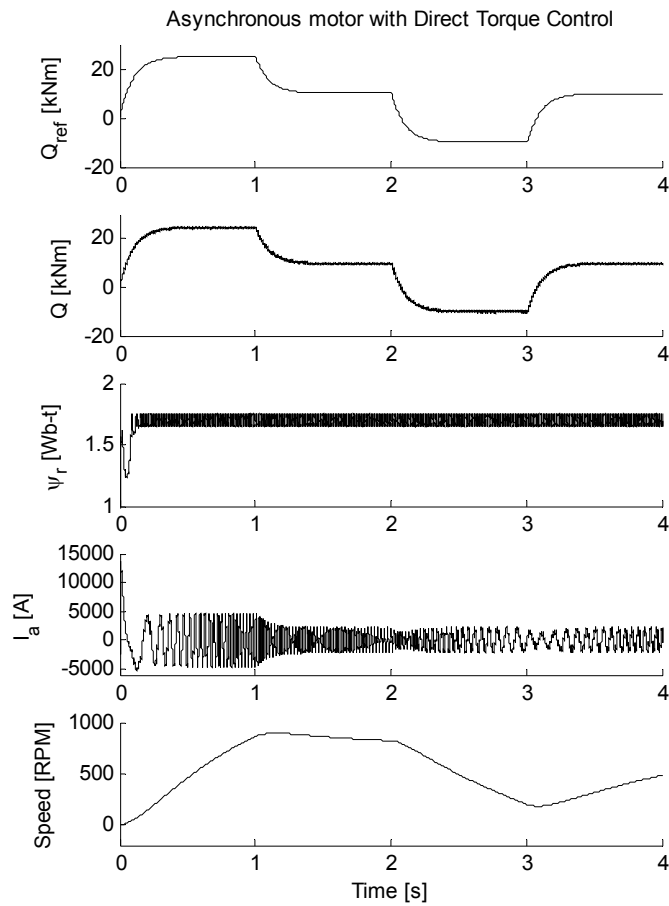


Figure 4.31: Asynchronous motor with direct torque control.

to 10 [kNm],  $t = 2$ ; torque reference is decreased to  $-10$  [kNm] and  $t = 3$ ; torque reference is again increased to 10 [kNm]. Resulting motor torque,  $Q$ , rotor flux linkage,  $\psi_r$ , phase current,  $I_a$  and shaft speed,  $\omega$ , are shown in Figure 4.31.

### Conclusion

The results presented in Figure 4.31 show that the motor torque follows the torque reference well. It may be noticed that the rotor flux linkage varies between 1.55 and 1.65 [Wb-t]. The rapid variation is caused by the direct torque control and the switching table given in Chapter 3.8.

The resulting motor current is almost sinusoidal, while the motor speed has a smooth variation.

## 4.4.2 Field oriented control

### System setup

The system setup for simulating the pulse width modulated converter using field oriented control (FOC) is shown in Figure 4.32. The setup is almost the same as for the PWM converter using DTC, but the inverter has been extended with a block “Sub oscillation method” which provide the ideal switches with the control signals  $S_1$  to  $S_6$ , see Figure 3.31. The FOC method is discussed in Chapter 3.8.3.

### Simulation

The simulation is accomplished with use of the same torque reference as for the PWM converter with DTC. Resulting motor torque,  $Q$ , rotor flux linkage,  $\psi_r$ , phase current,  $I_a$  and shaft speed,  $\omega_r$ , are shown in Figure 4.33.

### Conclusion

As for the previous simulation where direct torque control was used for controlling the asynchronous motor, the motor torque follows the torque reference well when using field oriented control of the motor. When using DTC a rapid variation was detected for the rotor flux linkage, while this variation was not observed when using FOC, see Figure 4.33.

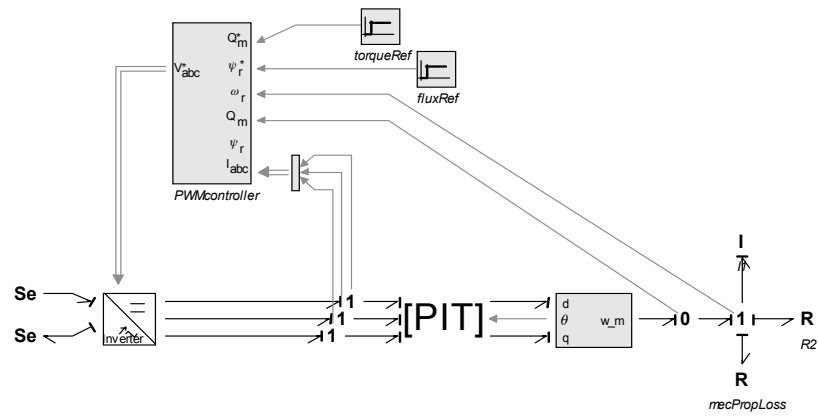


Figure 4.32: System setup for PWM converter using field oriented control.

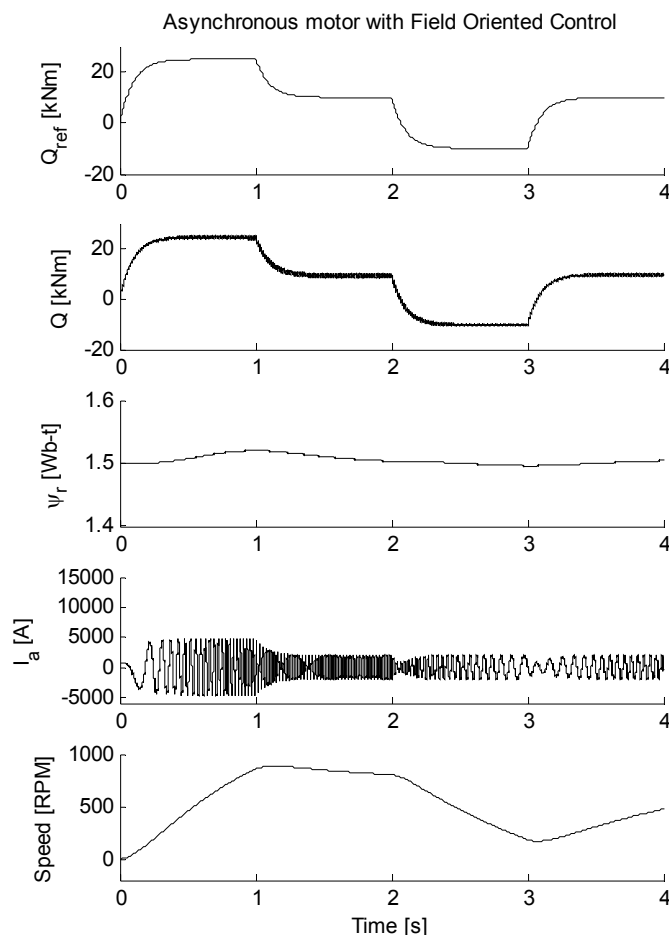


Figure 4.33: Asynchronous motor with field oriented control.

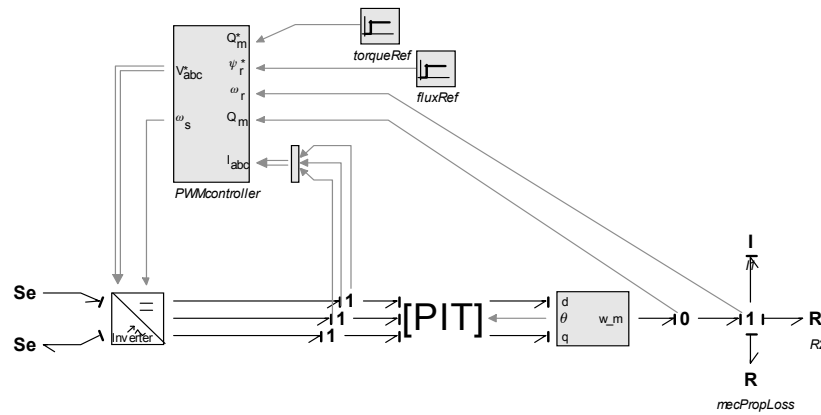


Figure 4.34: System setup for average inverter using field oriented control.

### 4.4.3 Field oriented control using average converter model

#### System setup

The average model of the inverter has been simulated using field oriented control. The system setup is seen in Figure 4.34, which is almost the same as used in previous section, but the inverter is replaced with the average inverter model. The bond graph representation of the average inverter is shown in Figure 3.38.

#### Simulation

The simulation is accomplished with use of the same torque reference as for the PWM converter with DTC. Resulting motor torque,  $Q$ , rotor flux linkage,  $\psi_r$ , phase current,  $I_a$  and shaft speed,  $\omega$ , are shown in Figure 4.35.

#### Conclusion

The results presented in Figure 4.35 is relatively similar to the results presented in Figure 4.33. The main difference between the two figures is the motor torque. When using ideal switches, the motor torque has small but fast variations in motor torque. For the average model, this rapid variation is gone, and instead the motor torque is smooth.

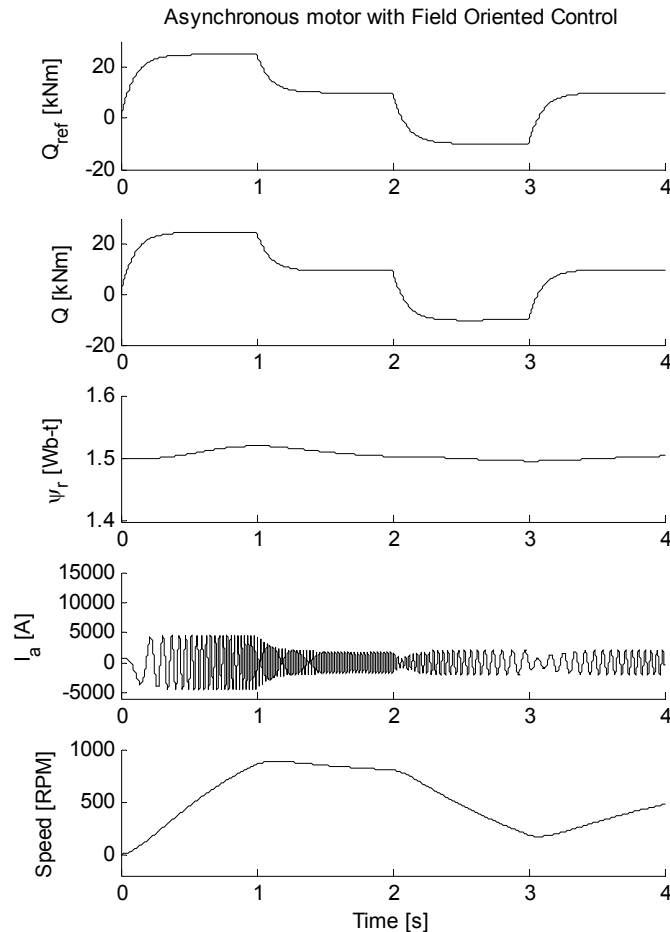


Figure 4.35: Asynchronous motor with field oriented control and use of average inverter model.

#### 4.4.4 Comparison of advanced and average inverter model

The inverter model using ideal switches is compared to the average model of the inverter in Figure 4.36 to Figure 4.38 which show phase current, motor torque and shaft speed. The systems have been simulated using Runge-Kutta 4 (RK4) with step size  $1 \cdot 10^{-5}$  as integration method. The variable step solvers Vode Adams and Backward Differentiation Formula (BDF) were not able to simulate the ideal switches model particular well. The computation time was very long, 300 seconds and more to simulate 4 seconds and the simulation results were inaccurate. The computational time for the same system when using the RK4 solver was 66 seconds to simulate 4 seconds. The computational time for the average model using RK4 was 10 seconds while the simulation time was only 0.1 seconds when using BDF.

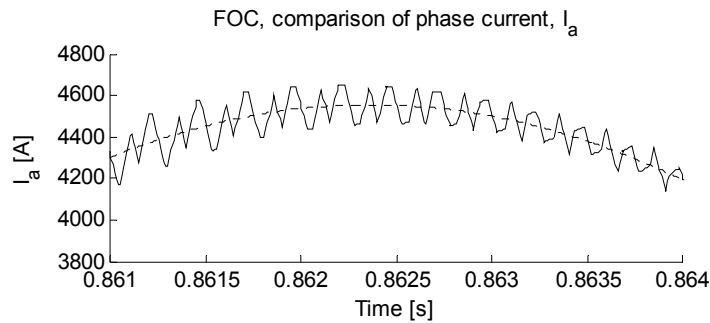


Figure 4.36: Comparison of phase current,  $I_a$ , ideal switches (—) and average model (---).

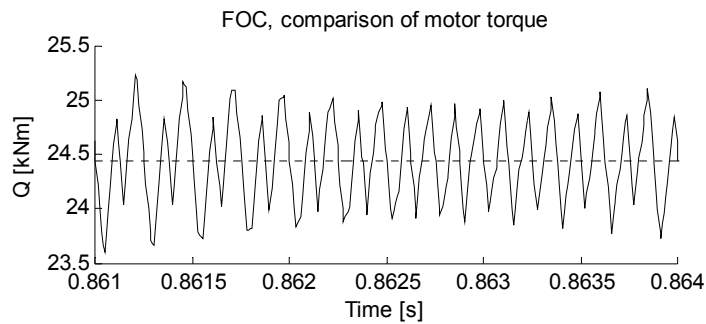


Figure 4.37: Comparison of motor torque, ideal switches (—) and average model (---).

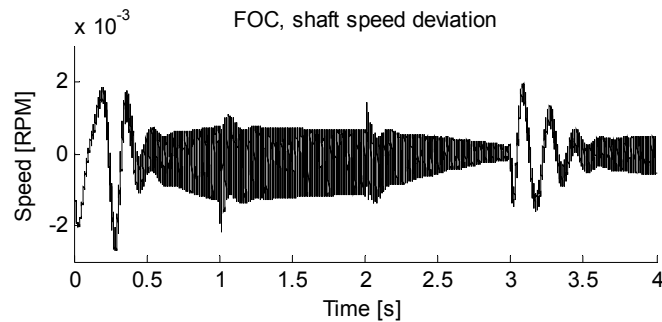


Figure 4.38: Shaft speed deviation.

Figure 4.36 show a comparison of motor current. One may notice that the resulting motor current when using the advanced inverter model varies rapidly around the smooth motor current resulting from the average inverter model. The same may be observed for the comparison of motor torque presented in Figure 4.37. Figure 4.38 presents the comparison of motor shaft speed. As may be seen from the figure, the speed deviation is small, such that the average model may be used when increased simulation speed is required. The model accuracy is still ensured when using the average model.

#### 4.4.5 Model characteristics of the average PWM converter

##### System setup

The last simulation with the converter is done to determine the model characteristics when used in a complete power plant. The power plant consists of one generator set, converter, asynchronous motor and a rotational load, see Figure 4.39.

The rectifier and the DC-link with brake are modeled according to Chapter 3.8.1 and Chapter 3.8.2, while the average model of the inverter is found in Chapter 3.8.3. The generator, asynchronous motor and PWM controller based on FOC are mentioned in Chapter 4.4.1 and Chapter 4.4.2. The generator frequency is assumed constant.

##### Simulation

Figure 4.40 to Figure 4.42 show the simulation results when the following events appeared:

The simulation was accomplished with varying thruster torque reference. At  $t = 50$  [s], the torque reference is increased from 0 to 1 [kNm], at  $t = 150$  [s],  $Q_{ref} = 10$  [kNm], at  $t = 200$  [s],  $Q_{ref} = 15$  [kNm], at  $t = 250$  [s],  $Q_{ref} = -15$  [kNm], at  $t = 300$  [s],  $Q_{ref} = -5$  [kNm], at  $t = 350$  [s],  $Q_{ref} = 5$  [kNm] and  $t = 400$  [s],  $Q_{ref} = -15$  [kNm]. The torque reference setup is summarized in Table 4.10.

Figure 4.40 shows torque reference together with power and speed of thruster, Figure 4.41 shows rms line to line voltage, active and reactive power, and field excitation voltage of the generator, while Figure 4.42 shows DC-link voltage together with rectifier power, inverter power and brake power.

##### Conclusion

In Figure 4.42 one may notice that the DC-link brake burn off excessive energy in the DC-link at  $t \approx 250$  [sec]. The DC-link overvoltage is caused by regenerative power from the inverter. The thruster torque reference change from  $T_{ref} = 15$  [kNm] to  $T_{ref} = -15$  [kNm] during a 5 second interval and the inverter is used for braking the thruster. Regenerative power from the inverter is supplied to the DC-link, causing overvoltage of the DC-link. The diodes stops rectifying causing a small increase in line to line voltage for the generator.

Although this simulation has not been verified using measurements from an existing power plant, the simulation result appears reasonable.

Time [sec]	0	50	150	200	250	300	350	400
Torque reference [kNm]	0	1	10	15	-15	-5	5	-15

Table 4.10 : Torque reference.

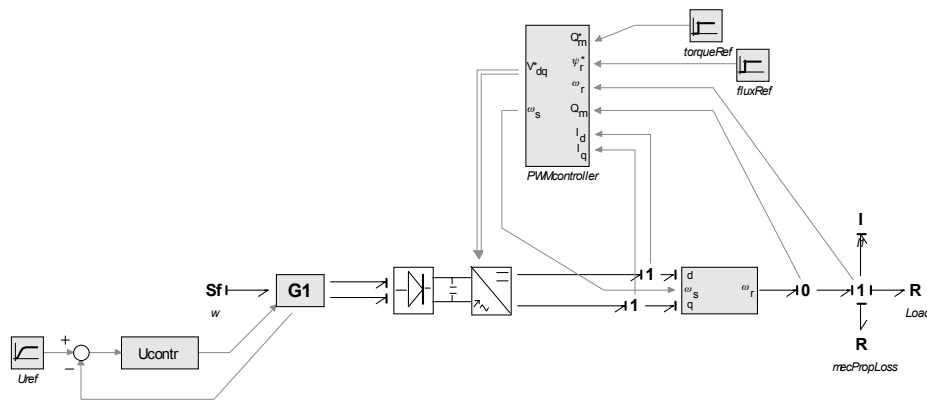


Figure 4.39: System setup for simulation of PWM converter modeled in  $dq$ -frame.

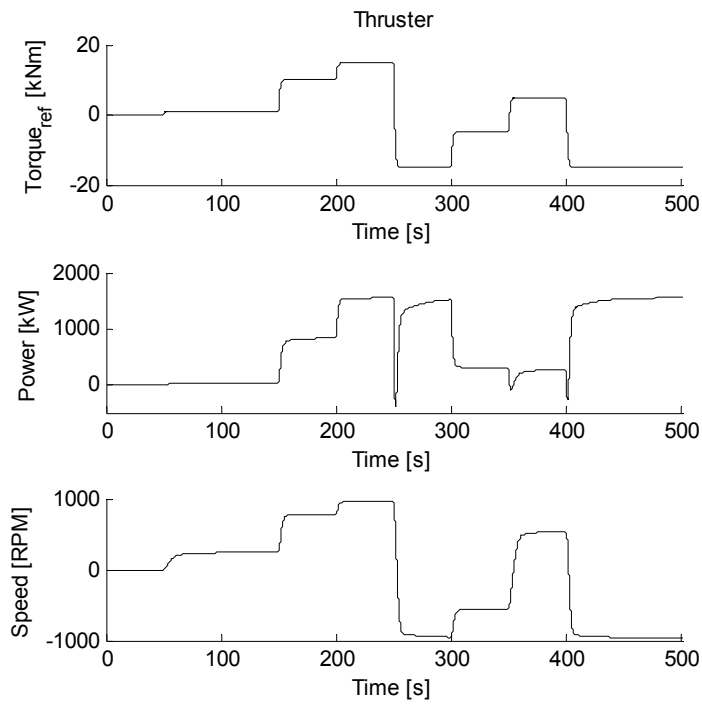


Figure 4.40: Torque reference, and power and speed measurement of the thruster.

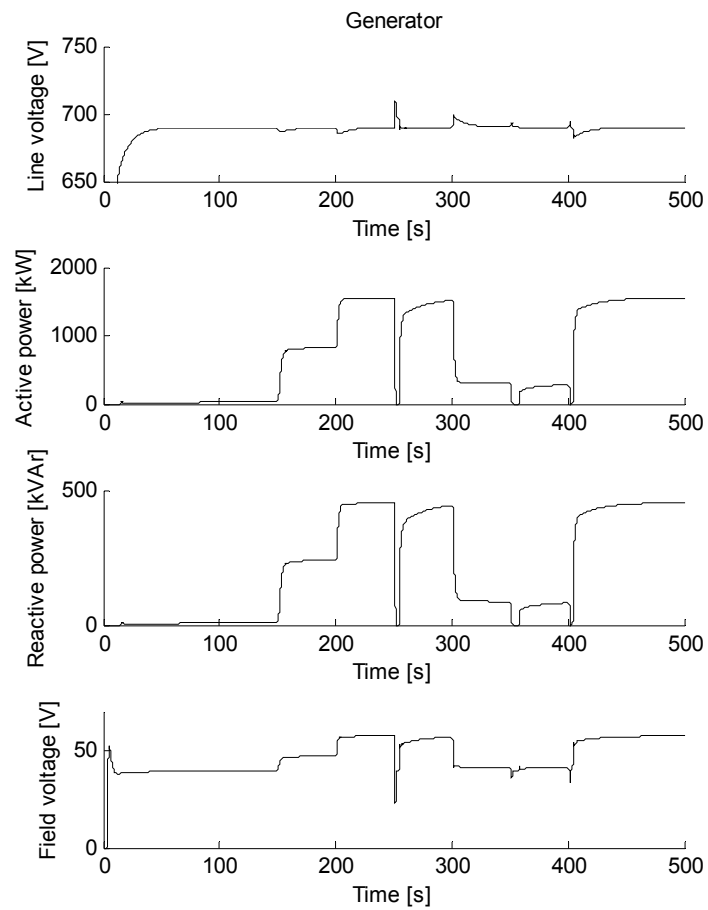


Figure 4.41: Line to line voltage, active/reactive power and excitation field voltage of generator.

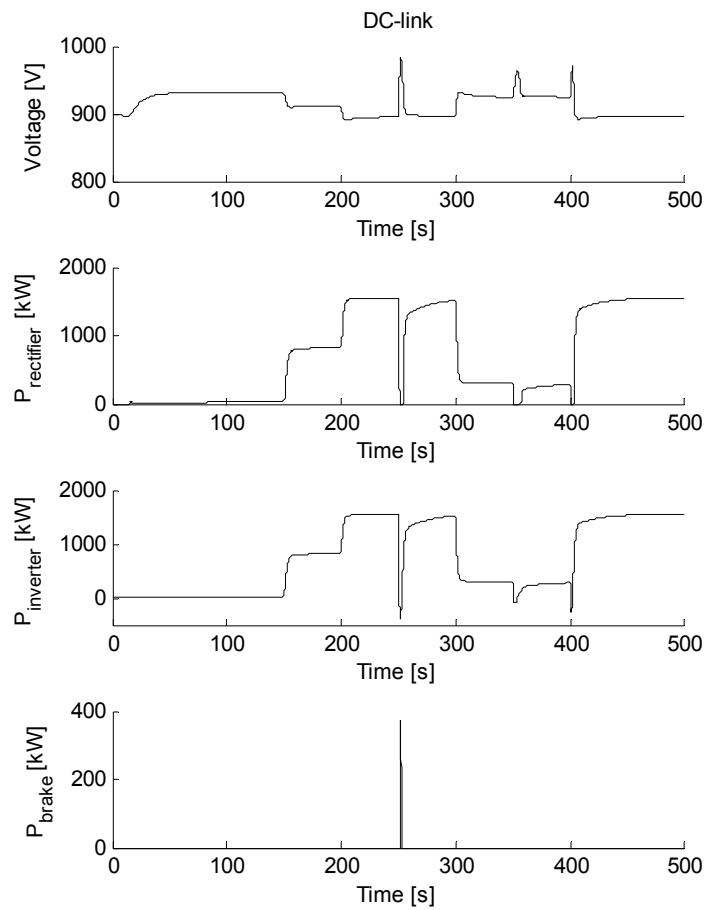


Figure 4.42: DC-link voltage together with rectifier, inverter and brake power.

## 4.5 Bow propeller

The purpose of the last simulation is to compare the bow thruster model with readings of speed and power from an actual bow thruster. For the bow thruster, only the diameter was given, other thruster data needed for the simulation were assumed. Therefore some deviation with regard to simulated power was expected.

### System setup

The system setup for verification of the nonlinear propeller model is shown in Figure 4.43. The propeller is connected to an induction motor using shaft and gear. The gear is assumed lossless. The induction motor is described in Chapter 3.7, while the converter is discussed in Chapter 3.8.3 together with the field oriented controller. The nonlinear propeller is described in Chapter 3.9.

Bow thruster readings from Viking Energy during a DP-operation are used as reference for this simulation.

### Simulation

Reading of thruster speed was used as input to the speed controller of the simulated system. The speed of the bow thruster together with a comparison of thruster power resulting from measurements and simulation are presented in Figure 4.44.

### Conclusion

Figure 4.44 shows that there are some differences between measured thruster power and simulated thruster power. There are several reasons for the deviation. The power is dependent on the thruster design, number of blades, pitch and so on. The propeller data have not been available, instead these data have been assumed. The power is also dependent on water inflow velocity which is affected by the ship speed, current and waves. For this simulation, the inflow velocity was set to 0.

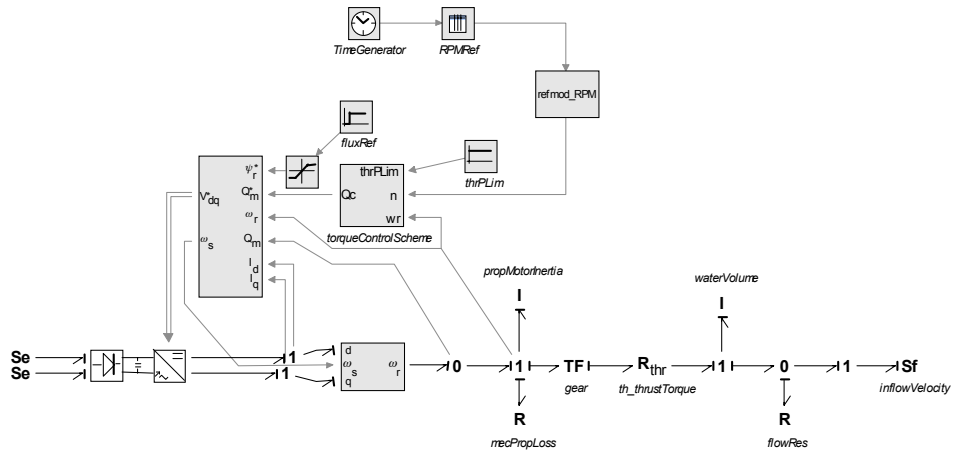


Figure 4.43: System setup for verification of nonlinear dynamic propeller model.

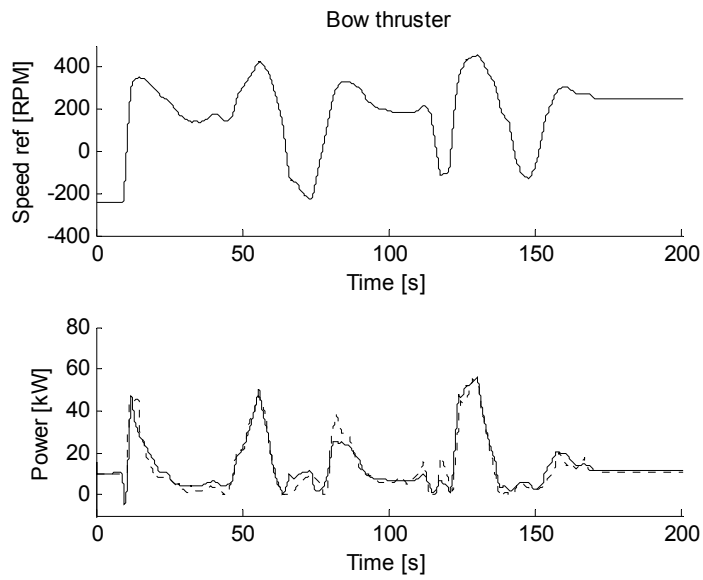


Figure 4.44: Bow thruster, speed and power, measurements (--) and simulation (—).



## Chapter 5

### Case simulation

The purpose of this chapter is primarily to demonstrate the use of the AES library discussed in previous chapters.

The power plant is controlled by a power management system (PMS), which handles start and stop of generator sets, connecting or disconnecting generator set to/from bus, generator load sharing and power limitation on thrusters.

Three different power plant layout will be simulated. In the first simulation, the sea state is rough sea. Generator sets are also suddenly disconnected from bus due to errors. The second simulation case simulates a typical DP-operation, while a fuel cell is used together with generators as power producers in the third simulation. Each simulation case will start with a description of the simulated system before the simulation results are presented and discussed.

#### 5.1 Case I: Extreme load variations

##### 5.1.1 System setup

The system setup for the first simulation is shown in Figure 5.1. The simulated power plant consists of 4 generator sets, 2 stern thrusters and 1 *otherLoads*. Each generator set has rated output of 1950 [kW], while each stern thrusters have rated output of 3300 [kW]. The *otherLoads* block is used for modeling other load consumers and rated power is not specified. Bus frequency is 60 [Hz] and the rms value of the line to line voltage is 690 [V].

The PMS determines when to start and stop generator sets based on predefined power and time limits and handles synchronization before connecting the started generator set to the bus. The PMS controls load sharing between generator sets that are connected to the bus and take care of off loading of generators before the generators are disconnected from bus. Bus frequency and voltage is also controlled from the power control system.

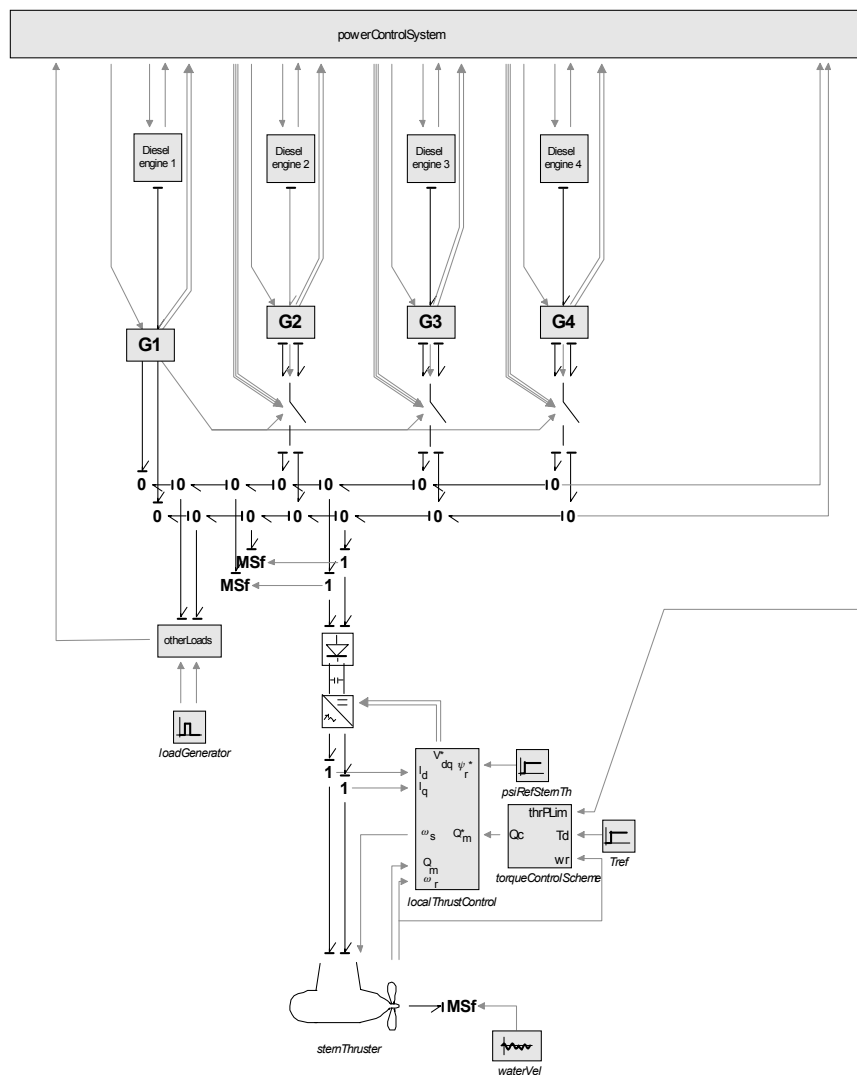


Figure 5.1: System setup, case I.

The mathematical description of the diesel engine is given in Chapter 3.1, while the generator models are described in Chapter 3.2. Saturation and hysteresis are neglected for the generator models. Generator 1 is used as primary generator setting voltage while generator 2, 3 and 4 are secondary generators with voltage as input. The circuit breakers between generator 2, 3 and 4 are modeled according to Chapter 3.5.

The system setup includes two stern thrusters, but only one model of the stern thruster is used. It is assumed that the two thrusters have the same torque reference and power output, thus only one thruster has to be simulated. The second thruster is modeled as two modulated flow sources having the same current output as the first

thruster. The pulse modulated converter described in Chapter 3.8 consists of a diode rectifier, a DC-link with brake and an inverter. The stern thruster is an asynchronous motor and the mathematical description of the thruster is given in Chapter 3.7, while the 4 quadrant propeller model is shown in Chapter 3.9. The thruster is exposed to waves and the inflow wave velocity is calculated according to Chapter 3.12. Field oriented control is used for controlling converter voltage and frequency. The *otherLoads* is described in Chapter 3.10 and is used to model hotel and auxiliary loads.

### 5.1.2 Simulation

3 generator sets are connected to bus at simulation start. Figure 5.2 to Figure 5.6 present simulation results when the following events appeared:

At  $t = 0$  [s], thrust reference is set to 500 [kN], while active/reactive power for hotel and auxiliary loads are set to  $800 \pm 50/200$  [kW]/[kVA]. At  $t = 50$  [s] and  $t = 200$  [s], generator 2 and 3 are tripped because of faults. The fault on generator 2 is fixed at  $t = 350$  [s]. At  $t = 500$  [s] the thrust reference is reduced to 300 [kN].

Figure 5.2 shows active and reactive power consumption for hotel and auxiliary loads. The active power consumption consist of one constant term and one varying term. The constant term is set to 800 [kW], while the varying term,  $\pm 50$  [kW], is generated by white noise. The reactive power consumption is set to 200 [kVA].

Torque and power for one of the stern thrusters is shown in Figure 5.3. Upper part of the figure show torque reference (--) and actual torque (—), while power limitation (--) and actual power (—) are presented in lower part of the figure. The difference between torque reference and actual torque is caused by power limitation on the thruster. At  $t = 50$  [s], generator 2 is tripped and this affects available power on bus. Maximum power the thruster is allowed to draw from the bus is reduced to protect the bus from black out. Another generator is started momentary after the trip, and the power limitation for the stern thruster is ramped up after the generator is synchronized and connected to the bus. At  $t = 200$  [s], the power limitation is reduced due to error on generator 3. Now there are errors on both generator 2 and 3, and there are no available generator sets to start, thus actual torque on stern thruster is limited by the power limitation. At  $t = 350$  [s], generator 2 is fixed and started. The generator is then synchronized and connected to bus, and the power limitation for the thruster is ramped up. At  $t = 500$  [s], the thrust reference is reduced. The thrust reduction leads to low load on generators and an automatic shutdown of one generator set is initiated after a predefined time limit.

Figure 5.4 show bus voltage and frequency. The bus voltage has two peaks at  $t = 50$  [s] and  $t = 200$  [s] which are caused by the generator errors. Similar peaks are seen for the bus frequency but in a much smaller scale.

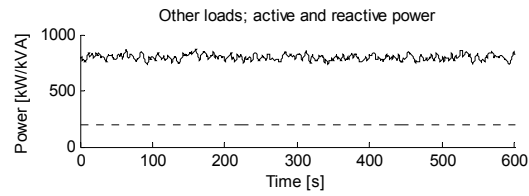


Figure 5.2: Converter; DC-link voltage and rectifier power.

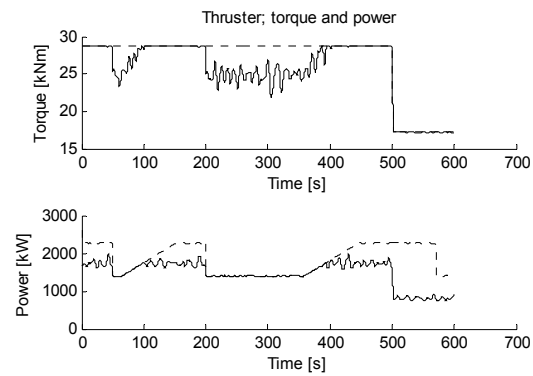


Figure 5.3: Thruster; torque reference (---), actual torque (—), power limitation (---) and actual power (—).

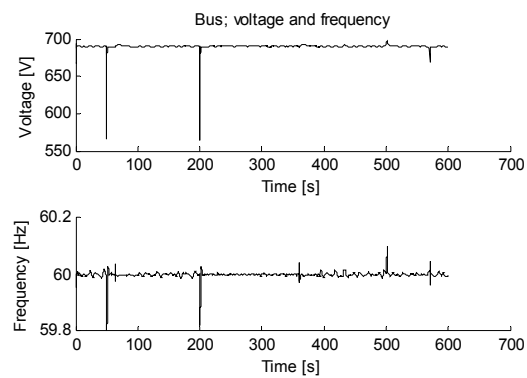


Figure 5.4: Bus; voltage and frequency.

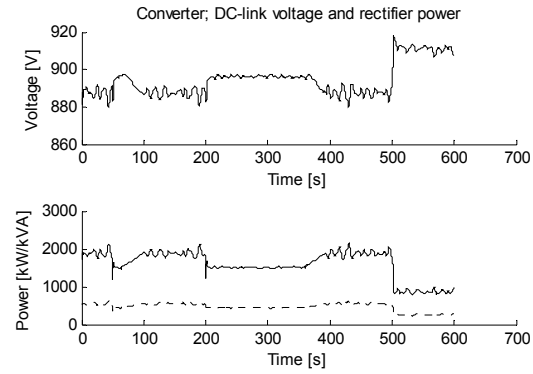


Figure 5.5: Converter; DC-link voltage and rectifier active (—) and reactive (---) power.

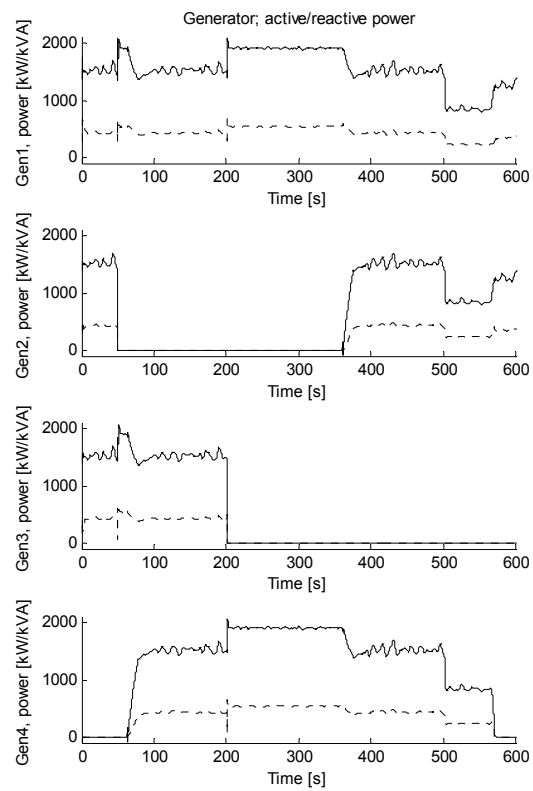


Figure 5.6: Generator; active (—) and reactive (---) power.

DC-link voltage and rectifier voltage for the converter feeding the stern thruster are presented in Figure 5.5. At  $t = 50$  [s] a reduction in rectifier active and reactive power is observed. The power through the rectifier is dependent on the difference between bus voltage and dc-link voltage and the converter load. When the bus voltage is suddenly reduced, the power through the rectifier will also be reduced leading to a dip in DC-link voltage. A small increase in DC-link voltage is then seen just after the dip. This increase is caused by reduced converter load. When one generator is disconnected from bus because of an error, the thruster power is limited, thus the power flow through the converter is reduced. After another generator is connected to the bus, the thruster torque is no longer limited and the power flow through the converter is increased leading to a decrease in DC-link voltage. The same behavior is observed when generator 3 is disconnected. At  $t = 500$  [s] the thrust reference for the stern thrusters are reduced, leading to reduced active and reactive power for the rectifier and increased voltage on the DC-link.

Figure 5.6 show active and reactive power for the generators. At start up, the load is equally distributed between generator 1 to 3,  $P \approx 1500$  [kW] and  $Q \approx 500$  [kW]. At  $t = 50$  [s] generator 2 is disconnected due to an error and the load is suddenly increased for the two remaining generators. Generator 4 is then started and connected to the bus after being synchronized. After generator 4 is connected, the generators start sharing load until they are equally loaded. At  $t = 200$  [s] generator 3 is tripped and generator 1 and 4 are maximum loaded until generator 2 is fixed, started and synchronized. At  $t = 500$  [s] the thrust reference is reduced. After the thrust reduction, the generators are running on relatively low load. After a predefined time limit one generator is off loaded and then disconnected from the bus.

## Conclusion

The figures show the power plant characteristics when the power plant is exposed to large load variations and errors on generator sets. The power limits for the thrusters are rapidly decreased when a generator is tripped due to an error, and the power limits are not increased before another generator set is synchronized and connected to bus. The figures also show how bus voltage and frequency suddenly drops due to generator tripping. Even though the simulation results are not verified using any kind of measurements, the behaviour of the modeled power plant seems right.

## 5.2 Case II: Dynamic positioning and errors on generators

### 5.2.1 System setup

The system setup for case II is almost similar to the system setup for case 1, the system setup is only extended with two bow thrusters with rated output of 1000 [kW], thus the power plant consist of 4 generator sets, two stern thrusters with belonging converters, two bow thrusters with belonging converters, one other loads and a power control system. The system setup is shown in Figure 5.7.

As for the stern thruster, it is assumed that both bow thrusters will have the same speed reference and also the same power consumption. Therefore, only one bow thruster is modeled using the asynchronous motor from Chapter 3.7, the other bow thruster is modeled using two modulated flow sources.

### 5.2.2 Simulation

The simulation results are shown in Figure 5.8 to Figure 5.15 when the following events appeared:

At startup two generators are connected to the bus. Active and reactive power consumption for hotel and auxiliary loads are set to  $P = 800 \pm 50$  [kW] and  $Q = 200$  [kVA]. The thrust reference for the stern thruster and the speed reference for the bow thruster are varied to give proper use of the stern and bow thruster during a DP-operation. At  $t = 150$  [s] generator 2 is tripped due to an error and at  $t = 370$  [s] generator 3 is also tripped. The generators are not repaired during this simulation.

Figure 5.8 show active and reactive power consumption for hotel and auxiliary loads. The power consumption is the same as used for the first simulation case.

Thrust and speed references for stern and bow thrusters are given in Figure 5.9. The references is generated using white noise, but is based on an actual DP-operation for the supply vessel Viking Energy operated in the North Sea.

Figure 5.10 and Figure 5.11 show resulting torque, speed and power for the stern and bow thrusters when using the thrust and speed references given in Figure 5.9. The power consumption for the thrusters are not limited even though generator 2 and 3 are tripped since the loading of the thrusters are low in first place.

Figure 5.11 show bus voltage and frequency. Two dips are observed, especially for the bus voltage. The dips occur when generator 2 and 3 are tripped. After tripping one generator the load shared by the two connected generators must be taken by the remaining generator that is still connected to the bus. A sudden increase in load will decrease generator voltage and frequency, and the control system for the generator will then compensate for this error in voltage and frequency by increasing the motor

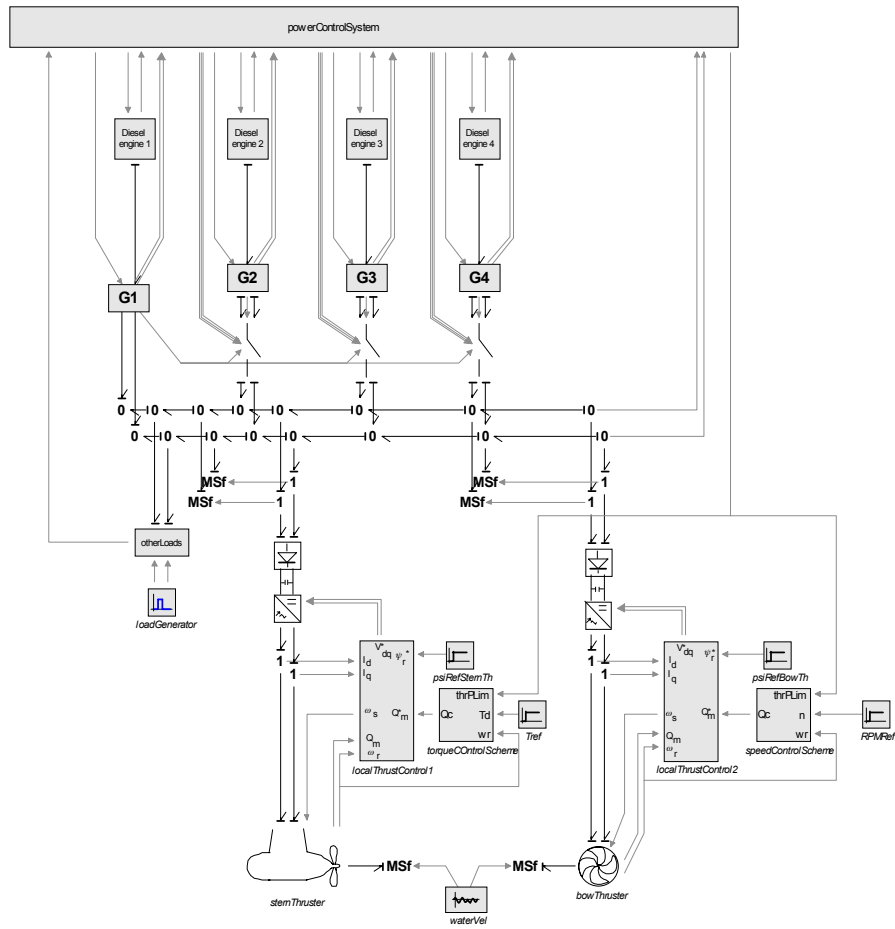


Figure 5.7: System setup, case II.

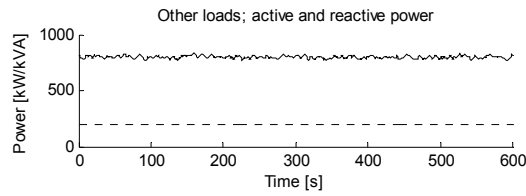


Figure 5.8: Other loads; active (—) and reactive (---) power.

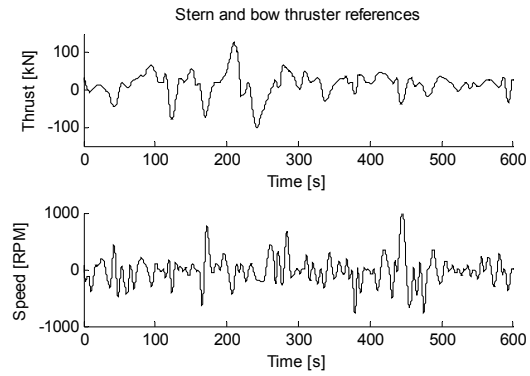


Figure 5.9: Stern thruster; thrust reference and bow thruster speed reference.

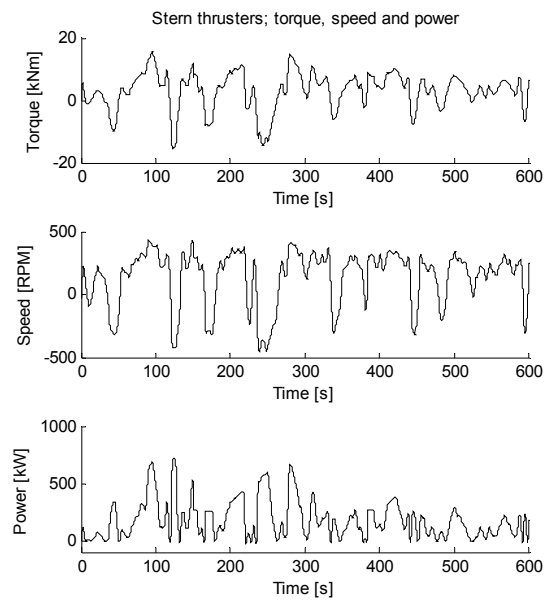


Figure 5.10: Stern thrusters; torque, speed and power.

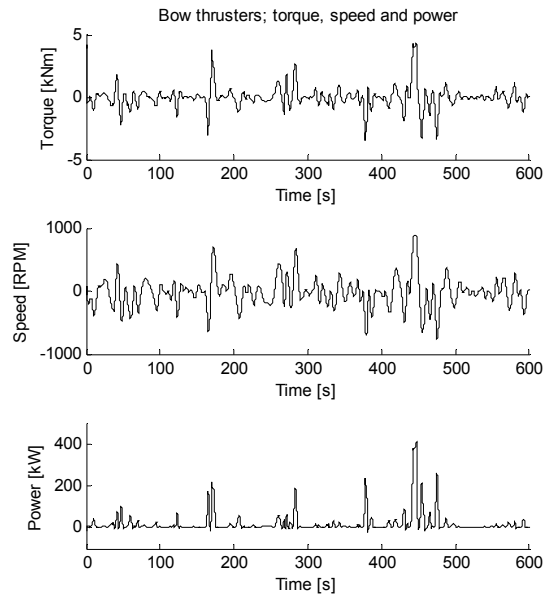


Figure 5.11: Stern thrusters; torque, speed and power.

speed reference and generator field magnetizing voltage.

The next two figures, Figure 5.13 and Figure 5.14, present DC-link voltage together with active and reactive power flow through the rectifiers for stern and bow thruster converters. The DC-link voltage is dependent on both the voltage difference between AC-side and DC-side of the rectifiers and the power flow through the converter. It is difficult to notice the influence of the bus voltage disturbance from generator tripping since the DC-link voltage is already varying much because of large variations in thruster load.

Figure 5.15 presents active and reactive power production for the four generators. At  $t = 150$  [s] and  $t = 370$  [s] generator 2 and 3 are tripped due to errors in the generators. When one generator is tripped the loading of the tripped generator is transferred to the remaining generator, until another generator is started, synchronized and connected to the bus. The connected generators will share both active and reactive power equally.

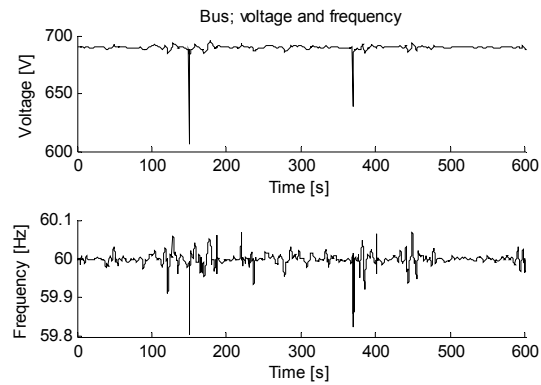


Figure 5.12: Bus; voltage and frequency.

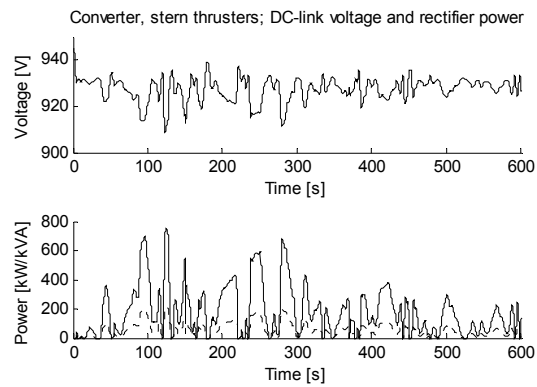


Figure 5.13: Converter, stern thrusters; DC-link voltage and rectifier active (—) and reactive (---) power.

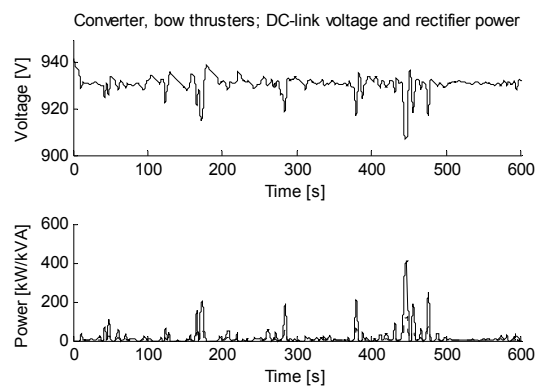


Figure 5.14: Converter, bow thrusters; DC-link voltage and rectifier active (—) and reactive (---) power.

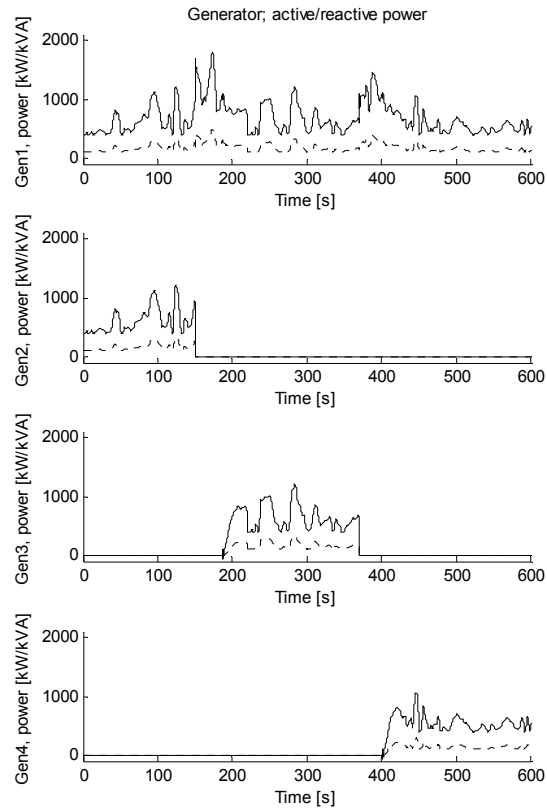


Figure 5.15: Generator; active (—) and reactive (--) power.

## Conclusion

The simulation results presented in Figure 5.8 to Figure 5.15 appear acceptable. Large thruster load variations causes large variation in DC-link voltage which also affect bus voltage and frequency and generators active and reactive power. Influence on bus voltage and frequency are also observed during sudden tripping of generators.

## 5.3 Case III: Generator and fuel cell in a combined power plant

### 5.3.1 System setup

The system setup for case III is presented in Figure 5.16. The power plant consists of 3 generator sets with rated output of 1950 [kW] and one fuel cell with rated output of 2000 [kW], 2 stern thrusters with rated output of 3300 [kW] and hotel and auxiliary loads. Bus frequency is 60 [Hz] and the rms value of the line to line voltage is 690 [V].

The power control system (PCS) is the same PCS as used in case I and II, but in addition the PCS also controls the loading of the fuel cell. The PCS has two methods for controlling the loading of the fuel cell. The loading may either be controlled independently of the loading of the generators, or the loading of the fuel cell may be controlled such that optimal loading with respect to fuel consumption on the connected generators are achieved. By using the last method and filtering out high frequency load variations, the fuel cell may be used to improve the performance of the bus connected generator sets.

Mathematical description of the fuel cell is given in Chapter 3.6. Since it is not possible to change the loading of the fuel cell very rapidly, at least one generator set must be connected to bus if sudden load changes are expected.

The other component modules used in the system setup are the same components used in case I and II.

### 5.3.2 Simulation

The last simulation has been accomplished to explore the behavior of a combined power plant consisting of several generator sets and a fuel cell. The fuel cell has two control modes, and both methods have been simulated. From  $t = 0$  [s] to  $t = 500$  [s] the fuel cell is controlled independently of generator load. At  $t = 500$  [s] the control mode is changed and the fuel cell is controlled to give optimal loading on bus connected generator sets.

Figure 5.17 to Figure 5.22 show simulation results when the following events appeared:

At  $t = 0$  [s] power consumption of hotel and auxiliary loads are set to  $P = 800 \pm 50$  [kW] and  $Q = 200$  [kVA] and the thrust reference for the stern thrusters are set to 200 [kN]. Hotel and auxiliary loads are not changed during the simulation. At  $t = 100$  [s] the thrust reference is reduced to 190 [kN], then increased to 240 [kN] at  $t = 300$  [s]. At  $t = 700$  [s] the thrust reference is reduced to 190 [kN], before it is increased to 240 [kN] at  $t = 1000$  [s] and to 340 [kN] at  $t = 1300$  [s]. The thrust reference is then reduced to 290 [kN] at  $t = 1600$  [s], before it is increased to 320 [kN] at  $t = 1800$  [s].

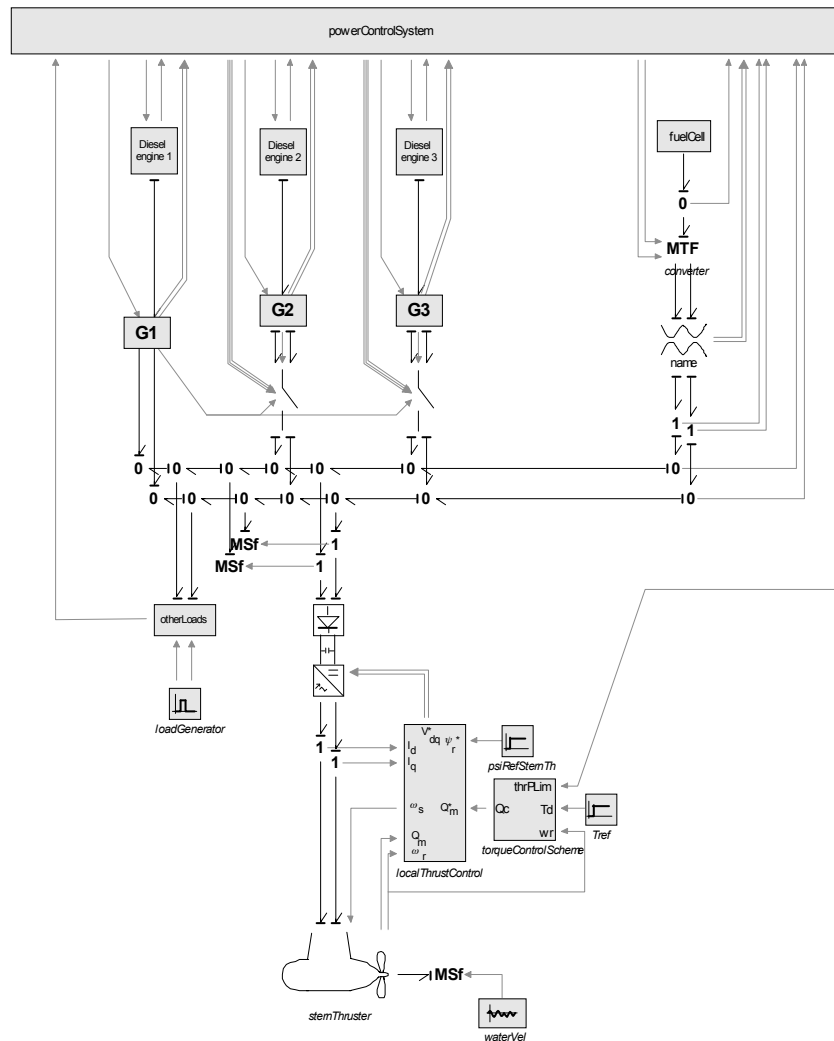


Figure 5.16: System setup, case III.

Active and reactive power consumption for hotel and auxiliary loads are presented in Figure 5.17. The active and reactive power consumption are the same as used in case I and II.

Figure 5.18 presents power limitation (--) and actual power (—) for one of the stern thrusters. The power consumption of the thruster is below the power limitation during the most of the simulation, but just after  $t = 1300$  [s] the thruster is actually limited by the power limitation. At  $t = 1300$  [s] the thrust reference had a large increase, and the bus connected generator sets and the fuel cell were not able to deliver adequate amount of power to the consumers such that it was necessary to limit the power of the thruster. Another generator was started and connected to the bus such that more power becomes available on the bus. After ramping up the

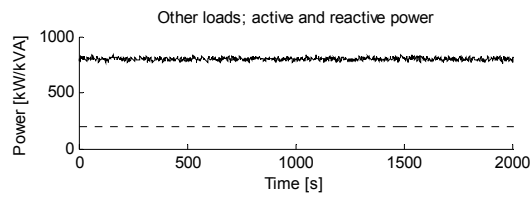


Figure 5.17: Other loads; active (—) and reactive (---) power.

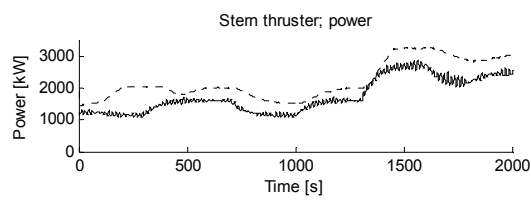


Figure 5.18: Thruster; power limitation (---) and actual power (—).

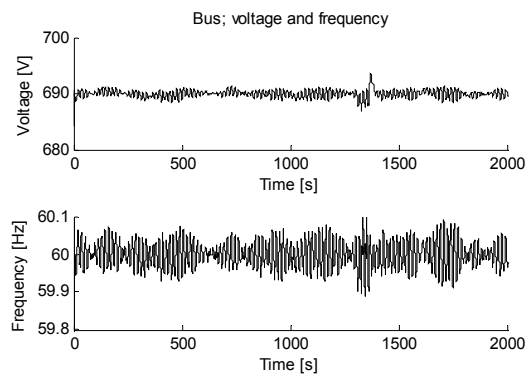


Figure 5.19: Bus; voltage and frequency.

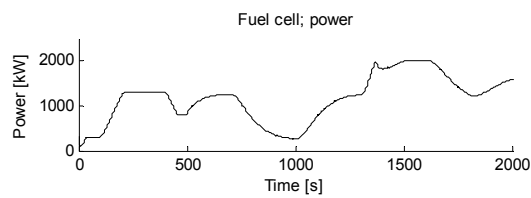


Figure 5.20: Fuel cell; power.

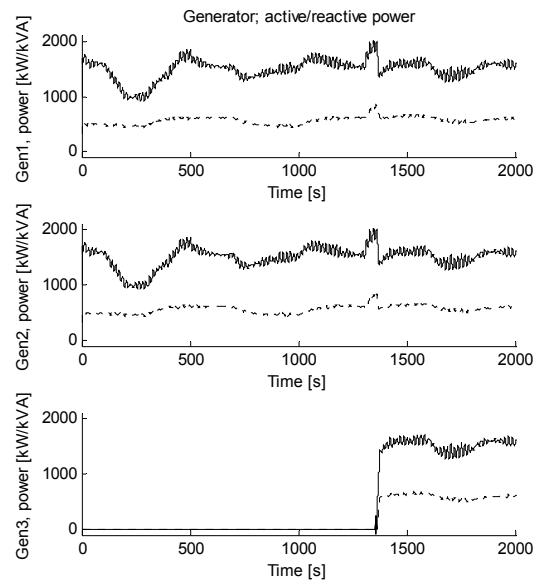


Figure 5.21: Generator; active (—) and reactive (--) power.

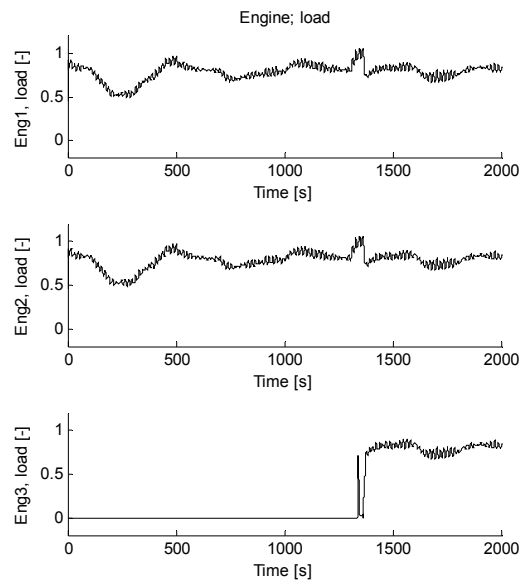


Figure 5.22: Engine load.

power limitation, the thruster power was no longer limited by the power limitation function.

The next figure, Figure 5.19, show bus voltage and frequency. The rippling behavior of the voltage and frequency is caused by varying load demand.

Figure 5.20, Figure 5.21 and Figure 5.22 show power output from the fuel cell and generators together with engine loading. From  $t = 0$  [s] to  $t = 500$  [s] the fuel cell output is controlled independently of the loading of the engines. At  $t = 0$  the reference power output is set to 300 [kW], at  $t = 100$  [s] the reference is increased to 1300 [kW], while the reference is decreased to 800 [kW] at  $t = 400$  [s]. As seen from Figure 5.22 the engine load varies between 0.5 [-] and 0.9 [-] dependent on bus load and fuel cell loading. At  $t = 500$  [s] the power control mode is changed from independent of the generator load to dependent on generator load. The power output of the fuel cell is then controlled to give optimum fuel consumption for bus connected generator sets. For this simulation, optimum fuel consumption is reached when the loading of the engines is approximately 80% of rated power output. The fuel cell power output is increased when control mode is changed since the engine load is above optimum load. At  $t = 700$  [s] the bus load is reduced and the engine load drops below optimum loading. The fuel cell loading is then reduced to increase engine load. At  $t = 1300$  [s] the bus load is so high, that connected generators and fuel cell are not able to take more load. Another generator set is therefore started and connected to the bus.

## Conclusion

The combined power plant consists of one fuel cell which may be controlled to give optimum fuel consumption per produced kW for the bus connected generator sets. The fuel cell is not able to suddenly change power output, thus if large and rapid load variations are expected, the fuel cell should be used in parallel with another power producer.

The results for the last simulation case are presented in Figure 5.17 to Figure 5.22. Also these results appear acceptable. Variation of bus voltage and frequency due to varying thruster and hotel loading are observed. Rapid load variation are taken by the bus connected generator sets while the fuel cell loading is slowly varying.

## 5.4 Summary

In this chapter, three different system layouts have been modeled to demonstrate the use of the AES library. During the first simulation the power plant was exposed to large variation in power demand due to large variation in thruster loads and sudden disconnection of two generator sets from bus. In the second simulation case a typical DP-operation was simulated. Again two generators sets were disconnected

due to errors. In the last simulation a combined power plant consisting of both generators and a fuel cell was simulated.

The three simulation cases presented in this chapter shows that the AES library may be used to model different power plant setups and results from the simulations appears reasonable. By using the AES library, the modeler may easily extend the power plant with additional components and combinations of different power producers may easily be simulated.

## Chapter 6

### Modified generator model

The synchronous generators presented in Chapter 3.2 have a small limitation. The generator models have either voltage or current as output, not both at the same time. If generator 1 is used as a primary generator setting voltage, this generator has to be connected to the bus throughout the simulation, while other generators serving as secondary generators may be connected or disconnected from the bus at any time.

A modified generator model with hybrid causality is therefore proposed such that any generator may serve as the primary generator.

#### 6.1 Mathematical description

The modified generator model is based on both the primary and the secondary generator model developed in Chapter 3.2. The primary and secondary generator models are shown in Figure 6.1 for simplicity. The  $I$ -fields in the secondary generator model have integral causality which give current as output on the  $d$  and  $q$  ports. The primary generator model on the other hand has  $I$ -fields with derivative causality which give voltage as output on the  $d$  and  $q$  ports.

The modified generator model has two additional power bond outputs, such that the generator model has both  $d$  and  $q$  ports with voltage as output and  $d$  and  $q$  ports with current as output. The 1-junctions are replaced with switched power  $1_s$ -junctions. When using switched power 1-junctions, two or more flow-deciding bonds are able to set flow on a  $1_s$ -junction, see Chapter 3.5. For the modified generator model, the  $1_s$ -junctions will have two flow-deciding bonds, and the variable  $U$  decides which of the two bonds that sets flow, see Figure 6.2.

Compared to the generator models presented in Chapter 3, the  $I$ -fields  $I_d$  and  $I_q$  of the modified generator model have one additional power bond each. Thus, the  $I$ -fields have both integral and derivative causality.

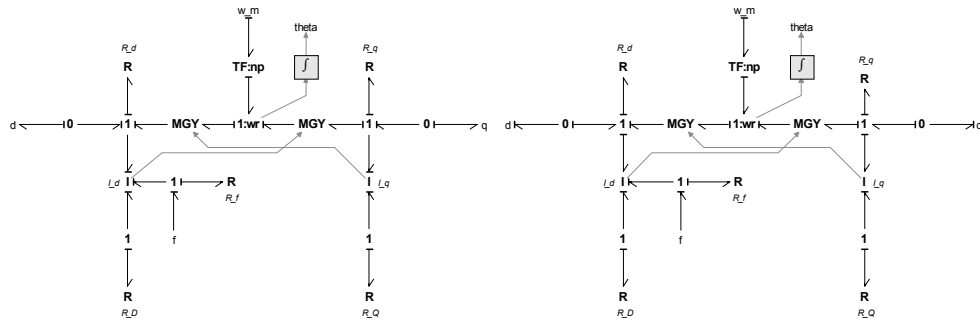


Figure 6.1:  $dq$ -model of generator with current as output.

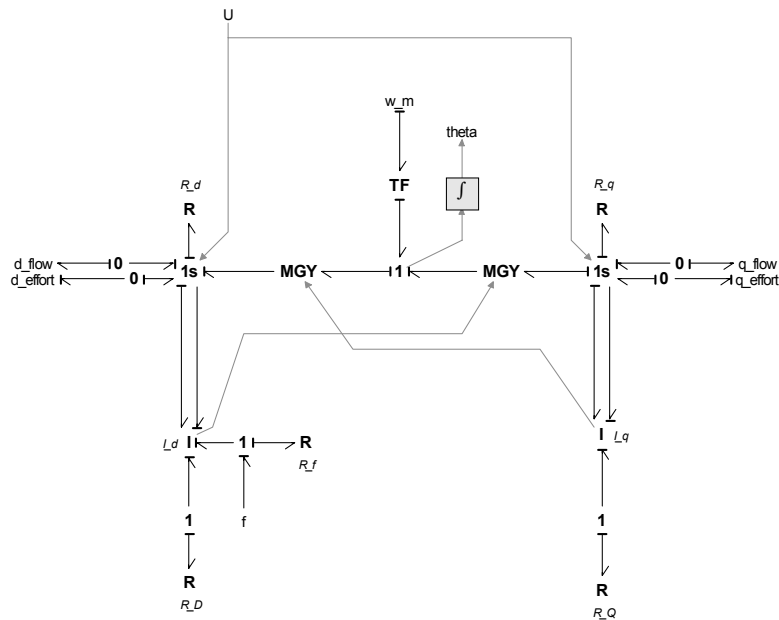


Figure 6.2: Modified generator model.

The modified generator model has the following input and output variables,

$$u = \begin{bmatrix} u_{d_{flow}} & u_{q_{flow}} & i_{d_{effort}} & i_{q_{effort}} & u_f & \omega \end{bmatrix} \text{ and}$$

$$y = \begin{bmatrix} i_{d_{flow}} & i_{q_{flow}} & u_{d_{effort}} & u_{q_{effort}} & i_f & T \end{bmatrix},$$

where  $u_{d_{flow}}$ ,  $u_{q_{flow}}$ ,  $i_{d_{flow}}$  and  $i_{q_{flow}}$  are voltage inputs and current outputs when generator is used as secondary generator, while  $i_{d_{effort}}$ ,  $i_{q_{effort}}$ ,  $u_{d_{effort}}$  and  $u_{q_{effort}}$  are current inputs and voltage outputs when generator is used as primary generator.  $u_f$  and  $i_f$  are generator magnetizing voltage and current,  $\omega$  is shaft speed and  $T$  is electromechanical torque.

The voltage balance for the modified generator model is given as

$$\dot{\psi}_{d_{flow}} = u_{d_{flow}} - R_d i_{d_{flow}} + \psi_{q_{flow}} n_p \omega_r, \quad (6.1)$$

$$\dot{\psi}_{q_{flow}} = u_{q_{flow}} - R_q i_{q_{flow}} - \psi_{d_{flow}} n_p \omega_r, \quad (6.2)$$

$$\dot{\psi}_{d_{effort}} = u_{d_{effort}} - R_d i_{d_{effort}} + \psi_{q_{effort}} n_p \omega_r, \quad (6.3)$$

$$\dot{\psi}_{q_{effort}} = u_{q_{effort}} - R_q i_{q_{effort}} - \psi_{d_{effort}} n_p \omega_r, \quad (6.4)$$

$$\dot{\psi}_f = u_f - R_f i_f, \quad (6.5)$$

$$\dot{\psi}_D = -R_D i_D \quad \text{and} \quad (6.6)$$

$$\dot{\psi}_Q = -R_Q i_Q. \quad (6.7)$$

It is reasonable to assume that the value of  $d$ - and  $q$ -axis current  $i_d$  and  $i_q$  and flux linkage  $\psi_d$  and  $\psi_q$  will be independent of generator mode, such that

$$i_{d_{flow}} \approx i_{d_{effort}} \quad \text{and} \quad i_{q_{flow}} \approx i_{q_{effort}}.$$

$$\psi_{d_{flow}} \approx \psi_{d_{effort}} \quad \text{and} \quad \psi_{q_{flow}} \approx \psi_{q_{effort}}.$$

These assumptions will be verified by simulations.

The flux linkages are given as

$$\psi_{d_{flow}} = -L_d i_{d_{flow}} + L_{df} i_f + L_{dD} i_D, \quad (6.8)$$

$$\psi_{q_{flow}} = -L_q i_{q_{flow}} + L_{qQ} i_Q, \quad (6.9)$$

$$\psi_{d_{effort}} = -L_d i_{d_{effort}} + L_{df} i_f + L_{dD} i_D, \quad (6.10)$$

$$\psi_{q_{effort}} = -L_q i_{q_{effort}} + L_{qQ} i_Q, \quad (6.11)$$

$$\psi_f = -L_{df} i_{d_{flow}} + L_f i_f + L_{fD} i_D, \quad (6.12)$$

$$\psi_D = -L_{dD} i_{d_{flow}} + L_{fD} i_f + L_D i_D \quad \text{and} \quad (6.13)$$

$$\psi_Q = -L_{qQ} i_{q_{flow}} + L_Q i_Q. \quad (6.14)$$

$L_d$ ,  $L_f$  and  $L_q$  are constant self inductances while  $L_{df}$ ,  $L_{dD}$ ,  $L_{fD}$  and  $L_{qQ}$  are constant mutual inductances.

Solving (6.8)-(6.14) with regard to  $\left[ i_{d_{flow}} \quad i_{q_{flow}} \quad \psi_{d_{effort}} \quad \psi_{q_{effort}} \quad i_f \quad i_D \quad i_Q \right]^T$  give

$$\begin{bmatrix} i_{d_{flow}} \\ i_{q_{flow}} \\ \psi_{d_{effort}} \\ \psi_{q_{effort}} \\ i_f \\ i_D \\ i_Q \end{bmatrix} = \begin{bmatrix} Z_{11} & 0 & 0 & 0 & Z_{15} & Z_{16} & 0 \\ 0 & Z_{22} & 0 & 0 & 0 & 0 & Z_{27} \\ 0 & 0 & Z_{33} & 0 & Z_{35} & Z_{36} & 0 \\ 0 & 0 & 0 & Z_{44} & 0 & 0 & Z_{47} \\ Z_{51} & 0 & 0 & 0 & Z_{55} & Z_{56} & 0 \\ Z_{61} & 0 & 0 & 0 & Z_{65} & Z_{66} & 0 \\ 0 & Z_{72} & 0 & 0 & 0 & 0 & Z_{77} \end{bmatrix} \begin{bmatrix} \psi_{d_{flow}} \\ \psi_{q_{flow}} \\ i_{d_{effort}} \\ i_{q_{effort}} \\ \psi_f \\ \psi_D \\ \psi_Q \end{bmatrix} \quad (6.15)$$

where

$$\begin{aligned}
Z_{11} &= \frac{-L_f L_D + L_{fD}^2}{-L_d L_f L_D + L_d L_{fD}^2 + L_{df}^2 L_D - 2L_{df} L_{dD} L_{fD} + L_{dD}^2 L_f}, \\
Z_{15} &= Z_{51} = \frac{L_{df} L_D - L_{dD} L_{fD}}{-L_d L_f L_D + L_d L_{fD}^2 + L_{df}^2 L_D - 2L_{df} L_{dD} L_{fD} + L_{dD}^2 L_f}, \\
Z_{16} &= Z_{61} = \frac{-L_{df} L_{fD} + L_f L_{dD}}{-L_d L_f L_D + L_d L_{fD}^2 + L_{df}^2 L_D - 2L_{df} L_{dD} L_{fD} + L_{dD}^2 L_f}, \\
Z_{22} &= \frac{-L_Q}{-L_q L_Q + L_{qQ}^2}, \\
Z_{27} &= Z_{72} = \frac{L_{qQ}}{-L_q L_Q + L_{qQ}^2}, \\
Z_{33} &= \frac{-L_d L_f L_D + L_d L_{fD}^2 + L_{df}^2 L_D - 2L_{df} L_{dD} L_{fD} + L_{dD}^2 L_f}{-L_f L_D + L_{fD}^2}, \\
Z_{35} &= \frac{L_{fD} L_{dD} - L_{df} L_D}{-L_f L_D + L_{fD}^2}, \\
Z_{36} &= \frac{L_{df} L_{fD} - L_f L_{dD}}{-L_f L_D + L_{fD}^2}, \\
Z_{55} &= \frac{-L_d L_D + L_{dD}^2}{-L_d L_f L_D + L_d L_{fD}^2 + L_{df}^2 L_D - 2L_{df} L_{dD} L_{fD} + L_{dD}^2 L_f}, \\
Z_{56} &= Z_{65} = \frac{L_d L_{fD} - L_{df} L_{dD}}{-L_d L_f L_D + L_d L_{fD}^2 + L_{df}^2 L_D - 2L_{df} L_{dD} L_{fD} + L_{dD}^2 L_f},
\end{aligned}$$

$$Z_{66} = \frac{-L_d L_f + L_{df}^2}{-L_d L_f L_D + L_d L_{fD}^2 + L_{df}^2 L_D - 2L_{df} L_{dD} L_{fD} + L_{dD}^2 L_f} \text{ and}$$

$$Z_{77} = \frac{-L_q}{-L_q L_Q + L_{qQ}^2}.$$

$u_{d_{effort}}$  and  $u_{q_{effort}}$  are then found by differentiation of  $\psi_{d_{effort}}$  and  $\psi_{q_{effort}}$ .

## 6.2 Basic setup with 2 generator models

The modified generator model is tested using a basic setup with 2 generator models, both able to set voltage. The system setup and simulation results are shown next.

### 6.2.1 System setup

The basic system setup used for testing the modified generator model is shown in Figure 6.3. Engine dynamics are not considered, such that the engines are replaced with modulated flow sources,  $M_1:MSf$  and  $M_2:MSf$ , setting generators shaft speed,  $\omega$ . The bus voltage is controlled by a PI controller which adjust the generator magnetization voltage. The *primaryGenSelector* selects which of the two generators setting bus voltage. The two generator models *G1* and *G2* are modeled according to the modified generator model developed previously, while the blocks *otherLoads* and *loadGenerator* are described in Chapter 3.10.

The bus consists of two  $0_s$ -junctions, one for the  $d$ -axis and one for the  $q$ -axis.  $0_s$ -junctions are used since both generators are able to set voltage.

### 6.2.2 Simulations

#### Verification

The first simulation is accomplished to verify the assumptions of  $d$ - and  $q$ -axis current ( $i_d$  and  $i_q$ ) and flux linkage ( $\psi_d$  and  $\psi_q$ ) being independent of generator mode. The derivative of  $\psi_{d_{effort}}$  and  $\psi_{q_{effort}}$  is found by solving a set of differential-algebraic equations using the implicit solver Backward Differentiation Formula (BDF).

Generator 1 is used as primary generator. At  $t = 0$  [s], generator voltage is 0. The reference voltage is ramped to 690[V] using a second order transfer function. The generator shaft speed is set to 75.4 [rad/s] which correspond to a bus frequency of 60 [Hz]. Figure 6.4 to Figure 6.6 show the simulation results when the following events appeared:

From  $t = 0$  to  $t = 50$ , total active and reactive power consumption are 0. At  $t = 50$  [s] active power consumption of *otherLoads* starts to increase to 1500

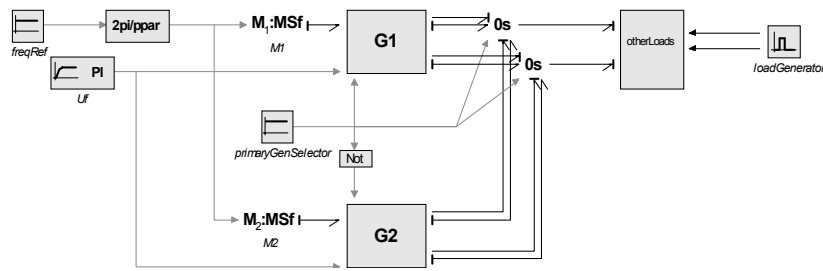


Figure 6.3: Basic setup with 2 generators models.

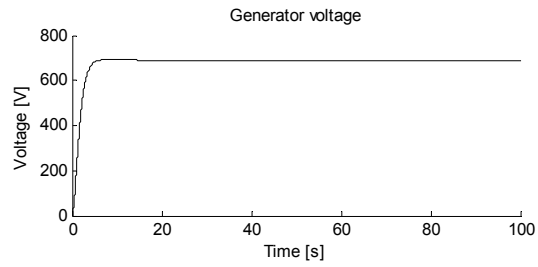


Figure 6.4: Generator voltage.

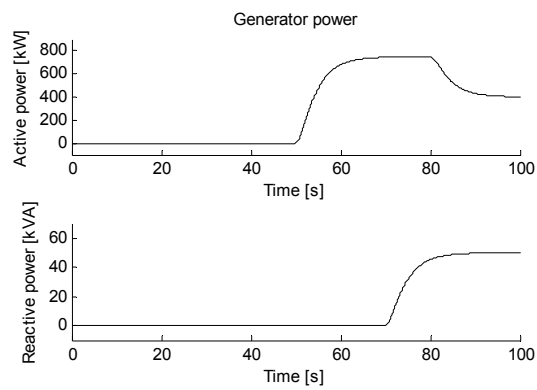


Figure 6.5: Generator, active and power.

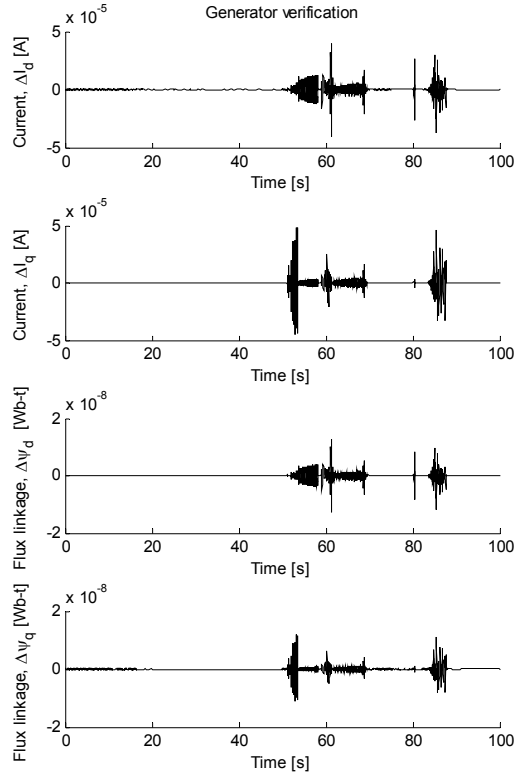


Figure 6.6: Generator current  $\Delta i_d$  and  $\Delta i_q$ , flux linkage  $\Delta \psi_d$  and  $\Delta \psi_q$  and voltage  $\Delta u_d$  and  $\Delta u_q$ . Derivative of  $\psi_d$  and  $\psi_q$  are found by solving a set of differential-algebraic equations.

[kW], and at  $t = 70$  [s] reactive power starts to increase to 100 [kVA]. At  $t = 80$  [s] the total active power consumption is decreased to 800 [kW]. Both generators are connected to the bus, and active and reactive load are equally shared.

The generator voltage is shown in Figure 6.4, while total active and reactive power consumption from *otherLoads* are shown in Figure 6.5. Figure 6.6 show generator currents  $\Delta i_d$  and  $\Delta i_q$ , flux linkages  $\Delta \psi_d$  and  $\Delta \psi_q$  and voltage  $\Delta u_d$  and  $\Delta u_q$  which are calculated as

$$\begin{aligned}\Delta i_d &= i_{d_{flow}} - i_{d_{effort}}, \quad \Delta i_q = i_{q_{flow}} - i_{q_{effort}}, \\ \Delta \psi_d &= \psi_{d_{flow}} - \psi_{d_{effort}}, \quad \Delta \psi_q = \psi_{q_{flow}} - \psi_{q_{effort}}, \\ \Delta u_d &= u_{d_{flow}} - u_{d_{effort}} \quad \text{and} \quad \Delta u_q = u_{q_{flow}} - u_{q_{effort}}.\end{aligned}$$

The comparison show that the difference between currents, flux linkages and voltages are very small ( $|\Delta| \leq 5 \cdot 10^{-5}$ ), such that the calculation of generator currents, flux linkages and voltages are independent of generator mode.

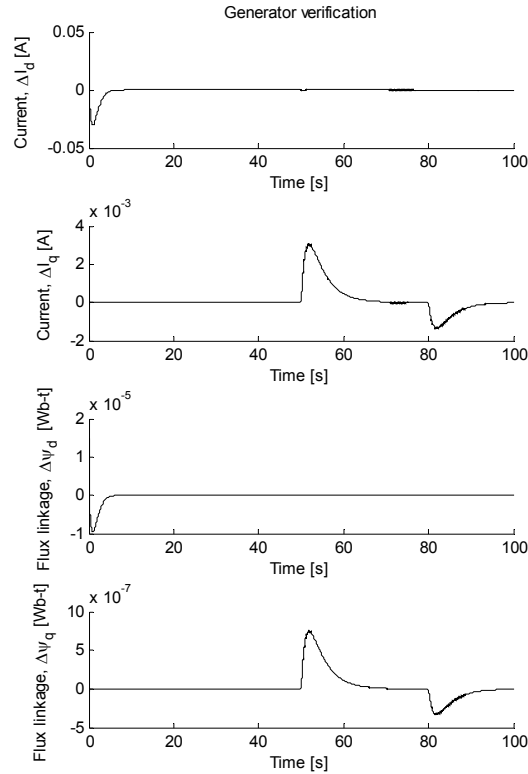


Figure 6.7: Generator current  $\Delta I_d$  and  $\Delta I_q$ , flux linkage  $\Delta \psi_d$  and  $\Delta \psi_q$  and voltage  $\Delta u_d$  and  $\Delta u_q$ . Derivative of  $\psi_d$  and  $\psi_q$  are found by numerical differentiation.

Next, the derivative of  $\psi_{d_{effort}}$  and  $\psi_{q_{effort}}$  is found by numerical differentiation. The transfer function for a first order filter and the derivative is given as, see Chapter 3.2,

$$h(s) = \frac{y(s)}{u(s)} = \frac{s}{1 + Ts}. \quad (6.16)$$

$T$  is a small time constant.

Figure 6.7 show the simulation results when the simulation setup and events are the same as the previous simulation. The small time constant is set to  $T = 1 \cdot 10^{-5}$ . From the figure one may notice that the differences  $\Delta i_d$ ,  $\Delta i_q$ ,  $\Delta \psi_d$  and  $\Delta \psi_q$  have increased compared to the previous simulation, and especially  $\Delta i_d$  has increased. The relatively large increase in  $\Delta i_d$  occurs when generator voltage is raised from 0 to 690 [V]. This “error” is caused by the filtration of  $\psi_d$  before the signal is differentiated, and the error is proportional to the time constant used in the filtration.

Despite the difference in  $\Delta i_d$ , it is assumed that the model is good enough for overall system dynamic studies.

### Change of primary generators when load demand is changed in steps

The next simulation has been performed with the following events:

From  $t = 0$  to  $t = 50$ , total active and reactive power consumption are 0. At  $t = 50$  [s] active power consumption of *otherLoads* starts to increase to 3000 [kW], and at  $t = 60$  [s] reactive power starts to increase to 100 [kVA]. At  $t = 80$  [s] the total active power consumption is decreased to 800 [kW]. Both generators are connected to the bus, and active and reactive load are equally shared.

At startup, generator 1 is chosen as primary generator. At  $t = 30$  [s], the primary generator is changed to generator 2, while generator 1 is set to be primary generator from  $t = 70$  [s].

Figure 6.8 to Figure 6.12 show the simulation results. Figure 6.8 show which of the two generators that are selected as primary generator. The next figure, Figure 6.9, show the voltage of generator 1 and 2, while generator field voltage is presented in Figure 6.10. The last two figures, Figure 6.11 and Figure 6.12, show active and reactive power for the load demand together with active and reactive power for generator 1 and 2.

The simulation show that switching between primary generators is done without difficulties and generator voltage, power generation and field voltage are not influenced by the switching.

### Change of primary generators with time varying load demand

The last simulation has been accomplished with time varying load demand. Figure 6.13 to Figure 6.16 show the simulation results when the following events occur:

Active power consumption are 0 from  $t = 0$  [s] to  $t = 15$  [s]. At  $t = 15$  active power demand is increased from 0 to 3000 [kW] and at  $t = 20$  an extra time varying active load demand  $|P| \leq 1000$  [kW] is added. At  $t = 60$  the constant active power demand is reduced with 1200 [kW]. Reactive power demand is held at 0 throughout the simulation.

As for the previous simulation, generator 1 is first selected as primary generator. Then generator 2 is set to be primary generator at  $t = 30$  [s], and generator 1 is primary generator from  $t = 70$  [s].

Selection of primary generator is indicated in Figure 6.13, while generator voltage and field voltage are presented in Figure 6.14 and Figure 6.15. Active power consumption of *otherLoads* together with active power generation are shown in Figure 6.16.

Once again the simulation show that there are no problems in connection with switching of primary generator and the switching do not affect the simulation results.

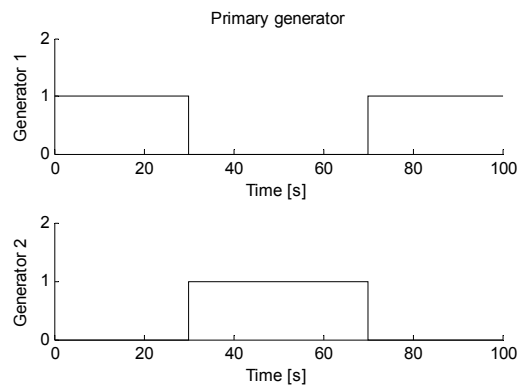


Figure 6.8: Selection of primary generator.

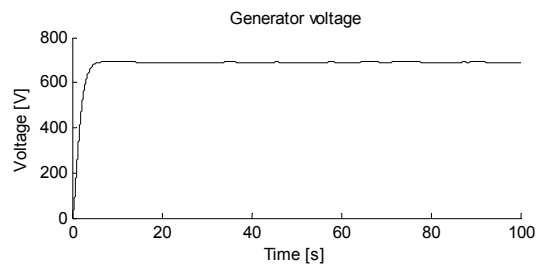


Figure 6.9: Generator voltage.

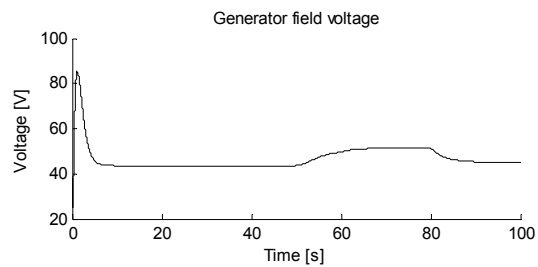


Figure 6.10: Generator field voltage.

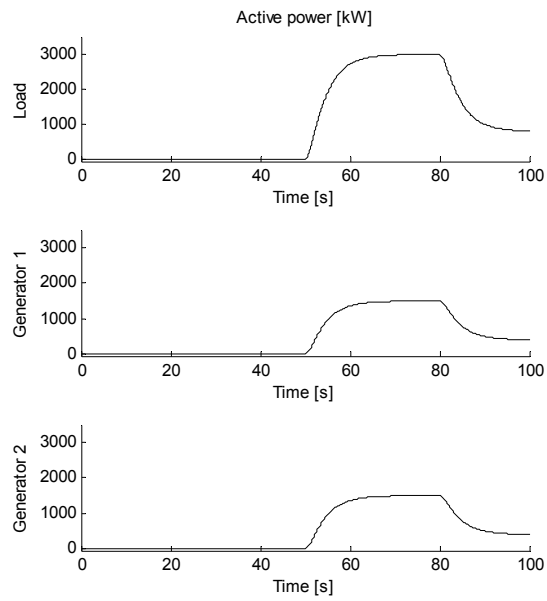


Figure 6.11: Active power, load, generator 1 and generator 2.

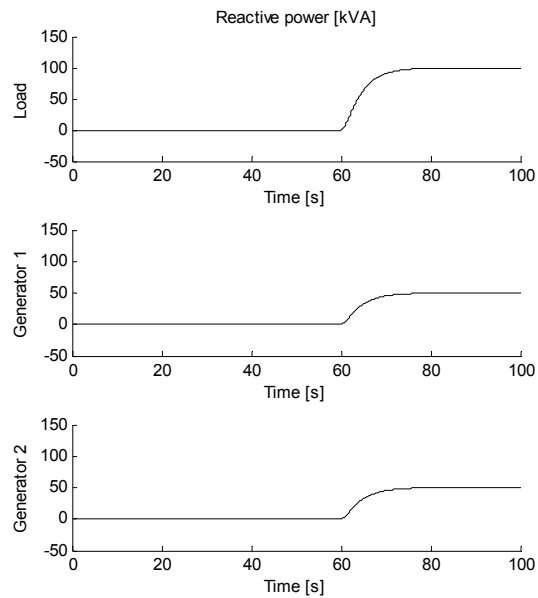


Figure 6.12: Reactive power, load, generator 1 and generator 2.

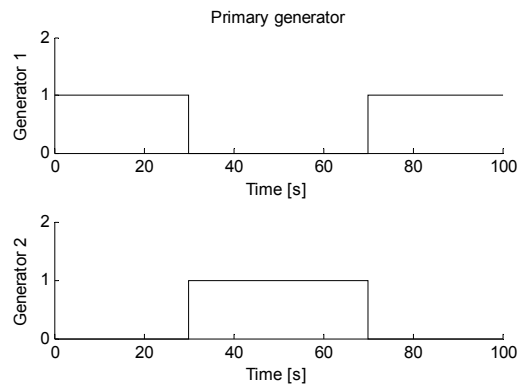


Figure 6.13: Selection of primary generator.

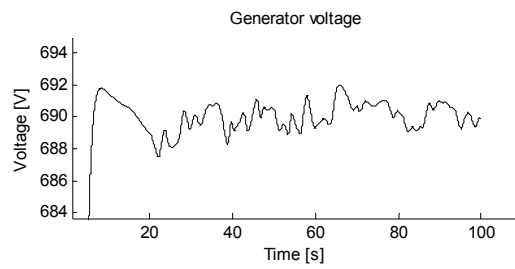


Figure 6.14: Generator voltage.

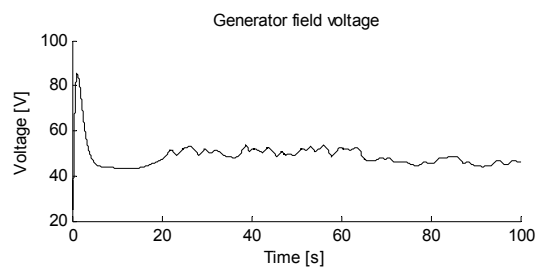


Figure 6.15: Generator field voltage.

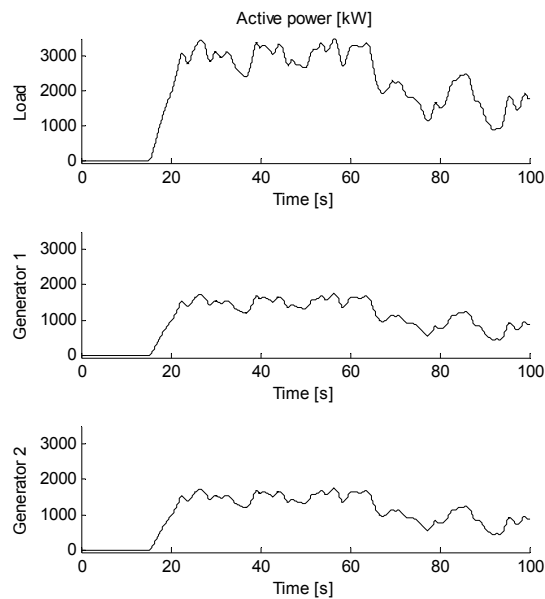


Figure 6.16: Active power, load, generator 1 and generator 2.

Next, a presentation of how the modified generator may be used to model a complete power plant is presented.

### 6.3 Use of modified generator model in a power plant

When modeling complex power systems, it is desirable that the modeling tool and library do not limit the possibility to recreate the system which is to be modeled. In an actual power plant, there is no constraint in which generator set that should be connected to the bus, and the power plant may consist of several buses which may run independent of each other.

By using the modified generator model, the modeler will be able to model complex power systems consisting of several generator sets, buses and power consumers. The different buses may run independent of each other, but they may also be synchronized and ran together as one bus. All generators may be connected to or disconnected from the buses independent of which generator that is primary generator. If a primary generator shall be disconnected, another generator will be set to primary generator, before disconnecting the first generator.

Use of the modified generator model is shown in Figure 6.17. The power plant consist of 4 generator sets, 4 circuit breakers, 2 buses, 1 bus tie, 2 stern thrusters, 2 bow thrusters and 2 set of *otherLoads* which model power consumption of hotel

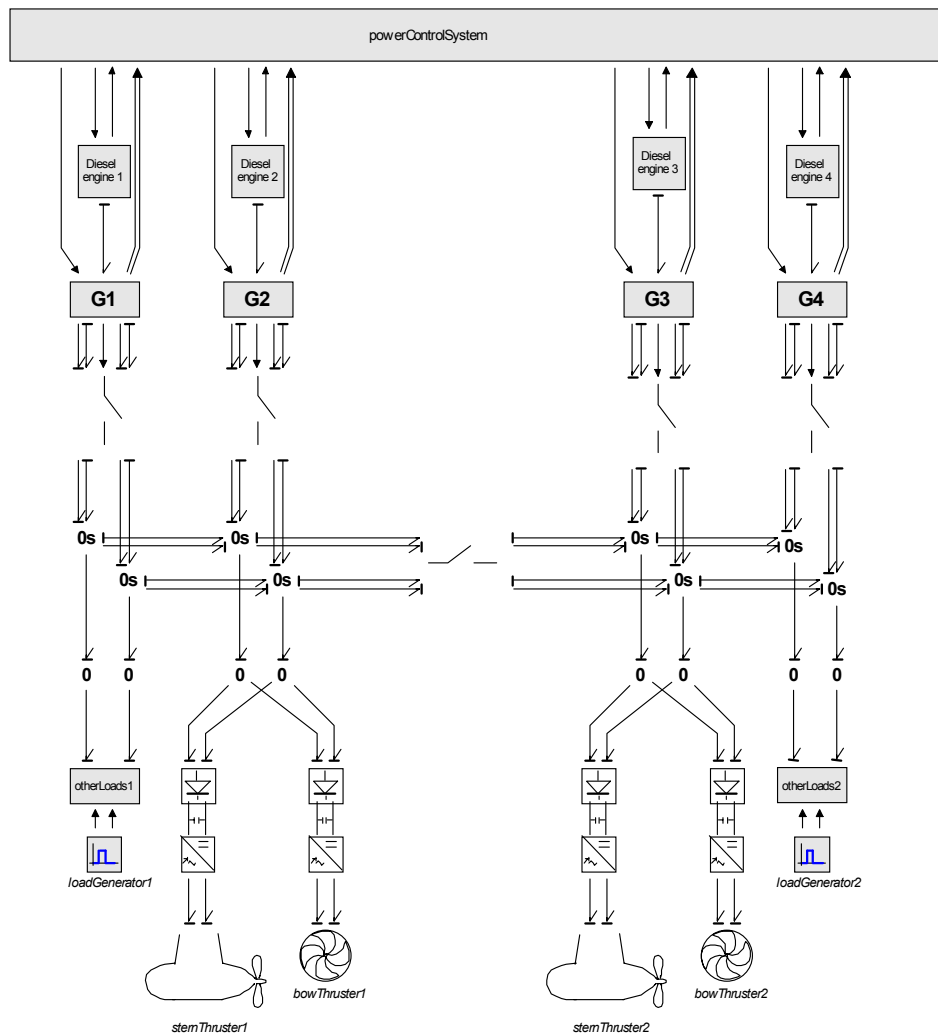


Figure 6.17: Bond graph representation of a complete power plant.

loads, pumps and other minor power consumers. The signal bonds used for setting primary generator are omitted.

Any of the four generator sets may be primary generator setting voltage on the bus. If the bus tie between the two buses is open, two generator sets, one on each side, are used as primary generator sets. If a close command is given for the bus tie, the two buses will be synchronized, and then connected. At the same time the bus tie is closed, one of the two primary generator sets, will switch from being a primary generator set to being a secondary generator set, and then only one generator set is used as primary generator set.

## Chapter 7

# Conclusions and recommendations

### 7.1 Conclusions

The main intension for writing this thesis was to develop a flexible component library that supports modularity and reuse of models and it was also a desire that the component library should strongly support the modeling phase across modeling disciplines.

An All Electric Ship library is presented in Chapter 2. The chapter starts with a discussion about modeling environments. By making the AES library platform independent, the component models could be developed in different modeling environments and then done platform independent by using a translator. Two problems may arise when making the component models platform independent; the resulting code may be complex and difficult to read and understand, and it may also be difficult to make a translator that is capable of handling all options when it comes to the written code. The idea of a complete platform independent library was abandoned, instead a component library that support and aid the modeler understanding during the modeling phase was developed using the bond graph methodology. The chapter ends with a presentation of a selected template for model documentation.

The different component models are developed in Chapter 3. First a mathematical description of the components are given and then the corresponding bond graph representation of the components are shown. The following power plant components are treated: Diesel and gas engine, synchronous generator with and without magnetic saturation, circuit breaker, fuel cell, asynchronous motor, power converter, propeller, hotel and auxiliary loads, ship and environmental loads.

The majority of the models developed in Chapter 3 have been verified in Chapter 4. The verification has been accomplished by using result of measurements collected during a two days trip with the supply vessel Viking Energy. Test measurements from component manufacturers have also been used for verification.

Chapter 5 presented three simulation cases. The first case dealt with extreme load variations, such as rough sea and sudden disconnection of generator sets due to

errors. The second case simulated a typical DP-operation, while the third case treated a combined power plant consisting of generators and a fuel cell.

The generator models developed in Chapter 3 have either current or voltage as output, and the generator with voltage as output has to be connected to the bus throughout the simulation. A modified version of the synchronous generator was therefore developed in Chapter 6. The new generator model had both current and voltage as output. Using the modified generator model when modeling power plants, all generators could be connected and disconnected from the bus. The first generator connected to the bus will have voltage as output, and the other generators will have current as output. If the first generator shall be disconnected, another generator will set voltage instead of the first generator, thus obtaining a more flexible simulation.

This thesis has focused on developing a flexible and modular component library. The component models have been tested, verified and used in modeling of different power plant layouts. The verification show that the models are able to reflect the behavior of real system components quite well and the system testing also show reasonable results. The modified version of the generator model gives additional flexibility to the modeler when modeling electric power systems.

## 7.2 Recommendations for future work

The power plant efficiency may be improved if combining a high temperature fuel cell and a gas turbine in a hybrid system. The fuel cell generates high temperature exhaust gas which could be used in a combined cycle with the gas turbine. The component library should therefore be extended with a generic gas turbine model and a more advanced thermodynamic model of the fuel cell, such that the library could be used to simulate such systems as well.

More advanced models including thermodynamic models of the diesel and gas engine together with waste heat consumers should also be developed to incorporate waste heat calculation. The exhaust gas temperature for the diesel and gas engine is high and if including waste heat calculations, the simulator could be used to optimize the power plant for higher efficiency.

The power plant behavior is controlled by a Power Management System which start and stop generator sets using a predefined start and stop table and calculates thrust limitation based on power available on the bus. More advanced optimization algorithms could be included in an Energy Management System which will optimize the power plant for high efficiency and at the same time low emissions.

The different models have been verified using test measurements and full scale measurements from a supply vessel. The complete power plant model could also be

---

verified using full scale measurements. In addition, the library could be used to model other power plants and verification could be done to those systems as well to check the goodness of the library.

The modified generator model developed in Chapter 6 has only been used in a small system consisting of two generators and a load to check the behavior of the generator model when the status of the generator is changed from primary generator to secondary generator. The modified generator model should be more completely tested in a more complex system, for instance the system shown in Figure 6.17.



## Bibliography

- [20-sim 2006] ControlLab Products B.V., *The 20-Sim user manual*, Version 3.6.0.11, 2006.
- [Ådnanes et al. 1997] Ådnanes, A. K., Sørensen, A. J. and Hackmann, T., *Essential characteristics of electrical propulsion and thruster drives in DP vessels*, Dynamic Positioning Conference, DPC, Houston, Texas, 1997.
- [Ådnanes 2003] Ådnanes, A. K., *Maritime Electrical Installations And Diesel Electric Propulsion*, ABB Marine AS, Oslo, Norway, 2003.
- [Allard et al. 1997] Allard, B., Morel, H., Lautier, P. and Retif, J-M., *Bond Graphs for Averaged Modeling of Power Converters*, Proceedings of International Conference on Bond Graph Modeling ICBGM'97, Simulation Series, vol 29, no 1, pp. 201-206, 1997.
- [Allard et al. 1999] Allard, B., Morel, H., Ghedira, S. and Ammous, A., *Building Advanced Averaged Models of Power Converters from Switched Bond Graph Representation*, Proceedings of International Conference on Bond Graph Modeling ICBGM'99, Simulation Series, vol 31, no 1, pp. 331-337, 1999.
- [Arrillaga and Watson 2002] Arrillaga, J. and Watson, N. R., *Power Systems Electromagnetic Transients Simulation*. Institution of Engineering and Technology, 2002.
- [Asher 1993] Asher, G. M., *The robust modeling of variable topology circuits using bond graphs*, Proceedings for International Conference on Bond Graph modeling, pp. 126-131, San Diego, CA, 1993.
- [Boldea and Nasar, 1988] Boldea, I and Nasar, S.A., *A General Equivalent Circuit (GEC) of Electric Machines*, IEEE Transactions on Energy Conversion, vol. 3, no. 3, pp. 689-695, 1988.
- [Borutzky et al., 1995] Borutzky, W., Dauphin-Tanguy, G., and Thoma, J.U., *Advances in bond graph modeling: theory, software and applications*, Mathematics and Computers in Simulation, Vol 39, pp. 465-475, 1995.
- [Borutzky 1999] Borutzky, W., *Bond Graph modeling from an object oriented modeling point of view*, Simulation Practice and Theory, Volume 7, Issues 5-6, pp. 439-461, 1999.
- [Breunese et al. 1998] Breunese, A. P. J., Top, J. L., Broenink, J. F. and Akkermans, J. M., *Libraries of Reusable Models: Theory and Application*, SIMULATION 71:1, pp. 7-22, 1998.

- [Broughton et al. 2004] Broughton, E., Langland, B., Solodovnik, E. and Croft, G., *Virtual Test Bed, User's Manual*, Univeristy of South Carolina, 2004.
- [Bruun and Pedersen 2007], Bruun, K. and Pedersen, E., *Bond Graph Model of a High Temperature Fuel Cell*, Proceedings of International Conference on Bond Graph Modeling ICBGM'07, Simulation Series, vol 39, no 1, 2007.
- [Buja and Kazmierkowski, 2004] Buja, G. S. and Kazmierkowski, M. P., *Direct Torque Control of PWM Inverter-Fed AC Motors - A Survey*, IEEE Transactions on Industrial electronics, vol. 51, no. 4, 2004.
- [Chen et al. 1996] Chen, S., Lipo, T. A. and Novotny, D.W., *Circulating type motor bearing current in inverter drives*, Conference Record - IAS Annual Meeting (IEEE Industry Applications Society), vol. 1, pp. 162–167, Oct. 1996.
- [Chwirka 2000] Chwirka, S., *Using the Powerful SABER Simulator for Simulation, Modeling and Analysis of Power Systems, Circuits and Devices*, IEEE Workshop on Computers in Power Electronics, pp. 172-176, 2000.
- [Corzine et al. 1998] Corzine, K. A., Kuhn, B. T., Sudhoff, S. D. and Hegner, H. J., *An improved method for incorporating magnetic saturation in the Q-D Synchronous Machine model*, IEEE Transactions on Energy Conversion, Vol. 13, No. 3, 1998.
- [Doerry and Davis 1994] Doerry, N. H. and Davis, J. C., *Integrated power system for marine application*, Noval Engineers Journal, pp. 77-90, 1994.
- [Doherty and Nickle, 1926] R. E. Doherty and C. A. Nickle, *Synchronous machines I and II, an extension of Blondel's two reation theory*, AIEE trans, Vol. 45, pp 912-947, 1926.
- [Dougal 2003] Dougal, R. A., *VTB Project Overview*, University of South Carolina, <http://vtb.engr.sc.edu/>, 2003.
- [Eidesvik 2008] Eidesvik Offshore ASA, Bømlo, Norway, web: <http://www.eidesvik.no/Fleet/PDF%20-%20Full%20Spec/Viking%20Energy.pdf>
- [Einang and Haavik 2000] Einang, P. M. and Haavik, K., *The Norwegian LNG Ferry*, Proceedings NGV 2000, 7th International Conference and Exhibition on Natural Gas Vehicles, Yokohama, Japan, 2000.
- [EL-Sharkh et al. 2004] El-Sharkh, M. Y., Rahman, A., Alam, M. S., Sakla, A. A., Byrne, P. C and Thomas, T., *Analysis of Active and Reactive Power Control of a Stand-Alone PEM Fuel Cell Power Plant*, IEEE Transactions on Power Systems, Vol. 19, No. 4, pp 2022-2028, 2004.
- [Erdman et al., 1996] Erdman, J. M., Kerkman, R. J., Schlegel, D.W. and Skibinski, G. L., *Effect of PWM inverters on AC motor bearing currents and shaft voltages*, IEEE Transactions on Industry Applications, vol. 32, pp. 250–259, 1996.
- [Faltinsen 1990] Faltinsen, O. M., *Sea Loads on Ship and Offshore Structures*, Cambridge University Press, Cambridge, UK, 1990.

- 
- [Fossen 1994] Fossen T. I., *Guidance and control of ocean vehicles*, John Wiley & Sons, Inc., 1994.
- [Fossen 2002] Fossen, T.I., *Marine Control Systems: Guidance, Navigation and Control of Ships, Rigs and Underwater Vehicles*, 1st. Ed., 3rd. Printing, Marine Cybernetics AS, 2002.
- [Fuentes et al. 2007] Fuentes, J.A., Molina, A., Ruz, F., Gomez, E. and Jimenez, F., *Wind Turbine Modeling: Comparison of Advanced Tools for Transient Analysis*, IEEE, Power Engineering Society General Meeting, pp. 1-6, 2007.
- [Getreu 1990] Getreu, I. E., *Behavioral modeling of analog blocks using SABER simulator*, Midwest Symposium on Circuits and Systems, pp. 977-980, 1990.
- [Hansen 2000] Hansen, J. F., *Modeling and control of marine power systems*, Doctoral thesis, NTNU, Norway, 2000.
- [Harley et al. 1995] Harley, R. G., Limebeer, D.J.N. and Chirricozzi, E., *Comparative Study of Saturation Methods in Synchronous Machine Models*, IEEE Proceedings, vol 127, Part B, January 1980.
- [Hasselmann et al. 1973] Hasselmann K., Barnett, T.P., Bouws, E., Carlson, H., Cartwright D.E., Enke, K., Ewing, J.A., Gienapp, H., Hasselmann, D.E. , Kruseman, P., Meerburg, A., Mller, P., Olbers. D.J., Richter, K., Sell, W. and Walden, H., *Measurements of wind-wave growth and swell decay during the Joint North Sea Wave Project (JONSWAP)*. Ergänzungsheft zur Deutschen Hydrographischen Zeitschrift Reihe A(8) (Nr. 12): 95, 1973
- [Heywood 1988] Heywood, B., *Internal Combustion Engine Fundamentals*, International edition, McGraw-Hill Book Company, 1988.
- [Hill et al. 1992] Hill, W. A., Creelman, G. and Misschke, L., *Control strategy for an icebreaker propulsion system*, IEEE Transactions on industry applications 28(4), pp. 887-892, 1992.
- [Hirayama 1995] Hirayama, K., *Practical detailed model for generators*, IEEE Transaction on Energy Conversion, Vol. 10, No. 1, 1995.
- [Hopkins 1991] Hopkins, J. K., *Fantasy and reality*, Trans IMarE 103, pp. 193-220, 1991.
- [IMO 1997] International Maritime Organization, *Prevention of Air Pollution from Ships*, [http://www.imo.org/Environment/mainframe.asp?topic\\_id=233](http://www.imo.org/Environment/mainframe.asp?topic_id=233), 1997.
- [Jonasson and Soder 2001] Jonasson, I. and Soder, L., *Power quality on ships - A questionnaire evaluation concerning island power system*, proceedings of the IEEE Power Engineering Society Transmission and Distribution Conference, v 1, pp. 216-221, 2001.
- [Junco et al. 2007] Junco, S., Diéguez, G and Ramirez, F., *On Commutation Modeling in Bond Graphs*, Proceedings of International Conference on Bond Graph Modeling ICBGM'07, Simulation Series, vol 39, no 1, pp. 12-19, 2007.

- [Karnopp et al. 1992] D. C. Karnopp, R. C. Rosenberg, *System Dynamics - A Unified Approach*, second ed., Wiley Interscience Publications, New York, 1992.
- [Krause et al. 1995] Krause, P. C., Wasynczuk, O. and Sudhoff, S. D., *Analysis of Electric Machinery*, IEEE Press, 1995.
- [Krause et al. 2002] Krause, P. C., Wasynczuk, O. and Sudhoff, S. D., *Analysis of Electric Machinery and Drive Systems*, second edition, IEEE press PowerEngineering Series, John Wiley & Sons, 2002.
- [Krean 1995] Krean Simulation software, web-page: <http://www.elkraft.ntnu.no/sw/krean.html>, ver 4.0, 1995.
- [Kron, 1935] G. Kron, *The application of tensors to the analysis of rotating electrical machinery - part III. The generalized rotating machine*, Gen. Elect. Rev., Vil. 38, pp 282-292, 1935.
- [Kwatny et al. 1996] Kwatny, H.G., Maffezzoni C., Paserba, J. J., Sanchez-Gasca, J. J. and Larsen, E. V. *The Control handbook*, Chap. 79 Control of Electrical Power, pp. 1453-1495, CRC Press, 1996.
- [Lammeren et al. 1969] Van Lammeren, W. P. A., Van Manen, J. D., Oosterveld, N.W.C, *The Wageningen B-Screw Series*, Transactions - Society of Naval Architects and Marine Engineers, Vol 77, pp. 269-317, 1969.
- [LIN-SHI et al. 2001] Lin-Shi, X., Retif, J-M., Allard, B. and Morel, H., *Averaged Model of a Boost Converter for Control Design*, Proceedings of International Conference on Bond Graph Modeling ICBGM'01, Simulation Series, vol 33, no 1, pp. 185-190, 2001.
- [Mahseredjian et al. 2001] Mahseredjian, J., Sybille, G. and Giroux, P., *Solution Methods and Tools, Part I: Solution Methods*, IEEE PES, panelSession Simulation of FACTS and Custom-Power controllers, Winter Meeting, Columbus, 2001.
- [Manitoba HVDC 2006] Manitoba HVDC Research Centre, *PSCAD, The Professional's Toolset for Power System Simulation, Online Help*, Version 4.2.1, 2006.
- [Mariani and Murthy 1997] Mariani, E. and Murthy, S.S., *Control of modern integrated power systems*, Advances in industrial control, Springer Verlag, 1997.
- [MARPOL 1973/1978] International Maritime Organization, *International Convention for the Prevention of Pollution from Ships, 1973, as modified by the Protocol of 1978 relating thereto*, web: [http://www.imo.org/Conventions/contents.asp?doc\\_id=678&topic\\_id=258](http://www.imo.org/Conventions/contents.asp?doc_id=678&topic_id=258).
- [MathWorks 2007] The MathWorks, Inc, *The Matlab/Simulink User Manual*, version 7.4.0.287 (R2007a), 2007.

- 
- [Middtveit and Nilsen 1987] Middtveit, R. and Nilsen, R., *Transformerte Modeller for Dreiefeltmaskiner*, Elektrisitetsforsyningens forskningsinstitutt A/S, NTH Trykk, Trondheim, Oslo, 1987
- [Miniovich 1960] Miniovich, I. Y., *Investigation of Hydrodynamic Characteristics of Screw Propellers under Conditions of Reversing and Calculation Methods for Backing of Ships*, Buships Translation 697, 1960.
- [Modelica 2007] Modelica Association, *Modelica - A Unified Object-Oriented Language for Physical Systems Modeling, Language Specification*, version 3.0, 2007.
- [Mohan et al. 1989] Mohan, N., Undeland, T. M. and Robbins, W. P., *Power Electronics: Converters, Applications and Design*, John Wilwy & Sons, Inc, 1989.
- [Morel et al. 1999] Morel, H., Allard, B., Ammous, A. and Ghedira, S., *Formal Causality Analysis*, Proceedings of International Conference on Bond Graph Modeling ICBGM'99, Simulation Series, vol 31, no 1, pp. 65-70, 1999.
- [Myrhaug 2000] Myrhaug, D., *Irregular seas*, Lecture notes, SIN1015 Marine Dynamics, Norwegian University of Science and Technology, 2004.
- [Nagel 2004] Nagel L. W., *Is It Time for SPICE4?*, Numerical Aspects of Circuit & Device Modeling, Workshop, Sandia National Laboratories, 2004.
- [Nilssen and Mo 1990] Nilssen, R. and Mo, Olve, *KREAN, A New Simulation Program for Power Electronic Circuits*, PESC Record - IEEE Power Electronics Specialists Conference, v 2, pp. 506-511, 1990.
- [Oosterveld and van Oossanen 1975] Oosterveld, M. W. C and Van Oossanen, P., *Further Computer Analyzed Data of the Wageningen B-Screw Series*, International Shipbuilding Progress Vol 22, n 251, pp. 251-262, 1975.
- [Ordys et al. 1994] Ordys, A., Pike A. W., Johnson, M. A. Katebi, R. and Grimble, M. J., *Modeling and Simulation of Power Generation Plants*, Advances in Industrial Control, Springer-Verlag, 1994.
- [Ouroua et al. 2005] Ouroua, A., Domaschk, L. and Beno, J. H., *Electric Ship Power System Integration Analyses Through Modeling and Simulation*, IEEE Electric Ship Technologies Symposium, pp. 70-74, 2005.
- [Ouroua 2007] Ouroua, H., *ONR Electric Ship; Power System Modeling and Simulation*, The University of Texas at Austin, web: [http://www.utexas.edu/research/cem/Electric\\_Ship\\_Hamid.html](http://www.utexas.edu/research/cem/Electric_Ship_Hamid.html), 2007.
- [Padullés et al. 2000] Padullés, J., Ault, G. W. and McDonald, J. R., *An integrated SOFC plant dynamic model for power system simulation*, Journal of Power Sources 86, pp. 495-500, 2000.
- [Palsson et al. 2000] Palsson, J., Selimovic, A. and Sjunnesson, L., *Combined solid oxide fuel cell and gas turbine systems for efficient power and heat generation*, Journal of Power Sources, v 86, n 1-2, pp. 442-448, 2000.

- [Panigrahi et al. 2006] Panigrahi, B. P., Dinkar, P. and Sabyasachi, S., *A simple hardware realization of switching table based direct torque control of induction motor*, Electric Power Systems Research, v 77, n 2, pp. 181-190, 2007.
- [Park 1929] R. H. Park, *Two reaction theory of synchronous machines, generalized method of analysis - part I*, AIEE Trans, Vol. 48, pp. 716-727, 1929.
- [Pedersen and Nilsen 1998] Pedersen, E. and Nilsen, R., *Alternative pu systems and models for synchronous motors*, in norwegian, Marintek, Norwegian Marine Technology Research Institute, 1998.
- [Pedersen and Engja 2003] Pedersen, E. and Engja, H., *Mathematical Modeling and Simulation of Physical Systems*, Lecture Notes in TMR4275 Modeling, Simulation and Analysis of Dynamic Systems, NTNU, Norway, 2003.
- [Pedersen 2005] Pedersen, E., *EE-AES Modeling Machinery Systems*, Presentation, Energy Efficient All Electric Ship workshop, NTNU, 2005
- [Posten 1984] Posten, R. M., *When does more documentation mean less work?*, Software Standards, IEEE Software, 1984.
- [PSCAD 2005] Manitoba HVDC Research Centre, *PSCAD™ Users Manual*, version 4.2, 2005.
- [Rendusara and Enjeti 1997] D. Rendusara and P. Enjeti, *New inverter output filter configuration reduces common mode and differential mode dv/dt at the motor terminals in PWM drive systems*, in Proceedings of IEEE Annual Power Electronics Specialists Conferenc, vol. 2, pp. 1269-1275, 1997.
- [Ruth 2008] Ruth, E., *Propulsion control and thrust allocation on marine vessels*, Doctoral Thesis, Department of Marine Technology, Norwegian University of Science and Technology, 2008.
- [Sahm 1979] Sahm, D., *A Two-Axis, Bond Graph Model of the Dynamics of Synchronous Electrical Machines*, Journal of The Franklin Institute, vol 308, No. 3, pp. 205-218, 1979.
- [Sallabank and Whitehead 1995] Sallabank, P. H. and Whitehead, A. J., *The practical application of modern simulation tool throughout the design and trials of a diesel electric propulsion system*, Trans ImarE 107, pp. 101-117, 1995.
- [Schriek and de Nijs 1991] Schriek, D. and de Nijs, J. W., *Royal Netherlands Navy M-class Frigate: Integrated Monitoring and Control System and Electrical Installation*, Trans IMarE 103, pp. 269-291, 1991.
- [Schonung and Stemmler 1964] Schonung, A. and Stemmler, H., *Static Frequency Changers with Subharmonic Control in Conjunction with Reversible Variable Speed AC Drives*, Brown Boveri Rev., pp. 555-577, 1964.
- [Sen 1997] Sen, P. C., *Principles of Electric Machines and Power Electronics*, 2nd edition, John Wiley & Sons, Inc., 1997.

- 
- [Singh et al. 2005] Singh, G. K., Singh, D. K. P., Nam, K., Lim, S. K., *A Simple Indirect Field-Oriented Control Scheme for Multiconverter-fed Induction Motor*, IEEE Transactions on Industrial Electronics, v 52, n 6, pp. 1653-1659, 2005.
- [Smith et al. 1985] Smith, J. R., Stronach, A. F. and Mitchell, A. T., *Prediction of the Electrical System Behaviour of Special Purpose Vessels*, Trans IMarE 97, pp. 11-22, 1985.
- [Smogeli 2006] Smogeli, Ø. N., *Control of Marine Propellers, From Normal to Extreme Conditions*, Doctoral Thesis, Department of Marine Technology, Norwegian University of Science and Technology, 2006.
- [Synopsys 2006] Synopsys, *Saber, The cutting Edge*, Saber Newsletter, 2006.
- [Sørensen 2005] Sørensen, A. J., *Lecture Notes: Marine Cybernetics, Modeling and Control*, Department of Marine Technology, NTNU, 2005.
- [Sozer et al. 2000] Sozer, Y., Torrey, D. A. and Reva, S. *New Inverter Output Filter Topology for PWM Motor Drives*, IEEE Transactions on Power Electronics, v 15, n 6, pp. 1007-1017, 2000.
- [Stevandic and Jiang 2003] Stevandic, S. and Jiang, J., *Standalone, Reduced-order Model and Control of a Grid-connected Fuel Cell Power Plant*, IEEE Power Engineering Society General Meeting, Conference Proceedings, v 2, pp. 679-686, 2003.
- [Stiller 2006] Stiller, C., *Design, Operation and Control Modeling of SOFC/GT Hybrid systems*, Doctoral Thesis, Norwegian University of Science and Technology, Trondheim, 2006.
- [Tanaka et al. 2000] Tanaka, K., Wen, C. and Yamada, K., *Design and Evaluation of Combined Cycle System with Solid Oxide Fuel Cell and Gas Turbine*, Fuel, v 79, n 12, pp. 1493-1507, 2000.
- [Tenca et al. 2005] Tenca, P., Stumberger, G. and Lipo, T. A., *Analysis and Modeling of Future Electrical Propulsion and Launch Systems at the Univeristy of Wisconsin - Madison*, IEEE Electric Ship Technologies Symposium, pp. 12-19, 2005.
- [Top et al. 1993] J. Top, J. E. Strömberg, U. Söderman, *Variable Causality in Bond Graph Caused by Discrete Effects*, in: Proceedings for International Conference on Bond Graph modeling, pp. 115-119, San Diego, CA, 1993.
- [Tronstad 2007] Tronstad, T., *Hydrogen Fuel Cell Ship Project On Track for 2008 Demo*, <http://www.greencarcongress.com/2007/08/hydrogen-fuel-c.html>, 2007.
- [Umarikar and Umanand 2005] A. C. Umarikar and L. Umanand, *Modeling of Switching Systems in Bond Graphs Using the Concept of Switched Power Junctions*, Journal of The Franklin Institute 342, pp. 131-147, 2005.
- [Veres] VESSEL RESponse program, *User manual*, Marintek.

- 
- [Wasynczuk et al. 1996] Wasynczuk, O., Sudhoff, S. D., Tran, T. D., Clayton, D. and Hegner, H. J., *A Voltage Control Strategy for Current-Regulated PWM Inverter*, IEEE Trans. on Power Electronics, vol. 11, no. 1, pp. 7-15, 1996.
- [Woodward 2004] Woodward, *Governing Fundamentals and Power Management*, Reference Manual, Woodward Governor Company, web: <http://www.woodward.com/>, 2004.
- [Yoerger et al. 1991] Yoerger, D. R., Cooke, J. G. and Slotine, J. J. E., *The Influence of Thruster Dynamics on Underwater Vehicle Behavior and Their Incorporation Into Control System Design*, IEEE Journal of Oceanic Engineering, Vol 15, n 3, pp. 167-179, 1991.
- [Zhu and Tomsovic 2002] Zhu, Y. and Tomsovic, K., *Development of Models for Analyzing the Load-Following Performance of Microturbines and Fuel Cells*, Electric PowerSystem Research 62, pp. 1-11, 2002.

# Appendix A

## Introduction to Bond Graph Modeling

An introduction to Bond Graph modeling is given next. The literature is found in [Karnopp et al. 2000] and [Pedersen and Engja 2003] and the references therein.

### A.1 Basics

The behavior of a real physical system is controlled by accumulation, dissipation and interchange of various forms of energy. The components or physical phenomena, which make up a system, may be thought of as energy manipulators. Some elements will interact and exchange energy and their interaction points are called power ports. The power interaction between two ports is represented by a single line, the power bond, see Figure A.1. A power bond is considered to conduct power instantaneously and without loss from one port to another.

### A.2 Generalized variables

The power,  $P(t)$ , flowing into or out of a port is expressed as

$$P(t) = e(t)f(t), \quad (\text{A.1})$$

where  $e(t)$  is an effort variable and  $f(t)$  is a flow variable.

Two types of energy variables are important when describing dynamic systems. The energy variables are the generalized momentum,  $p(t)$ , and the generalized displacement,  $q(t)$ , defined as

$$p(t) = \int_0^t e(t)dt = p_0 + \int_{t_0}^t e(t)dt \text{ and} \quad (\text{A.2})$$

$$q(t) = \int_0^t f(t)dt = q_0 + \int_{t_0}^t f(t)dt. \quad (\text{A.3})$$

$p_0$  and  $q_0$  are initial momentum and displacement, respectively.

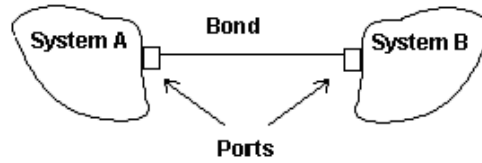


Figure A.1: Basic bonding [Pedersen and Engja 03].

The energy,  $E(t)$ , which has passed into or out of a port from  $t = t_0$  is the time integral of the power flowing in to or out of a port, thus

$$E(t) = \int_0^t P(t) dt = \int_0^t e(t)f(t) dt + E_0, \quad (\text{A.4})$$

where  $E_0$  is initial energy at  $t = t_0$ .

### A.3 Bond graph elements

The bond graph method utilize nine basic elements or building blocks which may represent physical subsystems, components or phenomena in every energy domains. The elements are classified according to their ability to supply, accumulate, dissipate and transfer energy.

Two bond graph elements are used to represent power supply. The effort source,  $S_e$ , maintains the effort independently of the flow, and the flow source,  $S_f$ , maintains the flow independently of the effort. Both elements are ideal.

In the bond graph terminology there are two storage elements, which may store and return energy without loss. The capacitive element stores energy in form of potential energy and is denoted as  $C$ . In the generalized case, the capacitor is characterized by constitutive relations of the form  $q = \phi_C(e)$  and  $e = \phi_C^{-1}(q)$ , where  $\phi_C$  is a general function relating the two variables  $q$  and  $e$ . The inertia element, denoted by  $I$ , is the second energy storage element storing kinetic energy. The constitutive relations are on the form  $p = \phi_I(f)$  and  $f = \phi_I^{-1}(p)$ , where  $\phi_I$  relates  $p$  and  $f$  using a general function.

The next element handles power dissipation and is denoted as  $R$ . The  $R$ -element is characterized by a static relation between  $e$  and  $f$  written in the generalized case as  $e = \phi_R f$  and  $f = \phi_R^{-1} e$ , where  $\phi_R$  is the static function relating  $e$  and  $f$ .

Energy transformation is handled by transformer and gyrator elements. The elements are ideal, meaning that power is conserved and there is no power accumulation during energy transformation. The transformation elements are denoted by  $TF$  and  $GY$ , respectively. The constitutive relations for the transformer

are  $e_1 = me_2$  and  $mf_1 = f_2$ , where  $m$  is the transformer modulus. The gyrator has the following constitutive relations,  $e_1 = rf_2$  and  $rf_1 = e_2$ .  $r$  is the gyrator modulus. Both  $m$  and  $r$  can be functions of time or the energy variables  $p$  and  $q$ . The transformation elements are then denoted *MTF* and *MGY*.

The last two of the nine basic bond graph elements are the junction elements 0-junction and 1-junction. They are defined as power-continuous, they transmit power instantaneously between its ports without storing or dissipating energy. The constitutive relations for the 0-junction are  $e_1 = e_2 = \dots = e_n$  and  $f_1 + f_2 + \dots + f_n = 0$ . The 1-junction has the following relations;  $f_1 = f_2 = \dots = f_n$  and  $e_1 + e_2 + \dots + e_n = 0$ .  $n$  is the number of bonds adjoining the 0 and 1 junctions.

The constitutive relations for the nine basic bond graph elements are summarized in Table A.1.

## A.4 Causality and state equations

There exist both an effort and a flow variable at each port, and either one of the variables may be controlled, but both of them can not be controlled simultaneously. In bond graphs a causal stroke specifies which of the two variables that is input to an element. The causal stroke is a short perpendicular line made at one end of the bond, and it indicates the direction of which the effort signal is directed.

By looking at the constitutive relations for the R element, one may immediately see that the one port resistor may have two different causal strokes. When the causal stroke is on the left side of the power bond, see Figure A.2, the relation is given as  $e = \Phi_R(f)$  where  $f$  is input. If the causal stroke is on the right side of the power bond,  $e$  will be input and the constitutive relation is given as  $f = \phi_R^{-1}(e)$ .

In bond graphs the displacement variable  $q$  and the momentum variable  $p$  are the state variables which completely determines the behavior of the system for any time  $t \geq t_0$  if the initial values  $q_0$  and  $p_0$  are known at  $t = t_0$  and the inputs to the system are known for  $t \geq t_0$ . Thus, the number of *C* and *I* elements with integral causality determines the number of state variables in the system. Figure A.3 shows *C* and *I* elements with integral causality. If the storage elements do not have integral causality, they have derivative casualty, meaning that the energy variable is dependent of other energy variables or source constraints.

Bond graph element	Name	Constitutive relations
<b>Se</b> $\xrightarrow{e}$	Effort source	$e = e(t)$
<b>Sf</b> $\xrightarrow{f}$	Flow source	$f = f(t)$
$\xrightarrow{e} \mathbf{C}$ $\xrightarrow{f}$	Capacitor	General : $q = \Phi_C(e)$ Linear : $q = Ce$
$\xrightarrow{e} \mathbf{I}$ $\xrightarrow{f}$	Inertia	General : $p = \Phi_I(f)$ Linear : $p = If$
$\xrightarrow{e} \mathbf{R}$ $\xrightarrow{f}$	Resistor	General : $e = \Phi_R(f)$ Linear : $e = Rf$
$\xrightarrow{e_1} \mathbf{TF} \xrightarrow{e_2}$ $\xrightarrow{f_1} \quad \quad \quad \xrightarrow{f_2}$	Transformer	$e_1 = e_2 m$ $f_1 m = f_2$
$\xrightarrow{e_1} \mathbf{GY} \xrightarrow{e_2}$ $\xrightarrow{f_1} \quad \quad \quad \xrightarrow{f_2}$	Gyrator	$e_1 = f_2 r$ $f_1 r = e_2$
$\xrightarrow{e_1} \mathbf{0} \xrightarrow{e_2}$ $\xrightarrow{f_1} \quad \quad \quad \xrightarrow{f_2}$ $e_3 \downarrow f_3$	0-function	$e_1 = e_2 = e_3$ $f_1 - f_2 - f_3 = 0$
$\xrightarrow{e_1} \mathbf{1} \xrightarrow{e_2}$ $\xrightarrow{f_1} \quad \quad \quad \xrightarrow{f_2}$ $e_3 \downarrow f_3$	1-junction	$f_1 = f_2 = f_3$ $e_1 - e_2 - e_3 = 0$

Table A.1 : Basic bond graph elements.



Figure A.2: Resistor elements with causal stroke.

Figure A.3:  $C$  and  $I$  elements with integral causality.

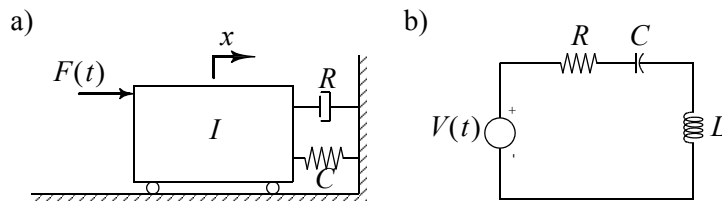


Figure A.4: a) Mass-spring-damper system and b) electric system.

### A.5 Mechanical and electric system example

Two different systems are seen in Figure A.4. In Figure A.4a) a single mass is free to move in the  $x$ -direction. The mass is exposed to a time variant force,  $F(t)$ , a damper force and a spring force. In Figure A.4b) an electric circuit is shown consisting of a voltage source, a resistor, a capacitor and an inductor.

A bond graph representation of the mechanical system is presented in Figure A.5a) The effort source  $S_e$  represents the time variant force, while the resistance element,  $R$ , and the capacitance element,  $C$ , represent the damper and spring force. The  $I$  element represents the inertia of the single mass. The flow source  $S_f$  sets wall velocity. The bond graph is simplified by assuming that the wall is not moving, such that the one junction  $1:w$  is removed. Now, the 0-junctions in connection with the damper and the spring have through-power, thus the 0-junctions may be replaced by single power bonds. The simplified bond graph representation of the mass-damper-spring system is seen in Figure A.5b).

Figure A.6a) shows the bond graph representation of the electric system. The effort source,  $S_e$ , represents the voltage source while the  $R$  element,  $C$  element and the  $I$  element represent the resistor, the capacitor and the inductor, respectively. The bond graph is simplified by deleting the 0-junction representing ground together with all

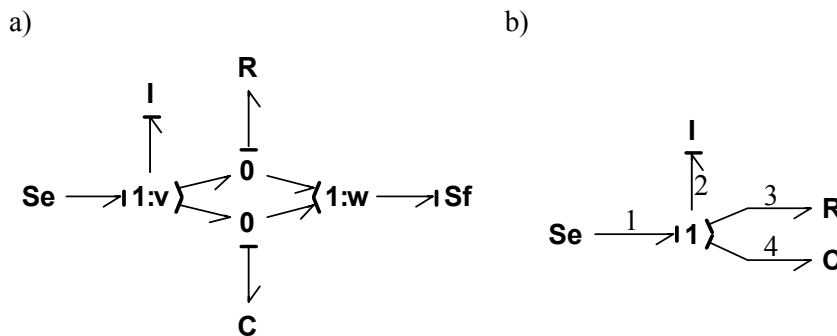


Figure A.5: Bond graph and simplified bond graph representation of mechanical system.



# Appendix B

## Contents of the AES library

The “All Electric Ship” library is divided into five sections, 1) power generation, 2) power consumption, 3) vessel, 4) environment and 5) system examples, see Figure B.1. The different models included in the library are explained in detail in Chapter 3 and Chapter 4.

Next follows a short description of the five library sections with included component models.

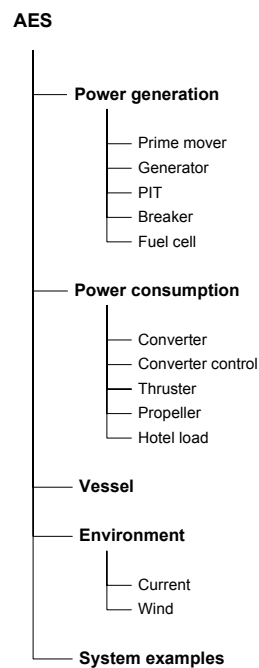


Figure B.1: The AES library.

## B.1 Power generation

The power generation section is divided into five subgroups. The prime mover includes two models of a diesel engine and models of a gas engine and a hybrid engine. The next group, generator, includes five models of a synchronous generator. Four of the generator models have either voltage as output (VO) or current as output (CO). Magnetic saturation (MS) is included in two of the models. The last generator model is a hybrid generator model. The power invariant transformation (PIT) group includes transformation of voltages and currents between the  $dq$ -frame and  $abc$ -frame. The breaker section includes one model of a circuit breaker while the last group includes a model of a solid oxide fuel cell (SOFC).

Figure B.2 shows an overview of the power generation section.

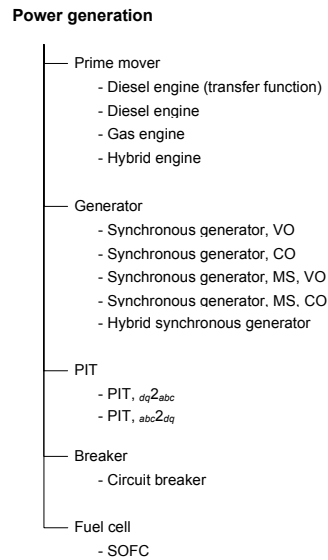


Figure B.2: Power generation.

## B.2 Power consumption

The power consumption section is also divided into five subgroups. The converter group includes an average rectifier model, advanced and average inverter model and an average model of the pulse width modulated (PWM) converter. There exist several methods for controlling the switching of the PWM converter and two control techniques are included in the converter control group, direct torque control and field oriented control. The thruster group includes two models of the asynchronous motor while the propeller group includes three models of the propeller, an one quadrant model, a four quadrant model and a nonlinear dynamic model. One model for hotel and auxiliary load is included in the hotel load group.

Figure B.3 shows an overview of the power consumption section.

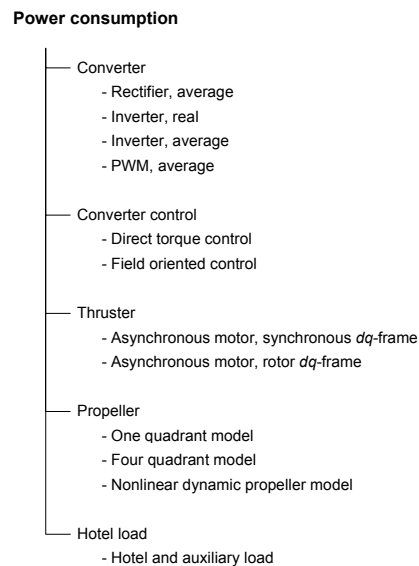


Figure B.3: Power consumption.

### B.3 Vessel

The vessel section includes a three degree of freedom (DOF) ship model, see Figure B.4.

**Vessel**  
- Ship model, 3 DOF

Figure B.4: Vessels.

### B.4 Environment

The environment section includes a current model and a wind model, see Figure B.5.

**Environment**

- Current  
- Current model
- Wind  
- Wind model

Figure B.5: Environment.

### B.5 System models

The last section includes complete system models, see Figure B.6. The models may work as an example of or as a basis for further development of a system model.

**System models**

- Hybrid engine
- Generator model – data verification
- Generator model – magnetic saturation
- 2 generator set connected to hotel loads
- Stand alone fuel cell
- Fuel cell, grid connected
- Asynchronous motor, data verification
- PWM converter, DTC
- PWM converter, FOC
- Propeller
- Naval vessel
- Supply ship

Figure B.6: System examples.

# Appendix C

## Generator

### C.1 Calculation of per unit scaling matrices

The pu system is discussed in [Mittvteit and Nilsen 1987].

When using power invariant transformation, the voltage balance for the transformed model is given as

$$\mathbf{u} = \mathbf{R}\mathbf{i} + \dot{\boldsymbol{\psi}} + \omega_r \mathbf{D}\boldsymbol{\psi}, \quad (\text{C.1})$$

where  $\omega_r$  is rotational speed of the rotor and

$$\mathbf{u} = [u_d \ u_q \ u_f \ 0 \ 0]^T, \boldsymbol{\psi} = [\psi_d \ \psi_q \ \psi_f \ \psi_D \ \psi_Q]^T, \mathbf{i} = [i_d \ i_q \ i_f \ i_D \ i_Q]^T,$$

$$\mathbf{R} = \text{diag}[R_d, R_q, R_f, R_D, R_Q] \text{ and}$$

$$\mathbf{D} = \begin{bmatrix} 0 & -n_p & 0 & 0 & 0 \\ n_p & 0 & 0 & 0 & 0 \\ 0 & 0 & 0 & 0 & 0 \\ 0 & 0 & 0 & 0 & 0 \\ 0 & 0 & 0 & 0 & 0 \end{bmatrix}.$$

$\boldsymbol{\psi}$  is given as

$$\boldsymbol{\psi} = \mathbf{L}\mathbf{i}, \quad (\text{C.2})$$

and the symmetrical inductance matrix  $\mathbf{L}$  is

$$\mathbf{L} = \begin{bmatrix} -L_d & 0 & L_{df} & L_{dD} & 0 \\ 0 & -L_q & 0 & 0 & L_{qQ} \\ -L_{df} & 0 & L_f & L_{fD} & 0 \\ -L_{dD} & 0 & L_{fD} & L_D & 0 \\ 0 & -L_{qQ} & 0 & 0 & L_Q \end{bmatrix}. \quad (\text{C.3})$$

Introducing the diagonal scaling matrices  $\mathbf{S}_u$ ,  $\mathbf{S}_i$  and  $\mathbf{S}_\psi$ , such that

$$\mathbf{u}_{pu} = \mathbf{S}_u \mathbf{u}, \mathbf{i}_{pu} = \mathbf{S}_i \mathbf{i}, \boldsymbol{\psi}_{pu} = \mathbf{S}_\psi \boldsymbol{\psi}. \quad (\text{C.4})$$

Multiplying (C.1) with  $\mathbf{S}_u$  and using (C.4) yields

$$\mathbf{u}_{pu} = \mathbf{S}_u \mathbf{R} \mathbf{S}_i^{-1} \mathbf{i}_{pu} + \mathbf{S}_u \mathbf{S}_\psi^{-1} \dot{\psi}_{pu} + n \omega_n \mathbf{S}_u \mathbf{D} \mathbf{S}_\psi^{-1} \psi_{pu}, \quad (\text{C.5})$$

where  $\omega_r = n \omega_n$ . Letting  $\mathbf{r}_{pu} = \mathbf{S}_u \mathbf{R} \mathbf{S}_i^{-1}$  and  $\mathbf{d}_{pu} = \mathbf{S}_u \mathbf{D} \mathbf{S}_\psi^{-1}$  gives

$$\mathbf{u}_{pu} = \mathbf{r}_{pu} \mathbf{i}_{pu} + \mathbf{S}_u \mathbf{S}_\psi^{-1} \dot{\psi}_{pu} + n_{pu} \omega_n \mathbf{S}_u \mathbf{S}_\psi^{-1} \mathbf{d}_{pu} \psi_{pu}. \quad (\text{C.6})$$

The scaling matrices may be given as

$$\mathbf{S}_\psi^{-1} = \text{diag}[\Psi_{dn}, \Psi_{qn}, \Psi_{fn}, \Psi_{Dn}, \Psi_{Qn}], \quad (\text{C.7})$$

$$\mathbf{S}_u^{-1} = \text{diag}[U_{dn}, U_{qn}, U_{fn}, U_{Dn}, U_{Qn}] \text{ and} \quad (\text{C.8})$$

$$\mathbf{S}_i^{-1} = \text{diag}[I_{dn}, I_{qn}, I_{fn}, I_{Dn}, I_{Qn}]. \quad (\text{C.9})$$

The base values of the stator are chosen to be equal to the rated values per phase of the generator, thus

$$I_{dn} = I_{qn} = I_n \text{ and}$$

$$U_{dn} = U_{qn} = U_n,$$

where  $I_n$  and  $U_n$  are rated values per phase of current and voltage. In addition,

$$\Psi_{dn} = \Psi_{qn} = \Psi_n = \frac{U_n}{\omega_n},$$

to make sure that  $L_{d_{pu}}$  and  $L_{q_{pu}}$  have the same values as  $x_{d_{pu}}$  and  $x_{q_{pu}}$ .

6 more base values may be determined by desiring symmetrical  $\mathbf{L}_{pu}$ -matrix. It is also desirable that the self inductances may be written as a sum of mutual inductance and a leak inductance, thus

$$x_{d_{pu}} = x_{dh_{pu}} + x_{s\sigma_{pu}}, \quad x_{q_{pu}} = x_{qh_{pu}} + x_{s\sigma_{pu}}, \quad x_{f_{pu}} = x_{dh_{pu}} + x_{f\sigma_{pu}}, \quad (\text{C.10})$$

$$x_{D_{pu}} = x_{dh_{pu}} + x_{D\sigma_{pu}} \text{ and } x_{Q_{pu}} = x_{qh_{pu}} + x_{Q\sigma_{pu}}.$$

$\mathbf{L}_{pu}$  may be given as  $\mathbf{L}_{pu} = \mathbf{S}_\psi \mathbf{L} \mathbf{S}_i^{-1}$ , such that

$$\mathbf{L}_{pu} = \begin{bmatrix} -L_d \frac{I_n}{\Psi_n} & 0 & L_{df} \frac{I_{fn}}{\Psi_n} & L_{dD} \frac{I_{Dn}}{\Psi_n} & 0 \\ 0 & -L_q \frac{I_n}{\Psi_n} & 0 & 0 & L_{qQ} \frac{I_{Qn}}{\Psi_n} \\ -L_{df} \frac{I_n}{\Psi_{fn}} & 0 & L_f \frac{I_{fn}}{\Psi_{fn}} & L_{fD} \frac{I_{Dn}}{\Psi_{Dn}} & 0 \\ -L_{dD} \frac{I_n}{\Psi_{Dn}} & 0 & L_{fD} \frac{I_{fn}}{\Psi_{fn}} & L_D \frac{I_{Dn}}{\Psi_{Dn}} & 0 \\ 0 & -L_{qQ} \frac{I_n}{\Psi_{Qn}} & 0 & 0 & L_Q \frac{I_{Qn}}{\Psi_{Qn}} \end{bmatrix}. \quad (\text{C.11})$$

The self inductances may be written as

$$L_d = L_{dh} + L_{s\sigma}, L_q = L_{qh} + L_{s\sigma}, L_f = L_{fh} + L_{f\sigma}, \quad (\text{C.12})$$

$$L_D = L_{Dh} + L_{D\sigma} \text{ and } L_Q = L_{Qh} + L_{Q\sigma}.$$

Combining (C.10), (C.11) and (C.12) gives

$$x_{d_{pu}} = L_d \frac{I_n}{\Psi_n} = (L_{dh} + L_{s\sigma}) \frac{I_n}{\Psi_n} = x_{dh_{pu}} + x_{s\sigma_{pu}} \text{ and} \quad (\text{C.13})$$

$$x_{q_{pu}} = L_q \frac{I_n}{\Psi_n} = (L_{qh} + L_{s\sigma}) \frac{I_n}{\Psi_n} = x_{qh_{pu}} + x_{s\sigma_{pu}}. \quad (\text{C.14})$$

It is desirable that  $\mathbf{L}_{pu}$  is on the form

$$\mathbf{L}_{pu} = \mathbf{x}_{pu} = \begin{bmatrix} -x_{d_{pu}} & 0 & x_{dh_{pu}} & x_{dh_{pu}} & 0 \\ 0 & -x_{q_{pu}} & 0 & 0 & x_{qh_{pu}} \\ -x_{dh_{pu}} & 0 & x_{f_{pu}} & x_{dh_{pu}} & 0 \\ -x_{dh_{pu}} & 0 & x_{dh_{pu}} & x_{D_{pu}} & 0 \\ 0 & -x_{qh_{pu}} & 0 & 0 & x_{Q_{pu}} \end{bmatrix}, \quad (\text{C.15})$$

thus the following equations must be satisfied

$$L_{df} \frac{I_{fn}}{\psi_n} = L_{dh} \frac{I_n}{\psi_n} \Leftrightarrow I_{fn} = \frac{L_{dh}}{L_{df}} I_n, \quad (\text{C.16})$$

$$L_{dD} \frac{I_{Dn}}{\psi_n} = L_{dh} \frac{I_n}{\psi_n} \Leftrightarrow I_{Dn} = \frac{L_{dh}}{L_{dD}} I_n, \quad (\text{C.17})$$

$$L_{qQ} \frac{I_{Qn}}{\psi_n} = L_{qh} \frac{I_n}{\psi_n} \Leftrightarrow I_{Qn} = \frac{L_{qh}}{L_{qQ}} I_n, \quad (\text{C.18})$$

$$L_{df} \frac{I_n}{\psi_{fn}} = L_{dh} \frac{I_n}{\psi_n} \Leftrightarrow \psi_{fn} = \frac{L_{df}}{L_{dh}} \psi_n, \quad (\text{C.19})$$

$$L_{dD} \frac{I_n}{\psi_{Dn}} = L_{dh} \frac{I_n}{\psi_n} \Leftrightarrow \psi_{Dn} = \frac{L_{dD}}{L_{dh}} \psi_n, \quad (\text{C.20})$$

$$L_{qQ} \frac{I_n}{\psi_{Qn}} = L_{qh} \frac{I_n}{\psi_n} \Leftrightarrow \psi_{Qn} = \frac{L_{qQ}}{L_{qh}} \psi_n \text{ and} \quad (\text{C.21})$$

$$L_{fD} \frac{I_{fn}}{\psi_{Dn}} = L_{dh} \frac{I_n}{\psi_n} \Leftrightarrow L_{fD} L_{dh} = L_{dD} L_{df}. \quad (\text{C.22})$$

Next, it is desirable to write the self inductances of the rotor windings as

$$x_{f_{pu}} = x_{fh_{pu}} + x_{f\sigma_{pu}} = x_{dh_{pu}} + x_{f\sigma_{pu}}, \quad (C.23)$$

$$x_{D_{pu}} = x_{Dh_{pu}} + x_{D\sigma_{pu}} = x_{dh_{pu}} + x_{D\sigma_{pu}} \text{ and} \quad (C.24)$$

$$x_{Q_{pu}} = x_{Qh_{pu}} + x_{Q\sigma_{pu}} = x_{qh_{pu}} + x_{Q\sigma_{pu}}, \quad (C.25)$$

such that

$$x_{f_{pu}} = L_f \frac{I_{fn}}{\Psi_{fn}} = (L_{fh} + L_{f\sigma}) \frac{I_{fn}}{\Psi_{fn}} = x_{fh_{pu}} + x_{f\sigma_{pu}}, \quad (C.26)$$

$$x_{D_{pu}} = L_D \frac{I_{Dn}}{\Psi_{Dn}} = (L_{Dh} + L_{D\sigma}) \frac{I_{Dn}}{\Psi_{Dn}} = x_{Dh_{pu}} + x_{D\sigma_{pu}} \text{ and} \quad (C.27)$$

$$x_{Q_{pu}} = L_Q \frac{I_{Qn}}{\Psi_{Qn}} = (L_{Qh} + L_{Q\sigma}) \frac{I_{Qn}}{\Psi_{Qn}} = x_{Qh_{pu}} + x_{Q\sigma_{pu}}, \quad (C.28)$$

which gives

$$L_{fh} \frac{I_{fn}}{\Psi_{fn}} = L_{dh} \frac{I_n}{\psi_n} \Leftrightarrow L_{df} = \sqrt{L_{fh} L_{dh}}, \quad (C.29)$$

$$L_{Dh} \frac{I_{Dn}}{\Psi_{Dn}} = L_{dh} \frac{I_n}{\psi_n} \Leftrightarrow L_{dD} = \sqrt{L_{Dh} L_{dh}} \text{ and} \quad (C.30)$$

$$L_{Qh} \frac{I_{Qn}}{\Psi_{Qn}} = L_{qh} \frac{I_n}{\psi_n} \Leftrightarrow I_{qQ} = \sqrt{L_{qh} L_{Qn}} \quad (C.31)$$

Using (C.29) and (C.30) together with (C.22) gives

$$L_{dh} = \frac{L_{df} L_{dD}}{L_{fD}}, L_{fh} = \frac{L_{df} L_{fD}}{L_{dD}} \text{ and } L_{Dh} = \frac{L_{dD} L_{fD}}{L_{df}}.$$

The basic values for the rotor voltages are determined by choosing  $\mathbf{S}_\psi = \omega_n \mathbf{S}_u$ .

The scaling matrices may now be given as

$$\mathbf{S}_\psi^{-1} = \Psi_n \text{diag} \left[ 1, 1, \frac{L_{fD}}{L_{dD}}, \frac{L_{fD}}{L_{df}}, \frac{L_{qQ}}{L_{qh}} \right],$$

$$\mathbf{S}_u^{-1} = U_n \text{diag} \left[ 1, 1, \frac{L_{fD}}{L_{dD}}, \frac{L_{fD}}{L_{df}}, \frac{L_{qQ}}{L_{qh}} \right] \text{ and}$$

$$\mathbf{S}_i^{-1} = I_n \text{diag} \left[ 1, 1, \frac{L_{dD}}{L_{fD}}, \frac{L_{df}}{L_{fD}}, \frac{L_{qh}}{L_{qQ}} \right].$$

## C.2 Calculation of model parameters

Before calculating model parameters, definitions of transient and sub-transient time constants are presented [Pedersen and Nilsen 1998]. Introducing the Laplace operator for the time derivative of the state space model of the system gives the following expressions for the flux linkages

$$\psi_{d_{pu}}(s) = x_{d_{pu}}(s)i_{d_{pu}}(s) + G_{pu}(s)u_{f_{pu}}(s) \text{ and} \quad (\text{C.32})$$

$$\psi_{q_{pu}}(s) = x_{q_{pu}}(s)i_{q_{pu}}(s). \quad (\text{C.33})$$

Using equations (C.32) and (C.33), the transient and sub transient time constants may be defined as

$$x_{d_{pu}}(s) = \frac{1 + (T_4 + T_5)s + T_4T_6s^2}{1 + (T_1 + T_2)s + T_1T_3s^2}x_{d_{pu}} \equiv \frac{(1 + T_d's)(1 + T_d''s)}{(1 + T_{d0}'s)(1 + T_{d0}''s)}x_{d_{pu}}, \quad (\text{C.34})$$

$$G_{pu}(s) = \frac{1 + T_{D\sigma}s}{1 + (T_1 + T_2)s + T_1T_3s^2} \frac{x_{dh_{pu}}}{r_{f_{pu}}} \equiv \frac{1 + T_{D\sigma}s}{(1 + T_{d0}'s)(1 + T_{d0}''s)} \frac{x_{dh_{pu}}}{r_{f_{pu}}}, \quad (\text{C.35})$$

$$x_{q_{pu}}(s) = \frac{1 + T_q''s}{1 + T_{q0}''s}x_{q_{pu}}. \quad (\text{C.36})$$

$T_1$  to  $T_6$  may be found from the transient and sub transient time constants by solving a non linear system of equations. There are big difference between some of the time constants which makes it possible to find these approximations:

$$T_1 = \frac{x_{dh_{pu}} + x_{f\sigma_{pu}}}{\omega_n r_{f_{pu}}} = \frac{x_{f_{pu}}}{\omega_n r_{f_{pu}}} = T_f \approx T_{d0}', \quad (\text{C.37})$$

$$T_2 = \frac{x_{dh_{pu}} + x_{D\sigma_{pu}}}{\omega_n r_{D_{pu}}} = \frac{x_{D_{pu}}}{\omega_n r_{D_{pu}}} = T_D, \quad (\text{C.38})$$

$$T_3 = \frac{1}{\omega_n r_{D_{pu}}} \left[ x_{D\sigma_{pu}} + \frac{1}{\frac{1}{x_{dh_{pu}}} + \frac{1}{x_{e\sigma_{pu}}}} \right] \approx T_{d0}'', \quad (\text{C.39})$$

$$T_4 = \frac{1}{\omega_n r_{f_{pu}}} \left[ x_{f\sigma_{pu}} + \frac{1}{\frac{1}{x_{dh_{pu}}} + \frac{1}{x_{s\sigma_{pu}}}} \right] \approx T_d', \quad (\text{C.40})$$

$$T_5 = \frac{1}{\omega_n r_{D_{pu}}} \left[ x_{D\sigma_{pu}} + \frac{1}{\frac{1}{x_{dh_{pu}}} + \frac{1}{x_{s\sigma_{pu}}}} \right], \quad (\text{C.41})$$

$$T_6 = \frac{1}{\omega_n r_{D_{pu}}} \left[ x_{D\sigma_{pu}} + \frac{1}{\frac{1}{x_{dh_{pu}}} + \frac{1}{x_{s\sigma_{pu}}} + \frac{1}{x_{f\sigma_{pu}}}} \right] \approx T_d'', \quad (C.42)$$

$$T_{D\sigma} = \frac{x_{D\sigma_{pu}}}{\omega_n r_{D_{pu}}}, \quad (C.43)$$

$$T_{q0}'' = \frac{x_{qh_{pu}} + x_{Q\sigma_{pu}}}{\omega_n r_{Q_{pu}}} = \frac{x_{Q_{pu}}}{\omega_n r_{Q_{pu}}} = T_Q \text{ and} \quad (C.44)$$

$$T_q'' = \frac{1}{\omega_n r_{Q_{pu}}} \left[ x_{Q\sigma_{pu}} + \frac{1}{\frac{1}{x_{qh_{pu}}} + \frac{1}{x_{s\sigma_{pu}}}} \right]. \quad (C.45)$$

Equation (C.37) to (C.45) gives the model parameters used in the  $dq$ -model. In addition to these parameters, the time constants seen from the stator windings are also given:

$$T_a = \frac{1}{r_{s_{pu}} \frac{\omega_n}{2} \left( \frac{1}{x''_{d_{pu}}} + \frac{1}{x''_{q_{pu}}} \right)}. \quad (C.46)$$

The transient and sub transient reactances are defined as

$$x'_{d_{pu}} = x_{s\sigma_{pu}} + \frac{1}{\frac{1}{x_{dh_{pu}}} + \frac{1}{x_{f\sigma_{pu}}}}, \quad (C.47)$$

$$x''_{d_{pu}} = x_{s\sigma_{pu}} + \frac{1}{\frac{1}{x_{dh_{pu}}} + \frac{1}{x_{f\sigma_{pu}}} + \frac{1}{x_{D\sigma_{pu}}}} \text{ and} \quad (C.48)$$

$$x''_{q_{pu}} = x_{s\sigma_{pu}} + \frac{1}{\frac{1}{x_{qh_{pu}}} + \frac{1}{x_{Q\sigma_{pu}}}}. \quad (C.49)$$

Next, parameters for a synchronous generator on board a supply ship are calculated using the above equations.

Data given for a synchronous generator are found in Table C.1.

The stator resistance is first calculated using pu, either by calculating the resistance at  $75^\circ C$  or using the expression for  $T_a$

$$r_{s_{pu}} = \frac{1}{T_a \frac{\omega_n}{2} \left( \frac{1}{x''_{d_{pu}}} + \frac{1}{x''_{q_{pu}}} \right)} = 0.00339.$$

---

Output:	2438 kVA
Power factor:	0.8
Voltage:	690V
Frequency:	60 Hz
Current:	2010 A
Poles:	10
Speed:	720 1/min
Moment of inertia:	331.9 kgm <sup>2</sup>

#### Reactances (pu)

$$x_{d_{pu}}(U) = 1.47, x'_{d_{pu}}(S) = 0.214, x''_{d_{pu}}(S) = 0.178$$

$$x_{q_{pu}}(U) = 1, x''_{q_{pu}}(S) = 0.208, x_{S\sigma_{pu}}(U) = 0.2$$

#### Resistances

$$R_s(75) = 0.00497 \text{ Ohm}$$

$$R_f(75) = 0.315 \text{ Ohm}$$

#### Time constants at 75°C

$$T_{d0} = 1.925, T'_{d0} = 0.008, T_d = 0.281, T''_d = 0.038$$

$$T''_{q0} = 0.05, T''_q = 0.0085, T_a = 0.15$$


---

Table C.1 : Data given for the synchronous generator.

The main reactances are calculated as

$$x_{S\sigma_{pu}} = x_{d\sigma_{pu}} = x_{q\sigma_{pu}} = 0.2,$$

$$x_{d_{pu}} = 1.47,$$

$$x_{dh_{pu}} = x_{d_{pu}} - x_{S\sigma_{pu}} = 1.27,$$

$$x_{q_{pu}} = 1 \text{ and}$$

$$x_{qh_{pu}} = x_{q_{pu}} - x_{S\sigma_{pu}} = 0.8.$$

The leakage- and self-inductances in the field winding may be found from the transient reactance,

$$x_{f\sigma_{pu}} = \frac{x'_{d_{pu}} - x_{s\sigma_{pu}}}{x_{dh_{pu}} - x'_{d_{pu}} + x_{s\sigma_{pu}}} x_{dh_{pu}} = 0.014156 \text{ and}$$

$$x_{f_{pu}} = x_{dh_{pu}} + x_{f\sigma_{pu}} = 1.28416.$$

The damper winding may be found in the same way using sub transient reactances,

$$x_{D\sigma_{pu}} = \frac{1}{\frac{1}{x''_{d_{pu}} - x_{s\sigma_{pu}}} - \frac{1}{x_{f\sigma_{pu}}} - \frac{1}{x_{dh_{pu}}}} = -0.00856,$$

$$x_{D_{pu}} = x_{dh_{pu}} + x_{D\sigma_{pu}} = 1.26144,$$

$$x_{Q\sigma_{pu}} = \frac{1}{\frac{1}{x''_{q_{pu}} - x_{s\sigma_{pu}}} - \frac{1}{x_{qh_{pu}}}} = 0.008081 \text{ and}$$

$$x_{Q_{pu}} = x_{qh_{pu}} + x_{Q\sigma_{pu}} = 0.8081.$$

The resistances in the damper windings may be calculated using transient and sub transient time constants. Using the approximated expressions for the time constants, the resistance values may differ dependent of the use of transient or sub transient values in the calculation. Here, it is decided to use the value which gives largest resistance.

$$r_{D_{pu}} = \frac{1}{\omega_n T_{d0}'} \left[ x_{D\sigma_{pu}} + \frac{1}{\frac{1}{x_{dh_{pu}}} + \frac{1}{x_{f\sigma_{pu}}}} \right] = 0.001805 \text{ and}$$

$$r_{Q_{pu}} = \frac{1}{\omega_n T_q''} \left[ x_{Q\sigma_{pu}} + \frac{1}{\frac{1}{x_{qh_{pu}}} + \frac{1}{x_{f\sigma_{pu}}}} \right] = 0.05245.$$

For the field winding one may use two different approaches to calculate absolute and pu values dependent on data given for the generator. Both methods are shown next.

If the resistance of the field windings are given, the parameters may be calculated as

$$r_{f_{pu}} = \frac{x_{f_{pu}}}{\omega_n T_{d0}'} = 0.00177 [-],$$

$$Z_{fn} = \frac{R_f}{r_f} = 178.033 [\Omega] \text{ and}$$

$$L_f = \frac{x_f}{\omega_n} Z_{fn} = 0.606 [H].$$

The basis for the power may be written as

$$S_n = \frac{U_{fn}^2}{Z_{fn}},$$

which gives

$$U_{fn} = \sqrt{Z_{fn} S_n} = 20834 [V] \text{ and}$$

$$I_{fn} = \frac{U_{fn}}{Z_{fn}} = 117 [A].$$

If the field current is given at rated voltage and the generator is operated at no-load, the parameters may be calculated as

$$I_{fn} = x_{dh_{pu}} I_{f0},$$

$$U_{fn} = \frac{S_n}{I_{fn}} = \frac{S_n}{x_{dh_{pu}} I_{f0}} \text{ and}$$

$$Z_{fn} = \frac{U_{fn}}{I_{fn}} = \frac{U_{fn}}{x_{dh_{pu}} I_{f0}}.$$

The absolute values of the parameters for the field winding may now be calculated as

$$R_f = r_{f_{pu}} Z_{fn} \text{ and}$$

$$L_f = \frac{x_{f_{pu}}}{\omega_n} Z_{fn}.$$

Currents and voltages in the damper winding are not measurable. One may therefore choose one equivalent winding which put up the same field and has the same resistance as the real windings. Letting the equivalent winding have the same basis values as the real windings gives

$$U_{Dn} = U_{Qn} = U_{en},$$

$$I_{DN} = I_{Qn} = I_{en},$$

$$Z_{Dn} = Z_{Qn} = Z_{en},$$

$$R_D = r_{D_{pu}} Z_{Dn} = 0.3214 [\Omega],$$

$$L_D = \frac{x_{D_{pu}}}{\omega_n} Z_{Dn} = 0.5957 [H],$$

$$R_Q = r_{Q_{pu}} Z_{Qn} = 9.3383 [\Omega] \text{ and}$$

$$L_Q = \frac{x_{Q_{pu}}}{\omega_n} Z_{Qn} = 0.3816 [H].$$

Calculation of absolute values of mutual and stator inductances are found using pu values and calculated base-values,

$$L_{df} = x_{dh_{pu}\omega_n} \frac{U_n}{I_{en}} = 0.01622 [H],$$

$$L_{dD} = x_{dh_{pu}\omega_n} \frac{U_n}{I_{Dn}} = 0.01622 [H],$$

$$L_{fD} = x_{dh_{pu}\omega_n} \frac{U_{Dn}}{I_{Dn}} = 0.5998 [H],$$

$$L_{qQ} = x_{qh_{pu}\omega_n} \frac{U_n}{I_{Qn}} = 0.01022 [H],$$

$$L_d = x_{d_{pu}\omega_n} \frac{U_n}{I_n} = 0.0007615 [H] \text{ and}$$

$$L_q = x_{q_{pu}\omega_n} \frac{U_n}{I_n} = 0.0005180 [H].$$

The model parameters are summarized in Table C.2.

$L_d$	0.0007615
$L_D$	0.5957
$L_f$	0.6064
$L_{dD}$	0.01622
$L_{df}$	0.01622
$L_{fD}$	0.5998
$L_q$	0.000518
$L_Q$	0.3816
$L_{qQ}$	0.01022
$R_d$	0.00497
$R_D$	0.3214
$R_f$	0.3150
$R_q$	0.00497
$R_Q$	9.338

Table C.2 : Model parameters for the induction motor.

# Appendix D

## Induction motor

### D.1 Calculation of model parameters

The model parameters may be found from an equivalent circuit model of the induction motor, see Figure D.1. The equivalent circuit model, see e.g. [Sen 1997], may be obtained from the manufacturer or calculated using test results from a no-load test, a blocked rotor test and measurements of the dc resistance of the stator windings.

Data given from a manufacturer of a specific induction motor is shown in Table D.1.

Next, test results from two different tests, a no-load test and a short circuit test, are used to calculate the parameters of the equivalent circuit model. The model parameters of the induction motor are then calculated.

The no-load test is accomplished at rated voltage. The machine runs on no-load with a free shaft extension at rated frequency. Readings of stator voltage, stator current and input power are measured at nominal voltage and given in Table D.2. The short-circuit point test is carried out at rated current with blocked rotor. Readings of stator voltage, stator current and input power at nominal current are given in Table D.3.

The no load test gives information about exciting current and rotational losses. The test is performed by applying balanced polyphase voltages to the stator windings at rated frequency. The rotor is kept uncoupled from any mechanical load. The small power loss in the machine at no load is due to core losses and the friction and winding losses. The blocked rotor test gives information about leakage impedances. In this test the rotor is blocked so that the motor cannot rotate. Balanced polyphase voltages are applied to the stator terminals.

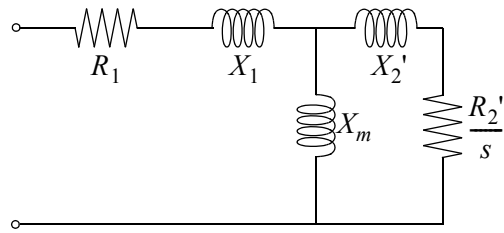


Figure D.1: IEEE-Recommended Equivalent Circuit [Sen 1997].

Rated output:	3300 [kW]
Voltage:	690 [V]
Frequency:	60.3 [Hz]
Speed:	1199 [RPM]
Current:	3270 [A]
Poles:	6
Inertia rotor:	175 [kgm <sup>2</sup> ]

Table D.1: Given data for an induction motor.

No-load point				
$f$ [Hz]	$U_1$ [V]	$I_1$ [A]	$P_1$ [kW]	$p.f.$
60.3	689.0	672.20	25.40	0.032

Table D.2: Reading of frequency, stator voltage, stator current and input power.

Short circuit point				
$f$ [Hz]	$U_1$ [V]	$I_1$ [A]	$P_1$ [kW]	$p.f.$
60.3	177.0	3268.5	115.6	0.115

Table D.3: Reading of frequency, stator voltage, stator current and input power.

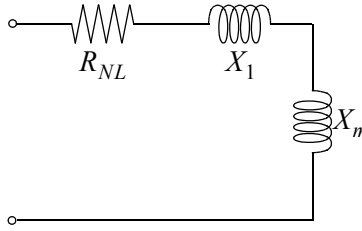


Figure D.2: No load equivalent circuit [Sen 1997].

Blocked rotor resistance is found as

$$R_{BL} = \frac{P_{BL}}{3I_1^2} = \frac{115.6 \cdot 10^3}{3 \cdot 3268.5^2} = 0.003607 [\Omega].$$

The stator resistance was not given in the test result. Instead stator resistance was assumed a little higher than half the blocked rotor resistance. Using the same ratio  $R_1/R_{BL}$  as another induction engine from the same manufacturer gives

$$R_1 = 0.001948.$$

No load rotational loss may be calculated using the readings from Table D.2,

$$P_{Rot} = P_{NL} - 3I_1^2 R_1 = 25.4 \cdot 10^3 - 3 \cdot 672.2^2 \cdot 0.001948 = 22.75 [kW].$$

For the no load condition  $R_2'/s$  is very high, therefore, in the equivalent circuit of Figure D.1, the magnetizing reactance  $X_m$  is shunted by a very high resistive branch representing the rotor circuit. The reactance of this parallel combination is almost the same as  $X_m$ , thus the total reactance  $X_{NL}$  is essentially  $X_1 + X_m$ . The equivalent circuit at no load is shown in Figure D.2

The no load impedance is

$$Z_{NL} = \frac{U_1}{\sqrt{3}I_1} = \frac{689}{\sqrt{3} \cdot 672.2} = 0.5918 [\Omega]$$

and the no load resistance is

$$R_{NL} = \frac{P_{NL}}{3I_1^2} = \frac{25.4 \cdot 10^3}{3 \cdot 672.2^2} = 0.01874 [\Omega].$$

The no load reactance is

$$X_{NL} = \sqrt{Z_{NL}^2 - R_{NL}^2} = \sqrt{0.5918^2 - 0.01874^2} = 0.5915 [\Omega],$$

which gives

$$X_1 + X_m = X_{NL} = 0.5915 [\Omega].$$

For the blocked rotor test the slip is 1. In the equivalent circuit in Figure D.1, the magnetizing reactance  $X_m$  is shunted by the low impedance branch  $jX_2' + R_2'$ . Because  $|X_m| \gg |jX_2' + R_2'|$ , the impedance  $X_m$  can be neglected and the equivalent

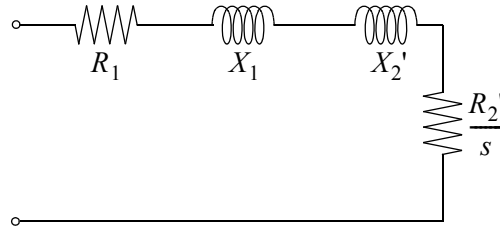


Figure D.3: Equivalent circuit for blocked rotor test [Sen 1997].

circuit for the blocked rotor test reduces to the form shown in Figure D.3.

The rotor resistance is given as

$$R_2' = R_{BL} - R_1 = 0.003606 - 0.001948 = 0.001659 \text{ } [\Omega].$$

The blocked rotor impedance is

$$Z_{BL} = \frac{U_1}{\sqrt{3}I_1} = \frac{177}{\sqrt{3} \cdot 3268.5} = 0.03127 \text{ } [\Omega].$$

The blocked rotor reactance is

$$X_{BL} = \sqrt{Z_{BL}^2 - R_{BL}^2} = \sqrt{0.03127^2 - 0.003606^2} = 0.03106 \text{ } [\Omega].$$

Assuming the same ratio  $X_1/X_2' = 1.35$  as another induction engine from the same manufacturer gives

$$X_{BL} = X_1 + X_2' = X_1 + \frac{1}{1.35}X_1 = 0.03106 \text{ } [\Omega],$$

$$X_1 = 0.01784 \text{ } [\Omega],$$

$$X_2' = 0.01322 \text{ } [\Omega],$$

and the magnetizing reactance is therefore

$$X_m = X_{NL} - X_1 = 0.5915 - 0.01784 = 0.5736 \text{ } [\Omega].$$

The equivalent circuit parameters are summarized in Table D.4.

Parameters for the model may now be calculated based on the equivalent circuit model

$$U_{RMS} = \frac{U}{\sqrt{3}} = 397.8 \text{ } [V],$$

$$I_{RMS} = 3270 \text{ } [A],$$

$$\omega_n = 2\pi f = 2\pi \cdot 60.3 = 378.9 \text{ } [rad/s],$$

$$U_{ref} = \sqrt{2}U_{RMS} = 562.6 \text{ } [V],$$

$$I_{ref} = \sqrt{2}I_{RMS} = 4624 \text{ } [A],$$

Stator resistance, $R_1$	0.001948 [ $\Omega$ ]	Rotor resistance, $R_2'$	0.001659 [ $\Omega$ ]
Stator reactance, $X_1$	0.01784 [ $\Omega$ ]	Rotor reactance, $X_2'$	0.01322 [ $\Omega$ ]
Magnetising reactance, $X_m$	0.5736 [ $\Omega$ ]		

Table D.4: Equivalent circuit parameters.

$$Z_{ref} = \frac{U_{ref}}{I_{ref}} = 0.1216 [\Omega] \text{ and}$$

$$L_{ref} = \frac{Z_{ref}}{\omega_n} = 0.0003211 [H].$$

Inductances are given in p.u. as

$$L_{spu} = x_s = \omega_n \frac{L_2}{Z_{ref}} = \frac{X_s}{Z_{ref}} = \frac{X_m + X_1}{Z_{ref}} = 4.862,$$

$$L_{rpu} = x_r = \frac{X_r}{Z_{ref}} = \frac{X_m + X_2}{Z_{ref}} = 4.824 \text{ and}$$

$$L_{mpu} = x_m = \frac{X_m}{Z_{ref}} = 4.716,$$

and in real values as

$$L_s = L_{spu} \cdot L_{ref} = 0.001561 [H],$$

$$L_r = L_{rpu} \cdot L_{ref} = 0.001549 [H] \text{ and}$$

$$L_m = L_{mpu} \cdot L_{ref} = 0.001514 [H].$$

The resistances are given in real values as

$$R_s = 0.001948 [\Omega] \text{ and}$$

$$R_r = 0.001659 [\Omega].$$

The no load rotational loss is not yet taken care of. Assuming linear friction torque, the rotational loss may be given as

$$P_{rot} = T_{fric} \omega_r = C_{fric} \omega_r^2,$$

where  $C_{fric}$  is friction torque coefficient and  $\omega_r$  is shaft speed. The coefficient becomes

$$C_{fric} = \frac{P_{rot}}{\omega_r^2} = \frac{22.756 \cdot 10^3}{\left(2\pi \cdot \frac{60,3}{3}\right)^2} = 1.427 [Nms/rad],$$

when it is assumed that the slip is approximately 0.

---

$L_s$	0.00156
$L_r$	0.00155
$L_m$	0.00151
$R_s$	0.00195
$R_r$	0.00166
$C_{fric}$	1.427

---

Table D.5: Model parameters for the induction motor.

The model parameters are summarized in Table D.5.

# Appendix E

## Full Scale Measurements

Full scale measurement were carried out during a two days round trip in the North Sea on board Viking Energy operated by Eidesvik [Eidesvik 2008] for StatoilHydro. Viking Energy transports goods and equipment from shore to several platforms in the Gullfaks, Snorre and Statfjord area. The weather was calm and the significant wave height  $H_s$  was not more than 1 [m]. The principal dimensions of the ship are: overall length 94.9 [m], breadth 20.4 [m] and summer draught 7.9 [m].

In the following the full scale measurements are tabulated.

### E.1 Synchronization of three phase generator to bus

#### E.1.1 Generator set 1

Time [s]	Speed [rpm]	Time [s]	Speed [rpm]
0.0	722.2	42.1	725.4
10.0	722.2	45.4	720.5
12.1	725.8	46.8	723.8
16.1	719.5	48.4	722.2
18.4	724.8	50.0	726.4
21.6	719.5	53.2	723.8
25.7	724.8	57.9	725.4
29.8	720.0	65.8	724.3
34.2	724.3	72.1	723.8
38.2	720.5	76.8	724.8

Table E.1 : Speed of generator set 1.

Time [s]	Speed [rpm]	Time [s]	Speed [rpm]
80.0	723.8	95.8	724.3
84.7	7259	101.3	725.9
91.1	725.4		

Table E.2 : Cont. speed of generator set 1.

Time [s]	Voltage [V]	Time [s]	Voltage [V]
0.0	686.6	50.0	691.7
10.0	686.6	53.2	692.7
13.7	691.7	61.1	691.7
16.8	687.1	72.9	691.7
22.0	687.1	76.8	691.2
24.7	689.1	79.2	694.2
27.1	691.7	80.2	691.7
29.5	689.1	83.2	694.2
31.8	692.7	85.5	692.2
36.6	690.7	87.9	691.7
42.1	689.1	95.5	692.2
43.7	691.6	101.3	693.2
46.8	689.1		

Table E.3 : Voltage of generator set 1.

Time [s]	Active power [kW]	Time [s]	Active power [kW]
0.0	1721.5	56.0	1538.6
10.0	1721.5	61.1	1517.1
13.7	1710.7	64.1	1420.2
16.1	1717.2	65.8	1370.8
18.4	1710.7	70.2	1329.9
21.6	1719.4	72.1	1312.7
26.3	1717.2	72.9	1280.4
29.5	1721.5	76.1	1226.6
32.6	1715.01	78.4	1162.0
35.8	1738.7	82.4	1140.5
37.4	1712.9	84.0	1086.7
39.7	1721.5	87.1	1097.5
42.5	1715.0	90.3	1065.2
48.1	1717.2	94.2	1073.8
51.6	1603.2	98.2	1101.8
54.4	1573.0	101.3	1073.8

Table E.4 : Active power of generator set 1.

Time [s]	Reactive power [kVA]	Time [s]	Reactive power [kVA]
0.0	652.7	52.5	444.9
47.7	652.7	54.4	376.2
49.8	517.4	57.3	314.8

Table E.5 : Reactive power of generator set 1.

## E.1.2 Generator set 2

Time [s]	Speed [rpm]	Time [s]	Speed [rpm]
0.0	0.0	50.0	727.5
26.3	0.0	58.7	724.8
31.1	284.6	65.78	723.8
33.4	284.6	71.3	724.8
35.8	456.4	76.1	725.4
37.4	536.9	80.0	723.8
39.3	539.6	84.7	725.9
41.3	638.9	91.1	725.4
42.9	735.6	95.8	724.3
45.6	735.6	101.3	725.9

Table E.6 : Speed of generator set 2.

Time [s]	Voltage [V]	Time [s]	Voltage [V]
0.0	0.0	49.2	697.18
33.0	0.0	51.3	689.63
35.0	422.85	63.4	688.64
35.8	518.49	71.3	689.63
37.4	604.06	89.7	692.15
39.7	651.88	87.1	689.63
42.1	704.73	92.5	694.16
43.7	694.66	101.3	692.65

Table E.7 : Voltage of generator set 2.

Time [s]	Active power [kW]	Time [s]	Active power [kW]
0.0	0.0	73.7	432.5
47.6	0.0	75.0	505.7
49.8	96.8	76.8	516.5
51.6	79.6	79.8	581.0
56.8	152.8	83.1	621.9
58.7	206.6	84.7	682.2
61.8	215.2	87.1	634.8
63.4	322.8	91.1	656.3
65.3	327.1	95.0	634.8
67.1	357.2	97.4	643.4
69.7	376.6	99.0	621.9
71.8	428.2	101.3	626.2

Table E.8 : Active power of generator set 2.

Time [s]	Reactive power [kVA]	Time [s]	Reactive power [kVA]
0.0	0.0	51.5	178.3
47.7	0.0	53.3	229.0
48.7	59.2	55.4	293.9
50.7	120.7	57.3	346.9

Table E.9 : Reactive power of generator set 2.

## E.2 Bow propeller

Time [s]	Power [kW]	Time [s]	Power [kW]
0.0	10.0	59.2	22.7
10.7	10.0	61.6	8.5
11.3	43.3	63.6	0.0
14.5	45.7	66.6	0.0
14.8	30.9	69.8	5.9
16.6	23.5	73.6	9.7
17.1	19.2	76.6	5.6
19.8	10.0	77.7	0.0
21.5	7.9	79.2	0.0
24.2	8.0	79.8	16.4
25.7	7.3	80.1	25.8
28.0	3.8	82.1	38.1
31.8	1.0	83.9	29.3
36.2	1.8	86.2	29.0
39.4	4.0	88.6	16.9
40.8	3.4	90.9	9.5
42.8	2.1	92.4	10.4
43.4	0.0	96.5	5.9
44.9	0.0	100.0	5.6
47.2	10.3	102.5	6.2
47.8	21.2	104.2	8.8
50.5	21.5	106.4	4.2
52.2	33.8	109.2	9.0
55.7	47.1	112.0	15.6
58.1	37.8	112.8	8.6

Table E.10 : Power of bow propeller.

Time [s]	Power [kW]	Time [s]	Power [kW]
113.8	0.0	142.6	0.0
116.0	0.0	143.7	5.0
117.9	17.9	145.9	5.2
119.6	10.2	147.1	3.3
121.7	2.0	149.8	2.4
123.5	29.8	152.7	3.2
124.2	45.0	156.4	12.7
126.2	43.5	158.0	20.1
128.7	55.6	160.8	13.6
130.7	51.1	162.2	14.9
131.5	42.0	164.3	12.4
137.7	0.0	166.5	17.6
139.4	0.0	168.5	11.4
140.1	1.5	172.1	11.0
141.1	0.0		

Table E.11 : Cont. power of bow propeller.

Time [s]	Speed [rpm]	Time [s]	Speed [rpm]
0.0	49.4	21.9	248.5
8.9	49.4	27.8	179.2
10.9	205.2	31.8	135.9
12.9	281.4	34.8	142.9
13.9	352.4	36.8	138.9
14.9	351.4	38.8	153.3
19.9	309.1	40.2	179.2
20.9	257.1	42.0	170.6

Table E.12 : Speed of bow propeller.

Time [s]	Speed [rpm]	Time [s]	Speed [rpm]
44.0	135.9	110.8	196.5
48.0	151.5	112.0	221.7
49.0	258.9	114.0	179.2
53.0	361.0	117.9	-119.5
56.0	431.2	119.9	-102.2
60.0	363.0	121.9	218.2
62.0	240.0	123.5	365.4
63.9	135.9	126.3	434.6
64.9	49.4	130.5	456.3
65.9	-41.6	136.9	304.8
66.9	-139.4	138.5	174.9
68.9	-148.1	140.9	135.9
70.7	-206.1	142.9	-32.9
73.9	-236.4	144.9	-106.5
80.9	265.8	147.8	-132.5
82.5	300.4	150.8	-32.9
84.9	326.4	152.8	162.8
86.8	330.4	156.8	278.8
90.0	300.4	158.6	297.0
91.8	244.2	160.8	300.4
96.6	200.9	164.2	270.1
99.0	196.5	167.0	274.5
101.0	186.2	169.0	270.1
105.4	187.9	170.0	252.8
109.0	183.6	172.0	244.2

Table E.13 : Cont. speed of bow propeller.

**R A P P O R T E R**  
**U T G I T T V E D**  
**INSTITUTT FOR MARIN TEKNIKK**  
**(tidligere: FAKULTET FOR MARIN TEKNIKK)**  
**NORGES TEKNISK-NATURVITENSKAPELIGE UNIVERSITET**

UR-79-01 <u>Brigt Hatlestad</u> , MK:	The finite element method used in a fatigue evaluation of fixed offshore platforms. (Dr.Ing. Thesis)
UR-79-02 <u>Erik Pettersen</u> , MK:	Analysis and design of cellular structures. (Dr.Ing. Thesis)
UR-79-03 <u>Sverre Valsgård</u> , MK:	Finite difference and finite element methods applied to nonlinear analysis of plated structures. (Dr.Ing. Thesis)
UR-79-04 <u>Nils T. Nordsve</u> , MK:	Finite element collapse analysis of structural members considering imperfections and stresses due to fabrication. (Dr.Ing. Thesis)
UR-79-05 <u>Ivar J. Fylling</u> , MK:	Analysis of towline forces in ocean towing systems. (Dr.Ing. Thesis)
UR-80-06 <u>Nils Sandsmark</u> , MM:	Analysis of Stationary and Transient Heat Conduction by the Use of the Finite Element Method. (Dr.Ing. Thesis)
UR-80-09 <u>Sverre Haver</u> , MK:	Analysis of uncertainties related to the stochastic modelling of ocean waves. (Dr.Ing. Thesis)
UR-85-46 <u>Alf G. Engseth</u> , MK:	Finite element collapse analysis of tubular steel offshore structures. (Dr.Ing. Thesis)
UR-86-47 <u>Dengody Sheshappa</u> , MP:	A Computer Design Model for Optimizing Fishing Vessel Designs Based on Techno-Economic Analysis. (Dr.Ing. Thesis)
UR-86-48 <u>Vidar Aanesland</u> , MH:	A Theoretical and Numerical Study of Ship Wave Resistance. (Dr.Ing. Thesis)
UR-86-49 <u>Heinz-Joachim Wessel</u> , MK:	Fracture Mechanics Analysis of Crack Growth in Plate Girders. (Dr.Ing. Thesis)
UR-86-50 <u>Jon Taby</u> , MK:	Ultimate and Post-ultimate Strength of Dented Tubular Members. (Dr.Ing. Thesis)

UR-86-51 <u>Walter Lian</u> , MH:	A Numerical Study of Two-Dimensional Separated Flow Past Bluff Bodies at Moderate KC-Numbers. (Dr.Ing. Thesis)
UR-86-52 <u>Bjørn Sortland</u> , MH:	Force Measurements in Oscillating Flow on Ship Sections and Circular Cylinders in a U-Tube Water Tank. (Dr.Ing. Thesis)
UR-86-53 <u>Kurt Strand</u> , MM:	A System Dynamic Approach to One-dimensional Fluid Flow. (Dr.Ing. Thesis)
UR-86-54 <u>Arne Edvin Løken</u> , MH:	Three Dimensional Second Order Hydrodynamic Effects on Ocean Structures in Waves. (Dr.Ing. Thesis)
UR-86-55 <u>Sigurd Falch</u> , MH:	A Numerical Study of Slamming of Two-Dimensional Bodies. (Dr.Ing. Thesis)
UR-87-56 <u>Arne Braathen</u> , MH:	Application of a Vortex Tracking Method to the Prediction of Roll Damping of a Two-Dimension Floating Body. (Dr.Ing. Thesis)
UR-87-57 <u>Bernt Leira</u> , MR:	Gaussian Vector Processes for Reliability Analysis involving Wave-Induced Load Effects. (Dr.Ing. Thesis)
UR-87-58 <u>Magnus Småvik</u> , MM:	Thermal Load and Process Characteristics in a Two-Stroke Diesel Engine with Thermal Barriers (in Norwegian). (Dr.Ing. Thesis)
MTA-88-59 <u>Bernt Arild Bremdal</u> , MP:	An Investigation of Marine Installation Processes - A Knowledge - Based Planning Approach. (Dr.Ing. Thesis)
MTA-88-60 <u>Xu Jun</u> , MK:	Non-linear Dynamic Analysis of Space-framed Offshore Structures. (Dr.Ing. Thesis)
MTA-89-61 <u>Gang Miao</u> , MH:	Hydrodynamic Forces and Dynamic Responses of Circular Cylinders in Wave Zones. (Dr.Ing. Thesis)
MTA-89-62 <u>Martin Greenhow</u> , MH:	Linear and Non-Linear Studies of Waves and Floating Bodies. Part I and Part II. (Dr.Techn. Thesis)
MTA-89-63 <u>Chang Li</u> , MH:	Force Coefficients of Spheres and Cubes in Oscillatory Flow with and without Current. (Dr.Ing. Thesis)
MTA-89-64 <u>Hu Ying</u> , MP:	A Study of Marketing and Design in

	Development of Marine Transport Systems. (Dr.Ing. Thesis)
MTA-89-65 <u>Arild Jæger</u> , MH:	Seakeeping, Dynamic Stability and Performance of a Wedge Shaped Planing Hull. (Dr.Ing. Thesis)
MTA-89-66 <u>Chan Siu Hung</u> , MM:	The dynamic characteristics of tilting-pad bearings.
MTA-89-67 <u>Kim Wikstrøm</u> , MP:	Analysis av projekteringen for ett offshore projekt. (Licenciat-avhandling)
MTA-89-68 <u>Jiao Guoyang</u> , MR:	Reliability Analysis of Crack Growth under Random Loading, considering Model Updating. (Dr.Ing. Thesis)
MTA-89-69 <u>Arnt Olufsen</u> , MK:	Uncertainty and Reliability Analysis of Fixed Offshore Structures. (Dr.Ing. Thesis)
MTA-89-70 <u>Wu Yu-Lin</u> , MR:	System Reliability Analyses of Offshore Structures using improved Truss and Beam Models. (Dr.Ing. Thesis)
MTA-90-71 <u>Jan Roger Hoff</u> , MH:	Three-dimensional Green function of a vessel with forward speed in waves. (Dr.Ing. Thesis)
MTA-90-72 <u>Rong Zhao</u> , MH:	Slow-Drift Motions of a Moored Two-Dimensional Body in Irregular Waves. (Dr.Ing. Thesis)
MTA-90-73 <u>Atle Minsaas</u> , MP:	Economical Risk Analysis. (Dr.Ing. Thesis)
MTA-90-74 <u>Knut-Arild Farnes</u> , MK:	Long-term Statistics of Response in Non-linear Marine Structures. (Dr.Ing. Thesis)
MTA-90-75 <u>Torbjørn Sotberg</u> , MK:	Application of Reliability Methods for Safety Assessment of Submarine Pipelines. (Dr.Ing. Thesis)
MTA-90-76 <u>Zeuthen, Steffen</u> , MP:	SEAMAID. A computational model of the design process in a constraint-based logic programming environment. An example from the offshore domain. (Dr.Ing. Thesis)
MTA-91-77 <u>Haagensen, Sven</u> , MM:	Fuel Dependant Cyclic Variability in a Spark Ignition Engine - An Optical Approach. (Dr.Ing. Thesis)
MTA-91-78 <u>Løland, Geir</u> , MH:	Current forces on and flow through fish farms.

	(Dr.Ing. Thesis)
MTA-91-79 <u>Hoen, Christopher</u> , MK:	System Identification of Structures Excited by Stochastic Load Processes. (Dr.Ing. Thesis)
MTA-91-80 <u>Haugen, Stein</u> , MK:	Probabilistic Evaluation of Frequency of Collision between Ships and Offshore Platforms. (Dr.Ing. Thesis)
MTA-91-81 <u>Sødahl, Nils</u> , MK:	Methods for Design and Analysis of Flexible Risers. (Dr.Ing. Thesis)
MTA-91-82 <u>Ormberg, Harald</u> , MK:	Non-linear Response Analysis of Floating Fish Farm Systems. (Dr.Ing. Thesis)
MTA-91-83 <u>Marley, Mark J.</u> , MK:	Time Variant Reliability under Fatigue Degradation. (Dr.Ing. Thesis)
MTA-91-84 <u>Krokstad, Jørgen R.</u> , MH:	Second-order Loads in Multidirectional Seas. (Dr.Ing. Thesis)
MTA-91-85 <u>Molteberg, Gunnar A.</u> , MM:	The Application of System Identification Techniques to Performance Monitoring of Four Stroke Turbocharged Diesel Engines. (Dr.Ing. Thesis)
MTA-92-86 <u>Mørch, Hans Jørgen Bjelke</u> , MH:	Aspects of Hydrofoil Design: with Emphasis on Hydrofoil Interaction in Calm Water. (Dr.Ing. Thesis)
MTA-92-87 <u>Chan Siu Hung</u> , MM:	Nonlinear Analysis of Rotordynamic Instabilities in High-speed Turbomachinery. (Dr.Ing. Thesis)
MTA-92-88 <u>Bessason, Bjarni</u> , MK:	Assessment of Earthquake Loading and Response of Seismically Isolated Bridges. (Dr.Ing. Thesis)
MTA-92-89 <u>Langli, Geir</u> , MP:	Improving Operational Safety through exploitation of Design Knowledge - an investigation of offshore platform safety. (Dr.Ing. Thesis)
MTA-92-90 <u>Sævik, Svein</u> , MK:	On Stresses and Fatigue in Flexible Pipes. (Dr.Ing. Thesis)
MTA-92-91 <u>Ask, Tor Ø.</u> , MM:	Ignition and Flame Growth in Lean Gas-Air Mixtures. An Experimental Study with a Schlieren System. (Dr.Ing. Thesis)

MTA-86-92 <u>Hessen, Gunnar</u> , MK:	Fracture Mechanics Analysis of Stiffened Tubular Members. (Dr.Ing. Thesis)
MTA-93-93 <u>Steinebach, Christian</u> , MM:	Knowledge Based Systems for Diagnosis of Rotating Machinery. (Dr.Ing. Thesis)
MTA-93-94 <u>Dalane, Jan Inge</u> , MK:	System Reliability in Design and Maintenance of Fixed Offshore Structures. (Dr.Ing. Thesis)
MTA-93-95 <u>Steen, Sverre</u> , MH:	Cobblestone Effect on SES. (Dr.Ing. Thesis)
MTA-93-96 <u>Karunakaran, Daniel</u> , MK:	Nonlinear Dynamic Response and Reliability Analysis of Drag-dominated Offshore Platforms. (Dr.Ing. Thesis)
MTA-93-97 <u>Hagen, Arnulf</u> , MP:	The Framework of a Design Process Language. (Dr.Ing. Thesis)
MTA-93-98 <u>Nordrik, Rune</u> , MM:	Investigation of Spark Ignition and Autoignition in Methane and Air Using Computational Fluid Dynamics and Chemical Reaction Kinetics. A Numerical Study of Ignition Processes in Internal Combustion Engines. (Dr.Ing. Thesis)
MTA-94-99 <u>Passano, Elizabeth</u> , MK:	Efficient Analysis of Nonlinear Slender Marine Structures. (Dr.Ing. Thesis)
MTA-94-100 <u>Kvålsvold, Jan</u> , MH:	Hydroelastic Modelling of Wetdeck Slamming on Multihull Vessels. (Dr.Ing. Thesis)
MTA-94-102 <u>Bech, Sidsel M.</u> , MK:	Experimental and Numerical Determination of Stiffness and Strength of GRP/PVC Sandwich Structures. (Dr.Ing. Thesis)
MTA-95-103 <u>Paulsen, Hallvard</u> , MM:	A Study of Transient Jet and Spray using a Schlieren Method and Digital Image Processing. (Dr.Ing. Thesis)
MTA-95-104 <u>Hovde, Geir Olav</u> , MK:	Fatigue and Overload Reliability of Offshore Structural Systems, Considering the Effect of Inspection and Repair. (Dr.Ing. Thesis)
MTA-95-105 <u>Wang, Xiaozhi</u> , MK:	Reliability Analysis of Production Ships with Emphasis on Load Combination and Ultimate Strength. (Dr.Ing. Thesis)
MTA-95-106 <u>Ulstein, Tore</u> , MH:	Nonlinear Effects of a Flexible Stern Seal Bag on Cobblestone Oscillations of an SES. (Dr.Ing. Thesis)

MTA-95-107 <u>Solaas, Frøydis</u> , MH:	Analytical and Numerical Studies of Sloshing in Tanks. (Dr.Ing. Thesis)
MTA-95-108 <u>Hellan, øyvind</u> , MK:	Nonlinear Pushover and Cyclic Analyses in Ultimate Limit State Design and Reassessment of Tubular Steel Offshore Structures. (Dr.Ing. Thesis)
MTA-95-109 <u>Hermundstad, Ole A.</u> , MK:	Theoretical and Experimental Hydroelastic Analysis of High Speed Vessels. (Dr.Ing. Thesis)
MTA-96-110 <u>Bratland, Anne K.</u> , MH:	Wave-Current Interaction Effects on Large-Volume Bodies in Water of Finite Depth. (Dr.Ing. Thesis)
MTA-96-111 <u>Herfjord, Kjell</u> , MH:	A Study of Two-dimensional Separated Flow by a Combination of the Finite Element Method and Navier-Stokes Equations. (Dr.Ing. Thesis)
MTA-96-112 <u>Æsøy, Vilmar</u> , MM:	Hot Surface Assisted Compression Ignition in a Direct Injection Natural Gas Engine. (Dr.Ing. Thesis)
MTA-96-113 <u>Eknes, Monika L.</u> , MK:	Escalation Scenarios Initiated by Gas Explosions on Offshore Installations. (Dr.Ing. Thesis)
MTA-96-114 <u>Erikstad, Stein O.</u> , MP:	A Decision Support Model for Preliminary Ship Design. (Dr.Ing. Thesis)
MTA-96-115 <u>Pedersen, Egil</u> , MH:	A Nautical Study of Towed Marine Seismic Streamer Cable Configurations. (Dr.Ing. Thesis)
MTA-97-116 <u>Moksnes, Paul O.</u> , MM:	Modelling Two-Phase Thermo-Fluid Systems Using Bond Graphs. (Dr.Ing. Thesis)
MTA-97-117 <u>Halse, Karl H.</u> , MK:	On Vortex Shedding and Prediction of Vortex-Induced Vibrations of Circular Cylinders. (Dr.Ing. Thesis)
MTA-97-118 <u>Igland, Ragnar T.</u> , MK:	Reliability Analysis of Pipelines during Laying, considering Ultimate Strength under Combined Loads. (Dr.Ing. Thesis)
MTA-97-119 <u>Pedersen, Hans-P.</u> , MP:	Levendefiskteknologi for fiskefartøy. (Dr.Ing. Thesis)
MTA-98-120 <u>Vikestad, Kyrre</u> , MK:	Multi-Frequency Response of a Cylinder Subjected to Vortex Shedding and Support

	Motions. (Dr.Ing. Thesis)
MTA-98-121 <u>Azadi, Mohammad R. E.</u> , MK:	Analysis of Static and Dynamic Pile-Soil-Jacket Behaviour. (Dr.Ing. Thesis)
MTA-98-122 <u>Ulltang, Terje</u> , MP:	A Communication Model for Product Information. (Dr.Ing. Thesis)
MTA-98-123 <u>Torbergsen, Erik</u> , MM:	Impeller/Diffuser Interaction Forces in Centrifugal Pumps. (Dr.Ing. Thesis)
MTA-98-124 <u>Hansen, Edmond</u> , MH:	A Discrete Element Model to Study Marginal Ice Zone Dynamics and the Behaviour of Vessels Moored in Broken Ice. (Dr.Ing. Thesis)
MTA-98-125 <u>Videiro, Paulo M.</u> , MK:	Reliability Based Design of Marine Structures. (Dr.Ing. Thesis)
MTA-99-126 <u>Mainçon, Philippe</u> , MK:	Fatigue Reliability of Long Welds Application to Titanium Risers. (Dr.Ing. Thesis)
MTA-99-127 <u>Haugen, Elin M.</u> , MH:	Hydroelastic Analysis of Slamming on Stiffened Plates with Application to Catamaran Wetdecks. (Dr.Ing. Thesis)
MTA-99-128 <u>Langhelle, Nina K.</u> , MK:	Experimental Validation and Calibration of Nonlinear Finite Element Models for Use in Design of Aluminium Structures Exposed to Fire. (Dr.Ing. Thesis)
MTA-99-129 <u>Berstad, Are J.</u> , MK:	Calculation of Fatigue Damage in Ship Structures. (Dr.Ing. Thesis)
MTA-99-130 <u>Andersen, Trond M.</u> , MM:	Short Term Maintenance Planning. (Dr.Ing. Thesis)
MTA-99-131 <u>Tveiten, Bård Wathne</u> , MK:	Fatigue Assessment of Welded Aluminium Ship Details. (Dr.Ing. Thesis)
MTA-99-132 <u>Søreide, Fredrik</u> , MP:	Applications of underwater technology in deep water archaeology. Principles and practice. (Dr.Ing. Thesis)
MTA-99-133 <u>Tønnessen, Rune</u> , MH:	A Finite Element Method Applied to Unsteady Viscous Flow Around 2D Blunt Bodies With Sharp Corners. (Dr.Ing. Thesis)
MTA-99-134 <u>Elvekrok, Dag R.</u> , MP:	Engineering Integration in Field Development Projects in the Norwegian Oil and Gas Industry. The Supplier Management of Norne. (Dr.Ing.

	Thesis)
MTA-99-135 <u>Fagerholt, Kjetil</u> , MP:	Optimeringsbaserte Metoder for Ruteplanlegging innen skipsfart. (Dr.Ing. Thesis)
MTA-99-136 <u>Bysveen, Marie</u> , MM:	Visualization in Two Directions on a Dynamic Combustion Rig for Studies of Fuel Quality. (Dr.Ing. Thesis)
MTA-2000-137 <u>Storteig, Eskild</u> , MM:	Dynamic characteristics and leakage performance of liquid annular seals in centrifugal pumps. (Dr.Ing. Thesis)
MTA-2000-138 <u>Sagli, Gro</u> , MK:	Model uncertainty and simplified estimates of long term extremes of hull girder loads in ships. (Dr.Ing. Thesis)
MTA-2000-139 <u>Tronstad, Harald</u> , MK:	Nonlinear analysis and design of cable net structures like fishing gear based on the finite element method. (Dr.Ing. Thesis)
MTA-2000-140 <u>Kroneberg, André</u> , MP:	Innovation in shipping by using scenarios. (Dr.Ing. Thesis)
MTA-2000-141 <u>Haslum, Herbjørn Alf</u> , MH:	Simplified methods applied to nonlinear motion of spar platforms. (Dr.Ing. Thesis)
MTA-2001-142 <u>Samdal, Ole Johan</u> , MM:	Modelling of Degradation Mechanisms and Stressor Interaction on Static Mechanical Equipment Residual Lifetime. (Dr.Ing. Thesis)
MTA-2001-143 <u>Baarholm, Rolf Jarle</u> , MH:	Theoretical and experimental studies of wave impact underneath decks of offshore platforms. (Dr.Ing. Thesis)
MTA-2001-144 <u>Wang, Lihua</u> , MK:	Probabilistic Analysis of Nonlinear Wave-induced Loads on Ships. (Dr.Ing. Thesis)
MTA-2001-145 <u>Kristensen, Odd H. Holt</u> , MK:	Ultimate Capacity of Aluminium Plates under Multiple Loads, Considering HAZ Properties. (Dr.Ing. Thesis)
MTA-2001-146 <u>Greco, Marilena</u> , MH:	A Two-Dimensional Study of Green-Water Loading. (Dr.Ing. Thesis)
MTA-2001-147 <u>Heggelund, Svein E.</u> , MK:	Calculation of Global Design Loads and Load Effects in Large High Speed Catamarans. (Dr.Ing. Thesis)

MTA-2001-148 <u>Babalola, Olusegun T.</u> , MK:	Fatigue Strength of Titanium Risers - Defect Sensitivity. (Dr.Ing. Thesis)
MTA-2001-149 <u>Mohammed, Abuu K.</u> , MK:	Nonlinear Shell Finite Elements for Ultimate Strength and Collapse Analysis of Ship Structures. (Dr.Ing. Thesis)
MTA-2002-150 <u>Holmedal, Lars E.</u> , MH:	Wave-current interactions in the vicinity of the sea bed. (Dr.Ing. Thesis)
MTA-2002-151 <u>Rognebakke, Olav F.</u> , MH:	Sloshing in rectangular tanks and interaction with ship motions. (Dr.Ing. Thesis)
MTA-2002-152 <u>Lader, Pål Furset</u> , MH:	Geometry and Kinematics of Breaking Waves. (Dr.Ing. Thesis)
MTA-2002-153 <u>Yang, Qinzhen</u> , MH:	Wash and wave resistance of ships in finite water depth. (Dr.Ing. Thesis)
MTA-2002-154 <u>Melhus, Øyvinn</u> , MM:	Utilization of VOC in Diesel Engines. Ignition and combustion of VOC released by crude oil tankers. (Dr.Ing. Thesis)
MTA-2002-155 <u>Ronæss, Marit</u> , MH:	Wave Induced Motions of Two Ships Advancing on Parallel Course. (Dr.Ing. Thesis)
MTA-2002-156 <u>Økland, Ole D.</u> , MK:	Numerical and experimental investigation of whipping in twin hull vessels exposed to severe wet deck slamming. (Dr.Ing. Thesis)
MTA-2002-157 <u>Ge, Chunhua</u> , MK:	Global Hydroelastic Response of Catamarans due to Wet Deck Slamming. (Dr.Ing. Thesis)
MTA-2002-158 <u>Byklum, Eirik</u> , MK:	Nonlinear Shell Finite Elements for Ultimate Strength and Collapse Analysis of Ship Structures. (Dr.Ing. Thesis)
IMT-2003-1 <u>Chen, Haibo</u> , MK:	Probabilistic Evaluation of FPSO-Tanker Collision in Tandem Offloading Operation. (Dr.Ing. Thesis)
IMT-2003-2 <u>Skaugset, Kjetil Bjørn</u> , MK:	On the Suppression of Vortex Induced Vibrations of Circular Cylinders by Radial Water Jets. (Dr.Ing. Thesis)
IMT-2003-3 <u>Chezian, Muthu</u>	Three-Dimensional Analysis of Slamming. (Dr.Ing. Thesis)
IMT-2003-4 <u>Buhaug, Øyvind</u>	Deposit Formation on Cylinder Liner Surfaces

	in Medium Speed Engines. (Dr.Ing. Thesis)
IMT-2003-5 Tregde, Vidar	Aspects of Ship Design: Optimization of Aft Hull with Inverse Geometry Design. (Dr.Ing. Thesis)
IMT-2003-6 Wist, Hanne Therese	Statistical Properties of Successive Ocean Wave Parameters. (Dr.Ing. Thesis)
IMT-2004-7 Ransau, Samuel	Numerical Methods for Flows with Evolving Interfaces. (Dr.Ing. Thesis)
IMT-2004-8 Soma, Torkel	Blue-Chip or Sub-Standard. A data interrogation approach of identity safety characteristics of shipping organization. (Dr.Ing. Thesis)
IMT-2004-9 Ersdal, Svein	An experimental study of hydrodynamic forces on cylinders and cables in near axial flow. (Dr.Ing. Thesis)
IMT-2005-10 Brodtkorb, Per Andreas	The Probability of Occurrence of Dangerous Wave Situations at Sea. (Dr.Ing. Thesis)
IMT-2005-11 Yttervik, Rune	Ocean current variability in relation to offshore engineering. (Dr.Ing. Thesis)
IMT-2005-12 Fredheim, Arne	Current Forces on Net-Structures. (Dr.Ing. Thesis)
IMT-2005-13 Heggernes, Kjetil	Flow around marine structures. (Dr.Ing. Thesis)
IMT-2005-14 Fouques, Sebastien	Lagrangian Modelling of Ocean Surface Waves and Synthetic Aperture Radar Wave Measurements. (Dr.Ing. Thesis)
IMT-2006-15 Holm, Håvard	Numerical calculation of viscous free surface flow around marine structures. (Dr.Ing. Thesis)
IMT-2006-16 Bjørheim, Lars G.	Failure Assessment of Long Through Thickness Fatigue Cracks in Ship Hulls. (Dr.Ing. Thesis)
IMT-2006-17 Hansson, Lisbeth	Safety Management for Prevention of Occupational Accidents. (Dr.Ing. Thesis)
IMT-2006-18 Zhu, Xinying	Application of the CIP Method to Strongly Nonlinear Wave-Body Interaction Problems. (Dr.Ing. Thesis)
IMT-2006-19 Reite, Karl Johan	Modelling and Control of Trawl Systems.

	(Dr.Ing. Thesis)
IMT-2006-20 Smogeli, Øyvind Notland	Control of Marine Propellers. From Normal to Extreme Conditions. (Dr.Ing. Thesis)
IMT-2007-21 Storhaug, Gaute	Experimental Investigation of Wave Induced Vibrations and Their Effect on the Fatigue Loading of Ships. (Dr.Ing. Thesis)
IMT-2007-22 Sun, Hui	A Boundary Element Method Applied to Strongly Nonlinear Wave-Body Interaction Problems. (PhD Thesis, CeSOS)
IMT-2007-23 Rustad, Anne Marthine	Modelling and Control of Top Tensioned Risers. (PhD Thesis, CeSOS)
IMT-2007-24 Johansen, Vegar	Modelling flexible slender system for real-time simulations and control applications.
IMT-2007-25 Wroldsen, Anders Sunde	Modelling and control of tensegrity structures. (PhD Thesis, CeSOS)
IMT-2007-26 Aronsen, Kristoffer Høye	An experimental investigation of in-line and combined in-line and cross flow vortex induced vibrations. (Dr.avhandling, IMT)
IMT-2007-27 Zhen, Gao	Stochastic response analysis of mooring systems with emphasis on frequency-domain analysis of fatigue due to wide-band processes. (PhD-thesis CeSOS).
IMT-2007-28 Thorstensen, Tom Anders	Lifetime Profit Modelling of Ageing Systems Utilizing Information about Technical Condition.
	Dr.ing. thesis, IMT.
IMT-2008-29 Berntsen, Per Ivar B.	Structural Reliability Based Position Mooring. PhD-Thesis, IMT.
IMT-2008-30 Ye, Naiquan	Fatigues Assessment of Aluminium Welded Box stiffener Joints in ships. Dr.ing.-Thesis, IMT.
IMT-2008-31 Radan, Damir	Integrated Control of Marine Electrical Power Systems. PhD-Thesis, IMT.
IMT-2008-32 Norum, Viggo L.	Analysis of Ignition and Combustion in Otto Lean-Burn Engines with Prechambers. Dr.ing. thesis, IMT.
IMT-2008-33 Pákozdi, Csaba	A Smoothed Particle Hydrodynamics Study of

	Two-dimensional Nonlinear Sloshing in Rectangular Tanks. Dr.ing.thesis, IMT.
IMT-2008-34 Grytøy, Guttorm	A Higher-Order Boundary Element Method and Applications to Marine Hydrodynamics. Dr.ing. Thesis, IMT.
IMT-2008-35 Drummen, Ingo	Experimental and Numerical Investigation of Nonlinear Wave-Induced Load effects in Containerships Considering Hydroelasticity. PhD-Thesis. CeSOS.
IMT-2008-36 Skejic, Renato	Maneuvering and Seakeeping of a Singel Ship and of Two Ships in Interaction. PhD-Thesis. CeSOS.
IMT-2008-37 Harlem, Alf	An Age-Based Replacement Model for Repairable Systems with Attention to High-Speed Marine Diesel Engines. PhD-Thesis, IMT.
IMT-2008-38 Alsos, Hagbart S.	Ship Grounding. Analysis of Ductile Fracture, Bottom Damage and Hull Girder Response. PhD-thesis, IMT.
IMT-2008-39 Graczyk, Mateusz	Experimental Investigation of Sloshing Loading and Load Effects in Membrane LNG Tanks Subjected to Random Excitation. PhD-thesis, CeSOS.
IMT-2008-40 Taghipour, Reza	Efficient Prediction of Dynamic Response for Flexible amd Multi-body Marine Structures. PhD-thesis, CeSOS.
IMT-2008-41 Ruth, Eivind	Propulsion Control and Thrust Allocation on Marine Vessels. PhD-Thesis, CeSOS.
IMT-2008-42 Nystad, Bent Helge	Technical Condition Indexes and Remaining Useful Life of Aggregated Systems. Ph.d.thesis, IMT.
IMT-2008-43 Soni, Prashant Kumer	Hydrodynamic Coefficients for Vortex Induced Vibrations of Flexible Beams, Ph.d.thesis, CeSOS.
IMT-2009-43 Amlashi, Hadi K.K.	Ultimate Strength and Reliability-based Design of Ship Hulls with Emphasis on Combined Global and Local Loads. Ph.d-Thesis, IMT.